Canadian & Cold Regions Rail Research Conference 2024

SECOND CANADIAN & COLD REGIONS RAIL RESEARCH CONFERENCE

April 9 - 10, 2024
Edmonton, AB, Canada

CANADIAN RAIL RESEARCH LABORATORY

UNIVERSITY OF ALBERTA

SECOND CANADIAN AND COLD REGIONS RAIL RESEARCH CONFERENCE

April 9 - 10, 2024

Edmonton, AB, Canada

Proceedings of the Second Canadian and Cold Regions Rail Research Conference

9-10 April 2024, Edmonton, AB, Canada

Second Canadian and Cold Regions Rail Research Conference

Edited by

Dr. Parisa Haji Abdulrazagh, Dr. Michael T. Hendry & Dr. Renato Macciotta Pulisci

University of Alberta Canadian Rail Research Laboratory

University of Alberta Canadian Rail Research Laboratory Edmonton, Alberta, Canada

Published by: University of Alberta, Dept. of Civil & Environmental Engineering

ISBN 978-1-55195-513-1
Printed in Canada

FORWARD

It is with great pleasure that we present the Proceedings of the **Second Canadian & Cold Regions Rail Research Conference 2024 (CCRC 2024)**. Recognizing the need to bring together railroaders, regulators and researchers working in Canada and cold regions in one venue to share their expertise and innovative work, the CCRC 2024 Organizing Committee convened a Technical Committee with representatives from industry, government and academia to create this conference.

The Canadian Rail Research Laboratory (CaRRL) at the University of Alberta is proud to be the host and organizer of CCRC 2024. Established in 2010 by the Railroad Research Advisory Board, Transport Canada, and Canada's railway sector, CaRRL facilitates close collaboration among researchers, industry and government, and identifies emerging technologies for the improvement of safety, reliability, sustainability and economic feasibility of rail transportation. Dr. Michael T. Hendry is the Director of CaRRL and holds the NSERC Industrial Research Chair in Railway Engineering. Dr. Renato Macciotta Pulisci is the Associate Director of CaRRL, and Dr. C. Derek Martin served as inaugural Program Director and concurrently held the NSERC Industrial Research Chair in Railway Geomechanics and the Alberta Innovates – Technology Futures Tier One Industry Chair in Railway Geomechanics.

The aim of CCRC 2024 is to provide opportunities for professionals and researchers involved with railway engineering to present ideas, learn of new developments and technologies, make professional contacts and discuss issues related to railway engineering in Canada and cold regions. The Proceedings of CCRC 2024 represents the current state-of-practice in Canada's rail transportation sector. We are grateful for the authors and presenters who responded enthusiastically to the call for papers; their papers in the Proceedings benefit the Canadian rail sector and the public it serves through providing technical knowledge for current practitioners and educating the next generation of science and engineering students for careers in rail.

We would like to acknowledge the sponsors of CCRC 2024 who recognize the significant contribution of this conference to meeting the challenges of this most important industry—thank you for your support. We want to personally thank members of CaRRL and the Technical Committee for their encouragement and support. The conference would not have been possible without the dedication of Reza Mousapour, Dr. Parisa Haji Abdulrazagh, Jen Stogowski and Vivian Giang who provided so much assistance and leadership.

The importance of rail transportation to both the Canadian economy and the quality of life enjoyed by Canadians is significant. It was with this in mind that the session themes and manuscripts were selected for presentation and inclusion in the Proceedings. May you find further insights to enhance your understanding of the current state-of-practice in the rail industry through CCRC 2024.

Reza Mousapour, Parisa Haji Abdulrazagh, Michael T. Hendry and Renato Macciotta Pulisci
Co-Chairs, CCRC 2024 Organizing Committee

Canadian & Cold Regions Rail Research Conference 2024

Organizing Committee

Michael T. Hendry
Associate Professor, Faculty of Engineering, University of Alberta

Vivian Giang
Strategist (Communications/Grants/Events) University of Alberta

Renato Macciotta
Assistant Professor, Faculty of Engineering University of Alberta

Reza Mousapour
PhD Graduate Student University of Alberta

Parisa Haji Abdulrazagh
Chief Technology Officer, Matrix Engineering & Trading Ltd.

Jen Stogowski
Research Administrator University of Alberta

Technical Committee

Will Anthony
Christine Backs
Dan Blais
David Brown
Ben Chursinoff
Dominika Dubinsky
Vivian Giang
Janet Greene
Parisa Haji Abdulrazagh
Michael Hendry
Brooke Jones
Garrett King
Matthew Krech
Renato Macciotta
Paul Miller
Reza Mousapour
Alireza Roghani
Jen Stogowski
Liam Vass
Albert Wahba
Yi Wang

Thank you to our reviewers!

Dan Blais
David Brown
Ben Chursinoff
Dominika Dubinsky
Janet Greene
Parisa Haji Abdulrazagh
Brooke Jones
Paul Miller
Alireza Roghani
Albert Wahba
Yi Wang

Canadian & Cold Regions
Rail Research Conference
2024

Thank you to our sponsors!

PLATINUM

CPKC

Transport Canada

Transports Canada

SILVER

BGC

BOSSPAC

CN

PARADOX

Railmetrics

Railway Association of Canada

Association des chemins de fer du Canada

BRONZE

THE CANADIAN GEOTECHNICAL SOCIETY
LA SOCIÉTÉ CANADIENNE DE GÉOTECHNIQUE
Transportation Geotechnique Committee

COPPER

MET

TABLE OF CONTENTS

KEYNOTE PRESENTATIONS & SPECIAL PANEL

KEYNOTE PRESENTATION: ONE RAILROAD CONNECTED
Gordon Trafton (CPKC) 2

KEYNOTE PRESENTATION: RAIL DECARBONIZATION AND CLIMATE RESILIENCY – A BUSINESS PERSPECTIVE
Janet Drysdale (Canadian National Railway) 3

PANEL DISCUSSION: IMPACTS OF CLIMATE CHANGE ON RAILWAY INFRASTRUCTURE — HOW TO ADAPT?
Parisa Haji Abdulrazagh, Luc Faucher & Chris Bunce 4

SESSION 1: CLIMATE CHANGE RESILIENCY

WILDFIRE HAZARD IDENTIFICATION AND RISK ASSESSMENT FOR RAILWAY INFRASTRUCTURE
Maziar Jamshidi, Asdrubal Cheng Cen, Nima Shirzad & Mustafa Gül 6

OPERATIONAL RISK AWARENESS MATRIX FOR EXTREME WEATHER TRIGGERED GROUND HAZARD EVENTS IN BC
Tim Keegan, Christian Sampaleanu, Chris Johnson, Matt Cormier, David Brown & Trevor Evans 12

QUANTITATIVE ANALYSIS OF THE IMPACT OF CLIMATE CHANGE ON ROCKFALL HAZARDS IN BRITISH COLUMBIA
Nima Mirhadi & Renato Macciotta 20

SESSION 2: COLD REGIONS ENGINEERING

A PROPOSAL FOR TESTING CHEMICAL DEICERS AIMED TO USE ON THE THIRD RAILS IN WINTER
Jean-Denis Brassard & Gelareh Mome 27

BROKEN RAIL DETECTION IN DARK TERRITORY: APPLICATION
Dominika Juhaszova, Ali Al-Chaer, Sukhraj Kooner & Kyle R Mulligan 32

FREIGHT CAR AIR BRAKE SYSTEM PERFORMANCE IN COLD TEMPERATURES
Elton Toma, Alok Jahagirdar, Stephen Mackie & Albert Wahba 40

EVALUATING THE LONG-TERM IMPACT OF THERMOSYPHONS FOR EMBANKMENT STABILIZATION ON THE HUDSON BAY RAILWAY
Adam Gareau, Brett Young & Ryley Beddoe 48

SESSION 3: HUMAN FACTORS AND SAFETY

MENTAL WORKLOAD ASSESSMENT AND PREDICTION FOR TRAIN OPERATORS
Mona Ahmadi Rad, Lianne M. Lefsrud & Michael Hendry 57

INVESTIGATING THE EFFECTIVENESS OF MACHINE VISION-BASED RAILCAR INSPECTION TECHNOLOGY
Solange de Blois, Chathula Adikary, Brian Zou, Alireza Roghani, Yan Liu & Samy Metari 65

MACHINE VISION TO INSPECT AND ANALYZE TRACK CONDITION: AN OPPORTUNITY TO PERFORM PREDICTIVE MAINTENANCE ON RAIL JOINTS
Luc Faucher, Tony Ducheman, Mathieu Cody, Dave Arsenault, Simon-Olivier Vaillancourt, Guillaume Servat, David Hébert & Dominique Sirois 71

THE EFFECT OF BRAKE PIPE FLOW ON BRAKE CYLINDER PRESSURE
Yi Wang 76

SESSION 4: RISK AND RELIABILITY

3D-INSAR VELOCITY ANALYSIS: A CASE STUDY OF THOMPSON RIVER VALLEY
Sohrab Sharifi, Renato Macciotta & Michael Hendry 83

DEVELOPMENT OF A SCALABLE SEMI-QUANTITATIVE WASHOUT RISK ASSESSMENT FRAMEWORK
Patrick Grover, Sterling Mitchell, Pascal Szeftel, David Brown & Trevor Evans 91

INVESTIGATION ON THE EFFECT OF HYPERBOLIC HEAT CONDITION ON HIGH STRENGTH RAIL STEELS
Stephen Okocha, P.-Y. Ben Jar, Michael Hendry & Feng Yu 100

SESSION 5: INNOVATION AND EMERGING TECHNOLOGIES IN RAILWAY

AUTOMATED SENSING DATA ANALYSES FOR RAILWAY TRACK GAUGE MONITORING AND DEFECT DETECTION
Tangjian Wei, Yili (Kelly) Tang, Xinyu Liu, Oliver Wang, Juan Hiedra Cobo & Mohamed Zaki Hussein 109

COMPARATIVE INVESTIGATION OF FIELD MEASURED INSERTION LOSS OF RAILWAY TRACK WITH FEM AND 1-DOF THEORETICAL MODELS
M. Hassan Esmaeili, Reza Mousapour & Yazdan M. Haft-Cheshmeh *114*

A QUANTITATIVE EVALUATION OF THE IMPACT OF RAILWAY TRACK CHARACTERISTICS ON THE MAGNITUDE OF DYNAMIC LOADS
Danial Behnia & Michael T. Hendry *120*

SESSION 6: COLD REGIONS ENGINEERING

INVESTIGATION OF TIE PLATE ICING/ICE JACKING
Yin Gao & Dingqing Li *130*

EFFECTS OF COLD TEMPERATURE ON ULTRASONIC RAIL FLAW TESTING
Survesh Shrestha, Anish Poudel & Glenn Washer *140*

PERFORMANCE-BASED DESIGN PRINCIPLES IN COLD REGIONS: A REVIEW OF NORTH AMERICAN RAILWAY DESIGN STANDARDS
Payman Yousefi Mojir & Reza Mousapour *148*

EFFICACY OF GEOCELL MODULUS IN REDUCING DYNAMIC LOAD FACTOR ON RAILWAY TRACK SUBJECTED TO FREEZE-THAW
Arghya Chatterjee, Sanat Pokharel & Marc Breault *155*

SESSION 7: INNOVATION AND EMERGING TECHNOLOGIES IN RAILWAY

RAIL MONITORING SYSTEM
John Wallace *164*

ADVANCED TECHNOLOGY IN RAILWAY TRACK MONITORING USING THE GPR TECHNIQUE: A REVIEW
Farhad Kooban, Aleksandra Radlińska, Reza Mousapour & Maryam Saraei *168*

AUTOMATING TRACK INSPECTION THROUGH USING AN INSTRUMENTED HI-RAIL TRUCK
Alireza Roghani, Taufiq Rahman, Samy Metari, Abdelhamid Mammeri & Sylvie Chenier *176*

SESSION 8: RENEWABLE POWER SOLUTIONS & INNOVATION AND EMERGING TECHNOLOGIES IN RAILWAY

A COMPARATIVE LIFE CYCLE SUSTAINABILITY ANALYSIS OF HYDROGEN-POWERED AND DIESEL LOCOMOTIVES
Lizette Correa-Carrillo, Kasun Hewage, Faran Razi & Rehan Sadiq *181*

NON-DESTRUCTIVE APPROACH FOR HIGH STRENGTH RAIL STEEL CHARACTERIZATION USING BALL INDENTATION APPROACH
Stephen Okocha, P.-Y. Ben Jar, Michael Hendry & Feng Yu *188*

INJECTION OF POLYURETHANE FOAM FOR SOIL STABILIZATION AS PART OF A SHORT LINE RAILWAY BRIDGE WALL REPAIR
Rachel Mackenzie, Wayne Bacon & Evan Manning *196*

KEYNOTE PRESENTATIONS

ONE RAILROAD CONNECTED presented by:

Gordon Trafton

Chair, Risk and Sustainability Committee and Member, Integration Committee
Canadian Pacific Railway

Gordon Trafton's rail industry career spans nearly five decades, five railroads, four countries, and two continents. He has held positions of increasing and varied responsibility, from Operations management trainee through to his current roles as a Board member and Board Committee chair. Mr. Trafton has served in leadership positions at Burlington Northern Railroad (now BNSF), Illinois Central Railroad (now part of CN), Canadian National Railway and Canadian Pacific Railway (now CPKC). During his career, he has held senior executive positions in operations, marketing, and various aspects of corporate strategy. He has been responsible for key areas related to six mergers and acquisitions.

In 2017, Mr. Trafton joined the board of Canadian Pacific Railway (now CPKC) where today, he serves as Chair of the Risk and Sustainability Committee and is a member of the Integration Committee. In 2023, he became a board member of Pacific National, Australia's largest railroad, and currently serves as a member of the Health, Safety, and Environment Committee. Mr. Trafton holds a Bachelor of Science degree in Transportation and Traffic Management from the Leeds School of Business at the University of Colorado Boulder. As part of his philanthropic portfolio, he serves on the advisory board of his alma mater.

RAIL DECARBONIZATION AND CLIMATE RESILIENCY – A BUSINESS PERSPECTIVE presented by:

Janet Drysdale

Senior Vice-President & Chief Stakeholder Relations Officer
Canadian National Railway

Janet Drysdale is a seasoned and versatile executive with nearly 30 years of cross-functional leadership in the transportation industry having held executive positions in Finance, Sustainability, Corporate Development, and Investor Relations. Ms. Drysdale was appointed Senior Vice-President & Chief Stakeholder Relations Officer in March 2023. She is responsible for driving CN's stakeholder engagement and communications strategies and has direct accountability for North American public and government affairs, media relations, corporate communications, and investor relations. Ms. Drysdale has long been an advocate for the rail industry and North America's critical supply chains, increasing the representation of women in rail, and the transition to a low carbon economy.

Ms. Drysdale is an independent director of RumoS.A., Brazil's largest freight railway. She also sits on the boards of the Railway Association of Canada and the Canadian-American Business Council. In 2020, Ms. Drysdale was recognized by WXN as one of Canada's Top 100 Most Powerful Women in the executive leadership category, and by Railway Age for her leadership, collaboration, and innovation. Ms. Drysdale holds an Honours Bachelor of Science degree from Queen's University and an MBA from McGill University. In 2021, Ms. Drysdale completed the Global Competent Boards ESG program and certification (GCB.D).

PANEL DISCUSSION: IMPACTS OF CLIMATE CHANGE ON RAILWAY INFRASTRUCTURE – HOW TO ADAPT?

MODERATOR:

Paul Miller, MScE

PANEL SPEAKERS:

Parisa Haji Abdulrazagh, PhD

Luc Faucher, PhD

Chris Bunce, PhD

Session 1

CLIMATE CHANGE RESILIENCY

Canadian & Cold Regions
Rail Research Conference
2024

Wildfire hazard identification and risk assessment for railway infrastructure

Maziar Jamshidi, Asdrubal Cheng Cen, Nima Shirzad, & Mustafa Gül
Department of Civil & Environmental Engineering – University of Alberta, Edmonton, Alberta, Canada

ABSTRACT

Climate change has exacerbated the adverse impacts on both natural and built environments, with Canada experiencing warming at a rate double the global average, resulting in heightened occurrences of severe disasters such as floods, hurricanes, and wildfires. Among these, wildfires have recently emerged as a major concern. Canada's railway networks, essential for transportation and commerce, are increasingly vulnerable to the adverse impacts of wildfires, necessitating effective risk assessment methodologies. In response to this critical need, this research aims to develop a comprehensive and automated framework for assessing wildfire-related risks specifically targeting critical railway infrastructure. This project adopts a two-fold approach: firstly, the development of a methodology for exposure assessment and micro mapping of fuels, which entails identifying and compiling essential data from satellite and aerial images such as topography analysis and tree detection; and secondly, the deployment of an image capture system to collect and analyze ground level data to be employed for a more detailed and up-to-date fire behavior assessment, considering fuel conditions and seasonality effects. This data will serve as the foundation for training computer vision models to identify crucial parameters related to wildfire risks, including tree types and geometries as well as ground vegetation condition. In addition, seasonal indicators, such as the timing of spring snowmelt and tree leaf-out, both pivotal markers for the onset of the spring fire season will be captured in near real-time, enabling timely decision-making to enhance wildfire response efforts. Our approach, centered on deep learning and computer vision, seeks to provide continuous and updated insights into these critical indicators, complementing conventional data sources. Ultimately, this research endeavor enhances the safety and resilience of railway networks in the face of mounting wildfire threats, offering a comprehensive, data-driven solution to mitigate the adverse impacts of climate change on vital transportation infrastructure.

1 INTRODUCTION

Climate change imposes adverse effects on both built and natural environments. In Canada, the rate of warming surpasses the global average, resulting in a heightened occurrence of major disasters, including wildfires, which have increased in frequency over recent decades (Wotton et al., 2010; Bowman et al., 2020). Particularly, railway systems have experienced adverse impacts from wildfires in the past. Additionally, they face limited routing options when a critical element of rail infrastructure, such as a bridge, is damaged and rendered inoperable. Therefore, given the susceptibility of railway infrastructure to wildfire risks the railway industry stands to gain significantly from the timely development of methodologies for assessing wildfire-related risks and hazards.

A key component of railway operators' plans for the prevention and control of wildfires involves identifying and addressing fire hazards. For instance, the rules and regulations of Transport Canada obligate operators to have procedures in place to limit the growth of combustible vegetative fuels in railroad right-of-way and rail yards (Transport Canada, 2022). Additionally, it is common for railway owners to utilize available weather and fire risk forecasts produced by government agencies to monitor risk levels (Canadian Pacific Railway, 2022). However, these forecasts are generated based on forest attributes at the national scale, and their moderate resolution and limited scope of input data may render them less suitable for operational fire management (Beaudoin et al., 2014; Natural Resources Canada, 2024).

To address this limitation, the objective of this study is to propose a framework for wildfire risk assessment which involves the fusion of high-resolution satellite-based Earth observation data with ground-based visual data. The output of this framework includes responsive localized maps of risk indices that meet the necessary geographical and temporal scopes of wildfire hazard and exposure assessment for the railway infrastructure.

2 FIRE RISK ASSESSMENT OVERVIEW

Figure 1 illustrates an overview of the proposed fire risk assessment framework. Following the procedure outlined in the Canadian Forest Fire Behavior Prediction (FBP) system (Forestry Canada, 1992) in order the be able to assess the fire exposure to rail tracks and its critical infrastructure (e.g., bridges, stations, etc.) three categories of information are required, namely, the characteristics of the vegetative flammable fuels in the surrounding zones, weather parameters of the regions, and the topography of the terrain. The compounding effects of these factors determine the severity of the risk posed to the railroad in different locations and at different times of the year.

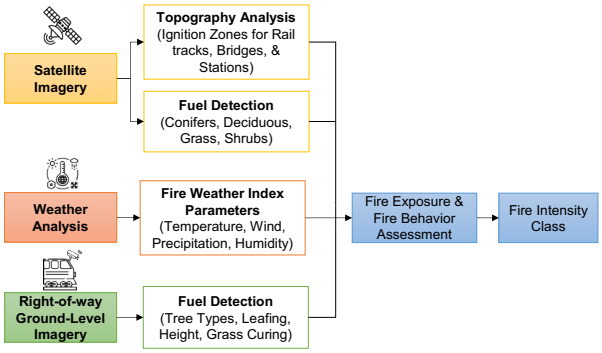

Figure 1. Overview of the proposed framework for railroad fire risk assessment

The Canadian Forest Fire Weather Index (FWI) System (Wagner, 1987) incorporates various weather parameters for analysis. These parameters include temperature, precipitation, humidity, wind intensity, and direction. The variables used in the FWI system can be acquired or estimated with reasonably proper spatial and temporal resolutions using data from weather stations provided by government agencies. Topography analysis involves determining the elevation, slope, and aspect of the terrain surrounding the railroad or infrastructure. This is accomplished by overlaying the geospatial databases of the national elevation maps and railway systems to predict fire behavior. This type of analysis is also essential to define the "Ignition Zones" around the railroad and its infrastructure determining their exposure to wildfire, and enabling the prioritization of wildfire risk mitigation efforts (Partners in Protection, 2003).

A crucial piece of information that drives the hazard and exposure of wildfire is the abundance of vegetative fuels as well as their characteristics and conditions. In addition to the extent of the vegetated land cover, it is essential to identify its species composition and structure (e.g., age, height, biomass, etc.) to determine the potential risk they pose to the surrounding environment. To address this, research efforts have primarily focused on remote sensing and satellite imagery. Earth observation missions conducted by major space agencies, such as the European Space Agency's Sentinel-2 and NASA's MODIS satellites, have provided researchers with open-access data regarding the Earth's surface, offering resolutions suitable for generating national-level vegetative fuel maps (e.g., (Pouliot et al., 2009; Stefanidou et al., 2022)).

When it comes to operational fire management at a scale pertinent to the rights-of-way around the railway system, higher-resolution fuel maps appear to be essential. Without such maps, the uncertainty in the existing maps may introduce inaccuracies in subsequent risk analysis. On the other hand, satellite images from commercial providers, such as Maxar Technologies, typically offer higher resolutions. Therefore, this source can be leveraged to investigate fuel composition.

3 VEGETATIVE FUEL DETECTION USING SATELLITE IMAGERY

In this study, the region of interest is selected from railway segments in the province of Alberta. For this region classified as Boreal Plains and Prairies ecozones, the dominant types of vegetative fuels—based on FBP system classification—are deciduous forest, conifer forest, and grass. Descriptions for each fuel class are provided in Table 1.

Table 1. Vegetative fuel classes

Fuel type	Description
Deciduous forest	trembling aspen; white birch; balsam poplar trees; medium to tall shrubs and herb layers
Conifer forest	spruce; jack or lodgepole pine
Grass	continuous standing or matted grass

Numerous studies have focused on the automated labeling of georeferenced satellite images, encompassing both visible and invisible wavelengths, for fuel detection (Alipour et al., 2023; Beaudoin et al., 2014; Tomppo et al., 2008; Wilson et al., 2012). These studies adopt statistical and machine learning methods to impute various attributes of vegetated land cover. Convolutional Neural Networks (CNNs) stand out as supervised deep neural networks extensively applied in various applications, with semantic segmentation being a notable example. In semantic segmentation, CNN-based models are trained to label every pixel in an image with a prescribed class or category. In the context of vegetative fuel detection, this means identifying the collections of pixels that belong to a specific fuel type. Therefore, with a dataset of images pre-labeled for specific fuel types, these networks can learn and extract relevant features from input images and become experts in distinguishing those fuel types in new, out-of-sample images.

In this study, the DeepLab segmentation network, developed by Chen et al. (2018), is utilized to identify vegetative fuel types described in Table 1 in satellite images. The details of the network and its architecture are presented in Figure 2. As illustrated, ResNet-50 (He et al., 2015) is chosen as the backbone feature extractor network in the encoder path of the model. Additionally, the Atrous Spatial Pyramid Pooling layer in the encoder enables the extraction of multi-scale information from the features obtained by the backbone. Further details of the operation within the network can be found in the work by Chen et al. (2018).

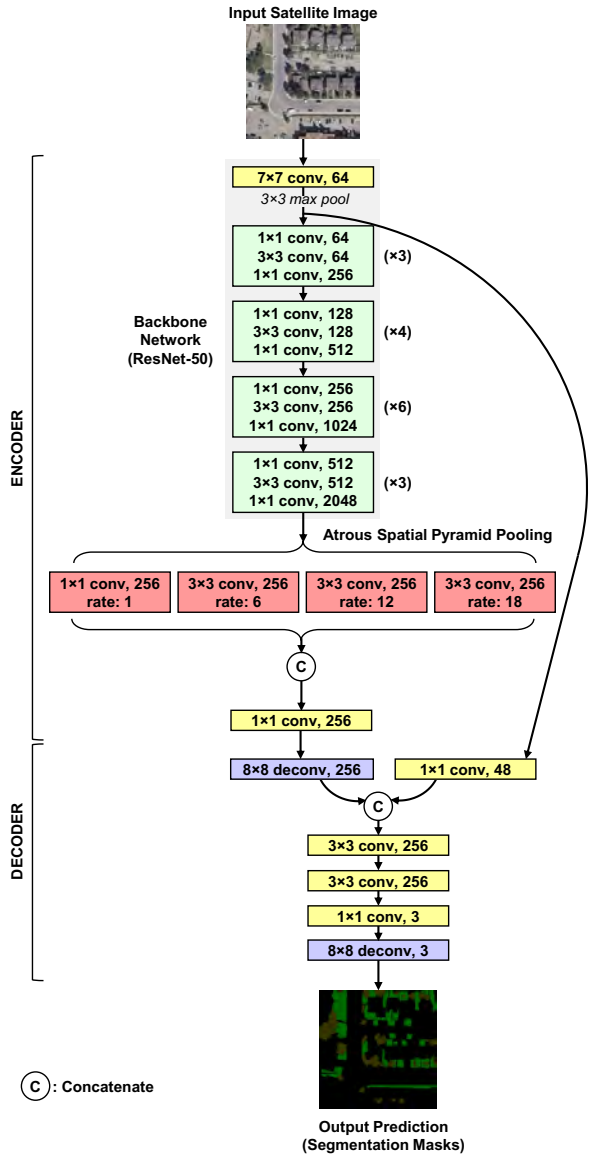

Figure 2. Segmentation network architecture

As the input to the segmentation network, summer satellite images can be utilized to distinguish forested and grasslands from other Earth features observed from the orbit (e.g., urban and agricultural areas). Specifically, the visual contrast between canopy covers and grass aids in labeling these fuel types. However, from a fire behavior perspective, tree species in the deciduous and conifer categories should be classified as two separate fuel types. Nonetheless, in summer satellite images, the visual appearance of canopies of different species can be indistinct. Therefore, for the classification of the type of forest and wooded land, winter images can be leveraged, where deciduous trees have lost their foliage, making conifer evergreens readily visible.

High-resolution satellite images—sourced from Maxar satellites through Google Maps API—were employed to establish datasets consisting of 496 summer images and 80 winter images, each with a resolution of 640×640 pixels and an approximate ground sampling distance of 20 cm/px. These images were selected from the Edmonton region in Alberta, Canada. These datasets are partitioned to train and test two separate segmentation networks: one for detecting grass and canopy areas in summer images and another for identifying coniferous areas in winter images. Overall, the networks trained for processing summer and winter images achieved high accuracies of 89.6% and 79.5%, respectively. Table 2 presents the breakdown of accuracy metrics associated with each class for the network trained for summer images.

Table 2. Accuracy metrics for the summer image test set

Class	Recall	Precision	IoU
Grass	0.8754	0.8520	0.7598
Canopy	0.8898	0.8103	0.7364
Background	0.9087	0.9503	0.8675
Mean	0.8913	0.8709	0.7879

Figure 3 illustrates the satellite images for summer and winter, capturing a sample section of the railway in the North of Edmonton. By employing the trained segmentation networks, Figure 4 presents the fuel map for this area. As shown, the networks can successfully identify and delineate the coniferous and deciduous forests around the railroad, as well as the grassland in the surrounding regions.

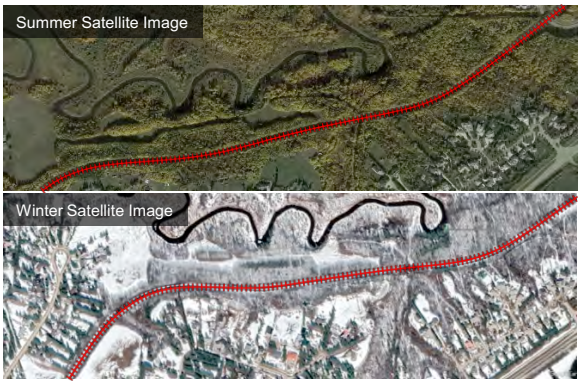

Figure 3. Winter and summer satellite images from the Edmonton region

It is important to note that Beaudoin et al. (2014) developed fuel maps specific to the Canadian context at the national scale. These maps were created using satellite imagery obtained through NASA's MODIS sensors and *k*-Nearest Neighbors classification algorithm to estimate various forest attributes relevant to fire behavior prediction. These maps have a resolution of 250 m and have been utilized by Natural Resources Canada to predict fire risk based on the Fire Behavior Prediction (FBP) system. In Figure 5, the FBP fuel map for the region under investigation in this study is presented. It is evident that the output of segmentation networks, as depicted in Figure 4, exhibits significantly higher resolution and detection accuracy. This improvement allows for a refined description of the fuel

map, thereby enhancing the reliability of the subsequent fire risk analysis.

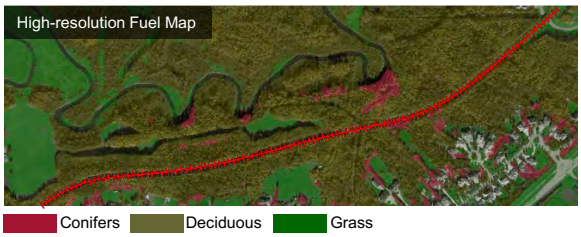

Figure 4. Fuel map produced by the segmentation network

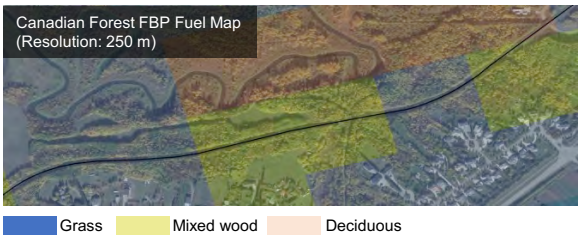

Figure 5. Canadian Forest FBP fuel map (Beaudoin et al., 2014)

4 FIRE BEHAVIOR PREDICTION

The fuel map developed in the previous section is the initial step in the fire risk assessment process. The Canadian FBP system serves as the foundation for systematically aggregating fuel type, weather parameters, topographical information, and vegetation moisture content. This aggregation enables the generation of quantitative estimates for the extent and growth rate of potential wildfires. One of the primary outputs of the FBP system is the Rate of Spread (ROS) which is the rate at which the front of the fire is growing and is measured in meters per minute. Another key output is Head Fire Intensity (HFI) which is the standard measure that is utilized to estimate the difficulty of suppressing a potential wildfire. HFI is derived from ROS and reflects the energy output, in kilowatts per meter, at the fire front (i.e., fire head).

In determining these key parameters, aside from the abundance of fuel type within a region, there are certain fuel-specific parameters that can either increase or decrease the fire hazard associated with that particular type of fuel. The phenological state (i.e., leafless or green) in deciduous trees and crown base height in coniferous trees, as well as percent of dryness (i.e., curing) and standing condition in grasses, are the most prominent examples of such parameters (Forestry Canada, 1992). Obtaining these attributes exclusively based on satellite images—observed from the Earth's surface—can be challenging. Therefore, as previously described in Figure 1, ground-based visual information can potentially be employed to supplement the satellite imagery, thereby providing a complete characterization of the fuel within a region.

As shown in Figure 4, the majority of forested area around the rail track in the investigated region is deciduous (93% deciduous versus 7% coniferous) with patches of grasslands in between. In a scenario where the trees are leafless and the grass is standing and moderately dry (i.e., 80% curing), as shown in Figure 6, heat maps for ROS and HFI can be generated, following the methodology outlined in the FBP system. In generating these maps, following the Fire Weather Index (FWI) system (Wagner, 1987), it is assumed relatively dry weather conditions with a Fine Fuel Moisture Code (FFMC) rating of 95, indicating highly flammable fine fuel and a Built-Up Index (BUI) equal to 300. The wind speed is at 25 km/h, blowing from the north. The detailed ROS and HFI maps in Figure 6 reflect the localized variations in the potential fire spread and intensity. This level of precision enables the railway owners to efficiently and consistently identify the fire exposure across the railway system allowing them to focus their mitigation efforts and resources on areas that are most vulnerable and at a higher risk.

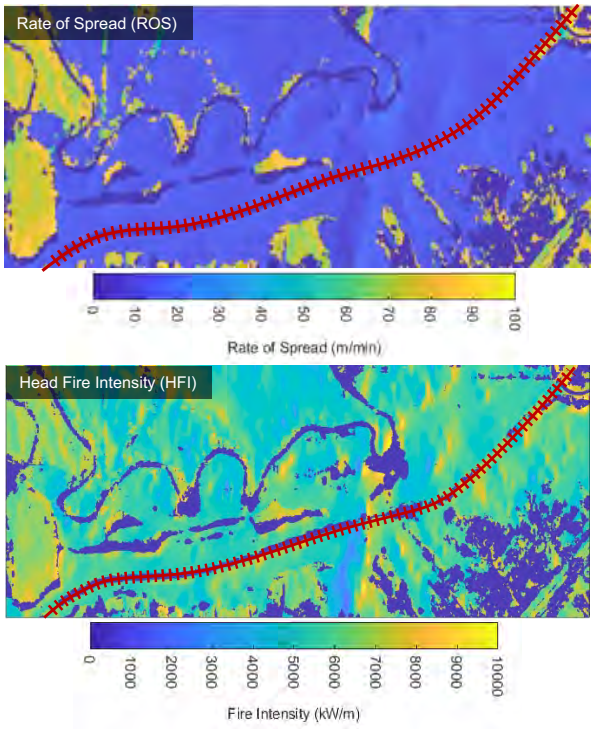

Figure 6. Fire behavior indices for the region

5 GROUND-BASED VISUAL INFORMATION

It should be noted that variations in fuel and weather parameters over time can result in significantly different fire analyses for a given region. Therefore, relying exclusively on normal seasonal patterns and neglecting the effect of unseasonal increases in temperature or drought may introduce errors in the results. While weather information from the network of weather stations is regularly updated, considering the expansive coverage of the Canadian railway systems, frequent

updates to fuel-specific parameters could be costly or even infeasible.

Meanwhile, the progress in computer vision, photogrammetry, and deep learning has enabled the accurate derivation of most fuel attributes, such as height, moisture content, and leafing out, from visual information gathered by both ground-level and airborne vehicles (Cameron et al., 2021, 2022; Phelps & Beverly, 2022). Therefore, trains or Hi-rail vehicles fitted with inexpensive internet-enabled cameras can provide continuous streams of visual data from vegetation around the rail tracks without causing any significant interruptions to the railway services. This is a scalable approach, following the concept of crowdsensing, through which low-level data is gathered from the environment by a large array of participants. The aggregated data is then processed to achieve a higher-level understanding of the environment—in this case, facilitating the wildfire risk assessment of the railway system.

6 SUMMARY AND FUTURE WORK

In this study, a framework is proposed to facilitate a more reliable monitoring of the risk posed to railway infrastructure by wildfires. The significance of high-resolution fuel detection is demonstrated through the integration of satellite imagery with state-of-the-art deep learning models. Additionally, the dependence of the fire risk assessment on a fuel detection system that is responsive to sudden changes induced by the effects of climate change is showcased. Furthermore, the contribution of ground-level visual information gathered from the vegetative fuel surrounding railroads in addressing this need is outlined.

Areas of future research involve the implementation and collection of ground-level images to be processed by deep-learning networks to obtain fuel-specific properties. Moreover, it is worth exploring the addition of spectral bands in near-infrared and short-wave infrared wavelengths. These bands, captured by onboard satellite instruments, can be combined with the visible information used in the current study to enhance the accuracy of the fuel detection process.

7 ACKNOWLEDGEMENT

The authors would like to express appreciation for the funding provided by Transport Canada to conduct this research. We also would like to thank Dr. Michael Hendry and the Canadian Rail Research Laboratory (CaRRL) at the University of Alberta for their supports.

REFERENCES

Alipour, M., La Puma, I., Picotte, J., Shamsaei, K., Rowell, E., Watts, A., Kosovic, B., Ebrahimian, H., & Taciroglu, E. (2023). A Multimodal Data Fusion and Deep Learning Framework for Large-Scale Wildfire Surface Fuel Mapping. *Fire*, *6*(2), 36. https://doi.org/10.3390/fire6020036

Beaudoin, A., Bernier, P. Y., Guindon, L., Villemaire, P., Guo, X. J., Stinson, G., Bergeron, T., Magnussen, S., & Hall, R. J. (2014). Mapping attributes of Canada's forests at moderate resolution through kNN and MODIS imagery. *Canadian Journal of Forest Research*, *44*(5), 521–532. https://doi.org/10.1139/cjfr-2013-0401

Bowman, D. M. J. S., Kolden, C. A., Abatzoglou, J. T., Johnston, F. H., Van Der Werf, G. R., & Flannigan, M. (2020). Vegetation fires in the Anthropocene. *Nature Reviews Earth & Environment*, *1*(10), 500–515. https://doi.org/10.1038/s43017-020-0085-3

Cameron, H. A., Díaz, G. M., & Beverly, J. L. (2021). Estimating canopy fuel load with hemispherical photographs: A rapid method for opportunistic fuel documentation with smartphones. *Methods in Ecology and Evolution*, *12*(11), 2101–2108. https://doi.org/10.1111/2041-210X.13708

Cameron, H. A., Panda, P., Barczyk, M., & Beverly, J. L. (2022). Estimating boreal forest ground cover vegetation composition from nadir photographs using deep convolutional neural networks. *Ecological Informatics*, *69*, 101658. https://doi.org/10.1016/j.ecoinf.2022.101658

Canadian Pacific Railway. (2022). *CP Extreme Weather Fire Risk Mitigation Plan*.

Chen, L.-C., Zhu, Y., Papandreou, G., Schroff, F., & Adam, H. (2018). *Encoder-Decoder with Atrous Separable Convolution for Semantic Image Segmentation* (arXiv:1802.02611). arXiv. http://arxiv.org/abs/1802.02611

Forestry Canada (Ed.). (1992). *Development and structure of the Canadian forest fire behavior prediction system*. Forestry Canada, Science and Sustainable Development Directorate.

He, K., Zhang, X., Ren, S., & Sun, J. (2015). *Deep Residual Learning for Image Recognition* (arXiv:1512.03385). arXiv. http://arxiv.org/abs/1512.03385

Natural Resources Canada. (2024). *Canadian Wildland Fire Information System*. https://cwfis.cfs.nrcan.gc.ca/background/dsm/fbp

Partners in Protection. (2003). *FireSmart: Protecting Your Community from Wildfire*. Partners in Protection. https://books.google.ca/books?id=qDFIAAAAYAAJ

Phelps, N., & Beverly, J. L. (2022). Classification of forest fuels in selected fire-prone ecosystems of Alberta, Canada—Implications for crown fire behaviour prediction and fuel management. *Annals of Forest Science*, *79*(1), 40. https://doi.org/10.1186/s13595-022-01151-x

Pouliot, D., Latifovic, R., Fernandes, R., & Olthof, I. (2009). Evaluation of annual forest disturbance monitoring using a static decision tree approach and 250 m MODIS data. *Remote Sensing of Environment*, *113*(8), 1749–1759. https://doi.org/10.1016/j.rse.2009.04.008

Stefanidou, A., Gitas, I. Z., & Katagis, T. (2022). A national fuel type mapping method improvement using sentinel-2 satellite data. *Geocarto International*, *37*(4), 1022–1042. https://doi.org/10.1080/10106049.2020.1756460

Tomppo, E., Haakana, M., Katila, M., & Peräsaari, J. (Eds.). (2008). *Multi-source national forest inventory: Methods and applications* (1. Ed). Springer Netherland.

Transport Canada. (2022, June 16). *Railway Extreme Heat and Fire Risk Mitigation Rules*. ASR 18691616; ASR. https://tc.canada.ca/en/rail-transportation/rules/railway-extreme-heat-fire-risk-mitigation-rules

Wagner, C. E. V. (1987). *Development and structure of the Canadian Forest Fire Weather Index System*. Minister of Supply and Services Canada.

Wilson, B. T., Lister, A. J., & Riemann, R. I. (2012). A nearest-neighbor imputation approach to mapping tree species over large areas using forest inventory plots and moderate resolution raster data. *Forest Ecology and Management*, *271*, 182–198. https://doi.org/10.1016/j.foreco.2012.02.002

Wotton, B. M., Nock, C. A., & Flannigan, M. D. (2010). Forest fire occurrence and climate change in Canada. *International Journal of Wildland Fire*, *19*(3), 253. https://doi.org/10.1071/WF09002

Canadian & Cold Regions
Rail Research Conference
2024

Operational risk awareness matrix for extreme weather triggered ground hazard events in BC

Tim Keegan, Christian Sampaleanu, Chris Johnson, & Matt Cormier
Klohn Crippen Berger, Ltd., Vancouver, BC, Canada

David Brown, & Trevor Evans
CN Rail, Edmonton, AB, Canada

ABSTRACT

Between 2017 and 2023, Canadian National Railway (CN) experienced four railway debris flow hazard scenario events that resulted in damage to track infrastructure in the Fraser Canyon, BC. All incidents investigated in this paper coincided with Atmospheric Rivers (AR), climatic events which have increased in frequency and severity during the same period. The evolving nature of these climate-change driven events requires a continuously proactive and targeted approach to manage the risk to infrastructure and personnel. CN and Klohn Crippen Berger (KCB), with assistance from Transport Canada through the Rail Climate Change Adaptation Program (RCCAP), investigated the associated Climate Trigger Signatures (CTS), adverse ground conditions, destabilizing processes and severity level that were coincident with the inferred increasing frequency and severity of the debris flow hazard scenario events between 2017 and 2023. The results of this investigation are used to develop a practical Operational Risk Awareness Matrix intended to be understandable, effective, proactive, and subject to continuous adaption and improvement to increase CN's resiliency to the elevated risk attributed to Climate Change.

1 INTRODUCTION

Between 2017 and 2023, Canadian National Railway (CN) experienced four debris flow events that resulted in damage to track infrastructure along its network in the Fraser Canyon, in British Columbia. All four events occurred between the months of September and February, and coincided with Atmospheric Rivers (ARs). ARs are climatic events which bring large amounts of warm air and moisture from the Pacific Ocean to the west coast of BC and result in periods of heavy rainfall inland. Their frequency and intensity have increased in recent decades due to climate change and are predicted to increase further in the coming decades (Payne et al., 2020).

This paper examines the Climate Trigger Signature (CTS) leading to each of the four events. A CTS refers to the real-time record (Keegan, 2007) of the relevant climate parameters from the time a climatic system can be forecasted until the system has passed. CTS parameters can include antecedent conditions like existing snowpack and antecedent rainfall, and triggering conditions like rainfall intensity and temperature leading to snow melt. These conditions are combined with increasingly adverse ground conditions, such as high wildfire burn severity in the drainage basins upslope of the track, to increase the risk of track outages and damage caused by steep creek hazards.

Based on the preliminary assessment of the five events outlined in this paper, an operational risk matrix was developed that can be used to quickly assess risk prior to an AR event impacting the coast and enhance CN's risk management process.

2 BACKGROUND

2.1 Study Area

This paper focuses on a segment of CN mainline in Southern British Columbia, that travels through the Fraser River Canyon. This stretch of track traverses through rugged mountainous terrain that is susceptible to geohazards including debris flows, debris floods, rockfalls and rockslides, and features significant ground stabilization and mitigation works. The susceptibility of this section of track was highlighted in November 2021 when a significant rainfall event (atmospheric river) resulted in several ground hazard events such as debris flows, landslides and rockfall, impacting all major linear infrastructure travelling through the corridor.

2.2 Geographical and Geological Setting

CN's rail corridor through the Fraser Canyon is located on the eastern extent of the Coast Mountains with the track switching between both banks of the Fraser River. The local topography generally consists of steep basins draining into the Fraser River Canyon. The area's geography is characterized by mountains up to 2,500 meters elevation with steep valley walls. Both the Fraser Canyon and surrounding highlands were formerly occupied by glaciers with post glacial down cutting of the river resulting in the formation of many terraces along the river's bank. Glacial retreat has been linked to slope movement processes, such as rock falls, rock avalanches, debris flows and debris slides.

The track segment is in the southern Canadian Cordillera and lies along the Fraser River Fault zone, which forms the southern boundary between the western Coastal Belt and eastern Intermontane Belt. Steep outcrops of sedimentary, igneous, and metamorphic rock are generally observed in upper slope basins, with mid basin covered by colluvial blanket and a drift blanket of till and the lower basin comprised a gravelly alluvial fan and talus comprised of local bedrock. Vegetation is typically classified as an Interior Douglas Fir biogeoclimatic zone which can exhibit periodic surface fires.

2.3 Climate Normals

The climate of the Fraser Canyon is primarily described as transitional. The climate ranges from a coastal climate with high precipitation in the south of the region, primarily in the winter, , to a semi-arid climate where precipitation primarily falls during the summer in the north of the region. Most of the Fraser Canyon experiences wet, winter precipitation, which transitions to an arid climate around Lytton. Historical climate data is shown for Environment and Climate Change Canada's Hope Slide weather station located near the south end of the Fraser Canyon, and Spence's Bridge weather station, located along the CN line, northeast of the study area in Figure 1.

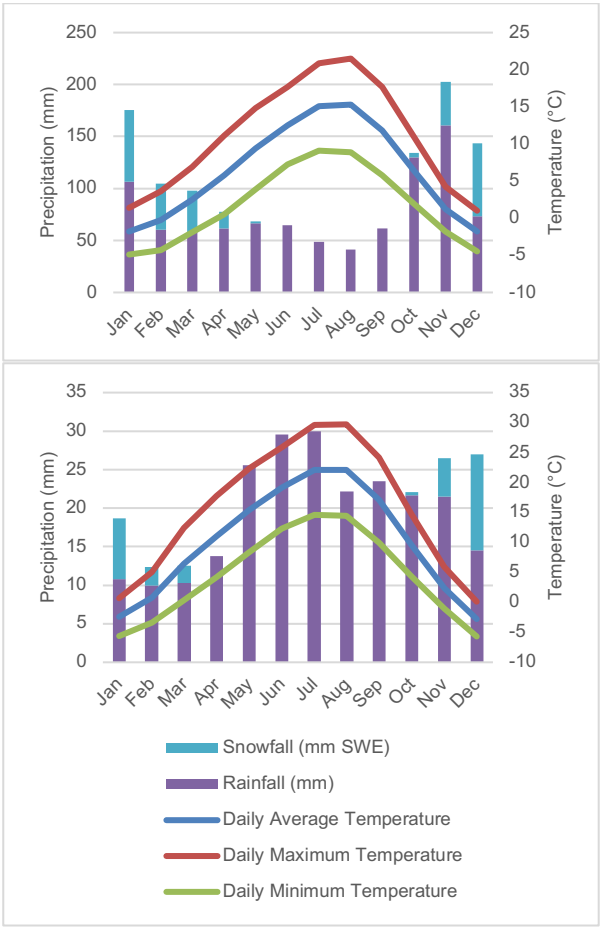

Figure 1. Climate Normals from 1981-2010 for Environment Canada Hope Slide (top) and Spence's Bridge (bottom) stations

2.4 Debris Flow Hazard Scenario

Debris flow hazards typically initiate in an upstream drainage basin and become channelized into the mainstem channel. Debris flows may impact rail operations directly by impacting and covering the track, striking a track support structure such as a bridge, or they may indirectly impact the track by causing a blockage upstream of the track and redirecting or avulsing stream flow. Avulsion refers to a stream or debris flow overtopping its existing bank and being redirected due to blockage of the existing channel or due to flows exceeding bankfull conditions. Avulsed streamflow can then scour and entrain debris which can impact the track, erode the track embankment, or oversaturate the track grade. This may result in gully erosion, seepage erosion, or downslope earth slides, resulting in a destabilized track.

3 CASE STUDIES

We reviewed the CTS for each of the four track-impacting events in the Fraser Canyon, BC, as well as two events that resulted in road failures not associated with CN operations located in Northern BC. For each event, the records for the nearest automated snow survey stations for the week preceding the event were examined and changes in snow water equivalent (SWE), total precipitation, and temperature were recorded. A summary of each event and the CTS parameters are shown in Table *1*. An example of a CTS weather record is shown in Figure *2*.

Table 1. Climate Trigger Signatures for Atmospheric River events reviewed in this study

Event Date	Location	Automated snow survey station	24 h total precipitation (mm)	SWE prior to event (mm)	24 h change in SWE (mm)	Mean temperature (°C)
2017-09-11	Horetzky Access Rd. (not CN)	Tahtsa Lake	94	0	0	5.5
2017-10-24	Horetzky Access Rd. (not CN)	Tahtsa Lake	76	214	-51	4.8
2017-11-23	CN track near Lytton	Spuzzum	32[2]	307	-35	NA[1]
2020-01-31	CN track near Boston Bar	Spuzzum	126[3]	813	10	3.6
2021-11-15	Multiple locations in Fraser Canyon	Spuzzum	79[2]	173	-40	4.4
2021-12-01	CN track near Boston Bar	Spuzzum	47[2]	188	-38	5.1

[1]Temperature sensor was not recording at this time
[2]Readings were taken at BC MoTI Jackass Weather Station
[3]Readings were taken at BC FLNRO Anderson Weather Station

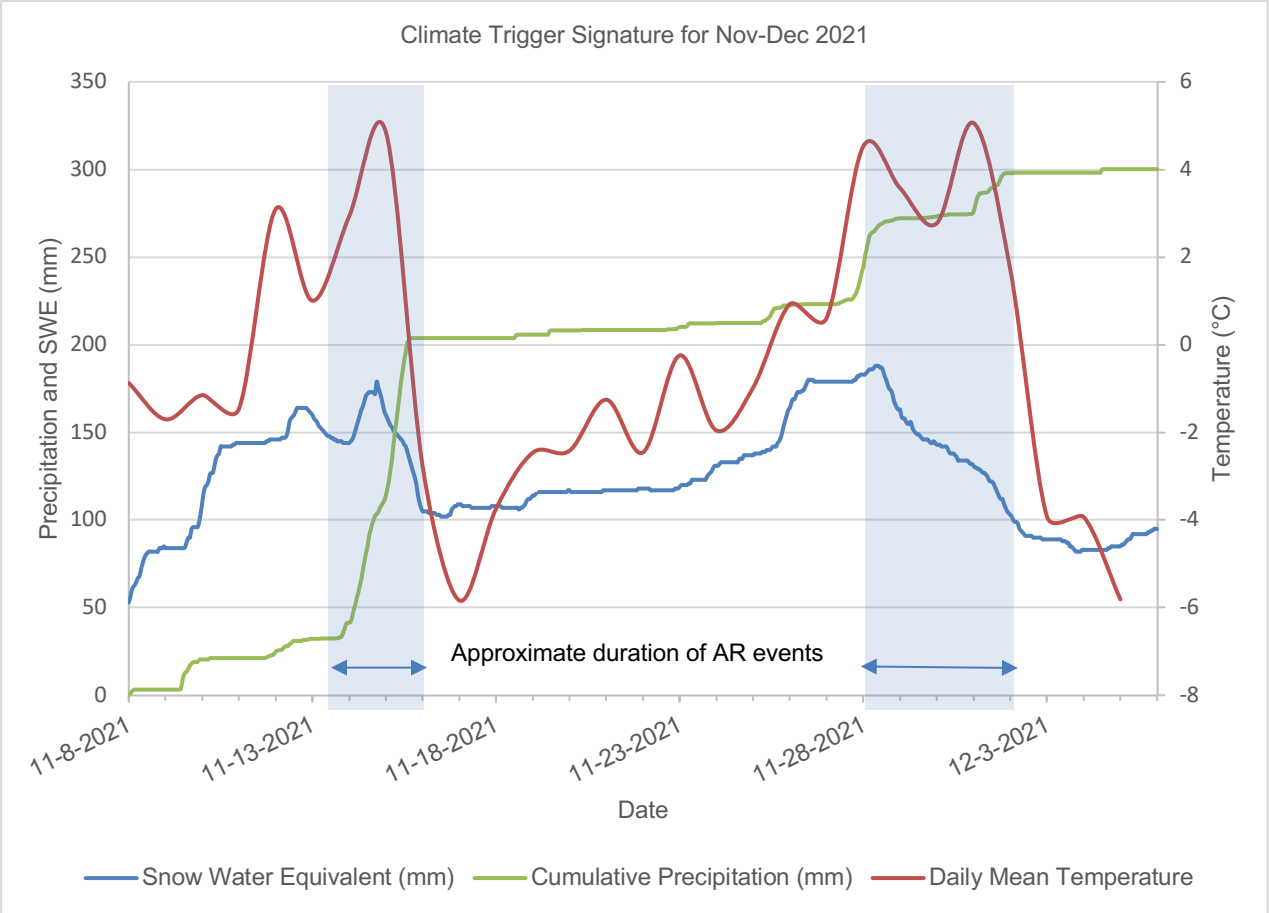

Figure 2.Example CTS for October 24, 2017 AR event. SWE and Temperature from Spuzzum snow survey station. Precipitation from BC FLNRO Four Barrel Test weather station.

3.1 September 11 and October 23-25, 2017 – Horetzky Access Road

Two ARs occurred in the fall of 2017 that impacted a portion of the Horetzky Access Road which runs parallel to Horetzky Creek at the base of Horetzky Mountain located approximately 50 km south of Kitimat, BC. The first event, in September 2017, did not cause any damage. The second event involved approximately 100 mm of rain and 70 mm of snow-water equivalent (SWE) melt, in a 45-hour period. All but one of the four road crossings failed as result of the ensuant debris flow hazard scenario.

These events are not located in the Fraser Canyon study area; however, they have been included as the physiographic and climatic conditions are similar to those encountered in the Fraser Canyon.

3.2 November 23, 2017 – CN Track Near Lytton, BC

From November 21st to 23rd, 2017, a significant AR event impacted the Fraser Canyon. The AR tracked directly eastward over the upper catchment upslope of the tracks, bringing warm temperatures and intense rain. The combination of rain and rapid snow melt resulted in significant run-off that triggered an estimated 50,000 m^3 debris flow that filled the available catchment on the upstream side of the track. The debris redirected the ensuing water westward along the ditch before cutting across the tracks, eroding out the track grade (Figure 3). This event was preceded by wildfires in the drainage basin upstream of the impact location in 2015.

Readings from the Spuzzum automated snow survey station indicated that an above average early snowpack started to form October 16th and by November 20th had climbed to 307 mm SWE which was near the maximum recorded for these dates. The abrupt change from snow to rainfall, related to the AR, occurred November 21st to 23rd.

During the event, the temperature, which was hovering around -5°C for three days prior, abruptly climbed to 5°C and after 40 hours dropped to around -3°C.. The intense warm rain started falling at the same time the temperature rose and accumulated at an average of 1.6 mm/hour, amounting to 63 mm by the end of the event. The snow cover melted at a rate of 0.9 mm of SWE per hour, amounting to a total SWE loss of 35 mm. The snow melt started and stopped simultaneously with the intense rain fall and significant temperature fluctuations. This indicates the rapid snow melt was caused primarily by the induction of latent heat from the rainwater that fell during the AR event.

This debris flow is inferred to have initiated in a drainage basin that was impacted by wildfires during the summer of 2015. Burn severity mapping from the BC Ministry of Forests, Lands, Natural Resource Operations and Rural Development (FLNRORD) indicated that approximately 60% of the surface area of the drainage basin was classified as either moderate or high burn severity in that year.

Figure 3. Debris (seen at far right of photo) filled the ditch and redirected drainage towards track east (top of the photo)

3.3 January 30th to February 2nd, 2020 – Multiple Locations near Boston Bar, BC

Between Jan. 30th and Feb. 2nd, 2020, a level 4 to 5 AR moved eastward from the Pacific Ocean and impacted multiple locations in the Fraser Canyon between Lytton and Hope, BC. The AR caused a recorded 120 mm rainfall in 24 hours at Environment Canada Hell's Gate weather station, equivalent to a 180-year return period based on available Intensity-Duration-Frequency (IDF) rainfall curves for that station. Temperatures at the Spuzzum automated snow survey station reached a maximum of 5.1°C the day of the event. The event was preceded by twelve days where the mean daily temperature ranged from -1.1°C to 0.3°C.

Despite the warm temperatures on the day of the event, recorded SWE at Spuzzum station, located at 1180 m elevation, increased by 10 mm the day of the event, and dropped only slightly the days following the event. However, it can be inferred based on the relatively high snowpack that significantly more melting likely occurred at lower elevations. The Anderson weather station, located at 630 m elevation, does not collect snowfall or snowpack data, but experienced mean daily temperatures between 0°C to 4°C in the preceding twelve days.

The AR resulted in debris flows along the corridor that impacted linear infrastructure and caused some instances of damage to CN track infrastructure.

3.4 November and December 2021 – Multiple Locations along Fraser Canyon

Two ARs impacted the Fraser Canyon in November and December 2021. The first AR occurred between November 14 and 15 and was associated with significant outages along most highways and other critical linear infrastructure in southwestern BC. This AR caused track washouts in several gullies, as well as blockages of upstream roadway culverts, causing avulsions and damage to track infrastructure (Figure 4).

The SWE at the Spuzzum snow survey station prior to the first event on November 14 was higher than the previously recorded high for that day. Over 160 mm of rainfall was recorded near track level at the BC FLNRORD Four Barrel Test weather station between November 14 and 15. The 24-hour rainfall on November 15 was equivalent to an approximately 100-400 year return period event, depending on the location, based on available IDF rainfall curves for Environment Canada's Lytton weather station.

One of the debris flows, near Jackass Mountain, initiated in a drainage basin that had experienced wildfires during the summer of 2021. Approximately 30% of the surface area of the drainage basin had a burn severity rating of medium or high.

Another AR impacted the region between November 28 and December 1, 2021. This event was less intense, bringing just over 50 mm of rainfall to the Fraser Canyon. However, it initiated ground hazards that impacted temporary works related to repairs from the previous AR.

Figure 4. Fan deposit of debris flow and washout material near Boston Bar, BC

4 PRELIMINARY OPERATIONAL RISK MATRIX

4.1 Risk Model

The risk model presented here estimates the relative risk of damage to track infrastructure associated with ground hazards. This model uses the railway ground hazard characterization methodology developed by (Keegan, 2007), which has been used by CN. The algorithm is expressed semi-quantitatively in terms of a relative risk associated with ground hazards encountered along the track. Relative risk means that the estimated risk is not an absolute value, but rather a value that allows comparison between ground hazard locations and types for ranking purposes. When broken down to its individual risk factors, it also provides a transparent indicator of where the higher risk value is coming from and thus insight into risk reduction and management. The relative risk of damage associated with ground hazards along the railway can be estimated using the following equation:

$$R = P_H \times P_{S:H} \times P_{T:S} \times V \times E \quad [1]$$

Where;

R = risk attributed to a hazard of a particular type, of a specific magnitude;

P_H = probability of the hazard occurring;

$P_{S:H}$ = spatial probability that the hazard will reach the tracks;

$P_{T:S}$ = temporal probability that a train will be impacted by the hazard;

V = vulnerability; and

E = exposure.

The term P_H can further be broken down as the product of the likelihood of adverse ground conditions existing – for example; recently burned forests, significant debris in channels that can be mobilized, erodible soil – and the likelihood of a triggering event such as an AR. As the probability of a triggering event increases, so does the probability of the hazard actually occurring.

Partial risk, also known as encounter probability, is the combination of the first two terms, $P_H \times P_{S:H}$. Encounter probability describes the likelihood that a ground hazard event reaches the track, without any consideration for the impacts on the track.

The temporal probability, $P_{T:S}$, describes the probability that a hazard will impact the track, or a train based on the amount of time they are exposed to the hazard.

Vulnerability describes the relative potential for damage or loss, given the impact of a ground hazard while exposure describes the actual elements at risk that could be potentially lost. Together, vulnerability and exposure define the consequence element of the risk equation.

From a railway operations perspective, the spatial probability, temporal probability, and consequence terms remain generally consistent on a day-to-day basis. However, the hazard probability, P_H, is dynamic and changes depending on the occurrence of triggering conditions such as atmospheric rivers. Therefore, from an operational perspective, the risk prioritization matrix focuses on the development of triggering conditions.

4.2 Climatic Triggering Condition Thresholds

The triggering effects of rainfall on landslides including debris flows and debris floods have been long understood, and several studies have attempted to identify rainfall thresholds for debris flow triggers (e.g. Caine, 1980; Crozier, 1999). Several studies have focused on southwestern BC and have examined antecedent weather conditions prior to debris flows and developed thresholds for precipitation and moisture conditions that increase debris flow risk. Church & Miles (1987) reviewed antecedent conditions to several debris flows in the Fraser and Coquihalla Valleys as well as Howe Sound and found a mean recorded precipitation of 58.7 mm in the preceding 24 hours for these events. Jakob & Weatherly (2003) developed climatic thresholds for debris flows specific to the North Shore Mountains north of Vancouver, which included 4-week cumulative rainfall prior to the event, 6-hour rainfall intensity during the storm, and discharge in a gauged stream. The stream discharge was used as a proxy for snowmelt caused by rain on snow. Guthrie et al. (2010) examined conditions associated with a November, 2006 storm and subsequent landslides on Vancouver Island, similarly finding that rainfall intensity, along with wind-driven rain and rain on snow events as the most significant contributors to landslide hazard.

Climatic triggering thresholds for risk management can either be based on observed conditions, as recorded at automated weather stations, or forecasted conditions, as predicted by relevant weather models such as Environment Canada's Regional Deterministic Prediction System (RDPS) model. Based on the assessment of the case studies above, the following triggering conditions were considered as most relevant:

- Wildfire burn extent and burn intensity in upstream drainage basin in previous 5 years
- Snow water equivalent (SWE) in upstream drainage basin
- 24-hour storm rainfall
- Mean daily temperature in alpine drainage basins
- Length of time in days of above freezing temperatures in alpine drainage basins

Ground hazard likelihood increases with burn intensity and extent within the drainage basin, and is generally highest the year following the wildfire. Contribution to hazard likelihood due to wildfire generally becomes negligible after about 5 years, although this depends on the rate of revegetation (Jordan, 2016).

Snowpack contributes to ground hazard likelihood through snowmelt caused by rain-on-snow events. The observed cased studies generally occurred in early season, when the snowpack was between 100-400 mm of SWE. This level of snowpack is observed to be more susceptible to warm rain-on-snow events due to its relatively lower density and heat capacity. A deeper mid to late season snowpack is less susceptible to rain events and therefore would produce less snow melt for an equivalent rain event.

Rainfall contributes both to melting of snow and to runoff which causes erosion, increases pore pressures in unstable slopes, and leads to high stream flows which can entrain debris. Finally, mean temperature and temperature duration above freezing contribute to the rate of snowmelt.

For including in the risk matrix, each triggering condition is rated on a scale of 0 to 4, using thresholds based on the observed case studies. A risk rating of 0 indicates that the risk factor is not present, and 4 indicates a very high level of risk. The thresholds used for each parameter are shown in Table 2.

Table 2 Risk ratings and associated thresholds for identified triggering conditions.

Risk Rating	Wildfire effects	SWE (mm)	24-hour rainfall (mm)	Mean daily temperature (°C, at alpine elevation)	Days above freezing at alpine elevation
0	None in the last 5 years	0	0-5	<-2	0
1	Low severity, limited extents, 3- 5 years prior	0-100	5-30	-2-0	NA
2	Low severity, <50% of drainage basin, 1-2 years prior	>1000	30-50	0-2	1
3	Moderate to high severity, <50% of drainage basin 3-5 years prior	400-1000	50-70	2-4	NA
4	Moderate to high severity, >50% of drainage basin, 1-2 years prior	100-400	>70	>4	>1
Weighting	0.2	0.2	0.4	0.1	0.1

The risk ratings for each of the identified triggering conditions are weighted based on the estimated contribution to ground hazard likelihood, as shown in Table 2. The subjective likelihood of a debris flow event occurring somewhere in the Fraser Canyon study area during a given rain event is provided in Table 3.

Table 3 Subjective likelihood of a debris flow event based on assigned risk ratings

Average risk rating	Subjective Likelihood
0-1	Event capable of causing track failure expected to occur infrequently
1-2	Event capable of causing track failure expected to occur occasionally
2-3	Event capable of causing track failure are probable to occur (typically event expected to occur every few CTS event)
3-4	Event capable of causing track failure expected to occur frequently

4.3 Back Calculation on Case Studies

The risk ratings were back calculated for each of the five events based on the recorded weather conditions. The risk ratings for each of the events is shown in Table *4*

Table 4 Overall relative risk ratings of case studies based on identified risk factors

		Risk ratings for individual risk factors (Scale of 1-4)					Overall Relative Risk Rating
Risk Factor		Wildfire effects	SWE	24-hour rainfall	Mean daily temperature (at alpine elevation)	Days above freezing at alpine elevation	
Weighting		0.2	0.2	0.4	0.1	0.1	
Event Date	Location						
2017-09-11	Horetzky Access Rd. (not CN)	1	0	4	4	4	2.6
2017-10-24	Horetzky Access Rd. (not CN)	1	4	4	4	2	3.2
2017-11-23	CN track near Lytton	4	4	2	3	4	3.1
2020-01-31	CN track near Boston Bar	3	3	4	3	0	3.1
2021-11-15	Multiple locations in Fraser Canyon	3	4	4	4	4	3.8
2021-12-01	CN track near Boston Bar	3	4	2	4	4	3

The results indicate that the five case studies had overall risk ratings that ranged from 2.6 to 3.8. The lowest risk rating corresponded to the only case study in which no damage was observed. The highest risk rating corresponded to the most damaging event observed in the case studies. The remaining case studies all had risk ratings greater than 3, indicating that an event capable of causing a track failure would be expected to occur frequently when impacted by this level of weather event.

4.4 Ongoing Model Refinement

The risk factors and thresholds presented in the previous section represent a method to quickly assess the increased risk brought on by incoming storm systems. However, they are based on a limited number of observations over a relatively short period of time. The risk model is intended to be continuously changing as further data is collected.

5 CONCLUSION

The CN track through the Fraser Canyon in BC is susceptible to impacts from ground hazards that initiate upstream of steep creek crossings and can cause damage or track outages. The likelihood of ground hazards initiating increases significantly during periods of heavy rainfall and snow melt, such as Atmospheric Rivers. Using Climate Trigger Signatures from five case studies, we identified the most relevant risk factors for initiation of damaging ground hazards, and developed thresholds to estimate the relative likelihood of ground hazard initiation.

Using climatic thresholds to forecast risk will aid CN to enhance its weather event preparation and responses. While the thresholds established in this paper are applicable to a specific segment of track, the general process for developing these thresholds can be followed for other regions. The magnitude of a triggering event may vary depending on factors such as typical rainfall, snowpack, elevation, and geographical setting, and therefore may vary from those presented in this study. The thresholds in this study are intended to be continuously refined as more events are observed.

REFERENCES

Caine, N. (1980). The Rainfall Intensity: Duration Control of Shallow Landslides and Debris Flows. *Geografiska Annaler. Series A, Physical Geography*, *62*(1/2), 23. https://doi.org/10.2307/520449

Church, M., & Miles, M. (1987). Meteorological antecedents to debris flow in southwestern British Columbia; Some case studies. In *Geological Society of America Reviews in Engineering Geology*.

Crozier, M. J. (1999). Prediction of rainfall-triggered landslides: a test of the Antecedent Water Status Model. *Earth Surface Processes and Landforms*, *24*(9), 825–833. https://doi.org/10.1002/(SICI)1096-9837(199908)24:9<825::AID-ESP14>3.0.CO;2-M

Guthrie, R. H., Mitchell, S. J., Lanquaye-Opoku, N., & Evans, S. G. (2010). Extreme weather and landslide initiation in coastal British Columbia. *Quarterly Journal of Engineering Geology and Hydrogeology*, *43*(4), 417–428. https://doi.org/10.1144/1470-9236/08-119

Jakob, M., & Weatherly, H. (2003). A hydroclimatic threshold for landslide initiation on the North Shore Mountains of Vancouver, British Columbia. *Geomorphology*, *54*(3–4), 137–156. https://doi.org/10.1016/S0169-555X(02)00339-2

Jordan, P. (2016). Post-wildfire debris flows in southern British Columbia, Canada. *International Journal of Wildland Fire*, *25*(3), 322–336. https://doi.org/10.1071/WF14070

Keegan, T. (2007). *Methodology for Risk Analysis of Railway Ground Hazards*. Ph.D Thesis, University of Alberta.

Payne, A. E., Demory, M.-E., Leung, L. R., Ramos, A. M., Shields, C. A., Rutz, J. J., Siler, N., Villarini, G., Hall, A., & Ralph, F. M. (2020). Responses and impacts of atmospheric rivers to climate change. *Nature Reviews Earth & Environment*, *1*(3), 143–157. https://doi.org/10.1038/s43017-020-0030-5

Canadian & Cold Regions
Rail Research Conference
2024

Quantitative analysis of the impact of climate change on rockfall hazards in British Columbia, Canada

Nima Mirhadi, & Renato Macciotta
Department of Civil and Environmental Engineering - University of Alberta, Edmonton, Alberta, Canada

ABSTRACT

The Canadian Cordillera in the province of British Columbia experiences numerous rock falls every year. Research based on recorded rockfall data in this region indicates that the rockfall hazard is closely linked to weather conditions, particularly precipitation and freeze-thaw cycles. The purpose of this paper is to study the rock fall phenomenon and how the rock fall hazard is expected to change in the future decades as a consequence of climate change. In this regard, a statistical approach is employed to quantify the relationship between monthly weather averages and rock fall frequencies for a section of a transportation corridor along the Fraser River in British Columbia, Canada. Circular distributions are used to find the best-fitted models to the recorded weather data in the period of 1990-2019. These models are then combined and calibrated to the recorded rock fall monthly frequency. The calibrated model is then used with input data from climatic predictions to see how rockfall distribution will be affected due to climate change in the future decades. Preliminary results show that more rockfall activity is expected in December, January, and February of each year relative to the reference period of 1990-2019. On the other hand, rockfall predictions indicate less number of events in some of the months. Based on the results, it is anticipated that the number of rockfall events decreases in October, November, March, and April. This study shows that new strategies for monitoring and reducing rockfall hazards can be developed in this area. Moreover, this study presents a method for quantifying changes in rockfall hazards for climate change scenarios, which will assist infrastructure authorities in prioritizing their monitoring resources for risk mitigation, as well as enhancing the resilience of transportation corridors during times of high rockfall hazards.

1 INTRODUCTION

The Canadian Cordillera experiences frequent rock falls annually, specifically in the province of British Columbia where on average 550 mm of precipitation falls between November and January of the following year. The Canadian National Railway (CN) and inter-provincial highways face annual financial losses due to these rock falls, with estimated damages ranging from CAD$100 to $148 million (Porter et al. 2019). Weather-related factors, especially precipitation and temperature, play a significant role in triggering rock falls. Studies by Leyva et al. (2022) and Macciotta et al. (2015) emphasize the relationship between rock falls and weather conditions, particularly precipitation and freeze-thaw cycles.

The climate change effects, which are predicted to intensify in the future (Bush and Lemmen 2019), may lead to increased erosion processes and rock fall frequencies. This paper investigates the rock fall occurrences on part of the CN's railway in the Canadian Cordillera and possible changes in their frequency due to climate change and presents a framework for estimating monthly rock fall distribution. The goal is to assist decision-makers in developing risk mitigation and resilience strategies for transportation corridors that are vulnerable to rock fall hazards in the context of climate change.

2 STUDY AREA

The section between miles 5 and 25 of the CN's Yale subdivision was selected as the study area. This part of the railway passes along the Fraser River and is characterized by steep valley walls and cuts. The location of the study area is shown in Figure 1. The region comprises various rock types, including sedimentary, metamorphic, intrusive, and volcanic rocks, which are prominently exposed throughout the Fraser River valley (Macciotta et al. 2011; Cui et al. 2017).

The modelled historical weather data between 1990 and 2019 for the study area show a range of temperatures, with a monthly average low of -3.9 °C in January and a monthly average high of 16.8 °C in July.

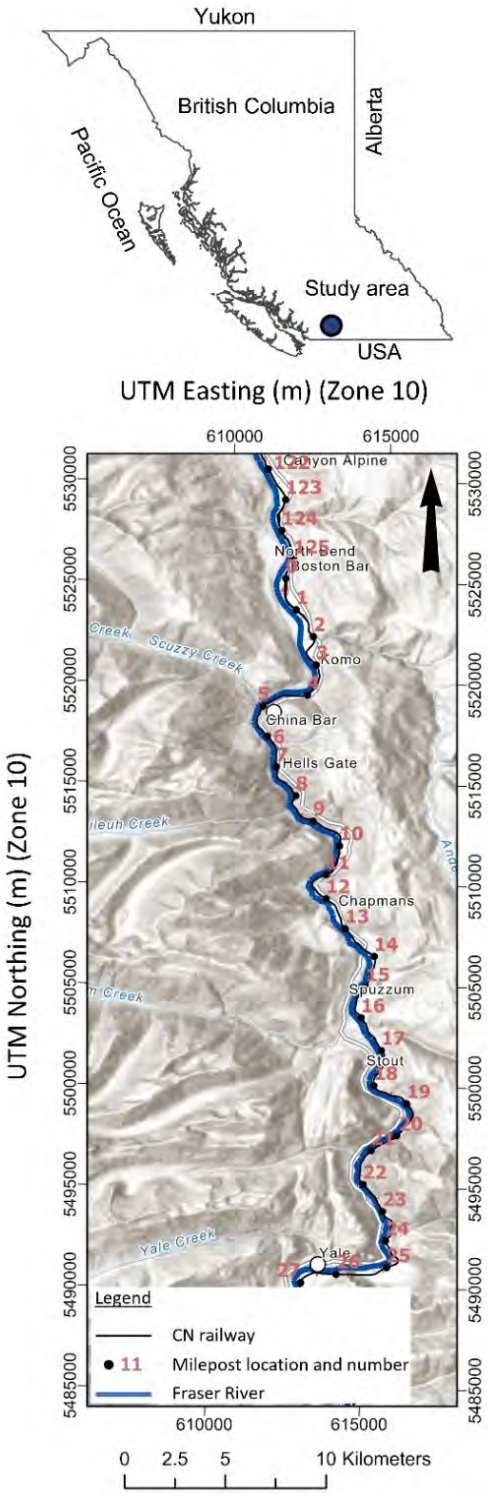

Figure 1. Study area

Figure 2 shows the average monthly temperature and precipitation throughout this period. Notably, the study area experiences an average of around 550 mm of precipitation from November to January, with temperatures below 0 °C from December to February of the following year.

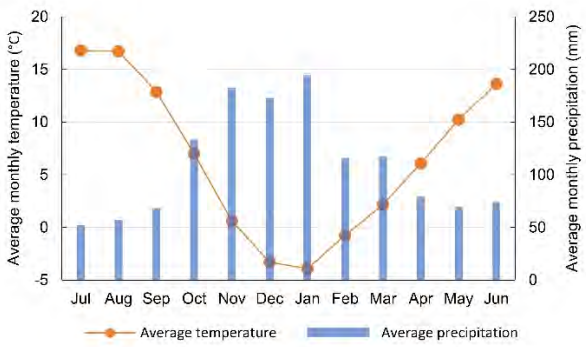

Figure 2. Average monthly weather data between 1990 and 2019

3 ROCK FALL DATABASE

The rock fall database used in this study includes time, location and approximate size of 401 rock falls between 1998 and 2011. The database shows that more than 80% of the rock falls in this period occurred between Mileposts 5 and 25. Based on the available data, 29 rock falls happen on average each year along this section of the railway.

4 METHODS AND MATERIALS

4.1 von Mises Distribution

The von Mises distribution method which is a circular distribution method is employed in this study to find a relationship between monthly precipitation and freeze-thaw cycles, and monthly rock fall records. The von Mises distribution is a simple, robust method which is particularly useful for statistical analysis on circular data (Mardia 1972). This technique is a powerful tool in establishing a relationship between climate data and rock falls and is defined with the following equation:

$$M(\mu_0, \kappa) = \frac{1}{2\pi I_0(\kappa)} e^{\kappa \cos(\omega - \mu_0)} \quad [1]$$

$$0 < \omega \leq 2\pi, \quad \kappa > 0, \ 0 < \mu_0 \leq 2\pi$$

In this equation, $M(\mu_0, \kappa)$ is the von Mises probability density function, ω is the variable and defined between zero and 2π, μ_0 is the mean direction and defined between zero and 2π, κ is a positive parameter known as the concentration parameter. $I_0(\kappa)$ is the modified Bessel function and is defined by the following equation:

$$I_0(\kappa) = \sum_{r=0}^{\infty} \frac{1}{r!^2} \left(\frac{\kappa}{2}\right)^{2r} \quad [2]$$

To find the relationship between weather data and recorded rock falls, the defined von Mises distributions need to be combined. The final multi-modal distribution, which should represent the recorded rock fall distribution

well, can be determined as a sum of weighted uni-modal von Mises distributions by the following equation:

$$F_M = \sum_{i=1}^{n} W_i F_i(\omega) \qquad [3]$$

$$and \;\; W_1 + W_2 + \cdots + W_n = 1$$

In Equation 3, F_M is the mixture distribution, $F_i(\omega)$ is the i^{th} von Mises distribution, W_i is the relative weight for the i^{th} distribution, and n is the number of von Mises distributions defined for that parameter.

4.2 Weather Database

The current weather station network does not cover the study area completely for the selected time period. Therefore, the modelled historical weather data, which were calibrated to actual recorded weather data, was used to create a 30-year weather database for the period of 1990-2019. Current and projected weather data were collected from the ClimateData.ca (2022) database. The monthly normalized precipitation was calculated based on the modelled daily data. For the freeze-thaw cycle, daily minimum and maximum temperatures were used, with freezing and thawing points set at -1°C and +1°C respectively. This is consistent with other studies which ensure freezing penetrates rock joints and gives frozen material enough time to thaw.

To investigate how monthly rock fall frequency may change in future due to climate change, the weather projections need to be calculated. For this purpose, two weather databases for 2041-2070 and 2071-2100 were created using 24 climate models considering the Representative greenhouse gas Concentration Pathway (RCP) 4.5 scenario. The RCP 4.5 is an intermediate emission scenario and predicts a peak in emissions around 2040 followed by a decline (Meinshausen et al. 2011). All available climate models show an expected increase in precipitation and average temperatures in the study area across all RCP scenarios. These changes in triggering factors significantly impact rock fall probability.

5 RESULTS AND DISCUSSION

5.1 Distribution Fits to the Monthly Precipitation and Freeze-Thaw Cycles

Three von Mises distributions for precipitation and two for freeze-thaw cycles were defined and mixed to find the best fit to the monthly normalized weather data. These distributions and the actual recorded weather data are shown in Figure 3. The parameters of these distributions are summarized in Table 1.

Figure 3 shows that the correlation coefficients between the recorded rock falls and the monthly precipitation and freeze-thaw cycle are 0.958 and 0.989 respectively which suggests that circular distributions such as von Mises can be used well to represent weather data.

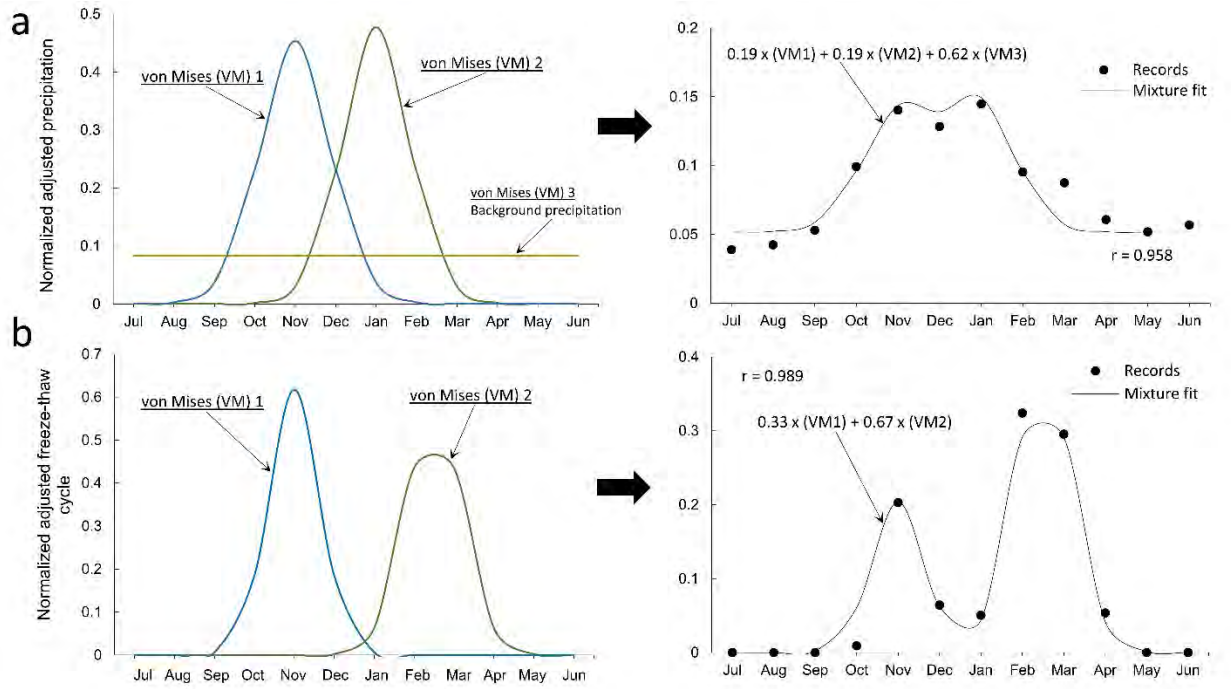

Figure 3. Defined von Mises distributions and the comparison between the combined distributions and the actual recorded data for precipitation (a), and freeze-thaw cycle (b)

Table 1. Properties of von Mises distributions (VM) for current climate data (1990-2019)

		μ_0	κ
Precipitation	VM*1	$\frac{9}{12}\pi$	5
	VM2	$\frac{13}{12}\pi$	5.5
	VM3	-	0
Freeze-thaw cycle	VM1	$\frac{9}{12}\pi$	9
	VM2	$\frac{16}{12}\pi$	7.5

*VM: von Mises distribution

5.2 Rock Falls and their Relationship with Current Climate Conditions

The relative weights to find the best fit to the recorded rock falls are shown in Table 2. These relative weights were used on distributions defined for precipitation and freeze-thaw cycle to create a combined multi-modal fit for the rock fall records. The result is shown in Figure 4. This combined fit has a correlation coefficient of 0.975, confirming that precipitation and freeze-thaw cycles are suitable and adequate parameters for finding the relationship between climate and rock fall events in the study area.

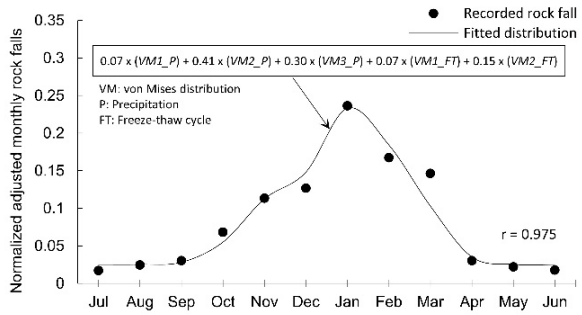

Figure 4. Comparison between the recorded rock fall data and the fitted multi-modal distribution

Table 2. Relative weights used to fit climatic data to rock fall records

	Precipitation			Freeze-thaw cycle	
Description	VM1	VM2	VM3	VM1	VM2
Relative weight	0.07	0.41	0.30	0.07	0.15

The relative weights show that precipitation has a major impact on rock falls in the study area, making up 78% of the total weight. This emphasizes that changes in precipitation patterns due to climate change can greatly affect the rock fall distribution.

5.3 Climate Change and its Effects on Rock Fall Distribution

Figure 5 shows the expected changes in monthly precipitation and freeze-thaw cycles for the periods 2041-2070 and 2071-2100 and compares them to the data from 1990-2019. According to climate predictions, higher precipitation is anticipated from November to January in the next decades, which aligns with the time when most rock falls occur (Fig. 4). Figure 5 also shows significant alterations in freeze-thaw cycles in the upcoming decades, with more cycles in December and January and less cycles in November and March, suggesting a shorter overall winter duration compared to the reference period of 1990-2019.

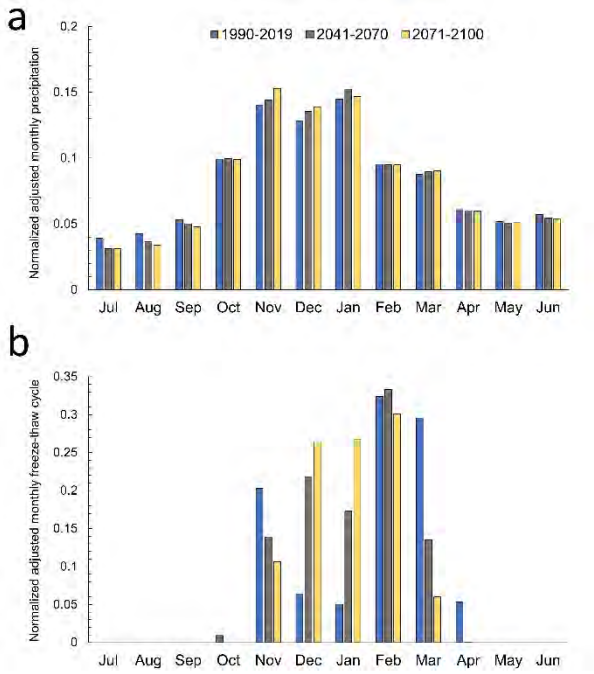

Figure 5. Comparison between the projected and current climate conditions for precipitation (a), and freeze-thaw cycle (b)

Climate projections, shown in Figure 5, suggest the need for three von Mises distributions to model monthly precipitation. These distributions represent background precipitation and two peaks in late fall and mid-winter and are independent of those defined for the current climatic conditions.

Also, predictions show that two von Mises distributions are enough to represent the predicted monthly freeze-thaw cycles in the upcoming decades. These two distributions represent the freeze-thaw cycle peaks in early winter and early spring.

To investigate how rock fall distribution may change due to climate change, the relative weights established for the current climate conditions, which are presented in Table 2, were applied to the corresponding distributions defined for predicted climatic data. Figure 6 shows how rock fall distribution may change in 2041-2070 and 2071-2100 due to climate change.

Results indicate an increase in rock fall activity, especially in winter, with at least a 13% rise in the period of 2041-2070. The maximum increase is predicted for January. Results also show that a 19% increase in the

rock fall activity in the period of 2071-2100 is expected in December relative to the reference period of 1990-2019. On the contrary, fewer rock fall events are expected in fall and spring, likely due to the projected shorter freeze-thaw cycles. This suggests that the hazardous period could be shorter but more intense in the future decades.

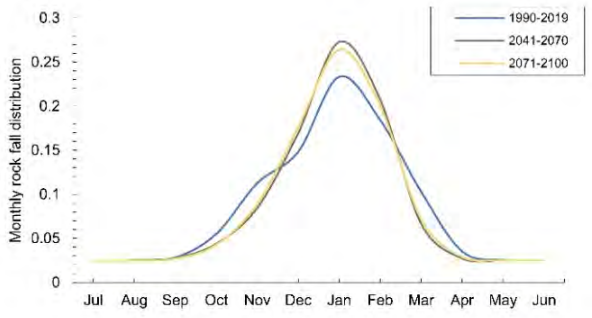

Figure 6. Comparison between current and projected monthly roc fall distributions in different time periods

The rate of increase in rock fall events is highest between the present time and 2041-2070, with a reduced rate of increase between 2041-2070 and 2071-2100. It's worth noting that rock fall events depend on the availability of triggers and unstable rock volumes on the slopes, and while changes in climatic data suggest an increase in rock fall events, feasibility must also be considered.

The results highlight an increased hazard between late November and February and a reduced hazard in October, November, March, and April.

Moreover, the results emphasize the need for rock fall risk mitigation strategies and investment in railway resilience, particularly for the specific railway section discussed in this paper.

6 CONCLUSION

The projected rock fall distributions indicate an anticipated increase of 9% to 19% in rock falls during the future winter months of December through February. Conversely, a decrease in rock falls is expected in other months, particularly in October, November, March, and April. Additionally, the study suggests a deceleration in the rate of change in rock fall events between the two time periods considered in this study.

These findings provide a basis for more precise monitoring of rock fall hazards and the development of effective risk reduction strategies in the studied area. Significantly, the methodology presented in this study offers a means to quantify changes in rock fall hazard under various climate change scenarios, enabling infrastructure authorities to allocate monitoring resources strategically and enhance resiliency along transportation corridors during periods of heightened rock fall hazards. The study underscores the importance of reliable weather databases and comprehensive rock fall records.

Variations in the rock fall recording standards after 2011 have limited the extension of the study to the present. It is recommended that robust rock fall records be developed and maintained to facilitate more comprehensive hazard assessments and forecasting, aiding in the evaluation of future infrastructure and operational resilience needs.

7 ACKNOWLEDGEMENT

This study was conducted with support from the Canadian Railway Ground Hazard Research Program (RGHRP). We express our gratitude to the Canadian National Railway Company (CN) for generously providing the rock fall data that made this research possible. Special thanks to Trevor Evans (CN) for sharing valuable insights regarding rock fall activity in the area, inferred kinematics and triggers, and providing valuable suggestions throughout the project.

REFERENCES

Bush E., Lemmen D.S. (2019). Canada's changing climate report. Environment and Climate Change Canada, Government of Canada, Ottawa, ON.

ClimateData.ca (2022). Climate data for a resilient Canada. https://climatedata.ca/. Accessed 18 Oct 2022

Cui Y., Miller D., Schiarizza P., Diakow L.J. (2017). British Columbia digital geology. British Columbia Ministry of Energy, Mines and Petroleum Resources, British Columbia Geological Survey Open File 2017-8, p 9

Leyva S., Cruz-Pérez N., Rodríguez-Martín J. et al (2022). Rockfall and rainfall correlation in the Anaga Nature Reserve in Tenerife (Canary Islands, Spain). Rock Mech Rock Eng. https://doi.org/10.1007/s00603-021-02762-y

Macciotta R., Cruden D.M., Martin C.D., Morgenstern N.R. (2011). Combining geology, morphology and 3D modelling to understand the rock fall distribution along the railways in the Fraser River valley, between Hope and Boston Bar, B.C. In: Slope Stability 2011: International symposium on rock slope stability in open pit mining and civil engineering. Vancouver, Canada

Macciotta R., Martin C.D., Edwards T. et al (2015). Quantifying weather conditions for rock fall hazard management. Georisk 9(3):171–186. https://doi.org/10.1080/17499518.2015.1061673

Meinshausen M., Smith S.J., Calvin K. et al (2011). The RCP greenhouse gas concentrations and their extensions from 1765 to 2300. Climate Change 109:213–241. https://doi.org/10.1007/s10584-011-0156-z

Mardia K.V. (1972). Statistics of directional data. Elsevier, London, New York

Porter M., Hove J. Van., Barlow P. et al (2019). The estimated economic impacts of prairie landslides in western Canada. In: Proceedings of the 72nd Canadian geotechnical conference. St. John's, Newfoundland and Labrador, p 8

Session 2

COLD REGIONS ENGINEERING

Canadian & Cold Regions
Rail Research Conference
2024

A proposal for testing chemical deicers aimed to use on the third rails in winter

Jean-Denis Brassard, & Gelareh Momen
Anti-Icing Materials International Laboratory, Université du Québec à Chicoutimi, Chicoutimi, Québec, Canada

ABSTRACT

This research paper presents a comprehensive study aimed at improving the reliability of rail transit systems during winter conditions. The focus of our investigation is on the utilization of chemical deicers for third rails and a proposal for testing the performance of these products. In regions where cold weather prevails, maintaining the conductivity of the third rail is paramount for the uninterrupted operation of electric trains. To this end, our research scrutinizes the properties of chemical deicers, with a particular emphasis on their impact on ice adhesion. Recognizing the growing importance of environmental sustainability, our research evaluates the environmental impact of using chemical deicers in rail transit systems. To assess the effectiveness of these deicing agents in mitigating ice adhesion, we propose a novel third rail adhesion test. This test provides a comprehensive evaluation of the product's performance in preventing ice accumulation on third rails and how it reduces the ice adhesion. Alternative strategies, such as conductive icephobic coatings, could provide more sustainable solutions to this problem. Additionally, such coatings could be applied to other strategic surfaces. In conclusion, our research significantly contributes to enhancing rail transit reliability in winter conditions. The proposed testing methods and results hold substantial promise for transit authorities and manufacturers, ensuring the efficiency, safety, and sustainability of rail operations in cold climates.

1 INTRODUCTION

Freezing and frozen precipitations occurring during that period of the year also affect the whole transportation systems (Laforte, Allaire et al. 1998). The accumulation of ice on airplanes, for example, can affect flight safety by altering the aerodynamic forces during flights (Leroux 2022). Above-deck ice buildup on ships and the freezing of sprayed supercooled water drops onto the exposed surfaces, alters the centre of gravity of vessels, and reduces their stability, thus heightening the risk of capsizing in Arctic shipping lanes (Brassard, Sarkar et al. 2015). Adverse winter weather exerts a notable influence on daily operations, especially on rails (Laforte, Allaire et al. 1998, Xia, Van Ommeren et al. 2013, Ludvigsen and Klæboe 2014). Ice and snow pose significant challenges to the seamless operation of trains, disrupting essential components and impeding overall performance (Ludvigsen and Klæboe 2014). The figure 1 show the main impact of winter the new "Reseau Express Métropolitain" of Montreal (Lemyre 2023).

Figure 1. Main impact of winter on newly built Montreal's REM (Lemyre 2023).

This new train is greatly affected by winter conditions (Ouellette-Vézina 2024). Ice may accumulate on the overhead electrical transmission lines (OLE), the pantographs, the rails, the railway contact wires, third rail and so on (Thornes and Davis 2002, Heyun, Xiaosong et al. 2012). Lower temperatures combined with high humidity and/or precipitations are susceptible of generating icing of those key parts of train transportation, leading to major problematic for the industry like arcing, OLE tripping, pantograph dewirements, etc.

These adverse weather conditions can obstruct proper contact between the pantograph and the cable, induce vibrations in the cable due to snow accumulation when windy, lead to malfunctioning doors, and render tracks slippery, compromising braking effectiveness (Ludvigsen and Klæboe 2014).

The presence of ice on conductive cables can profoundly impact their electricity transmission capabilities, giving rise to a phenomenon known as “galloping.” (Laforte, Allaire et al. 1998)

This occurrence entails the rapid movement of cables when exposed to high, gusty winds. The consequential swaying motion poses a risk to their contact with pantographs, which play a vital role in collecting electricity from overhead wires.

Furthermore, the accumulation of ice on the cables can compromise their conductivity, potentially resulting in power loss or even a complete outage.

Hence, it is imperative for railways to diligently monitor conductive cables, particularly during winter months. Ensuring these cables are free of ice and adequately maintained becomes paramount to preventing galloping and preserving optimal contact with pantographs. This proactive approach to maintenance safeguards against potential disruptions in electricity transmission and reinforces the reliability of rail operations in challenging weather conditions (Thornes and Davis 2002, Heyun, Xiaosong et al. 2012).

Consequently, railways must adopt specialized measures to safeguard the consistent and effective functioning of their conductive rails throughout the winter months. In this context, the utilization of chemical products designed to protect the conductive rail from adverse winter conditions is paramount. Despite the recognized importance of such products, it is noteworthy that currently, there is a lack of comprehensive laboratory tests to evaluate their efficacy in maintaining optimal electrical conductivity and preventing the detrimental effects of cold weather. Addressing this gap in testing protocols is essential for ensuring the reliability and performance of these chemical solutions in real-world rail transit scenarios.

To address these operational drawbacks, the development of comprehensive laboratory tests is essential. These tests aim to identify the most effective means to mitigate the impact of ice and snow on various critical elements of train functionality.

By systematically evaluating and refining solutions in controlled environments, these laboratory tests offer a pathway to resolve and enhance the reliability of train operations under challenging winter conditions.

In some other trains, the electricity is provided by the means of a third rail. As temperatures plummet, the contraction of the metal within the rails becomes a pivotal concern, inducing electrical resistance and diminishing the capacity for power transmission. Furthermore, the accumulation of snow and ice on the rails exacerbates the challenge, further compromising electrical conductivity and precipitating the risk of trains decelerating or halting altogether.

The aim of this article is to present a method used in laboratories to help rail industry in evaluating and designing deicing products, particularly concerning the application of liquid products aimed to reduce ice adhesion over the third rail.

2 MATERIALS AND METHODS

Three different components will be evaluated during this campaign. First, the way ice will be accumulated, secondly how easy ice is removed and finally how the products react after removal.

The ice coupons were meticulously prepared in a cold room under controlled temperature and precipitation conditions. Crafted from 1018 steel, the coupons measure 3 cm by 8 cm by 0.6 cm. To validate precipitation, eight substrates underwent icing simultaneously using a specialized setup—four as reference and four treated with the product. The ice coupons formed on the substrate tips under simulated freezing drizzle precipitation, achieved by spraying deionized water of 320 µm droplets in the cold room at a temperature of -10 ± 0.2 °C, where the supercooled droplets froze upon contact with the substrates, ensuring uniform ice coupon formation.

To measure the ice adhesion, we employed a microscopy tool named Microtom, chosen for its stability and controlled movement direction. The traditional razor blade was replaced with an aluminum piece replicating the shoe, and a Chatillon Digital force meter load cell was affixed to the moving part to measure the maximum force consistently under the same conditions and speed of displacement. The maximum force is typically reached when the ice delaminates from the substrate. The principle is presented on the Figure 2.

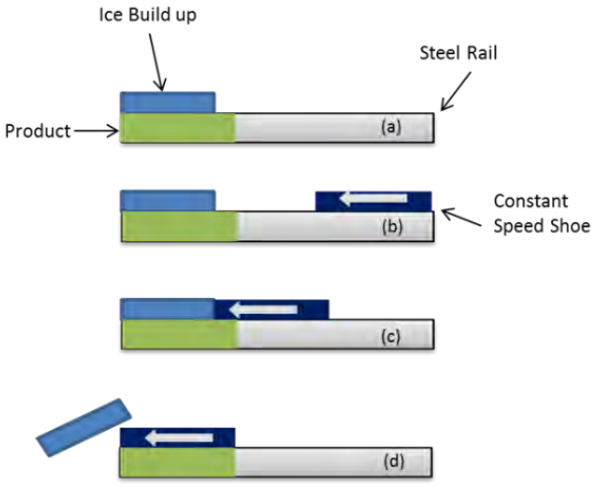

Figure 2. Simplify methodology (a) treated steel rail with ice buildup on its tip. (b) a constant speed shoe will move along the steel rail and measure the max force (c) push the ice tip to finally (d) remove the ice completely.

For proper apparatus validation, steel coupons and four distinct liquid chemical products were utilized. They were denominated as Product A, B, C and D. The products are all freezing point depressants of different viscosity. The identities of the fluids have been kept

confidential at the request of the client. All products were applied to follow the manufacturers' recommended methods, with 1 ml of each product uniformly spread on the coupon tip unless specified otherwise.

3 RESULTS AND DISCUSSION

The average ice mass accreted on steel is 4.8 ± 0.2 g, reflecting a variation of 4%. All mass variations for each product remain below 10%, ranging from 4.2 g to 5 g, indicating good reproducibility in the icing process. Mass for each product. Figure 3 presents the ice profiles obtained after a 30-minute precipitation for each substrate.

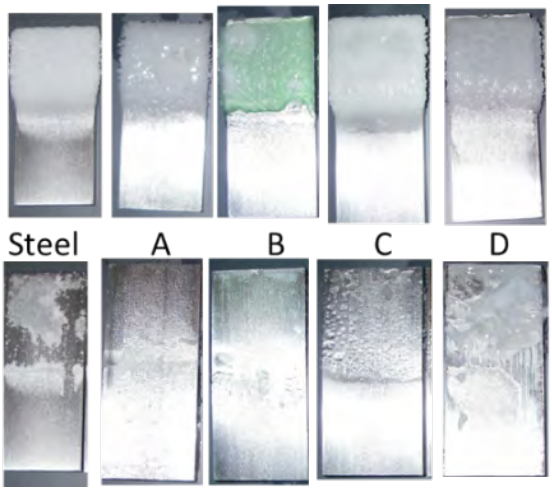

Figure 3. Ice accumulation over the steel substrate and the four different products A, B, C and D, after icing (top row) and after ice removal.

In the case of steel, it can be seen that the ice coupons are uniform and replicate an ice accretion that could be obtained in real environment. After the deicing, some ice remained stick to the substrate. The adhesion mode is a mix of adhesive and cohesive, mainly induce by the type of ice and type of external force used to de-ice. In the case of product, A, following the icing process, the ice coupon formed over the product exhibits noticeable differences compared to the reference. In certain areas, the ice displays perforations and appears denser than the reference steel substrate. Subsequent deicing results in the complete removal of the ice, and largely, the product is also eliminated, as depicted in the bottom picture. Product B, characterized by its green hue, effortlessly covers the substrates. Following the icing process, the majority of the ice adopts a green colour, with only a few sections remaining white. Post-deicing, all the ice is eradicated, along with the removal of most of the product, as illustrated in the bottom picture. Product C, possessing transparency, smoothly covers the substrates. Following the icing process, the density of the ice varies based on position, exhibiting both white and darker zones. Post-deicing, all the ice is eliminated, and predominantly, the product is also removed, as depicted in the bottom picture. However, it's noteworthy that more product residue remains compared to the other two products. Product D, similarly transparent, effortlessly covers the substrates. Following the icing process, the ice density exhibits variations depending on the position, featuring small darker zones. After deicing, all the ice is successfully removed, yet remnants of the product persist, as evidenced in the bottom picture. It's worth noting that the product exhibits increased viscosity and change in colour when mixed with water. During the deicing process, the max force for each substrate has been measured and their results are presented on the Figure 4.

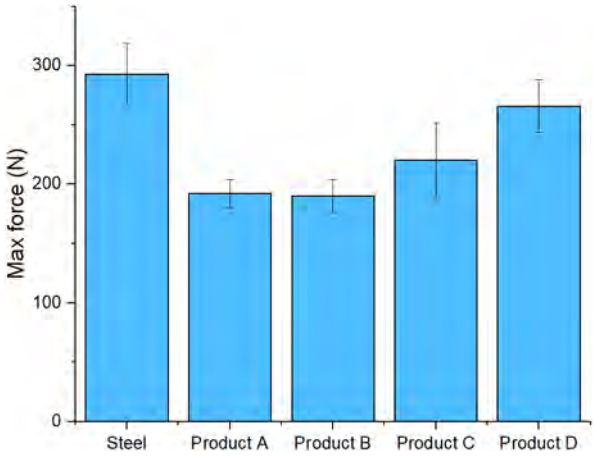

Figure 4. Average maximum forces measured on the reference steel substrates and on the different products.

The average maximum force measured on the steel reference substrate is 293 ± 26 N, indicating a variation of 9%. The average and standard deviation for the steel encompasses all values obtained in the five tests conducted during this study. With a variation below 10%, we can affirm that the test is both consistent and repeatable. Notably, Product D requires the highest force, reducing the maximum force by only 10%. During the testing of this specific product, discernible suction between the substrate and the product was observed.

The two most effective products proved to be Product A and Product B, reducing the maximum force by 34% and 35%, respectively. However, it's worth noting that product C could potentially yield better results in a second test run without reapplying products, as there seems to be more liquid remaining on the substrate. While Product C demonstrates a commendable reduction in maximum force compared to the steel substrate, a relatively high percentage of variation, 15%, indicates some instability in the product under these particular conditions.

While the mentioned products provide effective protection against ice for a single precipitation event, their efficacy diminishes with subsequent instances, as the contactor not only removes the ice but also eliminates the protective product. To withstand a strategy of continuous structural protection and minimize environmental impact, a more sustainable solution is worth considering. Our group used the same

setup but with different coatings considered hydrophobic and achieved the same range of force reduction giving these types of coating an enormous potential (Brassard, Villeneuve et al. 2020).

For such applications, the utilization of a conductive functionalized surface as an icephobic coating could be more sustainable (Brassard, Posteraro et al. 2021). Figure 4 illustrates the potential benefits of employing this type of surface in comparison to an unprotected metal surface. The unprotected surface exhibits uniform ice accumulation across almost its entire surface, resulting in high ice adhesion. This high adhesion could make it challenging to remove the ice efficiently in one pass, leading to potential disruptions in the electrical network and compromising overall functionality.

Contrastingly, the icephobic surface, showcased in Figure 5 below, is hydrophobic. This hydrophobic nature facilitates de-icing by (i) reducing the adhesion force and (ii) manipulating the ice formation process. This manipulation not only ease ice removal but also aids in identifying and managing ice formation more effectively. The beads that are formed, even at low intensity icing are more visible than very thin layer of ice. Such a surface offers a promising alternative for prolonged, sustainable protection against ice-related challenges.

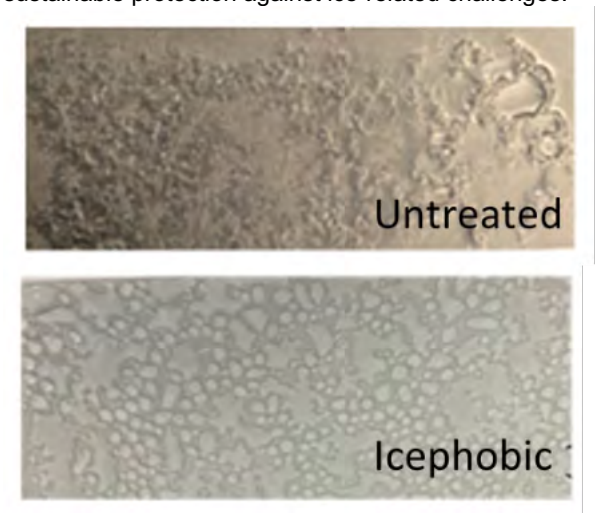

Figure 5. Ice accumulation over untreated substrate (top) and icephobic coating (bottom).

The creation of icephobic surfaces can be achieved through biomimetics, drawing inspiration from nature's intricate designs. Biomimicry takes cues from the remarkable features of the non-wettable lotus leaf, renowned for its sophisticated mechanisms. At UQAC, several endeavours have integrated these biomimetic characteristics into the development of several different icephobic materials (Shamshiri, Jafari et al. 2022, Bakhshandeh, Sobhani et al. 2023, Moghadam, Bakhshandeh et al. 2023, Shamshiri, Jafari et al. 2023, Sobhani, Bakhshandeh et al. 2023). Further exploration delves into biomimetics inspired by the carnivorous "Pitcher plant," where its oily surface mimics a skidding effect for insects (Shamshiri, Jafari et al. 2023).

Beyond railway applications, these coatings hold potential for various uses. Strategically applying them to automatic doors or emergency exits can prevent ice from acting as an adhesive, thereby enhancing safety. Coating critical surfaces also reduces ice buildup and the risk of falling, mitigating potential harm to passengers. Pantographs, when coated, can ensure better continuity even during freezing rain periods. Lastly, covering conductor cables can achieve structures free from icing-related issues. This broad application of icephobic coatings exemplifies their versatility and potential contributions to safety and efficiency in various contexts.

4 CONCLUSIONS

In conclusion, the comprehensive exploration of anti-icing technologies underscores their pivotal role in enhancing the reliability, safety, and efficiency of rail operations under challenging winter conditions. The development of this new method to assess the ability to reduce ice adhesion using liquid will help to select the best product in laboratory prior real condition application. By understanding the limitations of current liquid deicing products, such as their single-use effectiveness, and exploring sustainable alternatives inspired by biomimetics, new strategies could be designed and assessed. The potential of such icephobic coatings offers promising avenues for sustained protection against ice-related challenges, not only on rails but also in diverse applications aimed to support rail safety and maintenance.

REFERENCES

Bakhshandeh, E., S. Sobhani, R. Jafari and G. Momen (2023). "New insights into tailoring physicochemical properties for optimizing the anti-icing behavior of polyurethane coatings." Journal of Applied Polymer Science 140(44): e54610.

Brassard, J.-D., D. Posteraro, S. Sobhani, M. Ruggi and G. Momen (2021). "A Multi-Tool Analysis to Assess the Effectiveness of Passive Ice Protection Materials to Assist Rotorcraft Manual De-Icing." Applied Sciences 11(24): 11847.

Brassard, J.-D., D. K. Sarkar, J. Perron, A. Audibert-Hayet and D. Melot (2015). "Nano-micro structured superhydrophobic zinc coating on steel for prevention of corrosion and ice adhesion." Journal of Colloid and Interface Science 447: 240-247.

Brassard, J.-D., É. Villeneuve and C. Volat (2020). "Laboratory scaled third rail deicing comparative test." Results in Engineering 6: 100132.

Heyun, L., G. Xiaosong and T. Wenbin (2012). "Icing and anti-icing of railway contact wires." Reliability and safety in railway: 295-314.

Laforte, J. L., M. A. Allaire and J. Laflamme (1998). "State-of-the-Art on Power Line De-Icing." Atmospheric Research 46: 143-158.

Lemyre, É. (2023). "Decouverte." REM : les défis à surmonter (épisode 1). Aired March 26 2023.

Leroux, J. (2022). Guide to Aircraft Ground Deicing. S. o. A. E. G12: 400.

Ludvigsen, J. and R. Klæboe (2014). "Extreme weather impacts on freight railways in Europe." Natural Hazards 70(1): 767-787.

Moghadam, S. G., E. Bakhshandeh, R. Jafari and G. Momen (2023). "In-depth analysis of the effect of physicochemical properties of ionic liquids on anti-icing behavior of silicon based-coatings." Cold Regions Science and Technology 216: 104007.

Ouellette-Vézina, H. (2024). Reseau Express Métropolitain : Quatrième incident technique en quatre jours. Lapresse Plus.

Shamshiri, M., R. Jafari and G. Momen (2022). "An intelligent icephobic coating based on encapsulated phase change materials (PCM)." Colloids and Surfaces A: Physicochemical and Engineering Aspects 655: 130157.

Shamshiri, M., R. Jafari and G. Momen (2023). "A novel hybrid anti-icing surface combining an aqueous self-lubricating coating and phase-change materials." Progress in Organic Coatings 177: 107414.

Sobhani, S., E. Bakhshandeh, R. Jafari and G. Momen (2023). "Mechanical properties, icephobicity, and durability assessment of HT-PDMS nanocomposites: Effectiveness of sol–gel silica precipitation content." Journal of Sol-Gel Science and Technology 105(2): 348-359.

Thornes, J. E. and B. W. Davis (2002). Mitigating the impact of weather and climate on railway operations in the UK. ASME/IEEE Joint Railroad Conference, IEEE.

Xia, Y., J. N. Van Ommeren, P. Rietveld and W. Verhagen (2013). "Railway infrastructure disturbances and train operator performance: The role of weather." Transportation Research Part D: Transport and Environment 18: 97-102.

Canadian & Cold Regions
Rail Research Conference
2024

Broken rail detection in dark territory: Application

Dominika Juhaszova, Ali Al-Chaer, Sukhraj Kooner & Kyle R Mulligan
CPKC, Calgary, Alberta, Canada

ABSTRACT

North American Railways use periodic ultrasound inspections to detect internal rail defects and visual track inspections to find rail breaks along with joint pull-aparts to prevent train derailments. However, the ultrasonic defect detection rate is subject to the grinding quality, as rail surface fatigue might mask internal defects. Therefore, subsurface defects may go undetected and result in rail discontinuity, even within a short time period following the latest inspection. The breaks can go undetected resulting in a potential derailment or endangerment of the crew, public, and the environment. This paper presents a low-cost Rail Integrity Non-Vital Overlay Inspection System (RINOIS) that has been developed to detect near real-time rail breaks and to notify the approaching trains of potential danger. This paper also summarizes the processes that have been put in place to stop trains short of these locations where a potential rail break has been detected. The authors also propose a holistic approach to rail break detection achieved by combining the RINOIS with crossings at grade circuits.

1 INTRODUCTION

Undetected rail breaks can result in increased risk affecting train operations. Minimizing such risks is therefore critical for railroads in order to avoid potential consequences including, but not limited to: significant revenue loses, increased government regulation, reduced network velocity, the inability to serve customers, environmental impacts, or potential safety risks to the public and train crews. Right-of-ways in cold temperature climates are prone to higher rates of failure due to increased thermal cycling and a reduction in the yield strength of the rail (Ladubec and Magel 2011). The primary defences within the industry in preventing broken rail occurrences are passive and can include: the use of higher quality rail steels, controlled rail welding processes, considerations for rail neutral temperature when laying rail, rail scanning equipment to detect surface (e.g. Eddy Current) and sub-surface defects (e.g. (ultrasound (Juhaszova, et al. 2021)), and rail maintenance programs including rail grinding or milling. Rail scanning equipment are used to assess surface conditions for signs of Rolling Contact Fatigue (RCF) and subsurface conditions for defects created during rail manufacturing or post rail welding. Defect indications from these systems, known more commonly as Rail Flaw Detection (RFD) equipment are used by railroads to remove and replace rail sections through a combination of internally developed processes and regulation.

All of the above mentioned techniques and processes are intra dependent. The quality of ultrasonic testing is dependant on rail roughness, rail roughness is dependant on the quality and frequency of rail grinding, and rail grinding is dependant on the quality of pre-grind and crack depth scanning inspections. None of these techniques provide an active mechanism for detecting a rail integrity issue such as a break. This problem has been solved through the implementation of the Rail Integrity Non-Vital Overlay Inspection System (RINOIS) that sends near real time notifications and enables stopping of the approaching trains short of the location of a suspected break. The theory and operation of the RINOIS is described herein.

1.1 Broken Rail Detection Technologies

Canadian Pacific Kansas City (CPKC)'s network is 60% signalized also known as Centralized Traffic Control (CTC) territory, and 40% non-signalized or dark territory. CTC uses track circuits to provide traffic signals based on train occupancy. A break in the circuit triggers an Unidentified Track Occupancy (UTO), which can be caused by a broken signal bond or a broken rail. Therefore, CTC has the ability to detect rail breaks as a by-product of the system. In the event a UTO occurs, both signals and track employees are dispatched to the location at which point a rail break may be discovered.

Movements of train in dark territory or track are governed by Occupancy Control Systems (OCS) which do not require signals or track circuits. Dark territory network locations are essentially rail. Track Inspectors are employed to perform visual inspections to verify the integrity of the track looking out for a broken rail condition among other defects. In signalized crossing circuits, the continuous activation of the warning system will indicate a possible break.

Railways have deployed different technologies to detect rail breaks. The technologies can be circuit based

(Guillaumin, Ehrlich and Stark 1978), acoustic (Schwartz 2004), ultrasonic (Sireesha, et al. 2015), communications based (Kull 2014), and optic cable (Olson and Roop 2023).

CPKC has deployed two different systems in the dark territory: Alternating Current (AC) and Direct Current (DC) based technology. The DC based system can detect rail breaks in AC crossing circuits.

1.2 AC Based Detectors

The AC signal-based detectors are spaced one mile apart, with a shunt a half a mile from the detector on each side, creating 1 mile inductance loop. The system injects 3 AC signal burst frequencies in the rail at the set interval and scans for the change in the signal response (Gies 2022). The signal response is intended to measure the change in inductance of the one-mile section relative to a known circuit which includes a well-known resistance. When the system pulses, the signal response of the circuit which includes the known resistance is compared to the signal response propagated through the rail section. The rail section itself acts like a large resistance. Figure 1 shows the change in the amplitude and phase signal responses from the baseline value. When a train is present in the track circuit of the detector, and the axles short the rails, the signal response goes down because the inductance loop reduces in size. When a rail break occurs, the circuit opens, and the amplitude goes up as the inductance loops has significantly increased in size. Other factors, including ambient temperature and weather conditions can affect the signal response and must also be accounted for within the detection algorithms. The phase response of the signal also reacts to rail integrity changes and can go up or down depending on the frequency and the distance of the break from the detector. The data are compared against the thresholds for the phase and amplitude of each frequency that must be met for a specific alert to be published.

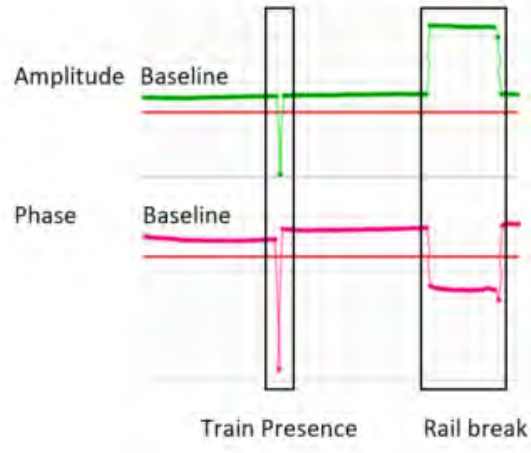

Figure 1. AC Signal response to train presence and rail break

1.3 DC Based Detectors

The DC current based detectors measure the integrity of the rail by monitoring changes in voltage. The system works in groups of detectors, between 1 and 10 detectors per group, where a detector transmits a very low voltage signal through the rail and adjacent detectors receive the voltage. Groups of detectors are separated using track shunts located on each end of the last detector within the group. Shunts are installed 1 mile from the end of each of the last detectors within a group. For shorter groups, as short as 0.2 miles, a single unit is placed halfway between the termination shunts. This is suitable for the track segments between two crossings at grade that do not overlap or track between crossing termination shunt and switch.

The systems scan 2 miles on either side of the detector while they are spaced only 1 mile apart. This configuration results in overlapping scanning zones and provides redundancy when one of the systems stops working, the neighbouring detectors provide broken rail detection for the track segment with the non-reporting detector. When a detector senses a rail break, the adjacent detectors validate the reading, e.g.: Detector A sends a pulse, Detector A and B take voltage measurements and return them to the back-office server (which can be Cloud based). Detector B sends a pulse, Detector A and B take voltage measurements and return them to the server. Subsequently, the voltages are compared via a rolling average algorithm. If there is a significant change in the rolling averages an alert is published. This cycle is repeated amongst the group of detectors and replicated throughout the dark territory subdivisions.

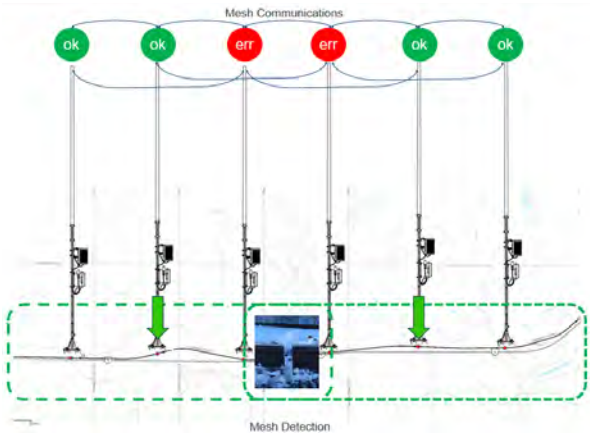

Figure 2. Configuration of a group of DC based detectors that are installed 1 mile apart. The detectors have mesh communication and detection systems that create a redundancy when one of the systems stop reporting

1.4 Communication System

For the detectors to communicate with one another a mesh network topology is implemented. A mesh topology is a network setup where each network device is interconnected with one another. This topology setup allows for most transmissions to be distributed even if

one of the connections goes down. It is a topology commonly used for wireless networks. Hot Box Detector (HBD) bungalows are integrated into the mesh network and act as gateway points to unload data into CPKC's back-office as these locations are equipped with 4G LTE modems. Additionally, all RINOIS also have 4G LTE and satellite capabilities to support redundant communication paths to CPKC's back-office.

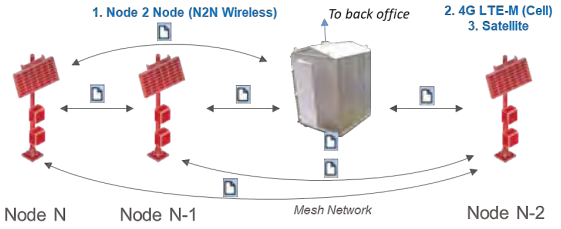

Figure 3. Wireless Mesh Network with 3 communication capabilities: Wireless, LTE, and satellite

1.5 Paper Objective

This paper presents the findings of the low-cost AC and DC based rail integrity non-vital overlay systems that have been deployed in dark territories of a Canadian railway company to significantly reduce the likelihood of broken rail derailments. The detected breaks could not have been identified by traditional methods as they occurred outside of the regular inspection hours. In addition to rail breaks, the RINOIS technology is sensitive enough to in some conditions identify loose joints and pull-aparts. The paper also proposes a holistic broken rail detection in non-signalled territory that can identify breaks within a circuit of crossings at grade.

2 MATERIALS AND METHODS

Data from 2023/2024 winter operations have been validated against field service failure reports to calculate the accuracy of the systems. The time of the broken rail alert notification is also compared against regular work hours of track inspectors to determine if the break would have been found through the existing visual inspection processes. The last ultrasonic inspection date prior to the break occurrence are also gathered to assess the reliability of ultrasonic based inspections (especially when the top of rail shows signs of RCF).

2.1 AC Detectors

The following section illustrates the various types of signal responses that have been recorded by the AC based detectors. The signal responses are divided into two (2) categories: clear break and a break over tie plate. A clear break is defined as a break which occurs between two crossties whereas a break over a tie plate occurs on a tie plate whereby the rail is still laterally supported. A break over a tie plate in CTC typically enables current to conduct which can mask the existence of a rail break.

When a clear break occurs, the signal response as shown in Figure 4 (a) typically rises rapidly. All subsequent data points remain tightly grouped with a low standard deviation. Breaks over tie plates or breaks where the rail ends maintain some form of contact will also have sharp rises in the signal response however, the standard deviation of subsequent data points do not remain tightly grouped as shown in Figure 4 (b) and Figure 4 (c). The advantage of storing all historical data from these systems in CPKC's back-office is that these events can be classified and specific alerts can be issued to detect these occurrences.

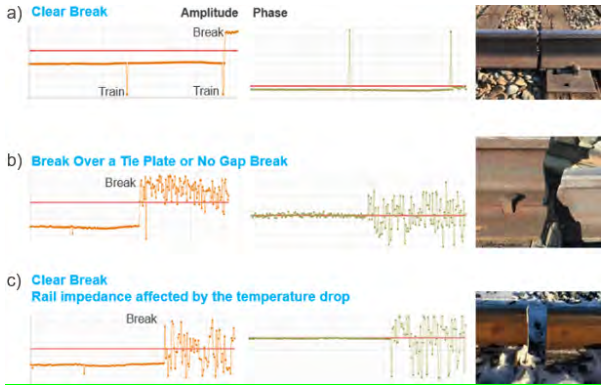

Figure 4. AC Detector signal response to various types of rail breaks

2.2 DC Detectors

When a rail integrity issue is detected by the DC system, the voltage sharply increases or decreases depending on the position of a rail break relative to the detector that is in the role of a transmitter. Detectors on the same side of the transmitter as the break respond by the increase in voltage. Contrarily, detectors on the transmitter's side opposite to the location of a break decrease voltage as show in Figure 5. The voltage values have a low standard deviation. Within a group of detectors, the estimated location of a break is near the detector with the highest change in voltage.

Figure 5. Rail break over a tie plate and associated voltage response of 3 detectors in a group

2.3 Jointed Track

Both RINOIS systems are affected by the number of joints within circuits. While the signal responses of rail breaks and loose joints are different, the higher the number of joints the higher probability of a false broken rail alerts. Therefore, rules in the back office have been implemented to distinguish actual rail breaks from loose or corroded joints. Upon field inspection it has been determined that high numbers of joints resulting in lower

continuity trigger alerts even if joints are compliant and fully supported, with bolts tightened. Replacement of bolts and cleaning of joints to remove rust between joint bars and rail alleviates false alerts, however, this is not feasible on territories with significant amounts of joints over short distances (e.g. more than 300 joints on 100 miles of track). Joint bonding in jointed territory is an option to manage signal response volatility but the limitation of joint bonding is that it may inhibit the detection of pull-aparts. Suspected loose joint reports for the field employees are generated based on the system's ability to identify areas with lower continuity which drive targeted inspections and maintenance work during daily patrol and joints are inspected and bolts are tightened until refusal.

a) b)

Figure 6. Photos of internal defects at the location of a break. a) transverse defect b) impurity

2.4 Broken Rail Alert Procedure

To publish a broken rail alert, the signal or voltage values must meet internal threshold from four (4) consecutive scanning cycles for amplitude and phase responses and standard deviation between the points. This time delay rule is in place to minimize false alerts that could be caused by joint movement during a train passing. Once all thresholds are met four (4) times, an alert is published, and email notification is sent to Engineering Services Operations Desk (ESOD). The ESOD then immediately verbally notifies a Rail Traffic Controller (RTC) (dispatcher). To prevent unnecessary track inspector dispatches, the RTC verifies that there is no active Track Occupancy Permit (TOP) (track warrant) at the location of a suspected break for track work that requires opening rail, as the system cannot distinguish between track maintenance and service failure. If there is no TOP, the RTC issues track blocking to prevent any approaching train from entering the location of a suspected break. After blocking is in place, the ESOD contacts a track inspector on-call to inspect the suspected track range. The inspector verifies the mile range designated in the alert and visually inspects for a broken rail, pull-a parts, or any other track integrity issue. If a defect is found, the inspector assesses whether a train can pass as per Movement Over Broken Rail (MOBR) instructions. If no defects are found, detector track connections and shunts are verified, a false alert is reported, and blocking is removed (i.e. train movement is permitted). No trains can proceed until the inspection is completed. This policy resulted in broken rail derailment elimination on the RINOIS territory. The broken rail alert procedure protects approaching trains from a derailment.

Additionally, CPKC has a rule in place to protect the rail network against trains with possible broken wheels that can damage the track and result in multiple broken rails. When multiple broken rail alerts are triggered within 20 miles and 60 minutes, the train traffic data are extracted to verify if there is a train travelling away from the locations of suspected breaks. The train is then stopped for a visual inspection of all wheels by the train crew. This example of data aggregation demonstrates that the systems can be used for additional purposes in order to maintain high levels of safety.

2.5 Non-reporting Detectors

As per CPKC's winter operating plan provided to Transport Canada in the rules respecting Higher Risk Key Trains (HRKTs), rail traffic may operate at 40 mph when the ambient temperature is below -15ºC given there is a form of broken rail detection. The RINOIS system therefore supports safely operating at higher operating speeds during winter operations, and benefits such as elimination to recrew schedule disruptions due to low speed train stalls. The implementation of these systems has resulted in benefits including, but not limited to, the following: decreases in cost related to recrews, higher operating speeds, decreases in stalls and incidents, cost savings in unexpected train service interruptions, and derailment cleanups, higher safety for train crews and public.

When a detector stops reporting or any other issue with a detector is identified, during winter operations, a general bulletin order is issued for HRKTs to slow to 30 mph at the affected locations when the temperature is -15ºC or colder.

2.6 Crossings at Grade

Currently within the industry, broken rails in crossings are found through prolonged crossing activation. Prolonged crossing activation warrants bystanders to contact railroads to resume conventional vehicle traffic resulting in a dual dispatch of a signal maintainer and a track inspector to determine the problem. Presently CPKC has deployed RINOIS systems in dark territory (OCS) through the implementation of two different voltage transmitting systems, DC and AC. The rail monitoring system is isolated from the crossing circuits through a shunt to mitigate any possible effects the detector signal may pose on the vital operation of the crossings. Contemporary track configurations consist of both rail monitoring systems installed adjacent to audio frequency and DC track circuit crossings. Next steps for CPKC will be to install a system within crossings to monitor the continuity and integrity of the rail such that these conditions can be reported to the back-office in real-time.

The audio frequency crossing electronics require the frequency observed on the rail to be less than 211 Hz,

therefore voiding the installation of the AC system within any audio frequency crossing due to its frequency being greater than the requirement. Installing the AC system within the DC track circuit crossing presents problems that may affect the integrity of the crossing circuits. The negative half cycle of the AC signal possesses the power to negatively affect any relays and voltage regulators therefore also voiding the installation of the AC system within a DC track circuit crossing. Installing the DC detector within a DC track circuit crossing was established to be non-viable due to destructive interference between the two DC signals. CPKC has established internal standards required when installing either type of RINOIS system, for example, the AC system must be installed at minimum a ¼ of a mile from 100% crossing approach to ensure there is no interference from the system to crossing. In addition to that condition, when a crossing is AC type terminated by a Narrow Band Shunt (NBS), a hard-wired shunt is installed 500 feet away from NBS resulting in a 500 feet blind zone between detector and crossings terminated by an NBS. Continued work in the space is on-going in order to reduce the frequency of blind zones. Note that train movements are not permitted higher speeds in these blind zones where there is no rail break detection present.

In theory, establishing the DC detector within an AC based crossing is viable due to the known effect of DC voltage superimposing the AC signal, ultimately increasing the root mean square voltage of the signal. Most modern grade-crossing signals use a constant warning time device, also known as a grade crossing predictor, or GCP. The GCP measures the speed of the approaching train by the change the train makes in the frequency of the audio overlay frequency therefore superimposing the DC voltage onto the AC system would not affect crossing operation since the frequency would not change. Installing the DC system within frequency-based crossings is contingent on the output of the detector system during an internal failure. The following test situations were observed to simulate the potential internal failures, output diode failed short, output diode simulated short using shunt wire, output regulator latched in ON state, simulated short across output regulator.

It was concluded that all failure states effectively shunt the crossing circuit at the connection points therefore eliminating the possibility of installing the DC detector within a DC crossing. An interesting concept was derived from the test results, installing the DC detectors at the crossings shunts would potentially allow for scanning through the crossings. The concept was tested, and it was determined that installing the DC detector on the shunts would allow for broken rail detection through the audio frequency crossings.

A solution for detecting through DC track circuit crossings is not possible solely through a detector, an alternate concept of monitoring the status of the relays in combination with a detector was investigated. The track circuit consists in a block section defined at each edge by insulated joints on the rails. The insulated joints provide electrical insulation between a track circuit and the adjacent tracks. The signal source is connected to the rails at one edge of the block section, while the receiver, a relay, is connected to the other edge. When no train is present, the track circuit is unoccupied, and the direct current supplied by the battery is transmitted by the rails to the relay and energizes it or “picks it up”. When the relay is energized, a signal for normal train operation is present. When a train approaches the block, its wheels and axles connect the two rails together shorting the battery and thereby reducing the current through the relay to zero. Using this knowledge, the conceptualization to incorporate a repeater relay and monitor the state of the relay using an I/O device in conjugation with a communication system was determined to be a viable solution. Additionally, a logic complimenting the relay monitoring can be built in the back office to validate train presence based on the RINOIS signal response. If a relay is activated for an extended time period and no train is detected on either side of the crossing, then the RINOIS system would trigger a broken rail alert.

Table 1. Rail integrity issues identified in January 2024

Defect Type	Defect Date	Alert Time	System Accuracy	Last Ultrasound Inspection Date
Broken Rail	1/3/2024	17:59 CT	Detected	12/12/2023
Broken Rail over tie plate	1/7/2024	07:33 CT	Detected	12/5/2023
Broken Rail over tie plate	1/8/2024	05:07 MT	Detected	12/11/2023
Broken Rail over tie plate	1/8/2024	13:37 MT	Not Detected	12/11/2023
Broken Rail over tie plate	1/8/2024	22:45 CT	Detected	12/7/2023
Broken Rail over tie plate	1/11/2024	02:13 CT	Detected	12/5/2023
Broken Rail over tie plate	1/11/2024	18:43 CT	Detected	12/5/2023
Broken Rail over tie plate	1/11/2024	14:05 PT	Detected	12/22/2023
Broken Rail	1/12/2024	03:55 MT	Detected	12/14/2023
Broken Rail	1/12/2024	12:32 MT	Detected	12/5/2023
Broken Rail over tie plate	1/12/2024	12:21 PT	Detected	12/15/2023
Broken Rail	1/13/2024	03:33 PT	Detected	12/22/2023
Broken Rail	1/13/2024	22:34 CT	Detected	12/11/2023
Broken Rail over tie plate	1/13/2024	00:55 CT	Detected	11/30/2023
Broken Rail over tie plate	1/13/2024	00:23 CT	Detected	11/30/2023
Broken Rail over tie plate	1/13/2024	09:11 CT	Detected	12/5/2023
Broken Rail	1/13/2024	09:45 CT	Detected	12/5/2023
Broken Rail	1/13/2024	14:35 CT	Detected	12/19/2023
Broken Rail over tie plate	1/13/2024	15:53 MT	Detected	12/7/2023
Broken Rail over tie plate	1/13/2024	03:25 MT	Detected	1/12/2024
Broken Rail over tie plate	1/13/2024	17:00 CT	Detected	12/19/2023
Broken Rail	1/14/2024	05:05 PT	Detected	12/22/2023
Broken Rail	1/14/2024	09:51 CT	Detected	12/7/2023
Broken Rail	1/14/2024	22:01 MT	Detected	1/4/2024
Broken Rail over tie plate	1/16/2024	06:33 CT	Detected	12/5/2023
Broken Rail	1/16/2024	00:35 CT	Detected	12/5/2023
Broken Rail	1/16/2024	07:01 CT	Detected	12/15/2023
Broken Rail	1/17/2024	08:23 PT	Detected	10/12/2023
Broken Rail over tie plate	1/18/2024	10:05 PT	Detected	1/16/2024

3 RESULTS AND DISUSSION

Since the installation of the RINOIS in dark territory the systems have detected 97 rail integrity issues. As shown in Table 1, between January 1 and 25, 2024 there were 29 rail breaks due to various root causes such as failed weld, internal defect or material impurity (Figure 6) within detection zones of RINOIS system. 28 of these breaks were detected, one break over a tie plate was not. The systems accuracy rate has increased through internal and external enhancements in alerting rules and increase in system reliability. The break that was not detected was found by track inspectors during patrols. Broken rail detection technology together with the efforts of track inspectors achieved decrease in broken rail derailments and increase in rail safety.

11 out of 29 breaks happened during regular work hours of inspectors, however, based on the tonnage, some subdivisions are patrolled only every 3 days and could have gone undetected by inspectors prior to the next train movement. 16 of the breaks were over a tie plate, one of them was not detected by RINOIS.

On average, the locations of the break were tested with ultrasound inspection 32 days prior to the occurrence of the break. The defects were either outside of the detection zone or there was no indication of an internal defect.

3.1 Future Work

3.1.1 AC Systems

At predetermined intervals, AC-based systems inject three AC signals of varying frequencies into the rail and observe any changes in the signal response. A rail break is identified as a deviation of the signal response significantly from its baseline value and from the signal response observed during the preceding set interval (Gies 2022). AC systems are constructed using the fundamental properties of the rail as an inductor connected in series with a resistor and a capacitor in a parallel circuit across the system as shown in Figure 7. It is necessary to initialize/rebaseline these systems during installation and after track maintenance in the field for detection of rail break using rail equivalent RLC values. AC Systems are initialize/rebaseline with a data cable connection to the tablet that is outfitted with the Configurator software.

Currently, rebaslining is necessary following each track maintenance procedure for these systems, as track work affects and change the baseline value. The change in a baseline value may result in the oversight of rail integrity issues until the systems are rebaselined by the field maintainers.

These systems necessitate a substantial investment of time and effort for both monitoring and tracing track maintenance, as well as rebaselining the systems.

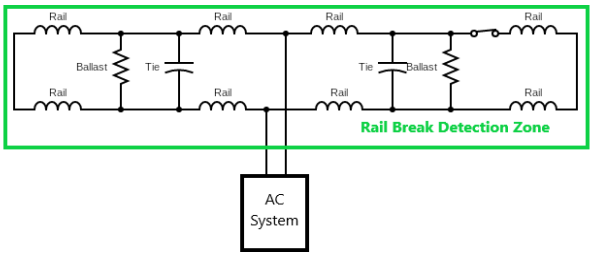

Figure 7. AC System RLC circuits – Switch in Normal Position

To account for baseline drift (Figure 8) caused by environmental factors, systems are engineered with threshold values that can be updated. The changes in environmental factors, such as the replacement of ballast and ties, have been identified as the cause of the progressive drift of the baseline over time. In order to revise the threshold values, periodic analysis of the impact of environmental factors is necessary.

Figure 8. Baseline drift

A considerable quantity of fundamental AC system signals is susceptible to the effects of high-frequency noise, as shown in Figure 9. Preliminary hypotheses posited that the root cause was frequency signal leakage originating from crossing circuits. Subsequent troubleshooting, however, has determined that frequency crossing in the circuit is not the underlying cause. There are ongoing troubleshooting efforts to rectify this issue.

Certain AC systems incorporate dedicated lightning arrestors as a precaution against perilous power surges that may occur during severe weather circumstances.

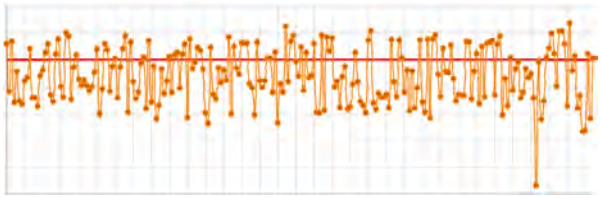

Figure 9. Unstable baseline (Noise)

The implementation of these lightning arrestors has resulted in a low amplitude issue whereby the system behaves as a difficult-to-identify short circuit. The issue generates a blind zone beyond the lightning arrestor box and prevent rail break detection beyond this box.

When the connection between the AC system and the rail is corroded or constricted, high amplitude issues ensue. Consequently, the system produces erroneous alerts and operates as an open circuit.

If the switch is installed between the system and the shunt (Figure 10), these systems can monitor the rail for breaks from the switch to the shunt, but only while the switch is in its normal position. Nevertheless, when the switch is in reversed position, it will issue erroneous alert and create a blind zone for monitoring beyond the switch until the shunt as well as it will limit the rail break detection range on the other side of the detector because of electrical characteristic of this system (Current will flow through low resistance loop).

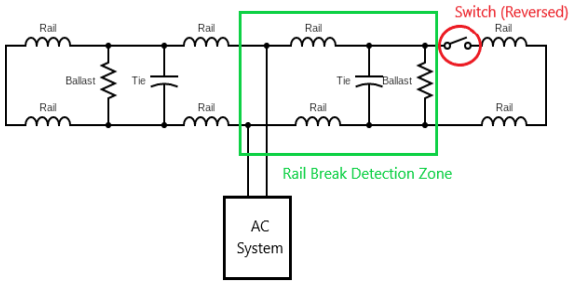

Figure 10. AC System RLC circuits – Switch in Reverse Position

3.1.2 DC Systems

At predetermined intervals, DC-based systems inject low voltage direct current pulses into the rail and observe any variation in the signal response. The DC systems are capable of operating both individually and in groups, with systems within the same group interacting with adjacent systems.

In the case of an individual or standalone system, shunts are positioned at predetermined distances on both sides of the system. However, when multiple systems are operating in a group, shunts are only installed at a predetermined distance from the outermost system in the group. Monitoring the adjacent system's area of the rail for break is possible if the system between two active systems fails to function; therefore, systems must be installed to overlap each other's coverage areas to obtain this benefit from group system installation.

Currently, direct current (DC) systems lack the capacity to monitor the rail section past the switch point or on the opposite side of the switch that separates the spur track from the main track, or between two switches that divide or separate the siding track from the main track. Switches can present as either a short circuit or as an open circuit. The electromechanical connections in a switch can be electrically opened or closed by the mechanical forces distributed throughout the switch during reversal or normalization. The electrical properties can also be affected similarly by the forces exerted on the electromechanical connections during a train pass. This can result in unstable electrical properties of the monitored circuit. When the switches and their corresponding components are in the normal position, they function as a shunt, which produces a stable and elevated signal response (baseline). However, when the switch position is reversed from normal, it acts as an open circuit, which causes false broken rail alerts due to the discontinuity in the DC circuit as defined by electrical fundamentals. This issue could be resolved by bonding all switch components.

Switch components have been upgraded with insulated components to prevent it from acting as shunt. To prevent the spur tracks and siding tracks from serving as an alternate pathway for DC signals rather than utilizing the main track, insulated joints were installed on both sides of the siding tracks and on the spur tracks that pass the switch. To maintain strength, durability, and longevity, specific track equipment and components, including switch frogs, guard rails, heel blocks, and switch points, are constructed from high-quality steel. The conductive property of these equipment's provides an alternative path for DC signals.

The gradual variation in system signal values caused by a change in the conductivity of the ballast and ties at low temperatures and during precipitation suggests that environmental factors must also be periodically analyzed in order to determine the threshold values and design a system that can compensate for those factors in order to enhance the performance of the system.

4 CONCLUSIONS

Rail Integrity Non-Vital Overlay System (RINOIS) is intended to detect rail integrity faults in CPKC's non-signaled or more commonly known as dark territories. The unique design of both AC and DC current based RINOIS take advantage of low-cost off the shelf components, resulting in systems that are 80% less expensive than implementing Centralized Traffic Control (CTC) in these subdivisions where train frequency does not justify the expense. However, because these subdivisions generally transport dangerous goods, having a wayside broken rail detection system provides safety overlay. Additional benefit to the low cost of the components, the system does not require all joints to be bonded to detect a rail break, keeping the cost of the installation low. Through deployment of the technology, advanced data analytics, alert procedures, rail inspection, and no movement prior to inspection, elimination of broken rail derailments on the territory equipped with the system elimination of broken rail derailments on the RINOIS territories was achieved, resulting in higher safety of CPKC train operations. As with the CTC, which does not detect 100% of the rail breaks, RINOIS technology complements visual inspections and does not replace them. All these tools are part of the suite of defense mechanisms used to protect railway safety.

The authors continue to implement new and advanced logic and have improved the system by redesigning the charging circuits, adding solar panels, upgrading communications to increase the reliability of the systems. CPKC is dedicated in further improvement of the system through alerting rules enhancements to improve accuracy and pull-apart detection, bonding of the switches to include them in detection, and deployment of communications systems in crossing at grades to provide detection through entire mainline.

Finally, these systems are cloud connected enabling raw data analytics and eventually integration of AI into the alert review process.

5 ACKNOWLEDGEMENT

Authors would like to express appreciation to the CPKC's field personnel for supporting the development of the system and for its maintenance, Test Department for the root cause analysis, ESOD for process support, and our vendors for reliability and accuracy improvements.

REFERENCES

Gies, Paul D. 2022. Broken Rail Detector. USA Patent Application 20220234632. April 15.

Guillaumin, Bruno, Anthony G Ehrlich, and Donald E, Stark. 1978. Broken rail detecting track circuits. Canada Patent CA1100594A. 01 09.

Juhaszova, Dominika, John Furlong, Adam Milligan, and Kyle R Mulligan. 2021. "Condition based rail surface management using EMFI technology." Canadian & Cold Regions Rail Research Conference. Edmonton: Canadian Rail Research Laboratory. 64-71.

Kull, Robert C. 2014. Broken Rail Detection System for Communications-Based Train Control. Canada Patent US20160107664A1. 05 06.

Ladubec, C, and E Magel. 2011. "NRC Publications Archive Canada." Winter railroading in Canada: a review of track and rolling stock. June 19. Accessed January 29, 2024. https://nrc-publications.canada.ca/eng/view/author/version/?id=039773d2-b4cb-42d3-af7e-7dbe3bd84a42#:~:text=Extreme%20cold%20temperatures%20may%20also,12%5D%2C%20%5B13%5D.

Olson, Leslie E, and Stephen S Roop. 2023. An Investigation into the Use of Buried Fiber Optic Filament to Detect Trains and Broken Rail . Report, Washington: Transportation Research Board.

Schwartz, Ken. 2004. Development of an Acoustic Broken Rail Detection System. Report, Washington: Transportation Research Board.

Sireesha, R, Ajay B Kumar, G Mallikarjunaiah, and Bharath Kumar B. 2015. "Broken Rail Detection System using RF Technology." SSRG International Journal of Electronics and Communication Engineering (SSRG-IJECE) – volume 2 . internationaljournalssrg.org. 11-15.

Canadian & Cold Regions
Rail Research Conference
2024

Freight car air brake system performance in cold temperatures

Elton Toma, Alok Jahagirdar, Stephen Mackie, & Albert Wahba
National Research Council Canada, Ottawa, Ontario, Canada

ABSTRACT

This paper presents results from controlled laboratory testing of the operational performance of 23 service worn and 21 refurbished freight car brake systems at temperatures ranging from +10°C to -40°C. The 44 systems were tested using service brake applications, and emergency brake applications from brake pipe pressures of 75 psi and 90 psi. Forces after 10 minutes are compared for service brake applications, forces after 10 and 90 minutes are compared for emergency brake applications. Air flow demand is compared. Findings are that service worn brake systems require up to 5 times more air at -40°C compared to a new brake system at the same temperatures; service worn brake systems demonstrate degraded performance at colder temperatures. The brake force degradation, both in maximum achieved peak force and the length of time the force is held has implications for rail operations during service braking, emergency braking, and during the recovery from emergency brake applications.

1 INTRODUCTION

Freight rail car air brakes form an interconnected system in a train which is controlled under normal operating conditions solely by the locomotive engineer. The air system depends on compressed air supplied by the locomotives to flow through the brake pipe to the individual freight cars. Each freight car stores air in reservoir tanks, and the air pressure within the brake pipe is controlled by the engineer who sends brake pipe pressure commands to control the brake actions within the train as a whole. The system critically depends on the brake pipe pressure and the air brake equipment installed on each freight car to work properly. A failure of the train line brake pipe will affect the entire train, while the failure of components on a single car may affect only that car, cars near to it, or possibly the entire train. Adequate air pressure in the train line brake system and the operation of each rail car is critical for safe train operation, and maintaining it depends on the proper functionality of many air brake components in the system.

An accident in Canada in February 2019 has tragically brought attention to an operational problem that North American railways have been dealing with since the advent and adoption of pneumatically controlled train braking systems: loss of air brake effectiveness in cold weather conditions. Loss of air brakes under any weather condition is a serious safety concern to onboard rail crew and passengers, as well as the surrounding environment and communities, as it nearly always results in an unintended and uncontrolled movement of the rail cars. In some cases, complete loss of air brake pressure can result in a “run-away” train, which can lead to disastrous circumstances. As noted by Transportation Safety Board (TSB) of Canada in Report R16W0242 (TSB 2019a):

“…while equipment runaways are generally considered low frequency, they can also be high-risk events and have extreme consequences, particularly if they involve dangerous goods…”.

Uncontrolled movements continue to be a serious safety risk, as summarized in the TSB 2022 Watchlist (TSB 2022) on unplanned and uncontrolled movements of rail equipment, where it is stated that in Canada since 2013 the TSB has published 18 investigation reports involving uncontrolled movements in which eight employees lost their lives and two employees were seriously injured.

Cold weather exacerbates the problem, as cold conditions increase the amount of air pressure leakage in the brake systems, and the greater the amount of air pressure leakage the greater the probability of an occurrence of loss of air brake effectiveness. The industry recognizes this, and the railways have procedures in place for dealing with winter conditions in all aspects of freight operations. For example, as outlined in their 2023-2024 Winter Contingency Plan Canadian Pacific Kansas City (CPKC) reduces train length, weight, and speeds when temperatures drop below -25°C (CPKC 2023). This helps to reduce delays in waiting for brake systems to recharge, keeps air pressures within allowable limits for the train length, and reduces braking demands by using lower tonnage trains.

Despite these and other operational rules, a full understanding of the air brake system and its associated deficiencies in cold weather conditions is lacking. Two previous air brake tests were identified that give a partial

picture of the brake performance in cold weather conditions, but neither fully address the issue of the operating performance of the approximately 1.4 million freight cars operating in North America. The Association of American Railroads (AAR) performed a test in 2015 of twenty railcars under cold weather conditions, however these tests were completed outdoors in uncontrolled conditions at temperatures which ranged from -8.3°C to +13.9°C. The conclusion of the AAR was that "There was no change in the brake system performance of any of the 20 cars throughout the course of the testing, regardless of the air temperature or off-air time prior to the test" (TSB 2022).

This range of temperatures is far above what many railways consider to be normal cold weather conditions during winter operations, and is above the -12.2°C temperature at which the Federal Railroad Administration (FRA) requires a railway to have cold weather operating procedures in place (USDOT 2012). These results are also not supported by the significant experience of the railways, or by tests completed by the TSB in support of investigation R19C0015. In this investigation, the TSB used thirteen grain hopper cars recovered from the February 2019 accident site, and tested the air brake performance at cold temperatures. Testing was completed in the field at a location near the original accident site (TSB 2019b). The TSB found that for the grain hopper cars tested, the service brake cylinder pressure was 56% of the expected maximum (and was dropping quickly), and that the emergency brake pressure at application was 86% of the expected maximum. As well, the holding ability of the emergency brake application after three hours was only 60% of the expected value.

The TSB field experiment proved that under cold weather conditions, the air brakes on the cars tested did not hold brake force as high as expected, or for as long as required. As well, the TSB found that all thirteen grain hopper cars failed additional brake testing using an automated single car test device (ASCTD) when the ambient temperatures during testing ranged between −21°C to −26°C. As this was a field test, temperatures were limited to those occurring naturally, and testing was limited to only the available test cars.

In a later published engineering analysis of the situation, as TSB Rail Safety Advisory (RSA) 617-04/19 (TSB 2019c), the TSB concluded that:
"In most operating scenarios, some leakage is expected and it will not initially compromise safety. However, it can create a reduced margin of safety when a train brake system is relied upon for an extended duration. The determination of an extended duration will depend on factors such as ambient temperatures, anticipated brake cylinder leakage rates and the percentage grade at the location where the train is stopped. If a critical loss of brake cylinder pressure occurs due to leakage effects, an uncontrolled movement can result."

Brake system leakage, or loss of brake cylinder pressure is controlled by specifications set by the AAR. AAR Specification S-401 (Brake Design Requirements) allows brake cylinder leakage of up to 4 psi in 10 minutes on any new freight car built for North American interchange service, and AAR Specification S-486 (Code of Air Brake System Tests for Freight Equipment – Single Car Test) specifies that a brake cylinder is condemned if the leakage is greater or equal to 1 psi per minute (as measured 3 minutes after reducing brake pipe pressure from 90 psi to 80 psi) (TSB 2019c). These specifications set limits for new and service worn brake cylinders, however these leak-down rates are measured within the first 3 and 10 minutes of pressurization, whereas brake systems are relied on to hold pressure for much longer both under typical service conditions and following emergency brake application.

The time required for a brake cylinder to lose pressure for various leakage rates was investigated by the TSB in RSA 617-04/19 (TSB 2019c). As reported in (TSB 2019c), the time taken to lose 50% initial brake cylinder pressure of 78 psi resulting from an emergency brake application was approximately 3 hours and 10 minutes for a brake cylinder with an initial leak rate of 0.5 psi/min, and from the data presented in (TSB 2019c) it can be estimated that a brake cylinder with 1 psi/min initial leak down rate will take approximately 1 hour 40 minutes to leak down to 50% of the initial pressure. Although the data provided in (TSB 2019c) can be used to estimate the time a train will take to lose brake force on a grade before becoming an uncontrolled movement, it does not inform the industry, regulators or investigators what the performance of freight car brake systems are in-service in cold weather conditions.

Quantifying the performance of freight train air brakes under controlled and repeatable conditions requires the control of the external temperature of the air brake components as installed and operated on a freight car, and a controlled method of brake applications. To allow for such testing in controlled conditions, the National Research Council (NRC) Canada has built a Cold Weather Air Brake (CWAB) research facility to study freight car air brake systems under temperature-controlled conditions. The main goal of this research is to better understand the performance and operations of freight train air brakes under controlled and repeatable cold weather conditions.

2 MATERIALS AND METHODS

The CWAB facility was built by the NRC to allow for the testing of multiple freight car air brake systems in climate-controlled conditions in a space saving arrangement. The lab is currently able to operate up to fourteen complete working freight car air brake systems, representing approximately 600 feet of train length. The air brake systems are installed in a compact arrangement where each brake system test module has piping installed which equals forty feet of standard air brake train line, with cars connected using standard end-of-car hoses and glad hands. The air brake components which can be installed in the facility for testing are the car control valve (bracket, emergency portion, and service portion); body-mounted (foundation) brake cylinder; empty/load valve; and retainer valve. Each brake system is instrumented to collect brake pipe pressure (BPP), auxiliary reservoir pressure (ARP), emergency reservoir

pressure (ERP), brake cylinder pressure (BCP), brake cylinder force (BF), and brake piston displacement. The facility is able to perform standard air brake operations as would occur in a train in-service using an electronically controlled pneumatic air delivery system that allows for repeatable brake applications. The brake system supply air is filtered, dried and cooled to the test temperature before entering the individual air brake systems.

3 TEST PROCEDURE

Air brake systems presented in this research were tested in six separate testing rounds at the NRC's CWAB facility between November 2021 and February 2023. The service and emergency portions and brake cylinders were provided by partner short line railways and from the NRC's stock of air brake components. The first partner short line railway (denoted as RR1 in Table 1 and Table 2), provided components primarily from box and flat cars used to transport mixed freight, while the second short line railway (RR2) provided components from hopper cars used in iron ore service. The partner railways removed brake systems from cars which had recently passed air brake inspections. The ages of the air brake components were estimated from the dates of last service found on the service and emergency portions, and where these dates could not be found the NRC estimated the ages based on discussions with the providing railway.

The air brake components were installed in the brake system test modules, after which all air brake systems were tested with an AAR approved automated single car test device (ASCTD) as a complete and working air brake system prior to testing to verify their functionality against the single car air brake test (SCABT). The systems were then tested for a minimum of 7 hours each day at five temperatures: 0°C, -10°C, -20°C, -30°C and -40°C. An electronically controlled pneumatic air delivery system was used to make consistent and repeatable air brake applications at each test temperature. Test data was collected on a continuous basis for the duration of each test session at a sample rate of 200 Hz. The BPP was 90 psi (representing a front of train BPP) for one test day and 75 psi (representing a rear of train BPP) for a second day of testing. The air brake applications tested and discussed here include:

1. Minimum service brake application of 6 psi from fully charged (brakes released) state;
2. Full service brake application of 26 psi from fully charged state;
3. Emergency brake application, held for 10 minutes; and
4. Emergency brake application from fully charged state, held for 90 minutes.

After completing the testing of the service worn units the air brake systems were sent to an AAR approved facility for refurbishment where all worn components were replaced. The refurbished units were then installed in the CWAB facility and tested again under the same temperature conditions with the same series of air brake applications. Although a unit-to-unit comparison can be made from the data collected, the results presented in this paper will summarize the results of new and refurbished brake systems as a group in comparison to service worn systems as a group. A total of 44 brake systems are discussed: 23 service-worn systems and 21 refurbished systems.

4 RESULTS

Results for tests on 44 brake systems are presented: 23 service-worn systems and 21 refurbished systems. Each brake system was subjected to a minimum of twelve brake applications each day at two BPP (75 and 90 psi) and five test temperatures, resulting in data collected from over 5,280 controlled brake applications. The results are presented as the measured brake cylinder force, measured at the active end of the brake piston rod. Note that this force is not equal to the brake shoe force as would be seen on a freight car at the wheel as the applied brake shoe force is dependant on the type of and condition of the brake rigging installed.

4.1 Service Braking, Minimum and Full Service Applications

Figure 1 shows the brake force after 10 minutes following a minimum (6 psi) service brake application from 90 psi BPP for the service worn systems. Figure 2 shows the results for the refurbished systems. The new and service worn systems both produce forces which diminish with lowered temperatures, but the service worn systems display a greater variance in the force. New systems perform consistently to temperatures of -20°C and lose approximately 30% average braking force at -40°C. Service worn systems have lost on average approximately 30% average braking force, but over 60% lower than the force of a new system at 0°C.

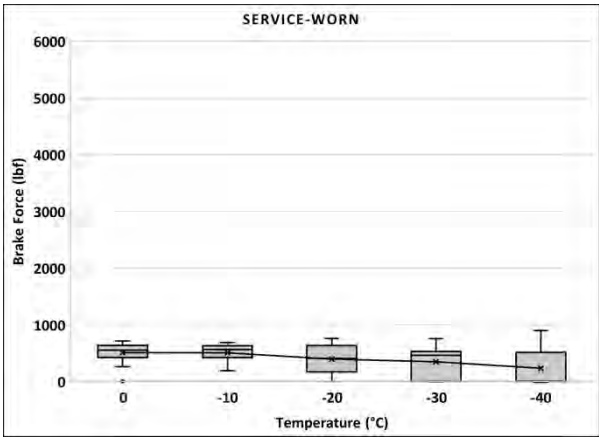

Figure 1. Minimum (6 psi) service brake force after 10 minutes (90 psi BPP): service worn systems

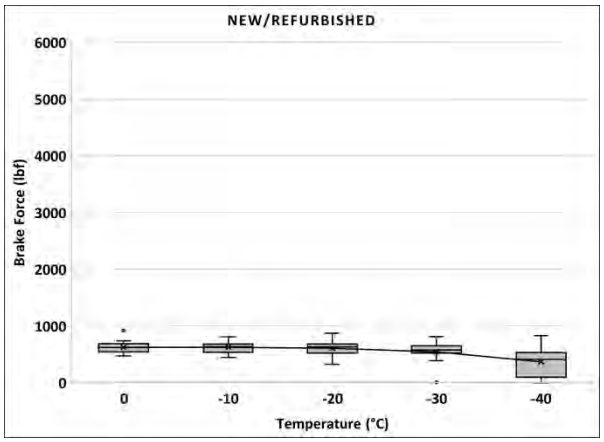

Figure 2. Minimum (6 psi) service brake force after 10 minutes (90 psi BPP): refurbished systems

Figure 3 shows the brake force 10 minutes after a full service (26 psi) brake application was made from 90 psi BPP the service worn systems. Figure 4 shows the results for the refurbished systems. The larger brake application more clearly shows the difference in performance of the new systems compared to the service worn systems. New systems perform consistently to temperatures of -20°C and lose approximately 20% average braking force at -40°C. At the same temperature service worn systems have lost on average approximately 30% braking force, but the force is 40% lower than the new system force at 0°C and with considerably more scatter, with several systems losing all braking force after the 10 minute holding time.

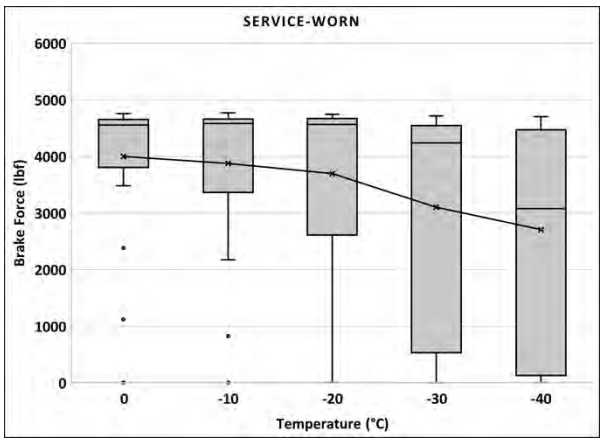

Figure 3. Full service brake force after 10 minutes (90 psi BPP): service worn systems

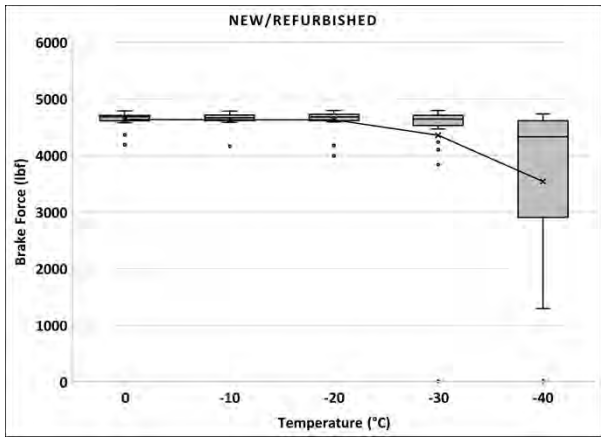

Figure 4. Full service brake force after 10 minutes (90 psi BPP): refurbished systems

Figure 5 shows the brake force after 10 minutes following a full service (26 psi) brake application from 75 psi BPP for the service worn systems. Figure 6 shows the results for the refurbished systems. With a lower BPP, the peak forces observed are lower, however the trend of loss in performance at lower temperatures remains. New systems perform consistently to temperatures of -30°C and lose approximately 10% average braking force at -40°C. Service worn systems have lost on average approximately 45% braking force, but with considerably more scatter with several systems losing all braking force after the 10 minute holding time.

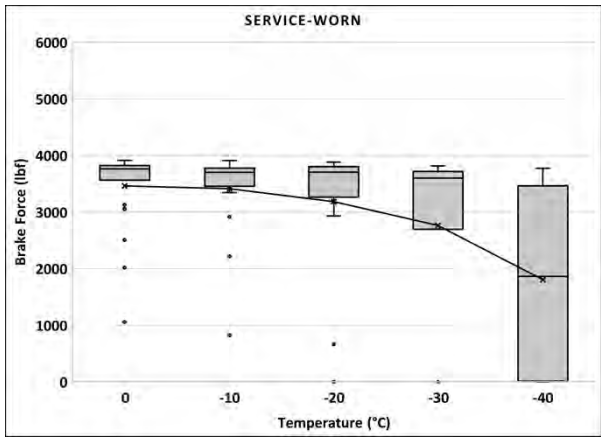

Figure 5. Full service brake force after 10 minutes (75 psi BPP): service worn systems

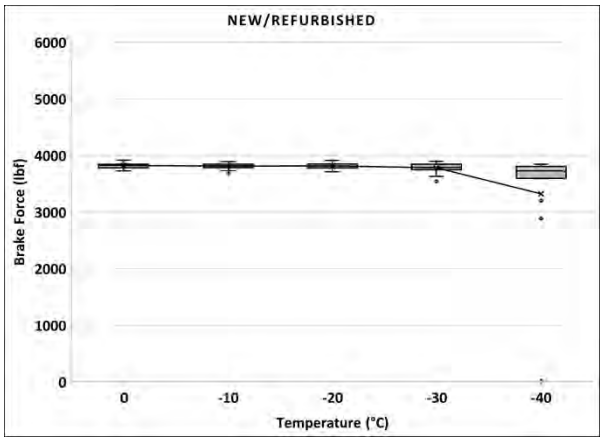

Figure 6. Full service brake force after 10 minutes (75 psi BPP): refurbished systems

4.2 Emergency Braking: 10 minutes after application

During an emergency brake application, the train may take several minutes to completely stop. The available braking force in this time period is captured by the test data for the brake force 10 minutes following the initial emergency brake application.

Figure 7 shows the emergency brake force after 10 minutes from 90 psi BPP for the service worn systems. Figure 8 shows the results for the refurbished systems. New systems perform consistently to temperatures of -20°C and lose approximately 20% average braking force at -40°C. Service worn systems have lost on average approximately 40% braking force, but are almost 50% lower than the new system force at 0°C and with considerably more scatter, with several systems losing all braking force after the 10 minute holding time.

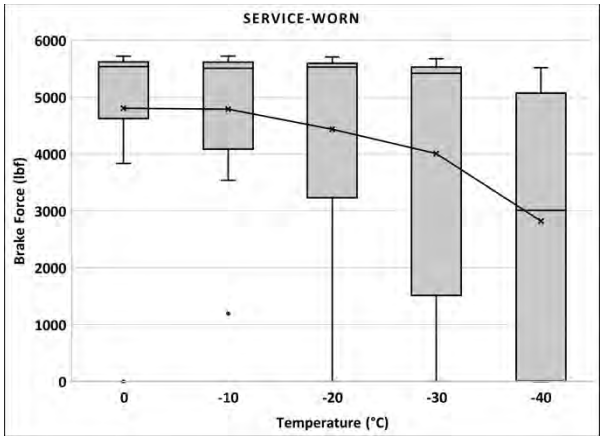

Figure 7. Emergency brake force after 10 minutes (90 psi BPP): service worn systems

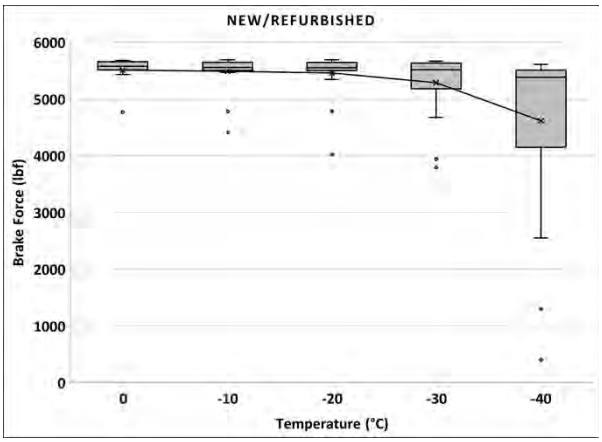

Figure 8. Emergency brake force after 10 minutes (90 psi BPP): refurbished systems

Figure 9 shows the emergency brake force after 10 minutes from 75 psi BPP the service worn systems. Figure 10 shows the results for the refurbished systems. New systems perform consistently to temperatures of -20°C and lose almost 20% average braking force at -40°C. Service worn systems have lost almost 50% average braking force, but are almost 55% lower than the new system force at 0°C and with considerably more scatter, with several systems losing all braking force after the 10 minute holding time.

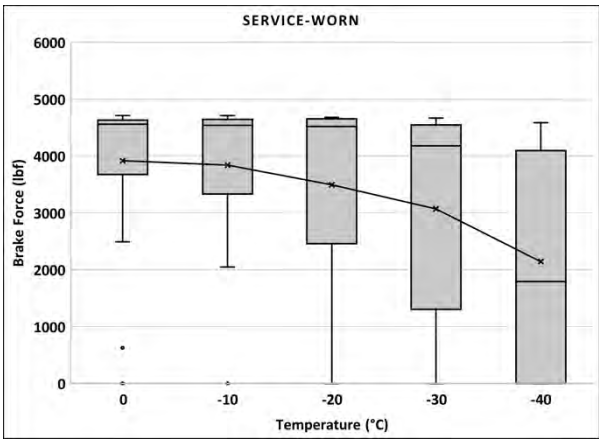

Figure 9. Emergency brake force after 10 minutes (75 psi BPP): service worn systems (left)

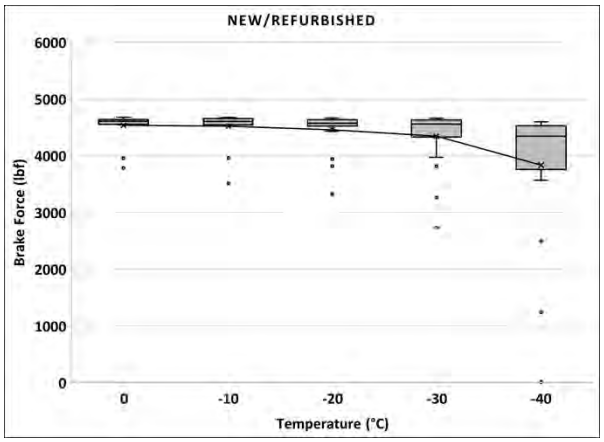

Figure 10. Emergency brake force after 10 minutes (75 psi BPP): refurbished systems

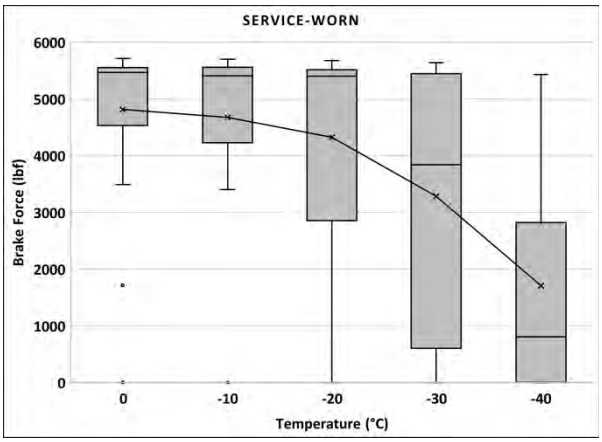

Figure 11. Emergency brake force after 90 minutes (90 psi BPP): service worn

4.3 Emergency Braking: 90 minutes after application

Following an emergency brake application, the crew of the train must perform operations to secure the train (TC 2021) and may need to investigate the cause of the emergency brake event. They must also perform operations to recover the train from the emergency brake application, which may include the application of hand brakes to freight cars, and/or the application of the retainer valve to be set to “hold pressure” (HP). These operations require time, and available braking force in this time period is captured by the test data for the emergency brake force 90 minutes following the initial emergency brake application.

Figure 11 shows the emergency brake force after 90 minutes from 90 psi BPP for the service worn systems. Figure 12 shows the results for the refurbished systems. The results show that service worn systems decline in brake holding force of over 60% at -40°C and are 70% lower than the new system force at 0°C. New or refurbished systems on average have lost approximately 25% of the braking force at -40°C after 90 minutes. Comparison with the results seen in Figures 4 and 5, which show the emergency brake force after 10 minutes of holding, shows that the service worn systems lose brake force more rapidly, and the loss in force continues immediately following the brake application.

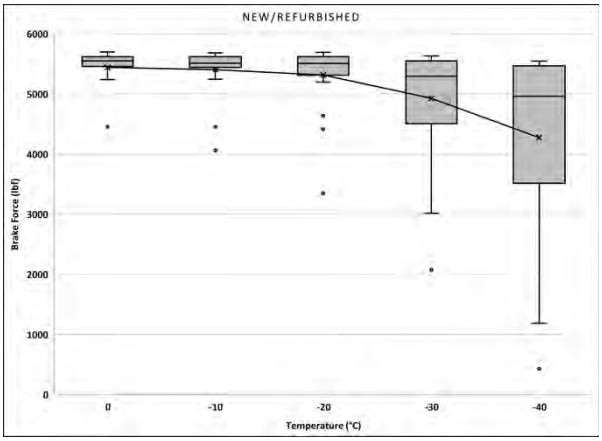

Figure 12. Emergency brake force after 90 minutes (90 psi BPP): refurbished systems

4.4 Effect of Time Since Refurbishment on Performance

Figure 13 shows the emergency brake force after 90 minutes for three age groups: systems where the time since refurbishment or manufacture of service worn systems was greater than fifteen years, less than fifteen years, and new/refurbished brake systems. Results for 0°C, -20°C, and -40°C are shown. The results show that new and refurbished systems provide as expected brake performance even at colder temperatures, and that air brake system performance does progressively decline with age. The range of performance decline is evident at -20°C, where systems up to fifteen years old have lost on average 50% emergency braking force after 90 minutes at -40°C, and systems older than fifteen years have lost on average over 80% of brake force. Note that all systems shown in these results passed the SCABT at temperatures of approximately 10°C or warmer.

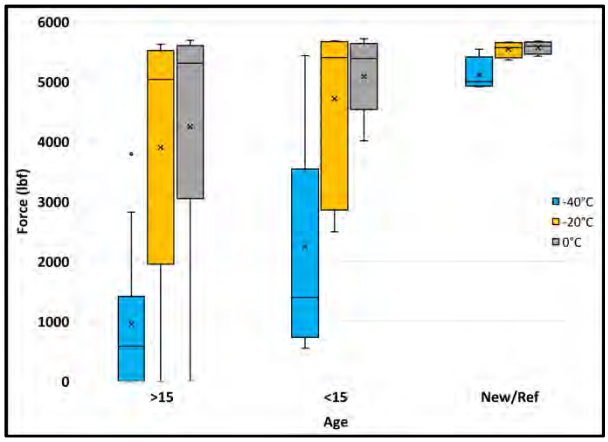

Figure 13. Emergency Brake Force after 90 minutes for 2 service worn age groups (>15 and <15 years) and new/refurbished brake systems; at 3 temperatures -40°C (blue), -20°C (yellow), and 0°C (grey)

4.5 Effect of Temperature on airflow requirements

Figure 14 shows the average air flow requirements for 6 service worn (SW) and 6 refurbished (RF) brake systems at 75 and 90 psi BPP. All tests are performed with new brake hoses and glad hands gaskets, therefore the differences in airflow shown can be attributed solely to increase in air leakage through the control valve portions. The implication of this result is that a train which passed the air flow test at warmer temperatures will likely fail the test if it travels into a location with significantly colder temperatures.

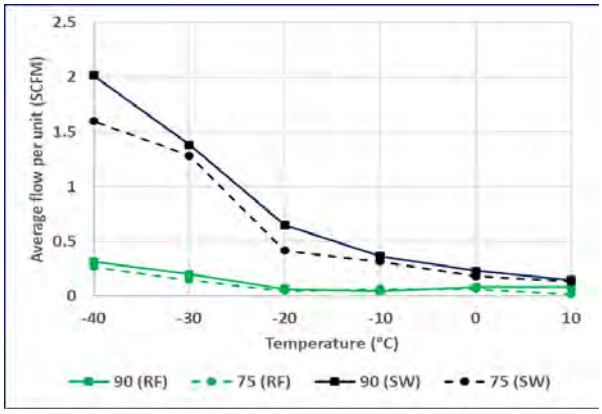

Figure 14. Airflow requirements for service worn (SW) and refurbished (RF) brake systems

4.6 Observed Failure Modes

Although loss of brake force is the concern in colder temperatures, the observed failures of the service worn brake systems at colder temperatures did not always occur in this manner. Other failure modes observed during testing include:

1. No response to brake pipe pressure changes, failure to pressurize the brake cylinder;
2. Initial pressurization of brake cylinder followed by immediate depressurization (release);
3. Proper brake cylinder pressurization soon followed by premature release;
4. Proper brake cylinder pressurization, followed by slow loss of brake cylinder pressure;
5. Loss of emergency reservoir pressure during service brake applications;
6. Proper brake cylinder pressurization, followed by continued pressurization of the brake cylinder (over braking); and
7. Complete loss of system response to brake pipe pressure commands, with air from the brake pipe pressurizing the reservoirs and brake cylinder at all times.

These observed failure modes were typically not consistent in their occurrence. An exception was mode 5 listed above – once a system reached a temperature where the emergency reservoir pressure was dropping with the auxiliary reservoir pressure during service brake applications the system continued to do so at colder temperatures. This is a flaw in that the emergency reservoir air is to be reserved for when an emergency brake application is demanded, and a loss of emergency reservoir air pressure during service brake applications is not standard.

For all the systems observed to fail in the modes listed above, these failure modes no longer occurred when the systems were operated again at warmer temperatures, proving that these are low temperature induced failures and not permanent failures of the systems which occurred during testing. New or refurbished systems did not display any of these failure modes during testing.

5 DISCUSSION

The brake systems tested and reported on in this paper were removed from working in-service freight cars owned by two short line railways in Canada. The complete systems were installed into the NRC's CWAB facility. Prior to testing at a range of temperatures, the brake systems were tested with an AAR approved ASCTD and found to pass the SCABT. Therefore, all the results presented here at a range of temperatures are from freight car air brake systems that would be considered to be typical of in-service systems and would not be considered out of specification for railway operation. The service worn systems varied in time since refurbishment of three years to greater than twenty.

The results show that the service worn brake systems showed a consistent loss of brake force at colder temperatures, and for the emergency brake forces where data was collected for considerable lengths of time, showed a decrease in holding force with time. This loss in performance was also seen to depend on time in-service. These lower brake forces have several relevant consequences for freight train operations:

1. Stopping distances in colder temperatures will be longer, as brake force will be lower than it

would be under comparable at warmer temperatures;
2. Lower available brake force when using the automatic (train) air brake system may require increased use of the locomotive independent brake or dynamic brake to control train speeds;
3. An emergency brake event will take longer for the train to stop compared to the same stop in warmer conditions;
4. Once stopped the crew will have less time compared to similar conditions at higher temperatures to set hand brakes to recover the train from the emergency brake situation before braking force is diminished; and
5. Use of the retainer valve may not hold the train or control train speed in the same manner as it would at warmer temperatures.

With the data collected by the NRC to date with 23 service worn systems the difference in performance with system age is clearly seen, with systems older than fifteen years showing an 80% reduction in emergency brake holding time at -40°C after 90 minutes compared to new air brake systems at the same temperature. As stated above, the time window to secure a train following an emergency brake application in winter compared with summer is shortened considerably with air brake systems of greater age. The loss of brake force may also have implications regarding the effective use of positive train control (PTC) systems, where estimated or modelled stopping distances are used as part of the PTC system (Shad 2019).

6 CONCLUSIONS

From the over 5,000 air brake applications recorded, the following are conclusions which can be made based on the results of testing at NRC concerning freight car air brake systems operating at colder temperatures:

1. New and refurbished systems do not lose performance to the same extent as service worn systems;
2. The time that sufficient emergency brake force is held to secure a train decreases with decreasing temperatures – consideration should be made for the time required to apply sufficient hand brakes on grades following emergency brake applications and;
3. Reduced air brake forces at lower temperatures will affect stopping times during service braking, as well as holding time following an emergency brake application.

7 ACKNOWLEDGMENT

The authors would like to express appreciation for the support of this research to:

1. Brett Young of Hudson Bay Railway (HBR), Subsidiary of Arctic Gateway
2. Pierre Michaud, of Quebec North Shore and Labrador Railway (QNS&L)
3. Transport Canada
4. NRC Automotive and Surface Transportation (AST) Resilient Ground Transportation (RGT) Program.

Great appreciation is given to the design, testing and instrumentation team at the NRC for their work in the creation and operation of the CWAB facility.

REFERENCES

(TSB 2019a) Transportation Safety Board, 2019, Rail transportation safety investigation R16W0242: Uncontrolled movement, collision and derailment. https://www.tsb.gc.ca/eng/enquetes-investigations/rail/2016/r16w0242/r16w0242.html

(TSB 2022) Transportation Safety Board, 2022, Watchlist 2022: Unplanned/Uncontrolled Movement of Rail Equipment https://tsb.gc.ca/ENG/surveillance-watchlist/rail/2022/rail-02.pdf

(CPKC 2023) Building Resiliency: 2023-2024 Winter Contingency Report September, 2023 CPKC-2023.24-Winter-Plan.pdf (cpkcr.com)

(USDOT 2012) Code of Federal Regulations (CFR) 232.107 Air source requirements and cold weather operations. US DOT, 2012 https://www.govinfo.gov/content/pkg/CFR-2012-title49-vol4/xml/CFR-2012-title49-vol4-part232-subpartB.xml

(TSB 2019b) Transportation Safety Board, Rail transportation safety investigation R19C0015: Uncontrolled movement of rolling stock and main-track train derailment. https://www.tsb.gc.ca/eng/enquetes-investigations/rail/2019/r19c0015/r19c0015.html

(TSB 2019c) Transportation Safety Board, 2019, Rail Safety Advisory 617-04/19 Prevention of uncontrolled train movements for trains stopped in emergency on grades of less than 1.8% https://www.tsb.gc.ca/eng/securite-safety/rail/2019/r19c0015/r19c0015-617-04-19-20190411.html

(TC 2021) Transport Canada, 2021, Canadian Rail Operating Rules, 66. Securing Equipment After an Emergency Brake Application on Grade https://tc.canada.ca/en/rail-transportation/rules/2021-2022/canadian-rail-operating-rules/operation-movements

(Shad 2019) P. Shad, R. Anaya, J. Brosseau, 2019, Freight Train Positive Train Control Braking Enforcement Algorithm Research and Testing, DOT/FRA/ORD-19/35. https://railroads.dot.gov/sites/fra.dot.gov/files/fra_net/19030/Freight%20Train%20PTC%20Braking%20Enforcement.pdf

Canadian & Cold Regions
Rail Research Conference
2024

Evaluating the long-term impact of thermosyphons for embankment stabilization on the Hudson Bay Railway

Adam Gareau, & Brett Young
Hudson Bay Railway, The Pas, Manitoba, Canada

Ryley Beddoe
Royal Military College, Kingston, Ontario, Canada

ABSTRACT

Hudson Bay Railway (HBR), located in Northern Manitoba, was constructed in the early twentieth century and has been in operation since 1929. HBR services Canada's only deepwater Arctic port located in Churchill, Manitoba, and plays a critical role in the transportation of goods in Northern Manitoba and the Kivalliq region. HBR is continuously faced with the challenge of intermittent permafrost thaw and subgrade instability, which reduces the operational efficiency, safety of the railway, and has historically resulted in significant track maintenance requirements and cost.

In the 1980's, Canadian National Railway (CN) conducted an Embankment Stabilization Program. Two problematic areas were identified on the Herchmer Subdivision by CN near the Lawledge (mile 377.5-382) and Charlebois (mile 362-365.2) sidings. Thermosyphons were installed between Mile 363 and 368 in the Charlebois region, however no thermosyphons were installed near Lawledge. This study compares the long-term effectiveness of thermosyphons on embankment stabilization near Charlebois to the Lawledge region where no thermosyphons were installed. The performance of rail bed stability has been investigated using track geometry measurements, track quality index (TQI) and ground penetrating radar (GPR) data. Based on track geometry data, TQI, and GPR data compared between Charlebois and Lawledge, the thermosyphons installed at Charlebois (Mile 362-365.2) have achieved their goal of reducing the impact of permafrost thaw and have significantly stabilized the subgrade in the Charlebois area.

1 INTRODUCTION

The Hudson Bay Railway (HBR) has been in operation between The Pas and Churchill, Manitoba, since 1929. The HBR traverses over 600 miles, connecting over 30 communities and one of the largest grain ports in the country. The Herchmer subdivision is the northernmost 183.7 miles of the track running from Gillam to Churchill, and is located in discontinuous through to continuous permafrost zones. The HBR is the only railway in Canada that operates over both continuous and extensive discontinuous permafrost.

The region of discontinuous permafrost begins north of Mile 340 on the Herchmer Subdivision, while the continuous permafrost region begins north of Mile 450. Historically, the discontinuous permafrost regions on the Herchmer Subdivision have been the most problematic, however in recent years significant permafrost thaw has also began affecting the continuous permafrost region. Permafrost found on the Herchmer Subdivision is typically ice rich permafrost.

Ice-rich permafrost thaw leads to vertical track deformations known as 'Sinkholes' (see Figure 1). Subgrade instability over permafrost is a problem that the HBR has had to face since railway construction was completed in 1929. In the late 1980's an Embankment Stabilization Program was initiated by CN Railway (who at the time owned HBR). As part of this program, over 400 thermosyphons were installed to stabilize sinkholes and the embankment across HBR.

Figure 1. Typical Sinkhole on the HBR.

The purpose of this study is to evaluate the long-term performance of these thermosyphons for a subset of the mitigated track. The comparison uses a comparison site, Lawledge, where no thermosyphons were installed, and the basis of the evaluation is the occurrence and severity of sinkholes to determine whether the thermosyphons installed in 1987 have effectively reduced the occurrence and severity of Sinkholes in the Charlebois region. To

do so, track geometry data and ground penetrating radar (GPR) are analyzed and compared between Lawledge (no thermosyphons installed) and Charlebois (thermosyphons installed).

2 BACKGROUND

2.1 Sinkholes

In the late 1970's, CN engaged EBA Engineering Consultants to study the Sinkhole mechanism and develop a theory of Sinkhole formation along with potential measures to reduce their occurrence. **Error! Reference source not found.** shows how EBA categorized Sinkholes as either 'Simple' or 'Complex' (EBA Engineering Consultants Ltd., 1987). EBA theorized that a simple sinkhole is caused when the permafrost at a transition between a fen and peat plateau (a "transition") thaws and subsides.

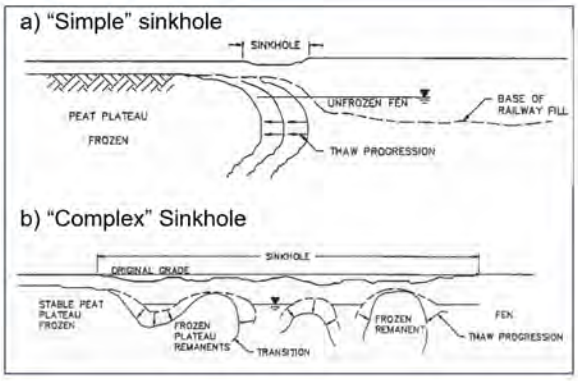

Figure 2. Sinkhole Classification diagrams, showing a) simple sinkhole, single transition, and b) complex sinkhole with multiple transitions (EBA, 1977).

Sinkholes on the Herchmer Subdivision typically occur at the transition between a fen and peat plateau transition. These peat plateaus are surrounded by ice-free 'fen' regions, which typically contain grasses and stagnant water (EBA Engineering Consultants Ltd., 1977). Figure 3 highlights an example section of track, where Sinkholes can be seen occurring between a peat plateau and fen area.

Figure 3: Typical Fen-Peat Plateau Topography on the Herchmer Subdivision showing Location of Sinkholes.

In the 1980's, the area on the Herchmer Subdivision with the most severe sinkhole problem was near the Charlebois siding at Mile 370. This is an area of discontinuous, ice-rich permafrost which lies under 'peat plateaus. By studying this region and others, EBA determined that Sinkholes accompanied thaw in the fen-peat plateau transitions as compressible peats and ice rich clay soils were thawed and consolidated (EBA Engineering Consultants Ltd., 1977).

In 1986, EBA had identified two of the worst regions on the Herchmer subdivision for Sinkhole severity. One region was near the Lawledge siding from Mile 377.5-382 (shown in Figure 4). The other region was near the Charlebois siding from Mile 362-365.2.

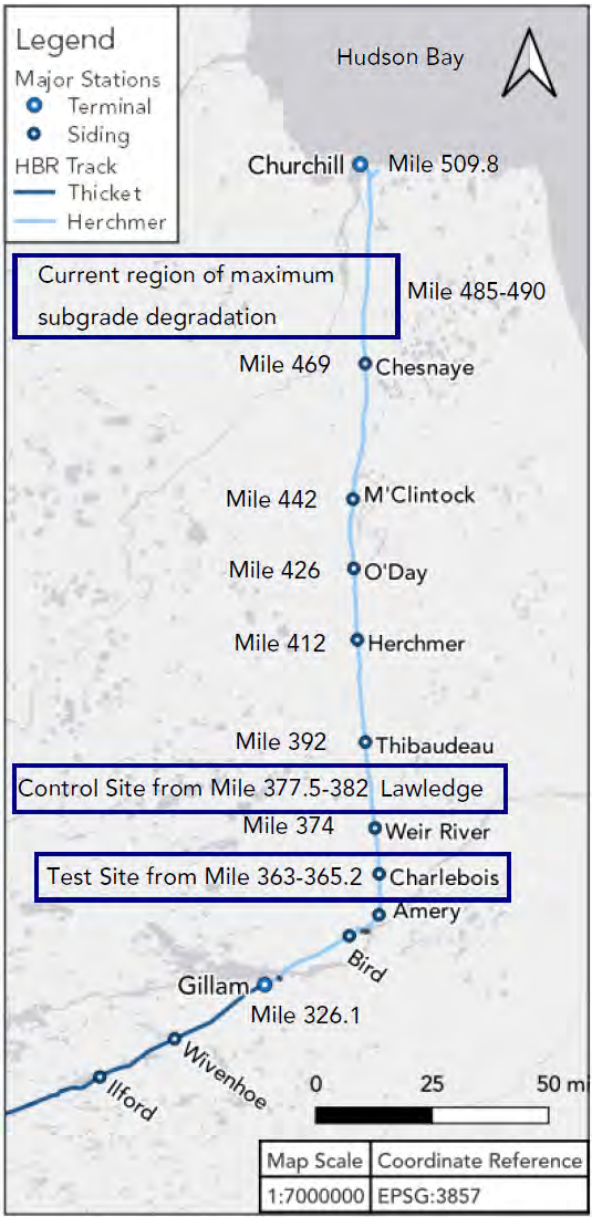

Figure 4. Hudson Bay Railway highlighting the Herchmer Subdivision and two site locations of this study.

2.2 Study sites and thermosyphon installation.

Ultimately, CN and EBA chose Charlebois as the "test site" where they would install thermosyphons. Thermosyphons were installed to reduce both the permafrost thaw at the transition between fen and peat plateau, and the occurrence of Sinkhole defects. In 1979, EBA installed two sets of cryo-anchor style thermosyphons in the Charlebois area. These proved to be successful in reducing subsidence, and a larger survey study was ordered. In 1986, an additional 47 sites were chosen based on a Sinkhole Survey. In 1987, EBA installed over 400 thermosyphons between Mile 363-365.2 at 49 fen-peat plateau transitions (47 plus the original 2 from 1979). An example of the location of therosyphons relative the Fen and Peat Plateau transitions is shown in Figure 5, and an example of the in-situ thermosyphon radiators shown in Figure 6.

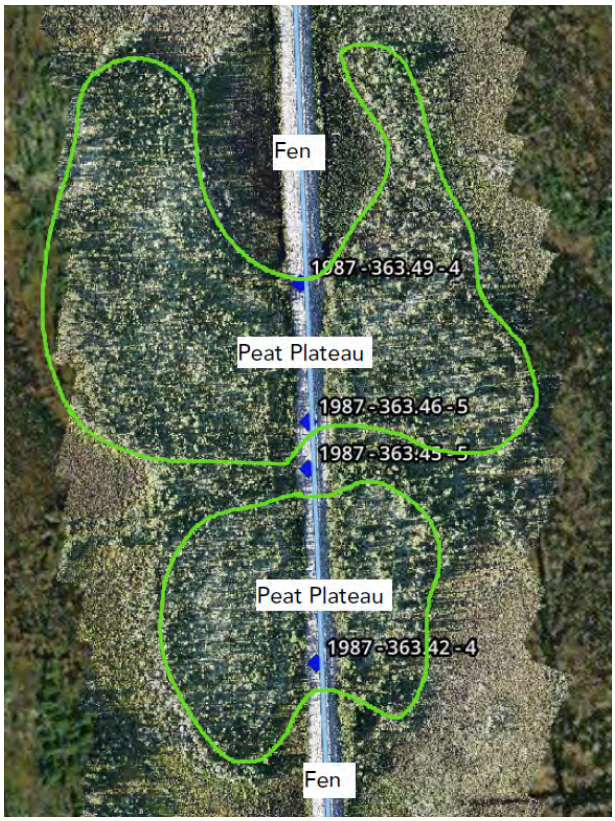

Figure 5. Charlebois Instrumented Test Sites, showing Fen and Peat Plateau areas.

Figure 6. Typical thermosyphon installations in the Charlebois area.

The sinkhole survey had identified that the Charlebois area (Mile 362-365.2) was the worst area on the HBR for Sinkhole quantity of actively degrading transitions. A second site at which CN considered installing thermosyphons in the Lawledge region between mile 377.5-382 of the Herchmer subdivision. This site was considered the second worst location on the Herchmer subdivision for sinkhole severity, after Charlebois. At the time, no thermosyphons were installed at Lawledge, but the area was extensively analysed. This quantitative analysis for Charlebois and Lawledge was completed using track geometry data.

2.3 Track Geometry Analysis

Transport Canada (TC) uses track classification to determine track geometry defect limits for track with different speed limits. Currently, HBR monitors and measures Sinkholes using a track geometry truck equipped with a commercially available software program, Andian's *SolidTrack.* Surface 62 (S62) and Runoff 31 (RUN31) are the two track geometry parameters used to measure the vertical surface profile across a 62- and 31-foot chord respectively. The allowable limits of S62 and RUN31 for all classes is shown in Table 1 (Transport Canada, 2022). Currently, HBR operates as a Class 2 railway, therefore a defect is identified when the geometry parameter at a specific location exceeds 80% of the Class 2 defect limits. Standard practice for HBR Herchmer Subdivision is performing a track geometry analysis monthly.

Table 1. Track Geometry Limits and Track Class Speed Limits (Transport Canada, 2022).

Measurement	Class 1 (C1) 10 mph	Class 2 (C2) 25 mph	Class 3 (C3) 40 mph
Runoff 31	Limit = 3.5"	Limit = 3"	Limit = 2"
Surface 62	Limit = 3"	Limit = 2.75"	Limit = 2.25"
Crosslevel	Limit = 3"	Limit = 2"	Limit = 1.75"

3 THERMOSYPHON PERFORMANCE ANALYSIS

Installing thermosyphons at Charlebois and not Lawledge has provided a unique opportunity to investigate the long-term effectiveness of thermosyphons on embankment stabilization. The performance of rail bed stability has been investigated using track geometry measurements, track quality index (TQI) and ground penetrating radar (GPR) data.

3.1 Track Geometry Analysis

The track geometry data in this study is considered in two ways. The first comparison is with respect to the quantity of Sinkholes, and resulting defect class. Second, the TQI is compared between Charlebois and Lawledge. This makes use of the control site of Lawledge where no thermosyphons were installed to help determine whether the thermosyphons have successfully reduced the severity and recurrence of Sinkholes at Charlebois.

3.1.1 Comparison of Defect Counts

In 1986, there were 49 track defects counted along the Charlebois test section. Each of these locations had thermosyphons installed and are therefore the baseline set of 49 sinkholes examined in this comparison. Using track geometry data from 2019-2023, the presence of sinkholes at each thermosyphon site was recorded. Track geometry data shows that the thermosyphons have not altogether eliminated track geometry issues. Of the 49 sites at Charlebois (from Mile 362-365.2):

- 28 (57%) have had no recorded track geometry defects of any kind at or near their location since 2019.
- 7 (14%) have experienced minor to moderate apparent heaves.
- 14 (29%) sites which have had slight, minor, moderate and/or severe Sinkholes.

When comparing the results of current track geometry data against the pre-thermosyphon installation sinkhole survey of 1986, there is a significant improvement. As seen in Table 2 , the difference between the two regions in actively degrading permafrost transitions over 30 years is evident.

Table 2. Comparison of Active Transitions per Mile in the Charlebois and Lawledge Regions, 1986 vs. 2023.

Region	Active Transitions per Mile		Percent Reduction
	1986	2023	
Charlebois Mile 362-365.2	22.7	2.4	90%
Lawledge Mile 377.5-382	13	8	40%

In 1990, there were 22.8 active transitions per mile and between 2021-2023 there were approximately 2.4 per mile at Charlebois. This represents a 90% reduction in the number of actively degrading transitions. At Lawledge there has also been a reduction in the number of active transitions. However, there has only been an approximate reduction of 40% in actively degrading transitions since 1990.

A more recent examination of the sinkholes at the two sites was also performed. In this case, a sinkhole count since 2019 was performed including their associated class limits reached (Table 3). The total number of Sinkholes recorded in the Lawledge region that exceed Class 1 or 2 limits since 2019 is 29.

Table 3. Comparison of Lawledge and Charlebois Sinkhole Severity from 2019-2023.

Region	Count of Defects Exceeding Class 1 Limits	Count of Defects Exceeding Class 2 Limits
Charlebois (Mile 362-365.2)	0	3
Lawledge (377.5-382)	17	12

In comparison, the total number of sinkholes recorded in the Charlebois region exceeding Class 1 or 2 limits is only 3 since 2019. The results in Table 3 show a clear indication that Charlebois has a much lower severity and frequency of Sinkholes compared to Lawledge in 2023.

3.1.2 Comparison of Track Quality Index

In addition to the count of defects, the track quality at Charlebois was compared to the track quality at Lawledge. The HBR uses a Track Quality Index (TQI) developed by CN rail, based on the standard deviation of the left and right surface 62 measures, as well as crosslevel. The benefit of using a TQI rather than counting discrete track geometry defects is that it provides a more holistic measurement of the overall track health. (American Railway Engineering and Maintenance-of-Way Association, 2022). This method uses foot-by-foot data exported from SolidTrack, so it provides a very accurate representation of track health overall. The TQI formula, shown in Eq 1 is as follows:

$$TQI_{HBR} = 1000 - 700 \cdot \frac{SD_{LS62}{}^2 + SD_{RS62}{}^2 + SD_{XLV}{}^2}{3} \quad \textit{(Eq. 1)}$$

Where:

SD_{LS62} is the standard deviation of the left surface 62 measurement, SD_{RS62} is the standard deviation of the right surface 62 measurement, and SD_{XLV} is the standard deviation of the crosslevel measurement.

The HBR TQI ranges from 0 to 1000, with 1000 being track that is perfectly flat longitudinally and vertically (Offenbacher, Neuhold, Welt, & Landgraf, 2020). In general, the best track on the HBR has a TQI of approximately 980, with relatively good track having a TQI above 920. Very poor track has a TQI of approximately 755.

Based on foot-by-foot track geometry data collected between 2016 and 2023, TQI in the Charlebois and Lawledge regions were calculated and the average TQI is:

- Charlebois (Mile 360-365) is 931.
- Lawledge (Mile 375-385) is 846.

This shows that the TQI in the Lawledge region is on average significantly worse than that in the Charlebois region. This further supports that thermosyphons have reduced the severity of Sinkholes at Charlebois.

3.2 Ground Penetrating Radar (GPR) Analysis

3.2.1 GPR Background

GPR is used in geophysics for the purpose of mapping subsurface geological structures, as it can detect zones and interfaces with strong dielectric contrasts such as wet-dry or frozen-unfrozen interfaces (Andersland & Ladanyi, 2004). In 1986, EBA Engineering conducted a GPR study on the Charlebois Region. In December 2021, the HBR commissioned Loram to conduct a GPR analysis on the entire Herchmer Subdivision (for the purpose of analyzing the ballast layer rather than the

subgrade, leading to some difficulty in interpreting the GPR data for this study's purpose).

The GPR data that is interpreted below is based on the fill layer depth, not the active layer depth of the permafrost. However, there is a relationship between fill depth and change in permafrost, whereby, as permafrost degrades at a transition, more fill is added to restore the track profile. Therefore, it can be inferred that locations with additional fill represent locations with additional permafrost thaw.

3.2.2 GPR Analysis of a Charlebois peat plateau

The 1986 and 2021 GPR data analyzed in this section were both collected in December. This is a benefit, as it limits variances in the GPR data based on seasonal impacts (eg. frozen vs unfrozen water content). The interpreted GPR radargram data from 2021 was overlayed onto the interpreted GPR data collected in 1986, and is shown in Figure 7 for a 200 ft stretch of track for a single peat plateau. In this peat plateau, there are 4 thermosyphons that were installed, two which appear in the centre of the plateau, and one in each transition to the fen. Based on the two profiles shown in Figure 7, it is evident that the thermosyphons have had impact on the quantity of fill required in the last 35 years. In the centre of the plateau, the thermosyphons appear to have largely maintained the permafrost, limiting the need for fill. In comparison, the thermosyphons at Mile 363.492 (far right) in the transition shows signs of limited performance, as the fill required there and into the peat plateau show clear signs of thaw and a significant 'simple' sinkhole progression.

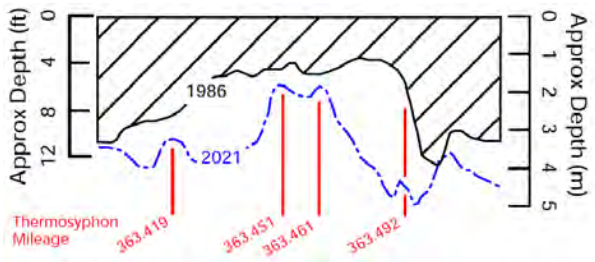

Figure 7. 1986 vs. 2021 Depth of Fill material for one instrumented test sites at Charlebois (hatched area in 1986, and blue dashed line in 2021).

In addition to a fill analysis, the thermosyphons at the instrumented test site have been partially successful at reducing the occurrence and severity of Sinkholes. At Mile 363.419, there has only been a minor Sinkhole that has rarely recurred annually since 2019, and generally appears as a Class 3 Warning. At Miles 363.451 and 363.461, there have been no recordable defects since 2019. At Mile 363.492, there has been a moderate Sinkhole (exceeding Class 3 limits), annually recurring Sinkhole since 2019.

3.2.3 GPR site comparison

GPR data for the entirety of Mile 362-363 in the Charlebois region and Mile 381-382 in the Lawledge region were compared in this study. Due to the potential for interpretation error in the 1986 GPR profiles, this was a qualitative comparison. In the Lawledge region (Figure 8) it is shown that there has been an increase of fill across almost the entire 1000 ft. This is especially true on the right transition, similar to what was seen in the Charlebois site in Figure 7. In comparison, the 1000 ft of track shown in Charlesbois in Figure 9 show almost no change in fill quantity. In fact, it appears as if there is now less fill, which has been attributed to likely interpretation error in 1986 rather than loss of fill. It does qualitatively show that there has bene limited change in permafrost conditions in this 1000 ft section, and that the thermosyhpons placed in the four transitions were performing well.

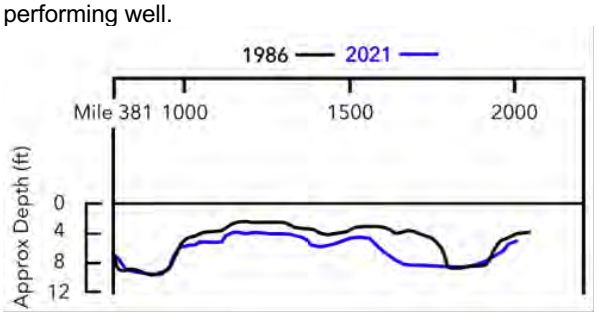

Figure 8. Sample GPR data for Lawledge Region between Mile 381 and Mile 382 in 1986 and 2021 for Fill.

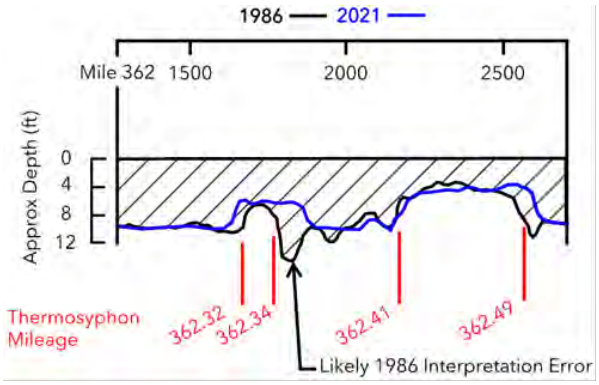

Figure 9. Sample GPR data for Charlebois between Mile 362 and Mile 363 in 1986 and 2021 for Fill Layer Depth.

The comparison in GPR data at locations with and without thermosyphons, indicate that thermosyphons have likely been the major contributing factor for retaining the permafrost and limiting sinkhole formations in locations where they were installed. Indeed, from track geometry and GPR analyses, it is clear that the thermosyphons at Charlebois (Mile 362-365.2) have reduced the number of active transitions leading to Sinkholes. However, there are various thermosyphon locations in the Charlebois region that appear to have been significantly less effective than others, such as the site at Mile 363.492 (Figure 7). This then leads to further investigations into the degree of effectiveness of thermosyphons as a mechanism for stabilizing rail embankments in warming permafrost conditions.

4 DISCUSSION OF THERMOSYPHON PERFORMANCE

4.1 Degree of Effectiveness of Thermosyphons

There are a variety of reasons for transitions where thermosyphons were installed to still have sinkholes present. In this study, three primary reasons are preliminarily explored, including: the location of thermosyphon installation, the selected number of thermosyphons at a single transition, and the impact of external influences, such as ponding water and changing climate.

4.1.1 Thermosyphons Being Improperly Placed

The original 49 locations selected were based on the sinkhole survey that was completed in the mid 1980's. In 1989 and 1990, EBA conducted a follow-up Sinkhole survey. In at least 6 locations, it was found that a Sinkhole appeared either immediately north or south of a set of thermosyphons. This therefore limited the influence the thermosyphons were having within the transition zone, and their overall effectiveness. In hindsight, these thermosyphons should have been placed closer to the peat plateau and less towards the fen in order to maximize their efficiency. An example of poor placement of a thermosyphon would be the thermosyphon shown in Figure 7, at Mile 363.492.

4.1.2 Insufficient Number of Thermosyphons

There is evidence in the Charlebois region that an insufficient number of thermosyphons have been installed. One example is the GPR data presented in Figure 7, where at Mile 363.419, as well as the historical 1990 sinkhole survey, it is likely that at this location there were not enough thermosyphons installed to maintain the permafrost layer. The thermosyphon appears to be working in a localized region (demonstrated by the decrease in fill required immediately at the thermosyphon location). However, in the historical survey from 1989 and 1990 there were severe and moderate sinkhole recorded at that location which continue to present themselves.

In addition, based on contemporary data since 2019, at least 11 of the 49 thermosyphon sites have recurring Sinkholes at the location of the thermosyphons. This indicates that there may be an insufficient number of thermosyphons to maintain the permafrost depth, given the yearly recurrence of these Sinkholes. A greater number of thermosyphons increases the heat flux out of the soil during the winter, and therefore reduces thaw.

4.1.3 Water Ponding

In a study, drone imagery was completed at 39 of the thermosyphon sites in Charlebois. It was noted that 3 sites with sinkholes had significant water ponding issues (at Miles 363.49, 364.26 and 364.4). However, two sites with some water ponding present show no sign of Sinkholes shown in Figure 10, at Miles 364.08 and Mile 364.1. Water ponding is known to be an accelerator of permafrost degradation, and therefore further investigation into the linkage of ponding water, thermosyphons and sinkhole development is required.

Figure 10. Mile 364.08 and Mile 364.1 Drone Orthomosaic showing Significant Water Ponding.

4.1.4 Summary of Thermosyphon Effectiveness

The comparison of TQI between Lawledge and Charlebois showed that the track quality where thermosyphons were installed is higher than where they were not. However, it also showed that the Lawledge region in this study still improved in TQI since 1986 with approximately 40% less active transitions today. Given that Lawledge has no thermosyphons, and is comparable in topography to Charlebois, this improvement must be attributable to factors other than thermosyphon installations. This would therefore indicate that a more reasonable estimate of the level of TQI improvement caused by the thermosyphons in Charlebois is closer to 60% rather than the full 90% improvement noted in section 3.1.2.

The other 40% improvement (along with improvement in Lawledge) would be derived from other geographical factors (such as an overall decrease in ice rich permafrost left to thaw) to a range of external factors, including but not limited to: annual operations and surfacing efforts by HBR, increase in fill material, and soil compaction. Further investigation to quantifying and scaling this mitigation factors is needed and will provide critical information for the overall operation of HBR.

5 CONCLUSION

The Herchmer Subdivision of the Hudson Bay Railway extends from Gillam to Churchill, Manitoba. The railway was built upon both discontinuous and continuous permafrost regions. This has led to an extensive number of Sinkholes, or regions of localized subsidence due to ice-rich permafrost thaw on the Herchmer Subdivision.

In 1986, CN rail installed 400 thermosyphons near the Charlebois siding (Mile 362-365.2). This region was chosen over an alternative region near the Lawledge siding (Mile 377.5-382). Based on track geometry data, TQI, and GPR data, compared between Charlebois and Lawledge, the thermosyphons installed at Charlebois

(Mile 362-365.2) have achieved their goal stabilizing the railways embankments.

First, track quality at Charlebois is much higher since the thermosyphons were installed in 1986. The number of active transitions leading to sinkholes has fallen from 22.8 per mile in 1986 to 2.4 per mile in 2021. In addition, 28 of the 49 sites have had no recordable track geometry defects since 2019 and 21 sites have had minor or moderate Sinkholes.

When track geometry data at Charlebois is compared to a comparable location on the Herchmer Subdivision near Lawledge, it is evident that the thermosyphons have had positive effect. The overall track quality index at Charlebois has been 931 on average since 2019, and at Lawledge it has been 867. Additionally, the overall number and severity of Sinkholes at Charlebois is significantly lower than at Lawledge. Only 3 Sinkholes exceeded Class 2 limits in Charlebois since 2019, whereas 29 defects exceeded Class 2 limits in Lawledge.

Finally, GPR data collected in 1986 and 2021 shows that the Charlebois region has been largely successful at maintaining the permafrost layer depth since 1986. The GPR data aligns closely to the track geometry data and shows that the majority of thermosyphon sites have had no permafrost degradation and need for fill. In addition, the instrumented test sites show that thermosyphons when properly placed and in sufficient number can retard the thaw of permafrost significantly. However, if they are not properly placed, in insufficient numbers, or subject to ponding water they may not maintain the permafrost layer perpetually.

A further study on the degree of effectiveness of thermosyphons is required to determine the residual improvement not caused by thermosyphons. Overall, the thermosyphon test sites installed in 1986 at Charlebois (Mile 362-365.2) have been remarkably effective given that this was the area on the Herchmer subdivision that was the most unstable then. Today, the Charlebois region has some of the best track on the Herchmer subdivision. What is perhaps most impressive is that this has occurred despite the thermosyphons not having been monitored or maintained between 1990 and 2019 when the monitoring and maintenance programs were not being funded. The Hudson Bay Railway sees future promise in this mitigation and adaptation measure, and is committed to moving forward with additional monitoring performance analysis of the thermosyphons, conducting related analyses of climate impact and the overall impact of deepening embankment fill on permafrost conditions.

6 ACKNOWLEDGEMENT

The authors would like to acknowledge the input from and give special thanks to Justin Panagapko of Arctic Foundations, the PermaRail research group, and Loram Maintenance of Way.

REFERENCES

Addison, P. (2015). *Characterizing Rail Embankment Stabilization Needs on the Hudson Bay Railway.* Michigan Technological University.

American Railway Engineering and Maintenance-of-Way Association. (2022). *Manual for Railway Engineering.*

Andersland, O., & Ladanyi, B. (2004). *Frozen Ground Engineering.* Hoboken, New Jersey: John Wiley .

Bankston, A., & Wilk, S. (2021). *Use of Track Based Inspection Technologies to Improve BNSF's Ballast Maintenance Planning*. Retrieved from Loram Maintenance of Way: https://loram.com/wp-content/uploads/01-Bankston-et-al.pdf

Bickle, I. (1995). *Turmoil and Triumph: The Controversial Railway to Hudson Bay.* Calgary, AB: Detselig Enterprises Ltd.

Brandt, O., Langley, K., Kohler, J., & Hamran, S.-E. (2007). Detection of buried ice and sediment layers in permafrost using multi-frequency Ground Penetrating Radar: A case examination on Svalbard. *Remote Sensing of Environment Volume III, Issues 2-3*, 212-227.

EBA Engineering Consultants Ltd. (1977). *Settlement of a Railway Embankment Constructed on Permafrost Peatlands.* Engineering Report Prepared for Canadian National Railways.

EBA Engineering Consultants Ltd. (1979). *Embankment Stabilization Research Grain Line Rehabilitation Hudson Bay Division, Test Site Construction and Instrumentation.* Engineering Report Prepared for Canadian National Railways.

EBA Engineering Consultants Ltd. (1980). *Embankment Stabilization Research Program, Grain Line Rehabilitation Hudson Bay Division, Test Site Performance and Monitoring.* Engineering Report Prepared for Canadian National Railways.

EBA Engineering Consultants Ltd. (1981). *Embankment Stabilization Research Program, Grain Line Rehabilitation Hudson Bay Division, Test Site Performance and Monitoring.* Engineering Report Prepared for Canadian National Railways.

EBA Engineering Consultants Ltd. (1982). *Embankment Stabilization Research Program, Branch Line Rehabilitation Hudson Bay Railway Herchmer Subdivision.* Engineering Report Prepared for Canadian National Railways.

EBA Engineering Consultants Ltd. (1986). *Embankment Stabilization Research Program, Branch Line Rehabilitation Hudson Bay Railway Wabowden to M'Clintock, Interim Report Route Data Collection and Comparative Heat Pipe Study.* Engineering Report Prepared for Canadian National Railways.

EBA Engineering Consultants Ltd. (1986). *Sinkhole Survey Data Hudson Bay Railway.* Engineering Report Prepared for Canadian National Railways.

EBA Engineering Consultants Ltd. (1987). *Requirements for Subgrade Stabilization, Hudson Bay Railway.* Engineering Report Prepared for Canadian National Railways.

EBA Engineering Consultants Ltd. (1988). *Heat Pipe Installation Phase, Hudson Bay Railway Prototype Stability Program.* Engineering Report Prepared for Canadian National Railways.

EBA Engineering Consultants Ltd. (1988). *Hudson Bay Railway Embankment Stabilization Program, Progress Report No. 2, Initial Performance Monitoring Data.* Engineering Report Prepared for Canadian National Railways.

EBA Engineering Consultants Ltd. (1989). *Hudson Bay Railway Embankment Stabilization Program, 1988 Progress Report No. 3.* Engineering Report Prepared for Canadian National Railways.

EBA Engineering Consultants Ltd. (1990). *Prototype Stability Program, Hudson Bay Railway.* Engineering Report Prepared for Canadian National Railways.

EBA Engineering Consultants Ltd. (1991). *Prototype Stability Program, Hudson Bay Railway, 1990/91 Heat Pipe Effectiveness Evaluation and Geotechnical Investigation.* Engineering Report Prepared for Canadian National Railways.

Environment and Climate Change Canada. (2022, April 25). *Climate Data for a Resilient Canada*. Retrieved from https://climatedata.ca/: https://climatedata.ca/explore/location/?loc=GAFAB&location-select-temperature=tnlt_-25&location-select-precipitation=r1mm&location-select-other=frost_days

Gacitua, G., Andres Uribe, J., Tamstorf, M., & Munch Kristiansen, S. (2011). Mapping of permafrost surface and active layer properties using GPR: A comparison of frequency dependencies. *6th International Workshop on Advanced Ground Penetrating Radar*, 1-5.

Government of Canada. (2022, April 25). *Environment and natural resources, Weather, Climate and Hazard*. Retrieved from Historical Data: https://climate.weather.gc.ca/historical_data/search_historic_data_e.html

Guo, Z., Dong, H., & Xiao, J. (2015). Detection of Permafrost Subgrade Using GPR: A Case Examination on Qinghai-Tibet Plateau. *Journal of Geoscience and Environment Protection*, 35-47.

Moorman, B., Robinson, S., & Burgess, M. (2007). Imaging near-surface permafrost structure and characteristics with Groun-Penetrating Radar. *Canadian Society of Exploration Geophysicists Recorder*, 23-30.

Offenbacher, S., Neuhold, J., Welt, P., & Landgraf, M. (2020, 11 14). Analyzing Major Track Quality Indices and Introducing a Universally Applicable TQI. Graz, Austria. Retrieved from https://www.mdpi.com/2076-3417/10/23/8490

Transport Canada. (2022, February 1). *Rules Respecting Track Safety.* Retrieved October 20, 2023, from https://tc.canada.ca/sites/default/files/2021-10/rules-respecting-track-safety-may-31-2021.pdf

Wang, Y., Jin, H., & Li, G. (2016). Investigation of the freeze-thaw states of foundation soils in permafrost areas along the China-Russia Crude Oil Pipeline (CRCOP) route using ground penetrating radar (GPR). *Cold Regions Science and Technology*, 10-21.

Western Canadian Shortline Railway Association. (2022, May 07). *About Us*. Retrieved from Western Canadian Shortline Railway Associatoin: https://www.wcslra.com/about

Zarambeski, A. (2023). *Comprehensive Rail and Track Related Research*. Retrieved October 21, 2023, from https://www.rta.org/comprehensive-rail-and-track-related-research

Session 3

HUMAN FACTORS AND SAFETY

Canadian & Cold Regions
Rail Research Conference
2024

Mental workload assessment and prediction for train operators

Mona Ahmadi Rad[1], Lianne M. Lefsrud[2], & Michael Hendry[1]
[1] *Canadian Rail Research Lab, Department of Civil & Environmental Engineering, University of Alberta, AB, Canada*
[2] *Department of Chemical and Materials Engineering, University of Alberta, AB, Canada*

ABSTRACT

Train protection and control systems are crucial for improving railway safety by reducing operator-related accidents. However, they shift operators from manual control to monitoring, presenting both advantages and challenges. This change requires rapid assimilation of vast information, risking mental overload and performance degradation. Therefore, assessment and prediction of the workload associated with train systems is essential.
This paper examines mental workload studies in train operator settings, categorizing them by their approaches (subjective-objective, analytical-empirical), methods, metrics, and the types of train cab systems studied. It also analyzes how train technology affects operator workload, emphasizing the importance of addressing workload during system design for safe and efficient railway operations. Our analysis highlighted a preference for the subjective-empirical approach for analyzing train operators' workload, often applied after system prototypes and simulator experiments are available. Early workload analysis is recommended for user-centred design, preventing operator errors and costly redesigns. Furthermore, the literature presented diverse findings on the effects of in-cab systems and automation on train operators' workload. These disparities may arise from system characteristics, individual differences, environmental factors, operational conditions, and infrastructure variations. Additionally, differences in the stages of information processing studied can contribute to varying workload outcomes for the same system.

1 INTRODUCTION

The concept of workload, as defined by Wickens and Tsang (2015), is the balance between the resources required for a task and those available to the operator. This balance includes various elements such as physical, visual, auditory, and cognitive aspects (Halliday et al., 2005). Mental workload, distinct from physical tasks, focuses on the cognitive demands on individuals (Hamilton and Clarke, 2005), and is the interplay between a task's demands and the operator's mental capacity (Kruger, 2008).

The impact of workload on operator performance is crucial and is illustrated in Figure 1.

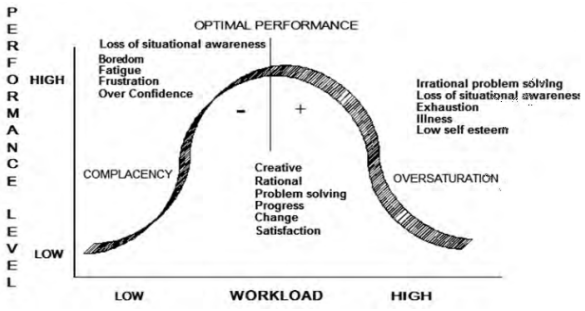

Figure 1. Workload versus performance (FRA, 2014).

Figure 1 highlights how both under-load and over-load can detrimentally affect performance. Specifically, under-load can lead to fatigue, boredom, and a decline in situational awareness, while over-load might result in exhaustion and compromised problem-solving abilities (FRA, 2014; Robinson et al., 2015).

Despite the importance of workload in system design and operator performance, there is no unifying approach for defining, quantifying, and measuring mental workload (Foulkes, 2004; Jex, 1988). This gap is particularly evident in the context of train operations, where workload intricacies are critical for safety and efficiency. Current methodologies include time-based assessments, which compute workload as a ratio of time spent on tasks to available time, and task-based evaluations, which contrast mental effort against individual capacity (Hamilton and Clarke, 2005; Parasuraman et al., 2008; Wang et al., 2016). Furthermore, various methodologies and tools exist for measuring mental workload. To gain a comprehensive understanding of mental workload, several scholars — Xie and Salvendy (2000), Miller (2001), Cain (2007), Kruger (2008), Young et al. (2015), Wilson et al. (2017), and Heard et al. (2018) — have reviewed and categorized different approaches for defining, quantifying, and measuring mental workload.

These techniques fall into two primary categories: objective-subjective and empirical-analytical (Nneji, 2019; Rusnock et al., 2015). Objective methods rely on real-world facts, such as task performance metrics and

physiological indicators, whereas subjective methods depend on personal perceptions of workload (Heard et al., 2018). Empirical and analytical classifications offer another perspective. Empirical techniques are based on observed evidence, often from laboratory or field studies, while analytical methods hinge on theoretical reasoning, frequently employed in early system design stages (Rusnock et al., 2015; Xie and Salvendy, 2000).

While many studies on train operators' workload exist, there is a lack of a comprehensive review that unifies these diverse approaches for a specific focus on train operators. Such a review is vital for enhancing system design and rail transportation efficiency. This paper fills this gap by analyzing the existing literature on this topic.

The paper is structured as follows: Section 2 presents the background, and Section 3 categorizes workload studies into subjective-empirical, subjective-analytical, objective-empirical, and objective-analytical. Section 4 summarizes these studies, and Section 5 concludes with key insights and implications of the review.

2 BACKGROUND

The measurement of mental workload, a pivotal aspect in the field of human factors and ergonomics can be dissected into two primary dimensions: objective versus subjective and empirical versus analytical. This categorization leads to four distinct categories of workload measurement approaches, each with its unique methods and metrics (see Figure 2) (Rusnock et al., 2015).

a. Subjective-Empirical Measures: This category comprises methods that gather subjective opinions, typically via self-report questionnaires following simulator experiments. Such methods aim to estimate workload as experienced by the individual directly. Prominent examples include the NASA-TLX (Hart and Staveland, 1988), SWAT (Reid and Nygren, 1988), Cooper-Harper (Cooper and Harper, 1969), MRQ (Boles and Adair, 2001), Overall Workload (Jung and Jung, 2001), and Workload Profile (Tsang and Velazquez, 1996). These tools are crucial in capturing the operator's perceived effort and stress, offering insights into their subjective experience of workload.

b. Subjective-Analytical Measures: In this approach, workload estimation relies on the expertise of subject matter experts or experienced users (Xie and Salvendy, 2000). These assessments are based on comparisons with similar systems or previous experiences. Techniques in this category, such as checklists and walkthrough methods (Evans, 2017), are particularly useful at the early design stages of systems, where empirical data from prototypes might not yet be available (Rusnock et al., 2015). They provide a preliminary understanding of the expected workload in new or modified systems.

c. Objective-Empirical Measures: This category involves the direct assessment of objective workload metrics. These metrics can include task performance indicators (like error frequency or response time) and physiological measurements (such as heart rate or eye movement). Such assessments are typically conducted in controlled environments like laboratories or simulators (Rusnock et al., 2015; Wilson et al., 2017; Xie and Salvendy, 2000). These methods are valuable for quantitatively assessing workload in scenarios that closely mimic real-world conditions.

d. Objective-Analytical Measures: These methods integrate task, environmental, and personal knowledge into mathematical models for workload assessment. They often involve detailed task analysis and understanding the system, operator, task, context, and modelling approaches. Techniques in this category are essential during the early design stages when empirical data are unattainable. Examples include Control Theory, Information Theory, Queuing Theory, Timeline Analysis and Prediction (TLAP), Visual Auditory Cognitive Psychomotor (VACP), W/INDEX, and various simulation models and human performance modelling tools like ATLAS, IMPRINT, and IPME (Rusnock et al., 2015; Wilson et al., 2017; Xie and Salvendy, 2000).

	Analytical	Empirical
Subjective	Comparison Expert opinion	Operator opinion-rating scales or questionnaire/ interview
Objective	Mathematical models Task analysis models Simulation models	Performance measures Psychophysiological measures

Figure 2. Workload measurement approaches and methods.

3 TRAIN OPERATORS' WORKLOAD ASSESSMENT STUDIES

Several studies have been conducted in the railway sector to explore the mental workload of train operators, examining both existing operational conditions and the impact of newly implemented train control systems. This section provides a comprehensive review of the diverse approaches employed in these studies to assess workload, offering a detailed insight into the methodologies and findings within this important area of research.

3.1 Subjective-empirical studies on train operators' workload

The study of subjective-empirical approaches to assess train operators' workload has been a focus of numerous researchers, including Gibson et al. (2007), Spring et al. (2009), Dunn and Williamson (2012), Scott and Gibson (2012), Large et al. (2014), Robinson et al. (2015), Basacik et al. (2015), Hely et al. (2015), Van Der Weide

et al. (2017), Brandenburger et al. (2018), Brandenburger et al. (2019), Huang et al. (2019), and Verstappen et al. (2022). This section reviews key findings from these studies, emphasizing their methodologies and contributions to understanding the workload in train operations.

Gibson et al. (2007) examined the impact of Train Protection Warning Systems (TPWS) on operators. Using simulator experiments, they collected subjective responses on workload through the Driver IWS rating, particularly for two improved TPWS driver machine interface (DMI) variants. Their findings underscored the potential benefits of these design modifications. Scott and Gibson (2012) also investigated the TPWS DMIs, employing the NASA-TLX method. Their results showed generally low workload measures, offering limited differentiation between the performances of the DMIs. Robinson et al. (2015) and Basacik et al. (2015) both utilized simulator experiments and the NASA-TLX for subjective workload measurement. Robinson et al. (2015) focused on the Automatic Warning System (AWS), uncovering that various factors influence workload. Notably, they found that AWS could lead to underloading in less demanding driving scenarios, and that increasing workload in such cases positively impacts self-reported measures of workload, arousal, and fatigue. Large et al. (2014) and Verstappen et al. (2022) conducted comprehensive studies on the Driver Advisory System (DAS) using subjective-empirical workload assessments. While Large et al. (2014) applied NASA-TLX, Verstappen et al. (2022) used the Rating Scale Mental Effort (RSME). Their research indicated that although DAS systems support efficient operation, they require operators to process considerable information, potentially leading to mental overload, especially in scenarios demanding rapid interpretation of prompts. Spring et al. (2009) explored the workload associated with the Automatic Monitoring Aid (AMA) system in Australia. Their methodology involved simulator experiments, assessing subjective workload perceptions using NASA-TLX and the Subjective Work Underload Checklist (SWUC). Their findings suggested that increased automation in train driving could reduce mental workload to suboptimal levels. Dunn and Williamson (2012) also used NASA-TLX to assess Australian train operators' perceived workload, discovering that task complexity significantly impacts mental workload. Hely et al. (2015) compared the workload under Automatic Train Protection (ATP) and non-ATP conditions, noting that ATP, while enhancing safety, also increases attentional demands.

Studies by Van Der Weide et al. (2017), Brandenburger et al. (2018), and Brandenburger et al. (2019) focused on the European Train Control System (ETCS). Using subjective workload metrics like NASA-TLX and DLR-WAT, these studies generally found that ETCS tends to reduce mental workload compared to traditional systems. Huang et al. (2019) conducted an analysis combining both objective and subjective-empirical approaches. Their subjective analysis, based on the NASA-TLX metric and real-world observations, concluded that the workload in manual driving mode is significantly higher than in automatic mode.

3.2 Subjective-analytical studies on train operators' workload

Research conducted by Wreathall et al. (2003), Foulkes (2004), Halliday et al. (2005), Wreathall et al. (2007a), Wreathall et al. (2007b), Roth et al. (2013), Simoes et al. (2016), and Van Der Weide (2017) represents pivotal subjective-analytical approaches in understanding train operators' workload.

Halliday et al. (2005) examined the In-cab Signal Reminder Device (ICSRD), noting its potential to enhance safety by reducing dependency on trackside signals. However, they identified an increase in cognitive demands, especially in interpreting semaphore signals. Wreathall et al. (2003) and Roth et al. (2013) delved into the implications of Positive Train Control (PTC) systems. Their research, leaning on expert opinions and subjective evaluations, suggested that PTC systems might reduce workload in simpler operations but increase it in complex or emergency scenarios. Further studies by (Wreathall et al., 2007a; 2007b) also highlighted the impact of PTC systems, finding an increased workload due to non-informative alarms and manual data input requirements. Foulkes (2004) and Van Der Weide (2017) explored the workload associated with the European Train Control System (ETCS). Based on Subject Matter Experts (SMEs), Foulkes's study indicated that ETCS Level 2, which eliminates lineside signals, could decrease mental workload relative to traditional systems but also flagged potential workload increases during transitions into and out of ETCS areas. Van Der Weide (2017) observed a generally lower workload for operators using ETCS compared to the legacy ATB system, with highly experienced operators even reporting instances of boredom. Simoes et al. (2016) undertook a subjective analysis using DALI (Driving Activity Load Index), an adaptation of the NASA-TLX. Their study leveraged expert insights to evaluate the workload impact of different train operation tasks. This approach offered a detailed understanding of how various operational aspects influence the mental workload of train operators.

3.3 Objective-empirical studies on train operators' workload

This section highlights studies employing objective-empirical methods, including works by Robinson et al. (2015), Basacik et al. (2015), Hely et al. (2015), Gillis (2016), Balfe et al. (2017), Sebok et al. (2017), Huang et al. (2019), and Nneji et al. (2019).

In the realm of train operators' workload studies, a substantial focus has been placed on objective-empirical approaches, with some researchers also integrating subjective metrics for a more comprehensive analysis. For instance, Robinson et al. (2015) focused on objective measures like heart rate and response times to study the workload effects of the Automatic

Warning System (AWS), supplementing these with subjective assessments such as the NASA-TLX. Basacik et al. (2015) combined reaction time and error rate analysis with physiological data (skin conductance, heart rate) and subjective feedback to explore cognitive underload in train driving. Hely et al. (2015) assessed workload in Automatic Train Protection (ATP) using objective metrics like speed, acceleration, and response times, alongside eye-tracking and subjective evaluations. Similarly, Huang et al. (2019) emphasized objective measures, particularly reaction times across shifts, and included subjective assessments to enrich their analysis.

Later studies, such as those by Gillis (2016), Balfe et al. (2017), Sebok et al. (2017), Huang et al. (2019), and Nneji et al. (2019), predominantly focused on objective-empirical methods. Gillis (2016) focused on Cognitive Task Analysis (CTA) of train operation tasks, combining simulator experiments with direct observations of train operators to scrutinize their responses in different scenarios. Balfe et al. (2017) extracted task load data from on-train-data-recorders (OTDR), analyzing task times and calculating task time pressures. Sebok et al. (2017) investigated the impact of Trip Optimizer (TO) and PTC systems on operator workload, assessing human error rates in different workload-level scenarios. Nneji et al. (2019) conducted a study on the workload effects of PTC systems, utilizing real-world observations. They applied Task Analysis (TA) and assessed time pressure to understand the system's impact. The study revealed that in heavy traffic conditions, automation provided by PTC systems could be more effective than a freight conductor in managing the workload of locomotive engineers. However, in contrast, this automation might negatively affect operator performance in typical short-haul freight rail scenarios.

3.4 Objective-analytical studies on train operators' workload

This section reviews the application of objective-analytical methods by researchers such as Foulkes (2004), Hamilton and Clarke (2005), Blanchard (2013), Groshong (2016), Verstappen et al. (2017), and Wang et al. (2021), highlighting their contributions to understanding the workload in train operations.

Foulkes (2004) investigated the mental workload in the European Train Control System (ETCS), employing Task Analysis (TA) and the Workload Assessment Tool (WAT) to focus on task duration and cognitive demands. Hamilton and Clarke (2005) used cognitive theory and Visual, Auditory, Cognitive, and Psychomotor (VACP) measures to model train operators' workload under ETCS, validating their model by comparing VACP predictions with observed NASA-TLX values. Blanchard (2013) performed a detailed analysis of Cambrian train operations, evaluating workload using VACP metrics. The study highlighted that while automation reduces manual task frequency, it increases the complexity and cognitive demands associated with in-cab tasks. Groshong (2016) explored how different train control systems affect cognitive aspects of train operation, particularly decision-making and information processing. Verstappen et al. (2017) assessed the workload in the Netherlands Railways' in-cab systems using the PARRC model, task analysis, and VACP analysis. They found that monitoring new devices while driving elevates workload due to increased visual and cognitive demands. Wang et al. (2021) developed a Timed Petri Net-based mental workload evaluation model, conducting a driving simulator experiment to validate their approach for system task optimization.

4 AN OVERVIEW OF THE TRAIN OPERATORS' WORKLOAD STUDIES

This section presents a consolidated overview of various studies on train operators' workload, as detailed in Table 1. This table methodically outlines the methodologies, metrics, and systems each study examined. The majority of the 30 studies reviewed, predominantly from the US and UK, varied in their approach – some analyzed workload under existing train systems, while others assessed the effects of new in-cab systems and automation.

Particularly in Europe and America, studies focusing on the European Train Control System (ETCS) and the Positive Train Control (PTC) system form a significant part of this research area. A marked trend in these studies is the preference for subjective-empirical methods, with the NASA-TLX tool being commonly used. Furthermore, the analysis indicates a preference for empirical workload assessment methods, combining subjective and objective metrics to validate findings, as shown in Figure 3. This preference suggests a tendency among railway companies to delay comprehensive workload analysis until the development of system prototypes or the availability of simulator experiments. While beneficial for testing in realistic or simulated environments, this strategy might overlook the advantages of early-stage analysis, which is crucial for optimizing operator interfaces, automation, and information presentation (Eggemeier et al., 1985; Endsley, 1995).

The findings from the train operators' workload studies reveal diverse and sometimes contrasting effects of in-cab systems and automation on train operators' workload. Such variability in outcomes emphasizes the intricate nature of workload assessment, which is affected by a multitude of factors, including system features, individual operator characteristics, environmental conditions, and operational dynamics.

Table 1. A review of the train operators' workload assessment and prediction studies.

ID	Authors	Country	Subjectiv/ Objective	Empirical/ Analytical	Data sources	Methods and Metrics	System
1	Wreathall et al. (2003)	US	Subjective	Analytical	SMEs	-	PTC
2	Foulkes (2004)	UK	Subjective, Objective	Analytical	SMEs	TA, Task time, WAT	ETCS
3	Hamilton and Clarke (2005)	UK	Objective	Analytical	Documents review	CTA, Task time, Time pressure, VACP analysis	ETCS
4	Halliday et al. (2005)	UK	Subjective	Analytical	SMEs	-	ICSRD
5	Wreathall et al. (2007a)	US	Subjective	Analytical	SMEs	-	PTC
6	Wreathall et al. (2007b)	US	Subjective	Analytical	Documents review, SMEs	-	PTC
7	Gibson et al. (2007)	UK	Subjective	Empirical	Simulator experiments	IWS	TPWS
8	Spring et al. (2009)	Australia	Subjective	Empirical	Simulator experiments	NASA-TLX, SWUC	AMA
9	Dunn and Williamson (2012)	Australia	Subjective	Empirical	Simulator experiments	NASA-TLX	-
10	Scott and Gibson (2012)	UK	Subjective	Empirical	Simulator experiments	NASA-TLX	TPWS
11	Roth et al. (2013)	US	Subjective	Analytical	SME, Observations	-	PTC
12	Blanchard (2013)	UK	Objective	Analytical	Documents review, Observations	TA, VACP, Frequency of driving tasks	-
13	Large et al. (2014)	UK	Subjective	Empirical	Simulator experiments	NASA-TLX	DAS
14	Robinson et al. (2015)	UK	Subjective, Objective	Empirical	Simulator experiments	NASA-TLX, Physiological & Performance measures	AWS
15	Basacik et al. (2015)	UK	Subjective, Objective	Empirical	Simulator experiments	NASA-TLX, Physiological & Performance measures	-
16	Hely et al. (2015)	Australia	Subjective, Objective	Empirical	Simulator experiments	NASA-TLX, Performance measures, & Eye-tracking	ATP
17	Groshong (2016)	US	Objective	Analytical	Documents review, SMEs	CTA, Number of actions	-
18	Simoes et al. (2016)	Portugal	Subjective	Analytical	SMEs	DALI (adapted the NASA-TLX)	-
19	Gillis (2016)	Belgium	Objective	Empirical	Simulator experiments Observations	CTA	-
20	Balfe et al. (2017)	Ireland	Objective	Empirical	OTDR	TA, Task time, Time pressure	-
21	Sebok et al. (2017)	US	Objective	Empirical	Simulator experiments	Performance measures	TO, PTC
22	Van Der Weide et al. (2017)	Netherlands	Subjective	Empirical	Simulator experiments	RSMI	ETCS
23	Van Der Weide (2017)	Netherlands	Subjective	Analytical	SMEs	-	ETCS
24	Verstappen et al. (2017)	Netherlands	Objective	Analytical	SMEs	TA, PARRC, VACP analysis	In-cab systems
25	Brandenburger et al. (2018)	Germany	Subjective	Empirical	Simulator experiments	NASA-TLX, DLR-WAT	ETCS
26	Brandenburger et al. (2019)	Germany	Subjective	Empirical	Simulator experiments	NASA-TLX	ETCS
27	Nneji et al. (2019)	US	Objective	Empirical	Observations	TA, Task time, Simulation, Time pressure	PTC
28	Huang et al. (2019)	China	Subjective, Objective	Empirical	Observations	TA, Task time, NASA-TLX, Physiological measures	-
29	Wang et al. (2021)	China	Objective	Analytical	Documents review	TPN	-
30	Verstappen et al. (2022)	Netherlands	Subjective	Empirical	Simulator experiments	Physiological measures and Rating Scale Mental Effort	DAS

This complexity necessitates a detailed and careful interpretation of workload study results within the context of train operations.

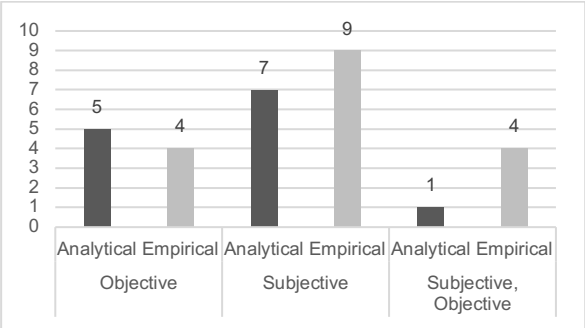

Figure 3. The applied approaches in train operators' workload studies.

5 CONCLUSIONS

This paper provided a review of studies focused on the mental workload of train operators, especially in the context of evolving train protection and control systems. Our analysis categorized these studies based on their methodologies—subjective vs. objective and analytical vs. empirical—while also considering the methods, metrics, and types of train cab systems examined.

This review highlighted the prevalent use of subjective-empirical methods in train operators' workload studies, with a focus on evaluations conducted post-prototype development or through simulator experiments. However, this approach sometimes overlooks the benefits of early workload analysis, which is essential for user-centric design and error prevention. Furthermore, the review revealed diverse impacts of in-cab systems and automation on workload, influenced by factors like system characteristics, operator individuality, and environmental conditions. This variability underscores the complexity of workload assessment in railway operations and the need for comprehensive evaluation methodologies.

For future research, there are two critical directions: Firstly, analyzing the workload of train operators in Canadian railways, particularly post-implementation of the Enhanced Train Control (ETC) system, would provide valuable insights into the effects of advanced control systems in different national contexts. Secondly, future studies should address the lack of consideration for contextual factors in analytical workload models. This would enhance understanding of how environmental and situational variables impact operator workload, leading to more effective and adaptive system designs.

Overall, a balanced approach is recommended to integrate both subjective and objective methods as well as analytical and empirical methods in the early and later stages of system development. Such a strategy will contribute significantly to ensuring railway operations' safety and efficiency while improving train operators' overall well-being and performance.

6 ACKNOWLEDGEMENT

This research was supported by the Alberta Innovates and Canadian Rail Research Laboratory (CaRRL). CaRRL is funded by the Natural Sciences and Engineering Research Council of Canada (NSERC), Canadian National Railway (CN), and Transport Canada (TC) [Grant# NSERC IRC 523369-18].

REFERENCES

Balfe, N., Crowley, K., Smith, B., Longo, L., 2017. Estimation of train driver workload: extracting taskload measures from on-train-data-recorders, Human Mental Workload: Models and Applications: First International Symposium, H-WORKLOAD 2017. Springer, Dublin, Ireland, pp. 106-119.

Basacik, D., Waters, S., Reed, N., 2015. Detecting cognitive underload in train driving: a physiological approach, Proceedings of the 5th International Rail Human Factors Conference, pp. 14-17.

Blanchard, H., 2013. A method for assessing drivability for ETCS cab retrofit, 4th International Conference on Rail Human Factors, pp. 191-200.

Boles, D.B., Adair, L.P., 2001. The multiple resources questionnaire (MRQ), Proceedings of the human factors and ergonomics society annual meeting. SAGE Publications Sage CA: Los Angeles, CA, pp. 1790-1794.

Brandenburger, N., Naumann, A., Jipp, M., 2019. Task-induced fatigue when implementing high grades of railway automation. Cognition, Technology & Work, 1-11.

Brandenburger, N., Thomas-Friedrich, B., Naumann, A., Grippenkoven, J., 2018. Automation in railway operations: effects on signaller and train driver workload, Proceedings of the 3rd German Workshop on Rail Human Factors. ITS Mobility, pp. 51-60.

Cain, B., 2007. A review of the mental workload literature, Human System Integration Section, Defence Research and Development, Canada.

Cooper, G.E., Harper, R.P., 1969. The use of pilot rating in the evaluation of aircraft handling qualities. National Aeronautics and Space Administration (NASA).

Dunn, N., Williamson, A., 2012. Driving monotonous routes in a train simulator: the effect of task demand on driving performance and subjective experience. Ergonomics 55, 997-1008.

Eggemeier, F.T., Shingledecker, C.A., Crabtree, M.S., 1985. Workload measurement in system design and evaluation, Proceedings of the Human Factors Society Annual Meeting. SAGE Publications Sage CA: Los Angeles, CA, pp. 215-219.

Endsley, M.R., 1995. Toward a theory of situation awareness in dynamic systems. Human factors 37, 32-64.

Evans, J., 2017. A systems approach to predicting and measuring workload in rail traffic management systems, Human Mental Workload: Models and Applications Symposium, Dublin, Ireland.

Foulkes, J., 2004. Impact of the european rail traffic management system on driver workload, Early human factors analysis for UK-ERTMS driving (Final Version), Human Engineering Limited for Rail Safety and Standards Board (RSSB), London, UK.

FRA, 2014. Collaborative incident analysis and human performance Handbook, Federal Railroad Administration (FRA), US Department of Transportation, Washington, DC, USA.

Gibson, W., Halliday, M., Sutton, L., Shelton, J., Bond, M., 2007. A train driving simulator experiment to investigate driver fault diagnosis, People and Rail Systems: Human Factors at the Heart of the Railway, p. 125.

Gillis, I., 2016. Cognitive workload of train drivers, People and Rail Systems. CRC Press, pp. 115-126.

Groshong, H.L., 2016. Task modeling and assessment for human-system interaction in freight rail operations. Massachusetts Institute of Technology.

Halliday, M., Gall, B., Gibson, H., Raggett, L., 2005. Assessing the effectiveness of an in-cab signal reminder device Rail Safety and Standards Board (RSSB), London, UK.

Hamilton, W.I., Clarke, T., 2005. Driver performance modelling and its practical application to railway safety. Applied Ergonomics 36, 661–670.

Hart, S.G., Staveland, L.E., 1988. Development of NASA-TLX (Task Load Index): Results of empirical and theoretical research, Advances in Psychology. Elsevier, pp. 139-183.

Heard, J., Harriott, C.E., Adams, J.A., 2018. A survey of workload assessment algorithms. IEEE Transactions on Human-Machine Systems 48, 434-451.

Hely, M., Shardlow, T., Butt, B., Friswell, R., McIntosh, A., Williamson, A., 2015. Effects of automatic train protection on human factors and driving behaviour, Proceedings 19th Triennial Congress of the IEA, Melbourne, Australia, pp. 9-14.

Huang, Y.-c., Li, L.-p., Liu, Z.-g., Zhu, H.-y., Zhu, L., 2019. Assessment of urban railway transit driver workload and fatigue under real working conditions. Transportation Research Record 2673, 891-900.

Jex, H.R., 1988. Measuring mental workload: Problems, progress, and promises, Advances in Psychology. North-Holland, pp. 5-39.

Jung, H.S., Jung, H.-S., 2001. Establishment of overall workload assessment technique for various tasks and workplaces. International Journal of Industrial Ergonomics 28, 341-353.

Kruger, A., 2008. A systems approach to the assessment of mental workload in a safety-critical environment, Faculty of Engineering, Built Environment and Information Technology. University of Pretoria.

Large, D.R., Golightly, D., Taylor, E.L., 2014. The effect of driver advisory systems on train driver workload and performance. Contemporary Ergonomics and Human Factors 15, 335-342.

Miller, S., 2001. Workload measures, National Advanced Driving Simulator (NADS), University of Iowa Driving Safety Research Institute, USA.

Nneji, V.C., 2019. A workload model for designing & staffing future transportation network operations, Department of Mechanical Engineering & Materials Science. Duke University.

Nneji, V.C., Cummings, M.L., Stimpson, A.J., 2019. Predicting locomotive crew performance in rail operations with human and automation assistance. IEEE Transactions on Human-Machine Systems 49, 250-258.

Parasuraman, R., Sheridan, T.B., Wickens, C.D., 2008. Situation awareness, mental workload, and trust in automation: Viable, empirically supported cognitive engineering constructs. Journal of Cognitive Engineering and Decision Making 2, 140-160.

Reid, G.B., Nygren, T.E., 1988. The subjective workload assessment technique: A scaling procedure for measuring mental workload, Advances in Psychology. Elsevier, pp. 185-218.

Robinson, D., Waters, S., Basacik, D., Whitmore, A., Reed, N., 2015. A pilot study of low workload in train drivers, Transport Research Laboratory, Crowthorne, UK.

Roth, E., Rosenhand, H., Multer, J., 2013. Using cognitive task analysis to inform issues in human systems integration in railroad operations, Federal Railroad Administration (FRA), US Department of Transportation, Washington, DC, USA.

Rusnock, C., Borghetti, B., McQuaid, I., 2015. Objective-analytical measures of workload–the third pillar of workload triangulation?, International Conference on Augmented Cognition. Springer, pp. 124-135.

Scott, A., Gibson, H., 2012. Red means stop, doesn't it? A human factors trial of a UK train safety system driver-machine interface, In: JR WIlson, A.M., T. Clarke, J.

Rajan, & N. Dadashi (Ed.), Rail Human Factors around the World: Impacts on and of People for Successful Rail Operations. CRC Press, pp. 457-464.

Sebok, A., Walters, B., Wickens, C., 2017. Simulator-based investigations of human error potential with railroad automation in the locomotive cab, Proceedings of the Human Factors and Ergonomics Society Annual Meeting. SAGE Publications pp. 1964-1968.

Simoes, A., Carvalhais, J., Ferreira, P., Correia, J., Lourenco, M., 2016. Research on Fatigue and Mental Workload of Railway Drivers and Traffic Controllers, People and Rail Systems: Human Factors at the Heart of the Railway. CRC Press, pp. 577-588.

Spring, P., McIntosh, A., Baysari, M., 2009. Counteracting the negative effects of high levels of train automation on driver vigilance, Proceedings of the 45th Annual Human Factors and Ergonomics Society of Australia Conference, pp. 93-101.

Tsang, P.S., Velazquez, V.L., 1996. Diagnosticity and multidimensional subjective workload ratings. Ergonomics 39, 358-381.

Van Der Weide, R., 2017. ERTMS roll out from a train driver's perspective, Sixth International Human Factors Rail Conference, London, UK.

Van Der Weide, R., De Bruijn, D., Zeilstra, M., 2017. ERTMS pilot in the Netherlands–impact on the train driver, International Human Factors Rail Conference, London, UK.

Verstappen, V.J., Pikaar, E.N., Zon, R.G., 2022. Assessing the impact of driver advisory systems on train driver workload, attention allocation and safety performance. Applied Ergonomics 100, 103645.

Verstappen, V.J., Wilms, M.S., Van Der Weide, R., 2017. The impact of innovative devices in the train cab on train driver workload and distraction, Sixth International Human Factors Rail Conference, London, UK.

Wang, L., He, X., Chen, Y., 2016. Quantitative relationship model between workload and time pressure under different flight operation tasks. International Journal of Industrial Ergonomics 54, 93-102.

Wang, P., Fang, W., Guo, B., 2021. Mental workload evaluation and its application in train driving multitasking scheduling: a Timed Petri Net-based model. Cognition, Technology & Work, 1-15.

Wickens, C., Tsang, P.S., 2015. Workload, In: Boehm-Davis, D.A., Durso, F.T., Lee, J.D. (Eds.), APA handbook of human systems integration. American Psychological Association.

Wilson, J.R., Pickup, L., Norris, B.J., Nichols, S., Mitchell, L., 2017. Understanding of mental workload in the railways, Rail Human Factors: Supporting the Integrated Railway. Routledge, pp. 309-318.

Wreathall, J., Roth, E., Bley, D., Multer, J., 2007a. Human factors considerations in the evaluation of processor-based signal and train control systems: human factors in railroad operations, Federal Railroad Administration (FRA), US Department of Transportation, Washington, DC, USA.

Wreathall, J., Roth, E.M., Bley, D., Multer, J., 2003. Human reliability analysis in support of risk assessment for positive train control, Federal Railroad Administration (FRA), US Department of Transportation, Washington, DC, USA.

Wreathall, J., Woods, D.D., Bing, A.J., Christoffersen, K., 2007b. Relative risk of workload transitions in positive train control, Federal Railroad Administration (FRA), US Department of Transportation, Washington, DC, USA.

Xie, B., Salvendy, G., 2000. Review and reappraisal of modelling and predicting mental workload in single-and multi-task environments. Work & Stress 14, 74-99.

Young, M.S., Brookhuis, K.A., Wickens, C.D., Hancock, P.A., 2015. State of science: mental workload in ergonomics. Ergonomics 58, 1-17.

Canadian & Cold Regions
Rail Research Conference
2024

Investigating the effectiveness of machine vision-based railcar inspection technology

Solange de Blois, Chathula Adikary, & Brian Zou
Canadian Pacific Kansas City Railway, Calgary, Alberta, Canada

Alireza Roghani, Yan Liu, & Samy Metari
National Research Council Canada, Ottawa, Ontario, Canada

ABSTRACT

In accordance with the Railway Freight Car Inspection and Safety Rules outlined by Transport Canada, railway companies are required to conduct safety inspections to ensure that freight cars are free from all safety defects. These visual inspections are performed by certified car inspectors at safety inspection locations such as where trains are made up, cars added to trains, or where cars are interchanged. The recent advancements in high-speed, high-resolution, advanced imaging devices and machine vision methods have great potential for automated and semi-automated inspection of railcar components. Canadian Pacific Kansas City (CPKC) railway has been implementing this technology at multiple locations across its network. Each inspection portal features strategically positioned cameras designed to capture high-resolution images of various train components under operational speeds and diverse climatic conditions. The on-site computer stores and sends images to a remote processing unit where images from all passing railcars are then reviewed by inspectors, supported by computer algorithms. This paper intends to introduce the technology employed by CPKC and provide a high-level description of the main advantages and limitations of this system.

1 INTRODUCTION

As per Transport Canada's Railway Freight Car Inspection and Safety Rules [Transport Canada, 2014], railway companies are mandated to perform safety inspection to ensure that freight cars are free from all safety defects. Certified car inspectors perform safety inspection at locations such as where trains are made up, cars added to trains, or where cars are interchanged. With the advancement of wayside and machine vision technologies, railroads worldwide are actively engaged in leveraging these technologies to enhance quality and efficiency of railcar inspections, thereby enhancing the overall safety of railway operations. Canadian Pacific Kansas City (CPKC) railway has been one of the industry leaders in adopting novel technologies in North America. It has implemented several types of wayside & camera-based inspection systems across its network with the aim to better identify safety defects and decrease risk to the railroads.

1.1 Wayside Inspection Technologies

In an effort to reduce likelihood of derailment and improve mechanical safety inspections, early wayside technology implementation focused on detecting issues with bearings, trucks and wheels. Defects with these components typically corresponded to high risk of derailment and substantial economic costs to the railroad.

1.1.1 Bearing Related Technologies

Overheated roller bearings are the leading mechanical cause of derailment in North America. For this reason, hot box detectors (HBDs) are the most widely used wayside technology, with thousands of systems installed [Singh, 2022]. At CPKC, HBDs are spaced between 15-25 miles apart throughout the network. HBDs (*Figure 1*) use infrared thermal scanners to monitor and detect temperatures of railcar bearings as a direct result of the wheelset rotation. Using these data and trending warm bearings over multiple detectors, railways increase the detection rate of failing bearings prior to overheating to the point of burning off the axle. More recently, the use of acoustic bearing detectors (ABDs) for bearing failure detection have gained prominence. ABDs are designed to measure acoustic signatures and can observe early signs of failing railcar roller bearings prior to heat signature detection by HBDs. This early detection has been used at CPKC to deploy predictive models around railcar bearing health for more proactive maintenance practices [Canadian Pacific Railway, 2017].

Figure 1. (L) Hot box detector, (R) Overheated roller bearing

1.1.2 Truck & Wheel Related Technologies

Railcars with degraded truck conditions leading to poor steering capabilities also rank highly in causes of mechanical derailments. To help prevent this truck performance (TPDs) and truck hunting detectors (THDs) are used. Detection method varies by system including optical geometry, strain gauge and vertical acceleration-based technology. These systems can detect indicators of poor performing trucks such as; excessive movement, high lateral over vertical ratios, high angle of attack, etc. At CPKC, THDs using strain gauge technology are often paired with wheel impact load detectors (WILDs) using the same sensing technology [L.B. Foster, 2023]. Used in conjunction with WILDs, incidents of truck hunting related derailments have substantially decreased at CPKC.

WILDs identify high vertical impacts due to out of round and tread defects on railcar wheels. They are especially critical in Canadian cold weather operations when shelling defects and high impact forces on rail have a greater chance of leading to damage in both rolling stock and infrastructure. While WILDs are suitable for finding shelling defects on wheel treads, they are not adept at finding broken wheels before they happen. Other technologies have been or are in development to attempt to predict wheel breaks before they happen. Some of these systems include use of ultrasonics, electromagnetic fields and vision systems.

1.1.3 Effectiveness of Wayside Implementation

The progressive implementation of wayside detection technologies in Class I railroads in North America have reduced the numbers of mechanical and track related derailments [Transportation Safety Board of Canada, 1994]. In a study conducted analysing the effectiveness of wayside technology in North America over a ten year period between 2003-2012, the Federal Railroad Association (FRA) concluded that had a significant impact on the reduction in mechanical and track related derailments and the associated costs [2]. This period saw a substantial growth in detector system installations across North America. Within CPKC, approximately 80% of mechanical defects on railcars are identified by wayside systems, including vision technologies.

1.2 Camera-based Train Inspection Technology

Looking ahead, vision technology has the potential to emerge as the next major advancement in enhancing efficiency, safety, and overall railway operations. By implementing machine vision, railways can reduce downtime and ensure the integrity of their rolling stock. This proactive approach not only improves safety but also contributes to the longevity of rail infrastructure, ultimately leading to cost savings and a more sustainable and reliable transportation system. Automated visual inspection systems can swiftly and accurately assess the condition of railcars, identifying defects, wear, or damages that might otherwise go unnoticed.

Within CPKC, these camera-based train inspection systems are called Train Inspection Portal Systems (TIPS). Each system is a modular suite of camera systems selected to target safety critical areas of a railcar for the purpose of the safety inspection. The cameras are designed to capture high-resolution images of various railcar components in a natural or moving state, operating at track speed and in diverse environmental conditions. On-site computers store and transmit images for manual visual review by certified car inspectors located in an office environment, referred to as Portal Office Inspection (POI). The office inspectors review the images and relay their findings to field inspectors for validation and implementation of necessary actions. CPKC also uses some AI algorithms to detect certain types of defects, but the outputs still need to be validated by the office inspectors before being dispatched to the field.

Figure 2. CPKC Train Inspection Portal System (TIPS), Maple Creek, SK

The technology deployed by CPKC (*Figure 2*) was originally developed by a North American, Atlanta based vendor [Wabtec, 2023]. The CPKC's portal comprises four distinct sets of views, each equipped with multiple line scan cameras (
Table 1). The deployment of over 35 cameras ensures a comprehensive coverage of entire component areas through up to 72 images per one freight car. The system is designed to provide redundant views, offering alternative perspectives in the event of an individual camera failure or obstruction. Additionally, the software

that is used by the office inspectors enables them to easily examine the portal images, adjusting contrast and brightness or zooming in and out as needed to identify any defective components. The office inspectors can also investigate the last time a railcar passed through the portal and compare the images with the most recent one. This system operates within a temperature range of -40 °C to +55 °C.

Table 1. Available camera views and number of images per railcar

Car Structural Component/Undercarriage View (CSCView); No. of cameras: 5; No. of images per car: 25

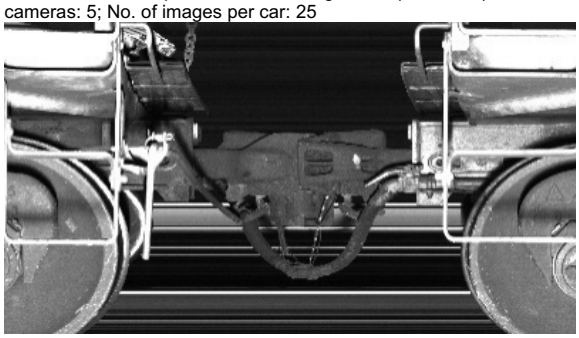

AirHoseView (AHView); No. of cameras: 4; No. of images per car: 5

TrainView (TRNV); No. of cameras: 20; No. of images per car: 20

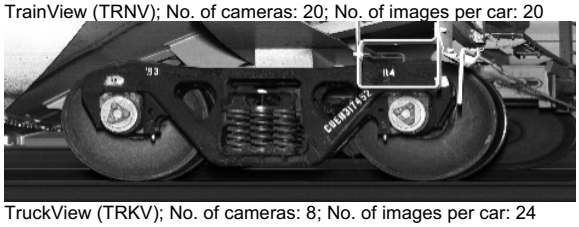

TruckView (TRKV); No. of cameras: 8; No. of images per car: 24

1.3 Study of the Effectiveness of Vision Technology

In 2021, a collaborative research initiative was undertaken by the National Research Council Canada (NRC), CPKC, and the University of Alberta and financially supported by the Transport Canada Innovation Center. This joint effort focused on comprehensively understanding and evaluating the performance of both the hardware and software components of the vision system utilized by CPKC, with a particular emphasis on its functionality under winter conditions. The project's scope was exclusively centered on the evaluation of technology, and it did not extend to the assessment of safety equivalence. This paper will discuss some of the relevant findings and observations from the project.

2 MATERIALS AND METHODS

Since November 2020, CPKC has been utilizing vision technology to conduct safety inspection on specific potash trains travelling between mines in Saskatchewan and ports in BC. An independent analysis by the NRC examined data collected over 15 months using this system for inspecting the trains. Approximately 70% of the target potash trains, totaling around 1000 trains, have been inspected through the portal system during the study period. The objectives of the study have been to determine the effectiveness of the technology in the identification of railcar safety defects and assessing factors that adversely affect the ability of the technology to perform in this capacity.

To determine effectiveness of the technology the study focused on the following categories: (a) parallel inspections comparing the results of the office inspections to field inspections; (b) image quality, ability to detect the anomalies as well as the factors affecting quality.

2.1 Evaluation Based on Field Tests

To narrow the focus of the study, a subset of potential railcar safety defects was selected for components of high interest for comparison (Table 2).

Table 2. Safety Defects Analyzed in Study

Defect Type
Angle cock
Axle cap screw missing
Bent brake beam
Centre sill cracked
Coupler body cracked
Cracked axle
Cracked coupler knuckle
Cracked draft gear
Hand brake
Side sill bent/cracked
Truck bolster crack
Truck spring
Wheel defects[1]

[1] Broken, chipped or cracked flange, rim, and plate. Thin flange, high flange, thin rim, and flange worn hollow not included.

Ground truth defect data are established by performing four (4) field visits at CPKC's Moose Jaw terminal to observe and participate in mechanical safety inspections (MSI) with CPKC inspectors. Data have been collected from 12 trains (1958 cars) during these trips. These data are compared to office inspections on the same train sets.

2.2 Image Quality Analysis

A thorough analysis of 124,940 images recorded by the CSCView and TruckView was conducted by the NRC. These image data are collected from 3 potash and 21 grain trains between March and June 2022. These are visually inspected to identify image quality issues. Examples of images captured during extreme weather conditions have been evaluated as well.

3 RESULTS AND DISCUSSION

3.1 Parallel Inspection Comparison

The portal can deliver high-quality images, notably of hard to inspect undercarriage components. Specifically, the CSCView, equipped with five cameras, provides a comprehensive perspective of the entire brake rigging system and end-of-car units, including the coupler, draft gear system, and end sill. The examination of available data confirmed the effectiveness of machine vision-based inspection in identifying defects in railcar undercarriage components. Comparatively, inspecting undercarriage components present substantial challenges for inspectors, requiring them to physically bend and crawl beneath the railcar body. This process, aside from being inconvenient, is impractical for each car within a train consist. Additionally, reviewing images taken from a moving train is more advantageous to inspect certain components such as draft gear system that may perform differently with and without loading. *Figure 3* illustrates two instances of high-quality images captured by CSCView cameras, which office inspectors used to detect a bent brake beam and a broken coupler carrier. The capability to manipulate these images enhances inspectors' efficiency and accuracy in defect detection compared to the demanding field inspection procedure.

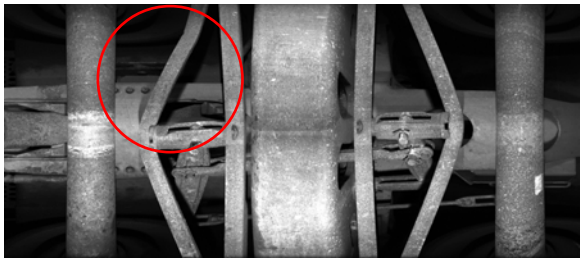

(a)

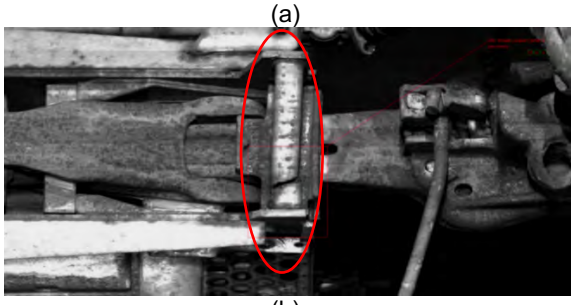

(b)

Figure 3. Image from brake rigging system, showing a bent brake beam (a), A broken coupler carrier visible through portal images (b)

According to a study conducted by [Leishman, 2017] on main track derailments data between 2001 and 2014, among all railcar components, wheel related issues pose the highest risk (high frequency of occurrence and high severity) to safety of railway operations in Canada. In the past, the only opportunity to visually inspect wheels is at yard. The inspection portal provides a new opportunity to check each wheel of a train during operation. *Figure 4* shows a chipped tread that was detected by reviewing portal images. Once the office inspectors identified this defect, the rail traffic controller and the train crew are promptly notified. They are then requested to stop the train at the nearest siding to set this car off. This incident is a noteworthy example of how technology employment was pivotal in preventing a potential derailment. CPKC has recently added more cameras to the portal that provides further views of wheel treads. The software image viewer has also been improved that enables office inspectors to inspect wheel treads more efficiently.

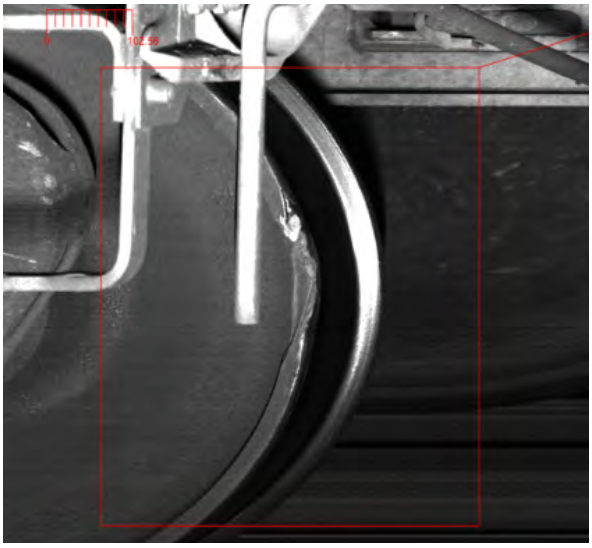

Figure 4. Chipped tread found through portal images

Table 3 outlines the technology's performance in detecting anomalies related to railcar safety defects during the study period. The precision value, representing the percentage of defects that are found to be visible through portal images, highlights the system's impressive ability to recall approximately 70% of known abnormalities from images captured at line speeds. Moreover, over 50% of the false positive cases are associated with wheel-related issues and occurred in the initial two quarters of the study. During this period, office inspectors, exercising abundant caution, flagged any suspicious cases for field verification. These flagged cases primarily turned out to be artifacts caused by shadows and grease on the wheel flange and tread. Subsequently, as office inspectors gained experience, the incidence of false positive cases significantly decreased. Nevertheless, there remains potential for further performance enhancement by minimizing the occurrence of false alarms.

Table 3. Summary of the results of CPKC's vision technology performance

True Positive	False Positive	False Negative	Recall	Precision
163	187	70	70%	47%

The outcomes of the parallel tests revealed that, while a high percentage of defects are discernible through portal images, the overall office inspection process demonstrates a lower recall percentage. This discrepancy is attributed to human factors influencing the efficacy of defect identification through portal images. Notably, when office inspectors have been provided with a second opportunity to review images, there was an observable increase in true positive cases and a reduction in false negatives. The U of A conducted a comprehensive analysis of factors contributing to human errors during office inspections, offering recommendations for their effective mitigation. It is noteworthy that the impact of human factors extends to field inspectors as well.

Looking ahead, the use of AI algorithms may help in mitigate human errors, however, the development of efficient algorithms is not a trivial task. It necessitates the development of an extensive dataset encompassing a diverse range of defects. Given the early stages of vision technology adoption, it is not feasible to develop efficient algorithms. Additionally, finding a balance between minimizing the number of false positives and absolutely not missing any true positives is the hardest task to achieve. Consequently, in the meantime, the successful implementation of vision technology is directly linked to the robustness of image review by certified car inspectors within an office environment.

3.2 Image Quality

Image quality is the most fundamental factor in the success of vision-based systems. Using line scan cameras in CPKC's portal brings several benefits in this regard. Infrared laser cameras are used to illuminate the components, reducing dependence on sunlight and ensuring consistent image quality. These cameras can capture detailed images across a wide area without sacrificing quality. They work by capturing one line at a time, which reduces the amount of data compared to other cameras. This makes them great for railcar inspection applications that need quick data transmission and efficient storage. Line scan cameras also need less light, making them adaptable to different lighting conditions. Additionally, their ability to continuously capture images is valuable for inspecting railcars that are moving through the portal.

Instances have been observed wherein the image quality from one or multiple cameras was compromised for various reasons such as illumination or underexposure. The most common quality problems are striping, saturation, and partial and full darkening effect as shown in Figure 5.

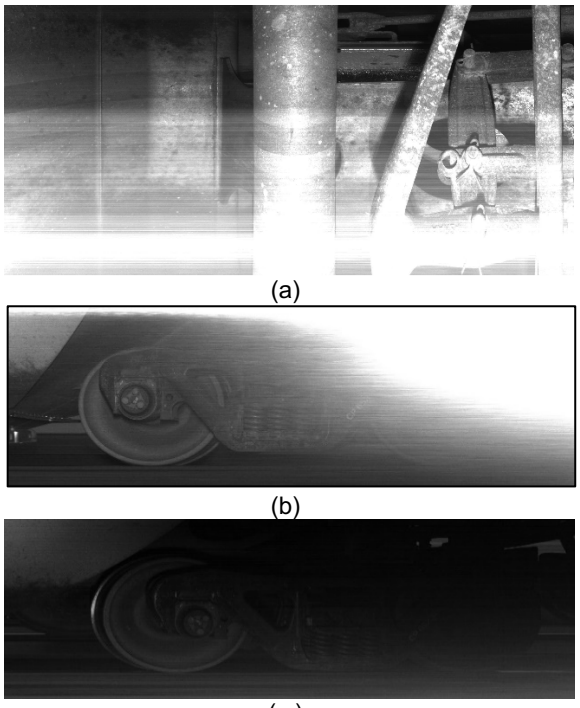

(a) (b) (c)

Figure 5. Example of images with compromised quality striping (a), saturation (b), and darkening (c)

Of all the images assessed, 0.89% had severe image quality issues and 40% hade minor image quality issues. Severe quality issues represent images either completely saturated or darkened, making them unavailable for inspection. For the minor quality issues, the images while affected are still usable for inspection purposes. The impact of compromised images can range widely, from negligible effects on remote inspections in the presence of redundant cameras, to prevention of office inspection due to substantial degradation in image quality when specific cameras are affected, or redundant images are unavailable.

3.3 Winter and Other Challenges

The harsh Canada winter environment can pose some challenges to both manual field inspections and the application of the vision technology alike, affecting the ability to see defects on the ground and the image quality and hardware of the inspection system.

Figure 6 illustrates a case study featuring images captured during the passage of a train through the portal amid a snowstorm. The presence of snowflakes (from the snowfall or the scattering of snowflakes accumulated on rail track induced by the passage of the train) has significantly affected the quality of the images, making the office inspection difficult. The degree of snow-related interference varies among different camera views, with CSCView experiencing more pronounced effects. Under such circumstances, CPKC will use an alternative view or in extreme cases leave the affected car or train for a complete manual inspection in yard. This is an extreme and infrequent event, happened for only about 0.48% of

all trains that have been inspected between Q1 2021 and Q3 2023. Installation of fences near the portal have partially mitigated the problem but the system is still not entirely immune to adverse conditions during heavy snowfall or when extreme winds drift snow towards the portal. In all but the most cases, even with blowing snow the images are valuable for identifying defects.

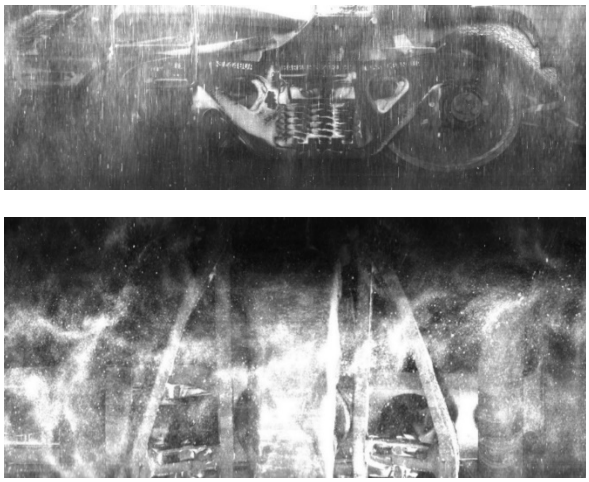

Figure 6. Image quality degraded due to presence of drifting snow

The extreme cold may also affect the shutters on the camera windows, filling them with ice and freeze shut. This issue has been mitigated to a large extent by installing heat pads on the windows of the cameras to prevent condensation as well as increasing the frequency of cleaning and maintenance during winter.

Another challenge that affects the system's performance is related to the power supply that may be affected due to various reasons such as extreme weather and utility outages. For instance, in April 2022, the system was out of service for 5 weeks due to a severe wind storm with wind speeds over 45 km/h and gusts up to 100 km/h. It knocked down power lines to over 70 miles of track in the area. CPKC has been working on different mitigation methods, including auxiliary power generator, to keep the system uptime to be as high as 95%.

4 CONCLUSIONS

This short paper discussed the relevance of machine vision-based inspection systems in railcar safety, focusing on the technology adopted by CPKC. The technical analysis of CPKC's portal highlights the advantages of using line scan cameras, especially in capturing high-quality images of undercarriage components. The images from undercarriage component is the most distinctive advantage of using vision technologies, facilitating detection of issues that may be challenging for field inspectors to find. Despite these benefits, challenges arise, such as compromised image quality due to environmental factors like snowfall as well as software and hardware issues. Several measures are put in place to mitigate the effect of adverse climate conditions, but the system is not entirely immune to severe weather events.

A key factor in the success of utilizing machine vision is the performance of office inspectors who review the portal images. The development of AI algorithms to supplement the office inspection can be a viable solution to realize the full potential of the vision technologies.

5 ACKNOWLEDGEMENTS

The authors sincerely thank the Canadian Pacific Kansas City Railway for their help throughout the execution of this project and Transport Canada Innovation Center for supporting this project. Special thanks to Kaveh Khalilian and Sasan Ebrahimi from Transport Canada, Kyle Mulligan from Canadian Pacific Kansas City, and Yves Noel, Chengbi Dai, and Hamid Mammeri from National Research Council Canada.

REFERENCES

Canadian Pacific Railway. (2017). Condition Based Maintenance of Railcar Roller Bearings Using Predictive Wayside Alerts Based on Acoustic Bearing Detector Measurements. US10513279B2 - Google Patents.

Leishman, E. (2017). Analysis of Canadian Train Derailments from 2001 to 2014. M.Sc. thesis, University of Alberta.

L.B. Foster. (2023). Total Track Monitoring - WILD. Accessed January 4, 2023, from WILD-IV | L.B. Foster (lbfoster.com)

Singh, S. P. (2022). Effectiveness of Wayside Detector Tech. Accessed January 20, 2024, from Effectiveness of Wayside Detector Technologies on Train Operation Safety (dot.gov)

Transportation Safety Board of Canada. (1994). A special study of main track derailments. Railway Safety Issues Investigation Report SR9401 - Transportation Safety Board of Canada (tsb.gc.ca).

Transport Canada. (2014). Railway Freight Car Inspection & Safety Rules. Accessed October 01, 2022, from Railway Freight Car Inspection & Safety Rules (canada.ca)

Wabtec. (2023). KinetiX Inspection Technologies Overview. Retrieved January 10, 2024, from kinetix-inspection-technologies-overview (wabteccorp.com).

Canadian & Cold Regions
Rail Research Conference
2024

Machine vision to inspect and analyze track condition: An opportunity to perform predictive maintenance on rail joints

Luc Faucher, Tony Ducheman, Mathieu Cody, Dave Arsenault, Simon-Olivier Vaillancourt, & Guillaume Servat
CEFRAIL Research Centre, Sept-Iles, Quebec, Canada

David Hébert
ArcelorMittal, Port-Cartier, Quebec, Canada

Dominique Sirois
Rio Tinto – IOC – QNS&L, Sept-Iles, Quebec, Canada

ABSTRACT

Pairing 3D scanning with artificial intelligence is steadily developing in the industrial sector. Combining both technologies has the advantage to scan and analyze the condition of complex components at a pace that is much higher than that of a human inspection. Machine vision makes it possible to identify defects that would not have been noticed otherwise. Several challenges arise when it comes to implementing this strategy to track analysis and maintenance. The data throughput produced is considerably voluminous. A 3D scan width of 11.2 feet at a 1 mm resolution produces folders of over 2.7 GB per mile. Different strategies must be put in place to acquire, transfer, process and analyze this data. Our group research aims at developing software to answer these needs while scanning hundreds of miles. So far, results include dashboards to visualize and take decisions about rail joints and ties. For a 260-mile-long track, the information is available in less than 36 hours. Eight surveys were carried out between September 2021 and June 2023. Depending on the time of the year, the partners of this project were able to localize as much as 3 322 joints, identify 90 joints with a gap over ¾ of an inch, 29 joints with missing bolts, 2 706 joints that could be welded, and the assets with the highest poor tie ratio. It has already been demonstrated that this data representation helps railway management to prioritize corrective maintenance. This includes the location and fixation of angle bars with missing bolts, joints with large gaps; and the planification of rail welding and tie changing operations. The actual study focuses on the possibility to perform predictive maintenance on joints with the cumulation and comparison of data through time. It discusses the observations made to date and different factors to take into consideration.

1 INTRODUCTION

Machine vision is constantly evolving in the industrial sector. This strategic approach combines imaging, autonomous analysis of objects or working environment, and extraction of valuable data. Data in general have taken a prominent role nowadays and are now considered a new class of economic assets (Tavera Romero, 2021). Value is created when paired with business intelligence, which leads to the improvement of processes and safety.

The way of seeing maintenance in the railway industry has changed and will continue to change with the implementation of these concepts. There are already a few technologies on the market. Some are used to analyze train cars and locomotives through inspection portals, and other are dedicated to the maintenance-of-way. This research aims at developing processes and software to facilitate the use of machine vision in the daily inspection of hundred miles of track. In this study, the Laser Rail Inspection System (LR*A*I*L*) was used to scan tracks on 11.2 feet wide at a surface resolution of 1 mm x 2 mm x 0.1 mm. The LR*A*I*L* can autonomously evaluates the status of a dozen component of the track (Fox-Ivey, 2020, 2020b; Faucher, 2021, 2023; Harrington, 2022; Edwards, 2023).

There are several challenges in using machine vision for track inspection. First, a high-resolution 3D scan of the track leads to a voluminous collection of data. Every mile of track produced folders over 2.7 GB. Different strategies must be put in place to acquire, transfer, process and analyze this volume of data. The second challenge is the way to present the results. It must be intuitive and easy to use. Only the data with added value must be presented. Some information is valuable individually, while other must be aggregated to make sense. Software was developed after scans were conducted on the tracks of ArcelorMittal and QNS&L in

northern Québec. They are approximatively 260 mile long each. The companies operate heavy-haul trains at temperature peaks varying from -60°C to 30°C between winter and summer. The rail temperature can also rise of fall by more than 25°C between days and nights of spring and autumn. This type of operation leads to important strains in the railway track and infrastructure. There is a high level of interest in studying these two tracks. The major stresses on the infrastructure, with the heaviness of load carried and multiple freeze-thaw cycles, impose perceptible changes between each scan. Eight complete surveys of these tracks were carried out between September 2021 and June 2023.

After the surveys, the information regarding joints and ties were gathered in a web-based application. These components were first prioritized for many reasons. During heavy-haul operations, angle bars face various strains coming from the heavy loads and the dilation of rails. The system is designed to absorb these constraints, but the constant emergence of new defects in the infrastructure weakens the joints. The rail must remain well seated on the plates, the ties and the ballast must be of good quality, the anchorage must be appropriate, etc. The global state of the railway ties is another major point of interest for railroads. For more than twenty years in Canada, the two main causes of declared derailments are either due to the geometry of the track or the breakage of the rail and its welds (Transportation Safety Board of Canada, 2023). The presence of several consecutive bad ties has an impact on rail geometry and the stability of the infrastructure.

Depending on the time of year, the partners of this project were able to localize as much as 3 322 joints, identify 90 joints with a gap over 3/4 of an inch, 29 joints with missing bolts, 2 706 joints that could be welded, and the assets with the highest poor tie ratio (Faucher, 2023). As seen in a previous study, this data representation helps railway managements prioritize corrective maintenance to locate and fix angle bars with missing bolts or joints with larger gaps; and to plan maintenance for rail welding and tie changing operations. These results also contributed to quickly act in hazardous places before winter while providing a global view of each asset. The actual study focuses on the possibility to perform predictive maintenance with the cumulation and comparison of data through time.

2 MATERIALS AND METHODS

2.1 The tracks

The first railway line used for this study is the one operated by ArcelorMittal in northern Québec, Canada. It has a length of 259 miles, has approximately half of its composition made up of curves. It is a Class 3 mainly used to carry over 26 million tons of concentrated iron ore every year from the Mont-Wright mine to the port of Port-Cartier. The northern part of the track, a 30-mile section, has a high level of traffic. It is also used to carry 16 million tons of ROM from Fire Lake to Mont-Wright annually, implying the transport of 80 MGT every year on this section. The track is made of continuous welded rail (CWR) and rail grading is 136 lbs. Most of the angle bars have a length of 36 inches and are fixed with 6 bolts for permanent joints, and with 4 bolts for temporary joints that still can be welded. Five surveys were conducted on the entirety of the main line during the months of September 2021, June 2022, September 2022, October 2022 and June 2023. At these times of the year, both temporary and permanent joints are present on the track.

The second railway line is owned by QNS&L. It is also located in northern Québec, Canada. It has a length of 260 miles and is composed of approximately 45% of curves. It is a Class 3 mainly used to carry over 41 million tons of concentrated iron ore every year. Over 63 MGT were transported on the track in 2022. An increase in volume is expected for the coming years. The track is made of continuous welded rail (CWR) and rail grading is 136 lbs. The length of angle bars is majorly 36 inches and they are usually fixed with 4 or 6 bolts. Three surveys were conducted throughout all the main line during the months of September 2021, August 2022 and November 2022.

Both railways have divided the track in four sections that are visually inspected twice a week. All joints are visually inspected twice a year.

2.2 The inspection system

The technology used for this study is the LRAIL system developed by Pavemetrics/Railmetrics. For this study, the system was operated on a road-rail vehicle at an inspection speed of 40 mph (Figure 1). The resolution of the scan was of 1 mm in X, 2 mm in Y and 0.1 mm in depth (Z). The 3D lines were merged into 2 m x 3.6 m images. For a track of 260 miles, this represents over 209 000 images. An inertial navigation system integrates the picture's latitude, longitude, and elevation into each 3D profile. After the survey, the images were analyzed by a trained Deep Convolutional Neural Network (DCNN) with the 4.82.2.0 version of the library. With artificial intelligence algorithms, the system has detected, evaluated, and located over twelve different types of components. For this study, the processed results for joints and ties were extracted from XML files and put into a database. Different 2D representations of the 3D images were also made available. A human has confirmed the initial results obtained for bolt count. The accuracy of the DCNN was between 96.5% and 98.7% for joints. The count includes insulated joints. A study evaluating the accuracy for tie inspection is currently underway.

Figure 1. The LRAIL system used in this study.

3 RESULTS AND DISUSSION

3.1 Characteristics of the software

Software including business intelligence (BI) principles are efficient to turn big data into decision-making. It has been demonstrated that this type of tool leads to a competitive advantage. BI provides analytical data insights regarding systems. It helps managers process performance optimization (Ahmad, 2020). Several particularities define a good BI software. It must be composed of key performance indicators (KPI) that can easily be turned into actions.

To efficiently see the status of joints with machine vision, a first dashboard was designed to provide a global view (Figure 2). It is composed of many features. The first one is a roadmap georeferencing every joint on the track. This roadmap is linked to a table showing the characteristics of each joint: its milepost, the joint gap, the number of bolts, the length of the angle bars, the side of rail where the joint is, the outside temperature, and the GPS coordinates. Filters can be applied to dynamically modify the content of the roadmap and the table. The filtering component provides filtering based on the milepost, the joint gap, the number of bolts, the length of the angle bars, the side of the rail and the unique identification number of the joint. The dashboard also shows the total count of joints and the number of joints that are displayed after the filters have been applied. The table can be downloaded at any time in a CSV file. Another feature of the dashboard is an image of the selected joint, as seen by the inspection vehicle. This image can be enlarged in another window. The image viewer module allows selecting the number of images that the user wants to see before and after the image of interest. The contrast of images can also be changed to better see a specific component. Indeed, images can be represented in a 3D-like manner, or with a contrast that is focused on the depth of the different surface components (by range), or on how much of the laser beam is reflected to the camera after hitting the inspected surface (by intensity). A layer with the system interpretation can also be added on the images. Finally, different charts are used to display the information.

3.2 Predictive maintenance for joints

Angle bars bind two rail ends, and this type of joint faces various strains. When it is not supported well, it becomes a weak link that might break through time. Machine vision offers an opportunity to analyze and compare the data collected during different surveys, and to pinpoint elements of risk. Since similar situations can be pointed out, predictive maintenance can prevent dangerous situations and derailments.

This study focuses on the comparison of results obtained amongst all surveys carried out at ArcelorMittal between September 2021 and June 2023, and the elements that could explain joint defects. During the five surveys, there were 79 occurrences where a bolt was missing on a joint. However, these occurrences were only at 49 different locations. This mean that some joints with missing bolts were either not found between two surveys, not corrected and then found again by the system, or that the bolts were added, but broke shortly afterwards. A closer look at the result showed that the second hypothesis is as valuable as the first one. Indeed, some joints were seen with a missing bolt during a survey, then showed as corrected during the subsequent one, and they were missing a bolt again a few months later. The joint on Figure 3 is a good representation of this situation. It had a different status for every survey, going from missing bolt to corrected and vice-versa each time. The broken bolt even appears on September 2022 survey.

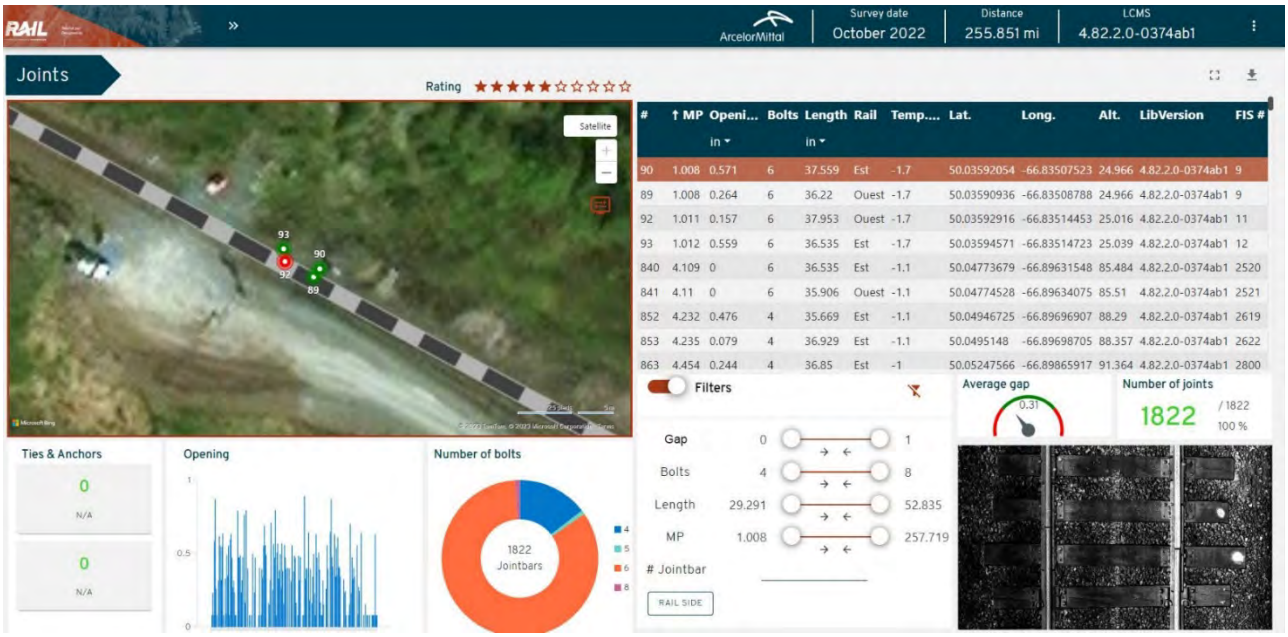

Figure 2. Dashboard for joint analysis

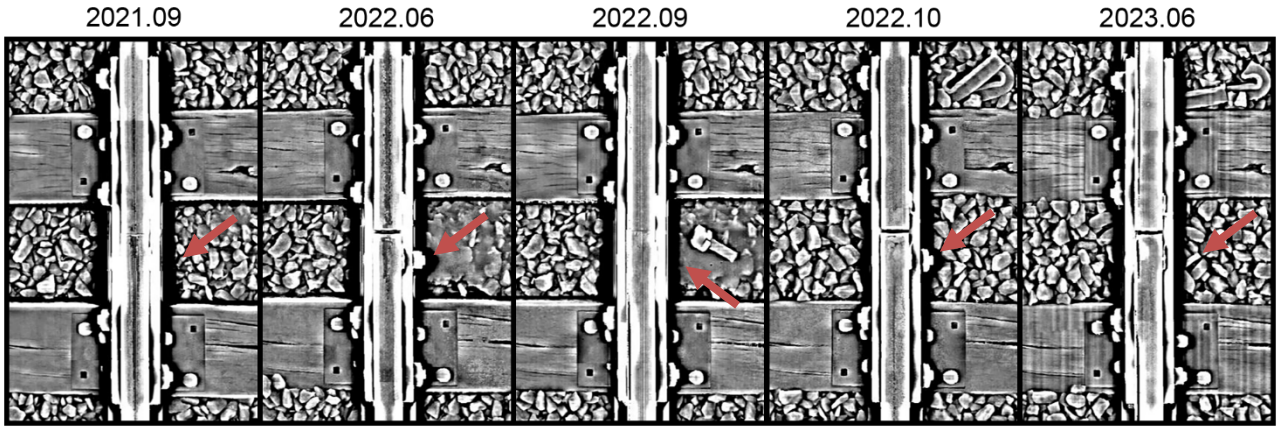

Figure 3. The evolution of a joint between September 2021 and June 2023. One can see that (A) a bolt was missing in September 2021. A bolt was (B) added before June 2022, then (C) was broken again in September 2022, (D) repaired another time before October 2022 and (E) finally broken in June 2023.

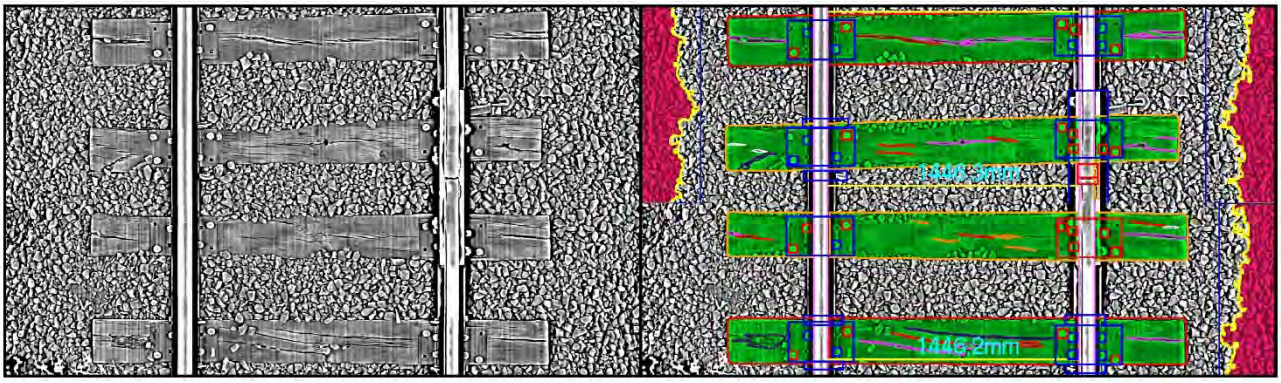

Figure 4. The image analyzed with machine vision shows the many defects around the joint. (A) The tie plates are sunken and all the spikes are lifted, (B) the joint rests on bad ties, and is also preceded and followed by a bad tie, (C) there is insufficient ballast in the shoulders, and (D) rail anchors are still installed in front of the joint.

There are many different parameters that can explain why a bolt would constantly break at a joint. As seen on Figure 4, machine vision has detected many of them. These parameters either allow the joint to move a lot during train movements or prevent the rest of the infrastructure from absorbing any bumps, so that all the impact is concentrated on the joint itself which is the only flexible part of the structure. The first element seen with machine vision is the fact that the tie plates are sunken, and all the spikes are lifted. The joint also lays on bad ties, and it is preceded and followed by a bad tie. There is also deficient ballast in the shoulders, and the rail anchors are still installed in the front of the joint. These are a some of the criteria to look at to properly assess joint condition. One could also add the variation of joint gaps through time, ballast fouling, rail surface damages, height and alignment mismatch at the joint, etc. as part of the assessment.

4 CONCLUSIONS

Machine vision is becoming a well-established tool to pinpoint where the joints are and their status. Indeed, visual inspections usually leave between 0.4% to 1.1% of joints with a missing bolt behind (Faucher, 2023). This study showed the potential to perform predictive maintenance on joints. By compiling the different information obtained with machine vision, the level of risk of a joint could be identified.

The next step of this project will be to establish all the parameters that could impact joint stability and rate the risk of failure of every joints. This will be a good indication of where the MOW team should focus its work. Before an angle bar breaks, the joint often loses a bolt. This first stage before an angle bar break is a good indicator to define where joints are already surrounded by bad conditions. Machine vision helps to better localize these joints and makes it easier to compile and compare data.

5 ACKNOWLEDGEMENT

This study was financed by NSERC, Transport Canada, ArcelorMittal, Rio Tinto – IOC – QNS&L and the Government of Québec. The authors would like to thank Marie-Chantale Genest, Yoland Gallant, Ghislain Boisvert, Magali Jarry, Pascal Ramdane and Emile Néron for their contribution. The authors would also like to thank Benoit Petitclerc, Richard Fox-Ivey,

John Laurent, Thanh Nguyen, Mario Talbot and Martin Dubé at Pavemetrics/Railmetrics.

REFERENCES

Ahmad, S. et al. 2020. Modeling of Business Intelligence systems using the potential determinants and theories with the lens of individual, technological, organizational, and environmental contexts-a systematic literature review. Appl. Sci. 10(9), 3208-3231

Edwards, J.R. et al. (2023) Leveraging 3D laser scanning data for track condition change detection. Proceedings of the International Heavy Haul Association Conference. 455-462

Faucher, L. et al. (2021) Assessment of the LRAIL system to detect and analyze the condition of angle bars on a 260-mile railroad. Proceedings of the Canadian and Cold Regions Rail Research Conference. 206-210

Faucher, L. et al. (2023) Big data straight from the track inspection technologies: seeing clearly. Proceedings of the International Heavy Haul Association Conference. 491-496

Fox-Ivey, R., Nguyen T., Laurent, J. (2020) Laser Triangulation for Track Change and Defect Detection. Report to the Federal Railroad Administration. Washington, DC. USA

Fox-Ivey, R., Nguyen T., Laurent, J. (2020) Extended Field Trials for LRAIL for Automated Track Change Detection. Report to the Federal Railroad Administration. Washington, DC. USA

Harrington, R. et al. (2022) Use of Deep Convolutional Neural Network (DCNNs) and Change Detection Technology for Railway Track Inspections. Proceedings of the Institution of Mechanical Engineers, Part F: Journal of Rail Rapid Transit. 1-9

Tavera Romero, C.A. et al. (2021) Business Intelligence: Business Evolution after Industry 4.0. Sustainability 13(18): 10026-10037.

Transportation Safety Board of Canada. Rail Transportation occurrences in 2021. Accessed April 14, 2023, from http://www.bst-tsb.gc.ca/fra/stats/rail/2021/sser-ssro-2021.html
.

Canadian & Cold Regions
Rail Research Conference
2024

The effect of brake pipe flow on brake cylinder pressure

Yi Wang
MxV Rail, Pueblo, CO, United States

ABSTRACT

Railways have battled the adverse effects of increased brake pipe (BP) leakage during winter operations since the early days. Canadian Railways have played a key role in developing the Air Flow Method in the initial terminal brake tests used today in Canada and the United States. Cold weather often leads to higher leakage from the BP and could prevent trains from meeting the brake test requirements for departure. The relationship between BP leakage, flow, and gradient has been extensively studied by conducting physical tests with induced leakage over the years. Still, large-scale trials of this kind remain impractical. A better understanding of BP leakage, flow, and gradient enhances the railways' ability to improve reliability and safety, especially in winter. To help gain a further understanding of the brake system, a feature to simulate concentrated BP leakage on user-selected cars has been implemented in Train Operations and Energy Simulator (TOES™). Simulations are performed to explore the effects of various leakage conditions from the BP and their effect on the functioning of the brake system. The number and size of the leakages and their locations were generated pseudo-randomly and applied to four 200-car trains of different locomotive configurations. The simulation results and observations are examined and compared against current testing requirements and could help identify requirements for physical validations.

1 INTRODUCTION

The No.1 and Class 1 brake tests are required for all trains departing from the initial terminal in Canada and the United States (U.S.). The check for brake pipe leakage is integral to the Class 1 and No. 1 brake tests. The leakage check can be conducted using either the traditional leakage method or the newer air flow method (AFM) test. Currently, the AFM test requires the train to have no fewer than 75 psi at the lowest point of the BP. For trains with a single locomotive consist, the maximum BP flow is not to exceed 60 standard cubic feet per minute (scfm); for trains with two or more locomotive consists, the maximum BP flow must not exceed 90 scfm.

Canadian railways first tested the AFM method over ten years between the 1970s and 1980s (Harubin, 1986). After completion of the tests, the railways formally proposed adopting the AFM method as an improved alternative to the then-existing leakage test. Canadian Pacific did further testing after the wide adoption of distributed power (DP), which increased the number of air sources on the train. The studies paved the way to increase the total allowable flow from 60 to 90 scfm for the No.1 and Class 1 brake tests (Aronian et al., 2013).

Leakages in the brake system are usually attributed to degradation in rubber gaskets. Coupled with shrinkage in other components, causing the loss of compressive forces on the gaskets, brake system leakage can increase significantly in cold temperatures. Higher BP flow due to leakage is one of the significant challenges in railway winter operations and is the primary reason for cold temperature-based train length restrictions. The brake system is essential for train safety. It is important to understand the effects of BP flow on the brake system's performance.

The BP leakage and flow have been studied since the early days of railroading, and rules of thumb have been developed over time. It is generally understood that the additional pressure drop due to a longer BP under the same flow conditions will result in a higher gradient. Currently, there is no established method to accurately predict the relationship between the two quantities (Hart, 1987; Miles, 1925). The development of the Train Operations and Energy Simulator (TOES™) enabled the modelling of the brake system's behavioural changes under operational conditions. However, the implementation of leakage simulation was limited to one uniform leakage on every vehicle on the train. The implementation of concentrated leakage modelling has now provided more opportunities to study and validate brake system behaviours when different leakage conditions on the train are considered.

2 AAR PNEUMATIC BRAKE SYSTEM

The pneumatic brake systems in North American interchange service are designed according to the Association of American Railroads (AAR) Standard S-401. The brake pipe, the only pneumatic connection between the locomotives and all cars on the train, supplies the air to the individual brake systems and transmits the application and release signal. A simplified

diagram depicting the essential components is shown in Figure 1.

The control valve on each car reacts to the pressure change in the BP and controls the brake application and release through the pressure equalization between volumes within the brake system.

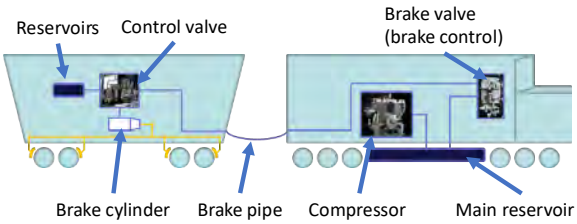

Figure 1. Simplified diagram of the pneumatic brake system.

When fully charged, the volumes in the car brake system equalize at the local brake pipe pressure, which is commonly set at 90 psi, and the brake cylinder pressure (BCP) is zero. Maximum BCP is attained in an emergency brake application, where both the auxiliary and emergency reservoirs on the car are connected to the brake cylinder to allow for equalization. Illustrations of pressure relationships in a car brake system are shown in Figure 2. In this figure, darker shaded volumes represent higher pressure. Bolded passages indicate airflow, and double-ended arrows indicate pressure equalization.

Under ideal working conditions, where there is no unwanted airflow between the volumes or the ambient, the BP flow is at zero, and the pressure at each control valve is equal to the locomotive feed valve setting (the maximum supply pressure). However, this is often not the case. Leakages occur, which induce airflow in the BP even while the system is fully charged. In this paper, the term flow refers to the induced flow at a fully charged state and not during the transient stages of normal brake system functions. The flow also causes a pressure difference in the BP, where the maximum attainable pressure is lower at control valves further away from the charging source or closer to the leakage source. This difference between the lowest and the highest pressure in the BP in the fully charged state is called gradient.

If the BP leakage condition is mild enough for the brake system to maintain the maximum BP pressure on all cars, the equalization BCP would not be affected. However, suppose BP leakage is severe enough to cause a gradient, i.e., there is a difference in the maximum attainable BP pressure on different cars throughout the train. In that case, the cars with lower attainable maximum BP pressure will have a lower equalization BCP. While BCP is not directly sensitive to BP flow, trains with higher gradients caused by BP leakage would exhibit steady-state BP flow and produce a lower average equalization BCP and, therefore, lower overall braking force.

3 SIMULATIONS

TOES™ is a longitudinal train dynamics (LTD) simulator that has been used for over 30 years. It is currently developed and maintained by MxV Rail. TOES has been validated many times by both laboratory testing and in revenue service (*Railway Age*, 1991; *Railway Age (Bristol)*, 1989). It is considered an industry standard for train dynamics modelling.

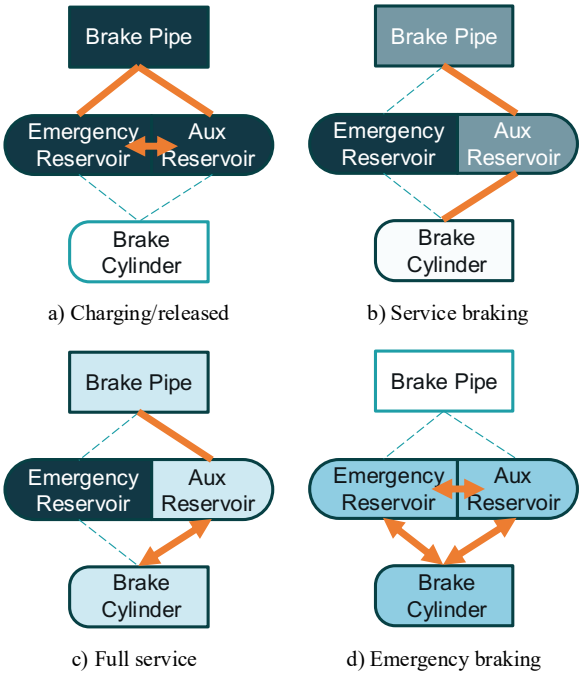

Figure 2. Pressure relationships in a car's brake system.

3.1 Brake System Modelling in TOES

One of the most important aspects of brake system modelling in the single-pipe brake system of freight trains is modelling flow and pressure in the BP. TOES models the brake pipe as a one-dimensional flow. The pressure and velocity of the flow along the BP are obtained by discretizing the following continuity and momentum equations and solving them numerically (Johnson et al., 1986).

$$\frac{\partial \rho}{\partial t} + \frac{\partial (\rho u)}{\partial x} + L = 0 \quad (1)$$

$$\frac{\partial (\rho u)}{\partial t} + \frac{\partial (\rho u^2)}{\partial x} + \frac{\partial p}{\partial x} + F = 0 \quad (2)$$

In the above equations, ρ and p denote the density and pressure of the air, respectively, t denotes time, u and x denote the velocity and displacement of the flow along the BP, L denotes the leakage per unit length of the BP, and F denotes the pipe frictional force resisting the airflow.

The behaviours of the car's brake system components are modelled by connecting up to three volumes by orifices, as illustrated in Figure 3.

In the figure above, the dashed components are optional, depending on the feature being modelled. P_i and V_i denote the pressure and volume of volume i, respectively. F_{ij} denotes the mass flow rate of air from volume i to volume j. C_{ji} denotes the sonic conductance between reservoirs i and j. Analogous to electrical conductance, the sonic conductance quantifies the maximum flow rate an orifice could allow.

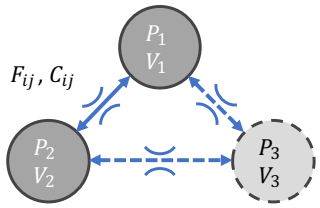

Figure 3. Modelling of volumes in TOES.

3.2 Simulations with Brake Pipe Leakages

Four train consists, each having 200 cars with identical BP lengths, were simulated. A pseudo-random generator was used to generate simulation scenarios where the number, magnitude, and locations of the brake pipe leakages were varied.

All train consists in the simulation contain identical cars, each having a BP length of approximately 63 ft. The locomotive is a standard 6-axle AC locomotive model in TOES. The leakages can be specified using the newly implemented TOES keyword LEAKAGE CONLEAK.

Table 1. BP leakage simulations after filtering by maximum flow at a single locomotive.

Simulation Consist	Shorthand notation	Simulation Count
Loco + 200 cars	L200	1122
Loco + 200 cars + rear DPU	L200L	1467
Loco + 133 cars + mid-DPU + 67 cars	L133L67	1392
Loco + 100 cars + mid-DPU + 100 cars + rear-DPU	L100L100L	1467

Since it is difficult to estimate the flow and leakage values without doing the simulations, it was decided that all combinations of the following factors would be generated and simulated, and then only the ones within a maximum acceptable flow boundary would be retained for analysis:

- Number of cars with BP leakage,
- Positions of the leaking cars,
- Magnitudes of the leakages.

An internal development version of TOES was used to perform the simulations, allowing for the refinement of the parameters within the TOES fluid dynamics model compared to the publicly released version. Field-measured data were used to validate the initial parameters of each consist at the nominal 60-scfm total flow states. For each simulation, the brake system was initialized by using an emergency application and then charging the brake system to a steady state for 3 hours of simulation time. The single locomotive flow values are taken directly from the initialization outputs at the end, and the total is the sum of all the flows from all locomotives. The gradient was calculated using the lowest BP pressure on the train, regardless of the vehicle position. The distributions of the steady-state gradients and brake pipe flow are shown in Figure 5.

After initialization, brakes were applied by reducing the BP by 6, 10, 15, and 26 psi with a release between the 10 and 15 psi reductions. Finally, the train was placed in an emergency application after being released from the 26-psi reduction. The time history of BP reductions is shown in Figure 4.

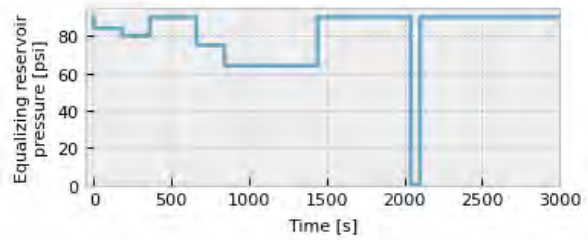

Figure 4. Time history of the brake commands issued in simulations.

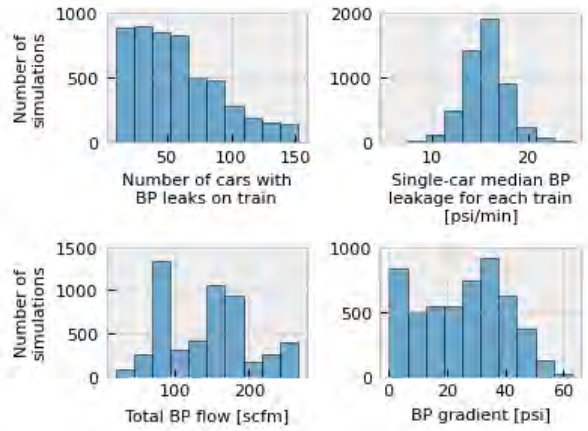

Figure 5. Distributions of the number of BP leaks, median BP leaks, total BP flow, and BP gradients in simulations.

Only those completed simulations having less than 90 scfm flow at any locomotive were selected. Table 1 shows the number of selected and analyzed simulations for each train consist. The distributions of the number and magnitude of leakages are shown in Figure 5.

For reference, uniform leakage conditions (i.e., the same amount of leakage applied to every car) producing comparable flow and gradient conditions were also simulated.

4 RESULTS

The simulations produced a significant amount of data. The results presented in this section focus solely on the BP leakage-induced flows and their effect on BCP as a proxy of overall brake force.

The relationships between BP flow and gradient from the simulation results are shown in Figure 6 and Figure 7. To allow for easier visual comparison, both the x and y-axes in each figure are on the same scale.

Figure 8 and Figure 9 show the average BCP from each brake application and simulation plotted against the total BP flow and the maximum BP flow at a single locomotive, respectively. The gray markers in these figures were the reference values when the same flow conditions were reached using a uniform leakage amount from every car on the train.

Figure 10 and Figure 11 show the percentage of cars with no effective BCP plotted against the total BP flow and the maximum flow at a single locomotive, respectively.

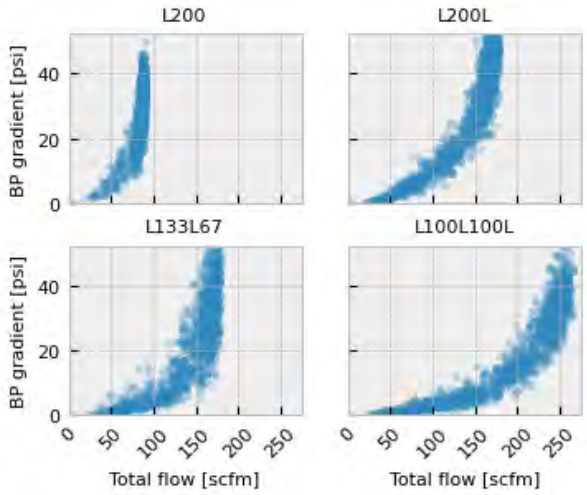

Figure 6. BP gradients plotted against total BP flow.

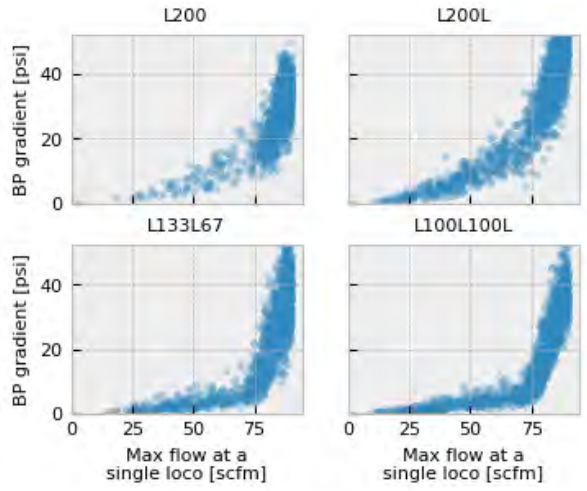

Figure 7. BP gradients plotted against maximum BP flow at a single locomotive.

5 DISCUSSIONS

The magnitude of the BP gradient depends on multiple factors, including the magnitude and location of the leakages and the overall BP length between air sources. Figure 6 shows that it takes more BP flow, in terms of leakage, for a train with a shorter BP length between locomotives to produce the same gradient as a train with a longer BP length between locomotives. The plots become more similar when the gradient is expressed as a function of the maximum BP flow at a single locomotive (Figure 7).

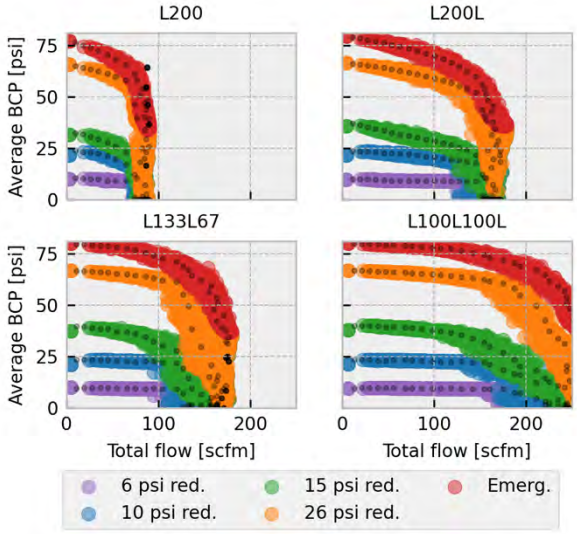

Figure 8. Average BCP plotted against maximum total BP flow. Gray markers inside coloured markers are reference values from simulations using uniform BP leakage.

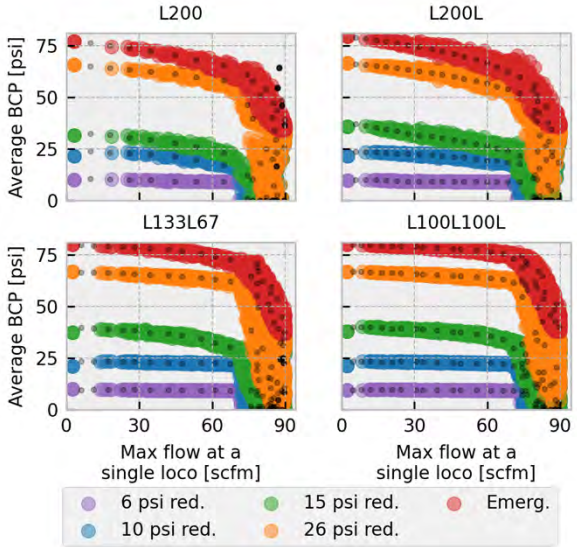

Figure 9. Average BCP plotted against maximum BP flow at a single locomotive. Gray markers inside coloured markers are reference values from simulations using uniform BP leakage.

The increase in BP gradient follows a similar pattern for a) the two consists with a longer BP length between locomotives (L200 and L200L), and b) the two consists with a shorter BP length between locomotives (L133L67 and L100L100L). In case a), the gradient more closely resembled an exponential increase, where higher flows result in larger increases in gradient. For b), there appears to be a clear inflection point at 75 scfm per locomotive, where the gradient starts to increase significantly, potentially indicating a physical limitation for the air sources to maintain BPP. In all cases, the gradients in b) remain relatively low compared to a) until the inflection point. At higher flows that result in higher gradients, the local car BPP at the bottom of the gradient is lower even at a fully charged state, resulting in a lower equalization pressure.

When plotted against the BP flow, as shown in Figure 8 and Figure 9, the average BCP is more sensitive to the maximum flow in a deeper reduction compared to a lighter reduction. As shown in the figures, the average BCP for trains with more locomotive consists is higher than the average BCP for trains with fewer locomotive consists, especially at higher BP flows. Consist L133L67 appeared to have produced higher average BCP than Consist L200L at higher maximum BP flows, potentially because the longest distance to travel from any car to an air source was 67 cars on L133L67 as opposed to 100 cars on L200L. Since pressure drop is a function of pipe length, given the same leakage, a shorter brake pipe would produce a smaller gradient and higher BC pressures.

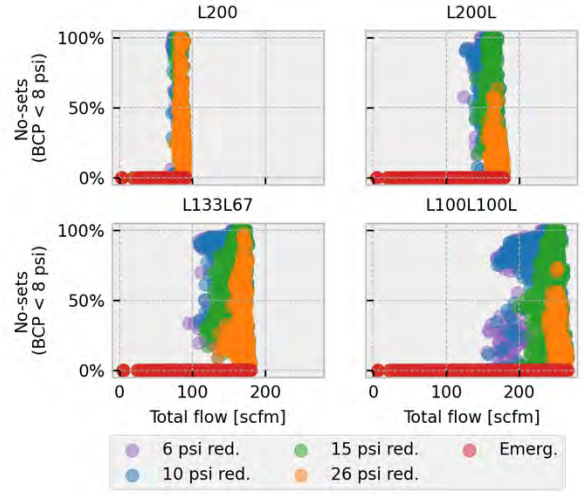

Figure 10. The percentage of no-sets (BCP < 8 psi) plotted against maximum total BP flow.

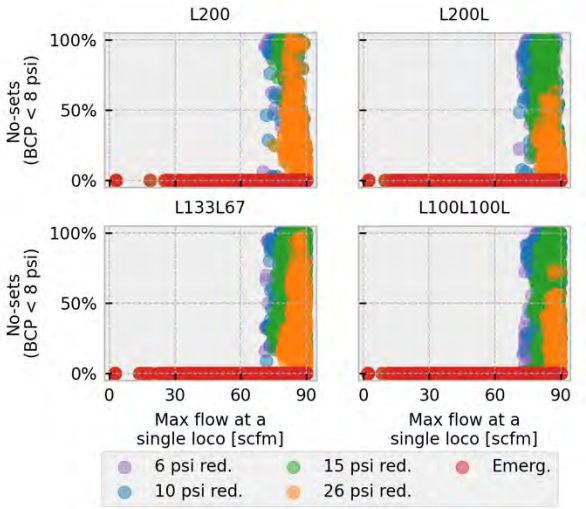

Figure 11. The percentage of no-sets (BCP < 8 psi) plotted against maximum BP flow at a single locomotive.

The gray markers in Figure 8 and Figure 9 represent the average BCP if the leakage conditions were produced by a train with uniform leakage from every car. These BCP are close to the average conditions of the concentrated leakage simulations. There appear to be more outliers at high flows, and they are potential indications of numerical instability and limitations in the current ability of TOES to perform calculations accurately in the most extreme cases.

A minimum BP reduction must achieve a BCP of 8 to 12 psi according to AAR Standard S-461. Therefore, the cars that produced less than 8 psi BCP were considered no-sets. The percentage of no-sets from the simulations was plotted against BP flows and are shown in Figure 10 and Figure 11. The minimum required BCP of 8 psi was achieved until the leakages produced very high BP flows. If the total BP flow was plotted, all cars would produce at least the BCP required for a minimum reduction up to flow levels currently allowed by rule, i.e., up to 90 scfm. Regardless of the BP leakage, all car brakes applied in emergency applications. The number of no-sets did not significantly increase until the flow exceeded 60 scfm at any locomotive consist. Above an approximate 70 scfm per air source, there is a risk for an indeterminate percent of no-sets for all reductions (except emergency), with more risk for the lower reductions.

Figure 9 and Figure 11 showed that the maximum BP flow at a single locomotive appeared to correlate well with the overall BCP. The results do not suggest the possibility of an increase in the current flow limit of 60 scfm at any locomotive consist without leaving some margin for performance variations in the brake system. On the other hand, Figure 8 and Figure 10Figure 9 showed a more considerable difference BCP in terms of the total BP flow, depending on the configuration of the train. Trains with a shorter BP length per air source had an advantage over those with a longer BP length and could develop more BCP despite leakage. For example, the average BCP for the for L100L100L consist at 100 scfm total flow is comparable to the average BCP for the L200L consist at 50 scfm total flow.

Under current operating scenarios, the true gradient on a DP train, especially under high leakage, is unknown. Since long BP distances combined with heavy BP flow rates could lead to large gradients and brake performance degradation, consideration should be given to the maximum distance between any car on a train and the nearest air source if a train struggles to maintain the maximum allowable gradient when the maximum flow at any locomotive consist is 60 scfm.

While the simulation results presented clear trends relating the average BCP to flow, testing has shown more nuance and additional complications. Operational issues, such as the functionality of backup safety systems for DP, also need to be taken into consideration (Aronian et al., 2011). Furthermore, the accuracy of TOES at extreme flow and leakage rates has not yet been validated by physical testing.

6 CONCLUSIONS

TOES simulations using pseudo-randomly generated concentrated BP leakages have shown that the flow limit of 60 scfm at a single air source is a good indicator of the train's ability to produce adequate BCP. Although physical validations should be performed, there is potential for the total allowable leakage to increase based on the number of air sources and the BP length between them while maintaining an adequate level of average BCP on the train.

7 ACKNOWLEDGEMENT

The work presented in this paper was completed as part of the AAR Strategic Research Initiative (SRI) program. The author would like to express appreciation for the AAR Member Railroads for their continued support of the SRI programs.

REFERENCES

Aronian A, Wachs K, Bell S, et al. (2011) Long train testing and validation at Canadian Pacific. In: *International Heavy Haul Conference*, Calgary, AB, 2011.

Aronian A, Wachs K, Jamieson M, et al. (2013) Testing and validation of long trains under high flow and gradient conditions. In: *2012 Joint Rail Conference*, 18 July 2013, pp. 183–193. American Society of Mechanical Engineers Digital Collection. Available at: https://dx.doi.org/10.1115/JRC2012-74036 (accessed 8 September 2023).

Hart JE (1987) Brake pipe leakage, air flow & gradient in freight trains. In: *Proceedings of the 79th annual convention and technical conference of the Air Brake Association*, Chicago, IL, 13 September 1987, pp. 207–224.

Harubin H (1986) AFM: development of an alternative method for testing trains. In: *Proceedings of the 78th annual convention and technical conference of the Air Brake Association*, Chicago, IL, 21 September 1986, pp. 149–157.

Johnson MR, Booth GF and Mattoon DW (1986) *Development of practical techniques for the simulation of train air brake operation*. ASME Winter Annual Meeting Report 86-WA/RT-4, 7 December. Anaheim, California, USA: The American Association of Mechanical Engineers.

Miles CB (1925) Air Brake Association committee on brake pipe leakage. In: *Proceedings of the 32nd annual convention of the Air Brake Association*, Los Angeles, CA, 26 May 1925, pp. 135–166.

Railway Age (1991) Train Operation and Energy Simulator (TOES) validation, evaluation. 1 September.

Railway Age (Bristol) (1989) Full train tests run for UDE study and for TOES validation. Bristol.

Session 4

RISK AND RELIABILITY

Canadian & Cold Regions
Rail Research Conference
2024

3D-InSAR velocity analysis: A case study of Thompson River Valley

Sohrab Sharifi, Renato Macciotta, & Michael Hendry
Department of Civil and Environmental Engineering– University of Alberta, Edmonton, Alberta, Canada

ABSTRACT

Landslides are widespread geohazards in Canada that pose a significant threat to the safe operation of the railway system. Integrating remote sensing techniques into monitoring systems offers clear advantages. Interferometric Synthetic-Aperture Radar (InSAR) is widely employed to measure ground displacements by analyzing phase shifts in microwaves emitted by orbiting satellites. InSAR, however, can only detect movements along a single geometry of its 1D line-of-sight (LOS). This paper presents an application of InSAR-driven velocity measurements to assess an at-risk railway corridor in Canada: Thompson River Valley in southeastern British Columbia. This corridor is affected by multiple slow-moving landslides, impacting both the Canadian National Railway Company (CN) and Canadian Pacific Kansas City Limited, formerly CP (CPKC). Among these landslides, the Ripley site stands out as the most extensively instrumented and is recognized by the International Consortium on Landslides. In this study, we explored two topography-inspired methods to decompose 1D LOS velocities into 3D vectors: the surface parallel flow method (SPFM) and the aspect-parallel flow method (APFM). By decomposing 1D velocities, we obtained a more intuitively understandable representation of both the magnitude and geometry of velocity vectors. These decomposed velocities were then compared against measurements from GPS units at Ripley. We mathematically analyzed the performance of each decomposition method to gain insights into their applicability for translational landslides. The results indicate that both APFM and SPFM were acceptable in interpreting the magnitude of velocities with an accuracy of 15-19 mm/yr or 18.75-23.75% of GPS values. Further, it is proved that both methods manifest LOS errors as geometrical distortions. SPFM tends to rotate vectors in the South-North direction while APFM over-steepens the vectors.

1 INTRODUCTION

The adverse combination of susceptible geology, high-ground relief and considerable precipitation have created a landslide-prone landscape in Western Canada (Bobrowsky & Dominguez 2012). The prevalence of this geohazard greatly compromises the integrity of infrastructures. Linear infrastructures face higher exposure to ground instabilities. According to a recent study, maintenance, and risk mitigation actions in Western Canada require about $28-44 million annually in the provincial transportation and railway sector (Porter et al. 2019).

In the past few decades, remote sensing monitoring means have secured a considerable share of applications in landslide risk management strategies. Interferometric synthetic-aperture radar (InSAR) is an example that uses microwaves to measure the ground displacement by gauging the phase changes between acquisitions (Figure 1). The displacement can be back-calculated using Equation 1 upon screening out the unwanted layers (e.g., atmospheric perturbations or orbital errors):

$$d_{LOS}=\Delta\varphi\times\frac{\lambda}{4\pi}, \quad [1]$$

where d_{LOS} is the InSAR-displacements, λ is wavelength and varies depending on the sensor (e.g., 5.4 cm for C-band sensors such as European Sentinel-1 or Canadian Radarsat-2).

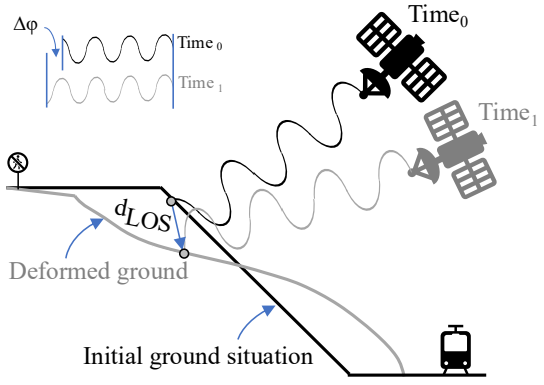

Figure 1. Displacement monitoring mechanism by InSAR using micro-wave phase difference between acquisitions

Contrary to its counterparts working in visual range, SAR technology is advantageous given its applicability in overcast/stormy days. Lower associated costs relative

to in-situ means of monitoring and large coverage extents (>1000 km^2) are also other benefits. InSAR, however, is an imperfect technique with a crucial limitation. Its sensor is only sighted to the activities along its line-of-sight (LOS). This completely obscures the true direction of velocities, homogenizing the aspect and travel angle of all velocities into what LOS dictates. The magnitudes are also abated given that the LOS velocity (V_{LOS}) is the projection of true velocity on LOS. The InSAR analysis outcome, V_{LOS}, is then a convoluted product of the magnitude and the geometry of velocity vectors that complicate setting the alarm thresholds incorporated in the monitoring systems (Schlögl et al. 2022, Bianchini et al. 2013). Decomposing LOS velocities into 3 dimensions has been a topic of interest for the landslide community.

LOS velocity decomposition calls for a systematic mathematical approach. The contribution of all components to the LOS velocity can be mathematically formulated using the geometry of acquisition (Figure 2). Given the relative movement between the earth and the satellite, there are times that the sensor looks at the target in the ascending orbit (orbiting from the south pole to the north pole) and other times in the descending orbit (orbiting from the north pole to the south pole). This indicates that two V_{LOS} can be determined for a target:

$$\begin{pmatrix} V_{LOS_A} \\ V_{LOS_D} \end{pmatrix} = \begin{bmatrix} \cos\theta_A & -\sin\theta_A \cos\alpha_A & \sin\theta_A \sin\alpha_A \\ \cos\theta_D & -\sin\theta_D \cos\alpha_D & \sin\theta_D \sin\alpha_D \end{bmatrix} \begin{pmatrix} V_V \\ V_{EW} \\ V_{SN} \end{pmatrix}, \quad [2]$$

where *A* and *D* subscripts denoted ascending and descending orbits respectively, α and θ are heading and incidence angle (Figure 2), and *V* and *EW* and *SN* subscripts denoted vertical, East-West and South-North directions.

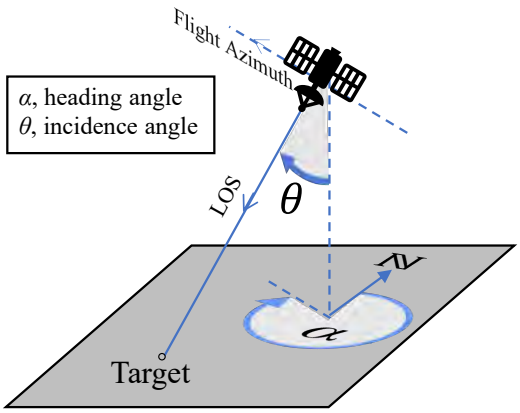

Figure 2. Geometry of acquisition

Equation 2 is a rank-deficient problem and to solve it, additional equations should be added. This has been accomplished in previous studies by assuming a relationship between different components using the ground topography. Some studies (Ren et al. 2022, Liu et al. 2021, Samsonov et al. 2020, Ao et al. 2019, Sun et al. 2016, Joughin et al. 1998) used Equation 3 so three components of the velocity follow the natural terrain:

$$V_V = i_{EW} V_{EW} + i_{SN} V_{SN}, \quad [3]$$

where i_{EW} and i_{SN} are elevation gradients in EW and SN directions, respectively. This method will be referred to as the surface-parallel flow method (SPFM). Zhu et al. (2022) and Soltanieh & Macciotta (2022a, b), on the other hand, pursued a different path and established a relationship as Equation 4 which only takes the horizontal components into account to follow the terrain aspect:

$$V_{EW} = V_{SN} \tan\beta, \quad [4]$$

where β is the terrain aspect angle. This method will be referred to as the aspect-parallel flow method (APFM).

It is reasonable to assume that each SPFM and APFM vary in interpreting the magnitude and the geometry of velocity vectors. However, there is no information regarding the advantages and disadvantages of these methods, especially in the context of the glacial morphology of Canada. The objective of this paper is to compare the performance of SPFM and APFM on the most active landslide along the Thompson River Valley: Ripley. This is achieved by analyzing a large stack of Sentinel-1 and Radarsat-2 SAR scenes.

2 STUDY AREA

The trackage of both Canadian Pacific Kansas City (CPKC) and Canadian National Railway (CN) run along the Thompson River Valley in southern British Columbia. More than a dozen slow-moving landslides traverse a segment of this valley downstream of Ashcroft. Figure 3 illustrates the location of these landslides. The strategic significance of this railway corridor in freight cargo has prompted research and practical efforts from academia, industry, and the government (Holmes et al. 2022, Huntley et al. 2022, Han et al. 2020, Bobrowsky et al. 2017, Schafer 2016, Hendry et al. 2015, Bishop et al. 2008, Eshraghian et al. 2008a, b, 2005). This corridor links the Port of Vancouver, Canada's largest, and consumers and producers throughout North America.

Some of these landslides experienced failure, a rapid downslope acceleration, such as the South slide before CPKC grade construction, Goddard in 1982, and the North Slide in 1880 (Huntley et al. 2021, Tappenden et al. 2018, Porter et al. 2002). Although risk analysis studies indicate a low risk of such events to recur, a proactive monitoring approach has been adopted to ensure the integrity of trackage and the underlying structure (Macciotta et al. 2016). Quaternary deposits compose the surficial geology in the region with strata of cobble gravel, Diamicton till, and Glaciolacustrine silt (from both late and mid-Pleistocene) overlying the Andesitic bedrock. Retrieved samples and field measurements indicate that the sub-horizontal basal shear surfaces of these landslides pass through a weak, highly plastic clay seam (residual friction angles less than 16°).

The focus of this study is on Ripley which falls close to the lower range of landslide size in the valley (0.4 to 15 × 10^6 m^3). However, due to the constant high activity state with velocities reaching 2 mm/day in the short term, it is one of the most studied and instrumented cases (Schafer 2016, Hendry et al. 2015, Macciotta et al. 2014). Ripley slide is within the CN and CPKC Directional Running Zone and, as such, a failure there would be detrimental to both Companies and to the multiple supply chains they support.

3 GPS units measure the landslide movements, and Figure 4 shows their locations and the reported average velocities from April 2008 to February 2020. Although Ripley undergoes periodic reactivation when the river elevation drops, the average velocity is well representative of the total slope's activity. The average velocity is 78-82 mm/yr as reported by GPS 1 and 2 while it rises to 117 mm/yr per GPS 3. The direction of movements in the horizontal plane (aspect angle) and the vertical plane (travel angle) is also strictly linear. The aspect and travel angles per GPS 1 and 2 are 62-66° and 14-17°, respectively. GPS 3, again, reports a more pronounced northward (56°) and a steeper direction (35°). GPS3 is installed on a retaining wall between CN and CPKC trackage and the wall's deformation seems to be affecting its results. As a result, only GPS 1 and 2 data are deemed proper representations of Ripley's kinematics and are used in this study.

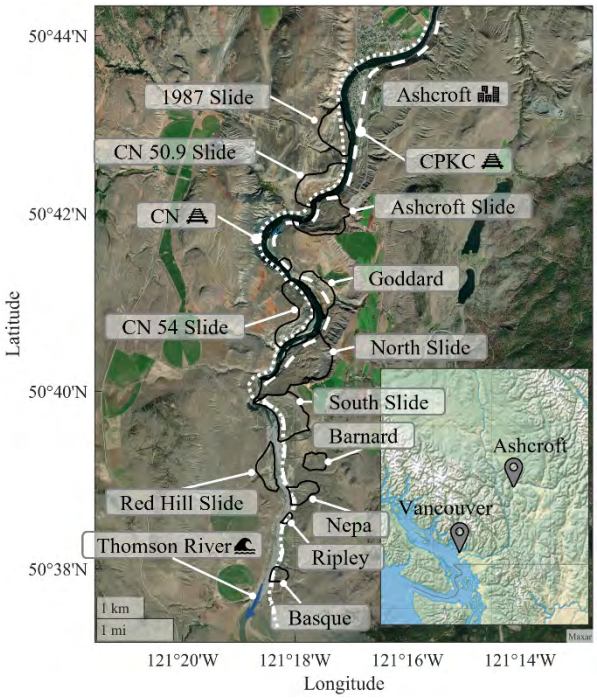

Figure 3. Daylighted boundaries of documented landslides along Thompson River Valley and CPKC and CN trackage

3 METHODOLOGY

InSAR analysis was conducted using a total of 119 Sentinel-1 scenes in the ascending orbit and 102 Radarsat-2 scenes in the descending orbit. Table 1 provides a summary of the scenes' metadata.

InSAR analysis was conducted by SARPROZ (Perissin & Wang 2011, www.sarproz.com/) using Persistent Scatter Interferometry to detect strong point-wise targets. It starts by stacking and co-registering the scenes, then, proceeds to subtract the effect of topography and atmospheric phase screening and concludes by sparse points processing. Interested readers are encouraged to refer to the following studies for further in-depth information regarding the analysis framework: Khoshlahjeh Azar et al. (2021), Tarighat et al. (2021), and Azadnejad et al. (2019). Given that Persistent Scatterer Interferometry is most reliable with the assumption of linear time-series displacement, the effect of noise filtration methods such as simple moving average was found negligible (Sharifi et al. 2022a, b, c, Sharifi et al. 2021). A line was then fitted on the displacements and the average velocities were used for LOS velocities in all the subsequent steps.

Table 1. Summary of scenes metadata

Sensor	Sentinel-1	Radarsat-2
Orbit	Ascending	Descending
No. of scenes	119	102
Revisiting time (d)	12	24
Resolution (m×m)	20×5	3×3
Heading angle (deg)	350	190
Incidence angle (deg)	40	45
Sensing Period (YYYY/MM/DD)	2016/03/09-2021/11/08	2013/11/16-2020/07/06

Having the average velocities from Sentinel-1 ascending (S1A) and Radarsat-2 descending (RS2D) scenes, the decomposition could be carried out by incorporating Equations 3 & 4 into Equation 2. Equations 5 & 6 are, respectively, mathematics of SPFM and APFM:

$$\begin{pmatrix} V_v \\ V_{ew} \\ V_{sn} \end{pmatrix} = \begin{bmatrix} \cos\theta_{S1A} & -\sin\theta_{S1A}\cos\alpha_{S1A} & \sin\theta_{S1A}\sin\alpha_{S1A} \\ \cos\theta_{RS2D} & -\sin\theta_{RS2D}\cos\alpha_{RS2D} & \sin\theta_{RS2D}\sin\alpha_{RS2D} \\ -1 & i_E & i_N \end{bmatrix}^{-1} \times \begin{pmatrix} V_{S1A} \\ V_{RS2D} \\ 0 \end{pmatrix}, \quad [5]$$

$$\begin{pmatrix} V_v \\ V_{ew} \\ V_{sn} \end{pmatrix} = \begin{bmatrix} \cos\theta_{S1A} & 0 & \sin\theta_{S1A}\sin\alpha_{S1A} - \tan\beta\sin\theta_{S1A}\cos\alpha_{S1A} \\ 0 & 1 & -\tan\beta \\ \cos\theta_{RS2D} & 0 & \sin\theta_{RS2D}\sin\alpha_{RS2D} - \tan\beta\sin\theta_{RS2D}\cos\alpha_{RS2D} \end{bmatrix}^{-1} \times \begin{pmatrix} V_{S1A} \\ 0 \\ V_{RS2D} \end{pmatrix}, \quad [6]$$

where V_v, V_{ew} and V_{sn} are estimated vertical, EW and SN velocity components, respectively, and other parameters are the same as before. To derive the aspect angle and ground elevations, 1-arcsec SRTM DEM was interpolated using the spline method. Another consideration was the spatial disparity of scatterers between S1A and RS2D. Targets on the ground can show different microwave reflectivity from different angles. Therefore, identified scatterers between these two SAR stacks were spatially non-conformant while the application of Equations 5 & 6 requires LOS velocities to correspond to the same location. A spatial interpolation is then needed in the decomposition process. In this study, a weighted *k*-nearest neighbouring search algorithm is employed (Sharifi & Hendry 2023).

To evaluate the performance of SPFM and APFM, the decomposed components were compared against the values reported by GPS 1 and 2. The vertical, EW and SN components were spatially interpolated for the location of GPS units. The accuracy of each method is then assessed by computing the error in total velocity magnitude, aspect and travel angles by subtracting the GPS-reported values. This error is referred to as a direct analysis error.

The accuracy of the decomposition method is not the only contributing factor to the direct analysis error. The reflectivity of targets determines the LOS velocity accuracy. Further, the post-processing calculations such as spatial interpolations also affect the results. Another approach is consequently taken in parallel which allows for a better isolation of decomposition methods from the above-mentioned effects. The GPS velocities were projected on the LOS of both S1A and RS2D. These back-projected LOS velocities were again decomposed using Equations 5 & 6 and the calculations conclude with computing the error using GPS values which is referred to as back-projection error. Although it may look futile, the decomposed results at this point were only the product of the decomposition method which allows for a better assessment of the decomposition method only. Having said that, both direct analysis and back-projection errors are significant. The latter indicates the upper bound of accuracy or to what degree a method 'could' be accurate while the other indicates how much of that potential is actually unfolded with all limitations in the practice.

4 RESULTS & DISCUSSION

4.1 Results at GPS locations on Ripley

Table 2 presents the direct analysis error in interpreting the magnitude, aspect and travel angles of total velocity after exercising SPFM and APFM at the location of GPS units. The average values are reported here given that very small variations at GPS locations were observed. The lowest error in magnitude interpretation belongs to APFM with 15 mm/yr or 18.75% of the GPS average velocities. However, SPFM's performance with magnitude is also not very much different with an error of 19 mm/yr or 23.76% of the GPS average velocities. It is then understood that there is no meaningful difference between the two in interpreting the magnitude of total velocity. On the other hand, when it comes to geometry, the differences are notable. SPFM shows a rather large error (36.7°) in the aspect angle while APFM's aspect angle error remains inconsiderable (1.5°). For the travel angle, the accuracies switch with SPFM being the most accurate in interpreting the steepness of velocity vectors with an error of 3.2° while APFM seems to be exaggerating the travel angle with an error of 14.4°.

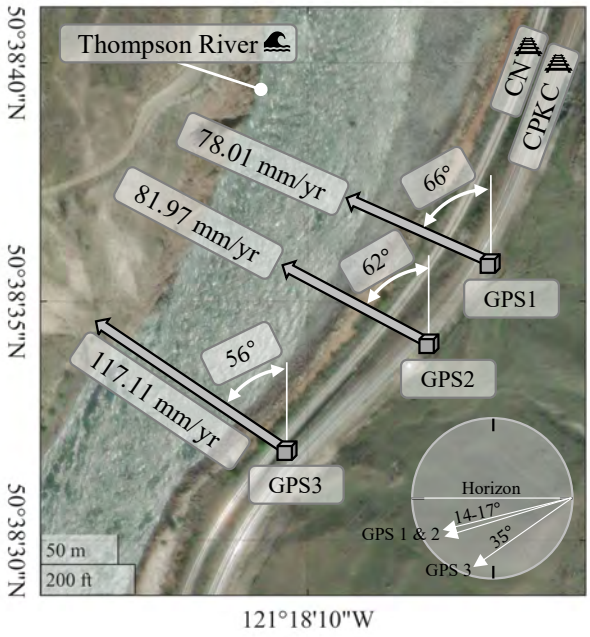

Figure 4. GPS locations on Ripley; vectors show the average velocity reported by these units corresponding to April 2008-February 2020

Table 2. Direct analysis error of SPFM and APFM in interpreting the magnitude and the geometry of velocity at GPS locations on Ripley

	SPFM	APFM
Error in velocity magnitude (mm/yr)	19	15
Above error relative to average GPS velocities	23.76%	18.75%
Error in aspect angle (deg)	36.7	1.5
Error in travel angle (deg)	3.2	14.4

Table 3 provides the back-projection error in interpreting the magnitude and geometry of velocities at the GPS locations on Ripley. The SPFM's error is 21 mm/yr or 26.25% of the GPS velocities while APFM's error drops to 5 mm/yr or 6.25% of the GPS velocities. Comparing these values with the values reported in Table 2 indicates that the APFM is the most affected one with the direct analysis limitations with a 10 mm/yr increase in errors. It is highlighted that in a general case where back-projection is not feasible, the direct analysis error is the true indicator of a decomposition method's performance. Therefore, while APFM in theory might be more aligned with the translational landslide mechanisms, the final result between SPFM and APFM

is virtually on the same reliability level. The back-projection errors for aspect angle in SPFM and APFM are 20 and 6.8° and for the travel angle are 7.1 and 2.1°, respectively. In comparison with the direct analysis error (Table 2), it seems that SPFM's aspect angle and APFM's travel angle aggravate in the direct analysis.

Table 3. Back-projection error of SPFM and APFM in interpreting the magnitude and the geometry of velocity at GPS locations on Ripley

	SPFM	APFM
Error in velocity magnitude (mm/yr)	21	5
Above error relative to average GPS velocities	26.25%	6.25%
Error in aspect angle (deg)	20	6.8
Error in travel angle (deg)	7.1	2.1

4.2 Overall results at Ripley

Figure 5 displays all the velocity characteristics (magnitude, aspect and travel angles) for the entire targets identified on Ripley. In Figure 5a & b, colours are indicative of the total velocity magnitude per the colour bar on the right and the overlying vectors are unit vectors of the velocity to show the direction of movements in the horizontal plane more clearly. The histograms of aspect angle, travel angle and magnitude are provided in sub-figures c-e, respectively. Figure 5a demonstrates that SPFM results are rotated toward the North (polar biasing) and Figure 5c confirms that SPFM vectors, on average, are 36° apart from GPS directions. This is in parallel with results at the location of GPS units (Table 2). While Figure 5b & c display the APFM's aspect angles are comparable to those GPS units report, Figure 5d suggests a considerable difference in the travel angles

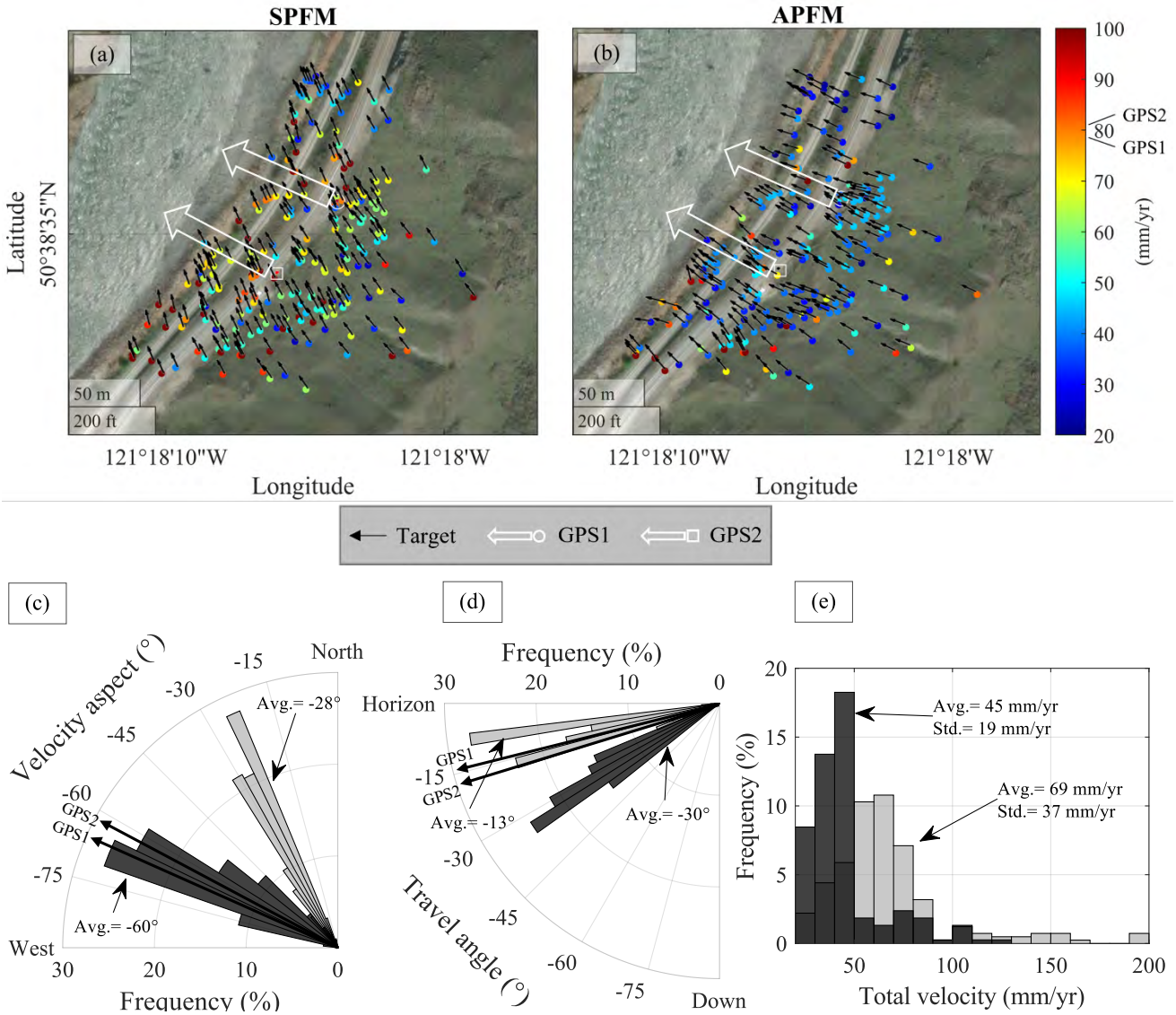

Figure 5. Map of total velocities and their unit vectors using (a) SPFM and (b) APFM; and histograms of (c) aspect angle, (d) travel angle and (e) velocity vectors magnitude (Sharifi et al. 2023)

interpreted by this method. The SPFM's travel angle remains tightly close to the GPS values but APFM interprets the dip of vectors about 15° steeper than GPS values (over-dipping). This observation, again, matches what direct analysis demonstrated (Table 2). The geometrical distortion of vectors by both methods could be attributed to the LOS errors.

Figure 5e shows the histogram of total velocities magnitude. It is seen that SPFM results are relatively right-skewed. The average and standard deviation are calculated 69 and 37 mm/yr, respectively. On the contrary, the average and standard deviation of magnitudes as interpreted by APFM are calculated 45 and 19 mm/yr, respectively. The reported GPS total velocity falls closer to the majority region of SPFM. Previous studies suggested Ripley moves as one block which corroborates SPFM's slight suitability in understanding the magnitude of velocities. However, its wider distribution in Figure 5e implies higher uncertainties associated with its application to this purpose. Exaggerated values in SPFM calculated higher than GPS values (>79 mm/yr) could be a result of over-estimating V_{sn} instead of solely rotation of the velocity vector. We calculated the Pearson's coefficient between the aspect angle and the magnitude of the velocity of points moving higher than 79 mm/yr and it turned out 0.55.

4.3 Discussion

A distortion in the geometry of vectors interpreted by SPFM and APFM is observed. It is speculated that polar biasing by SPFM and over-dipping by APFM could be attributed to the errors in LOS velocity. This hypothesis could be substantiated by different approaches. Firstly, looking at Table 2 and Table 3, it is seen that these geometrical distortions manifest only in direct analysis which differs from back-projection in the values of LOS velocity. These, however, can be also traced back to the very mathematical core of each method as explained in the following.

SPFM's main assumption is Equation 3. If velocity terms in Equation 3 are substituted with error terms and re-arrangements are made, Equation 7 will be a phrase to distribute errors between velocity components:

$$dV_{SN} = \frac{1}{i_{SN}} dV_V - \frac{i_{EW}}{i_{SN}} dV_{EW}, \qquad [7]$$

where 'd' denotes the error term for the succeeding component. Considering that $1/i_{SN}$ and i_{EW}/i_{SN} are large values for a valley running close to South-North, like the Thompson River Valley, dV_{SN} becomes very large and thus, an over-estimation of this component leads to the rotation of vectors to either South or North. However, polar biasing is not only a result of the LOS error, and it is expected to see polar biasing even without any LOS error as back-projection (Table 3) showed. This is simply because $1/i_{SN}$ and i_{EW}/i_{SN} also show up in a case with no LOS variance. By substituting heading and incidence angle values from Table 1 into Equation 5 and calculating V_{EW} and V_{SN}, the aspect angle is as follows (Equation 8):

$$\tan\beta = \frac{\left(0.72\frac{i_E}{i_N}+0.71\frac{1}{i_N}\right)V_{S1A}-\left(0.78\frac{i_E}{i_N}-0.64\frac{1}{i_N}\right)V_{RS2D}}{\left(0.11\frac{1}{i_N}-0.72\right)V_{S1A}-\left(0.78+0.11\frac{1}{i_N}\right)V_{RS2D}}. \qquad [8]$$

To delve into the root cause of APFM's over-dipping, we highlight that S1A had a much lower resolution (20×5 m^2) compared to RS2D (3×3 m^2). The reflectivity threshold to identify reliable targets had to be lowered for S1A to have a comparable density of targets between S1A and RS2D. This led to a variance of LOS velocity in S1A which is 2.1 times of RS2D. Please see Sharifi et al. (2023) for the detail of calculations. Similar to what was done for SPFM, if the velocity terms in Equation 5 are substituted with error terms (denoted by 'd'), Equation 9 explains the error distribution for APFM:

$$\begin{pmatrix} dV_V \\ dV_{EW} \\ dV_{SN} \end{pmatrix} = \begin{pmatrix} 1.85 \\ -0.4 \\ 0.23 \end{pmatrix} dV_{RS2D}. \qquad [9]$$

Equation 9 indicates that the error in V_V is 4.6 and 8.0 times larger than the errors in V_{EW} and V_{SN}, which explains the over-dipping.

5 CONCLUSIONS

The integration of InSAR in landslide monitoring programs is on the rise. However, the uncertainty associated with line-of-sight (LOS) velocities poses a challenge to obtaining a comprehensive understanding of landslide kinematics and is crucial for effective risk management such as early warning system development. To address this, it is recommended to decompose LOS velocities from 1D estimates into 3D. Among various approaches, topography-based methods have gained popularity due to their feasibility, accuracy, and efficient resource management. However, the choice of a specific method should be well informed.

This study processed 102 Radarsat-2 and 119 Sentinel-1 scenes acquired from opposing viewing geometries over landslides in the Thompson River valley. Two different methods, the surface parallel flow method (SPFM) and the aspect parallel flow method (APFM), were employed for decomposing 1D LOS velocities. The key findings are summarized as follows:

1. The incorporation of SPFM and APFM in decomposition resulted in errors of 19 (23.76%) and 15 (18.75%), respectively, for the Ripley landslide.
2. Vectors obtained by SPFM exhibited a bias towards South-North due to the exaggeration of V_{SN} in response to sensitivity to LOS variance.
3. APFM demonstrated greater success in appreciating the velocity aspect with lower sensitivity to LOS variance compared to SPFM. However, a restrictive assumption to align V_{EW} and V_{SN} with the valley's aspect manifested LOS variance mostly in V_V, leading to erroneous and steep travel angle estimations.

In conclusion, relying on a standalone method may sacrifice accuracy in at least one characteristic of magnitude, aspect, or travel angle. A hybrid approach for the 3D decomposition of 1D LOS velocities is recommended for analyzing translational landslides. Different decomposition methods should contribute to interpreting a specific vector attitude based on their performance. It is proposed to use either SPFM or APFM for magnitude estimation, APFM for the aspect angle, and SPFM for a reliable interpretation of the travel angle.

6 ACKNOWLEDGEMENT

This research was completed through the (Canadian) Railway Ground Hazard Research Program (RGHRP), which is funded by the Natural Sciences and Engineering Research Council of Canada (NSERC; ALLRP 549684-19), Canadian National Railway, Canadian Pacific Railway, and Transport Canada. RGHRP also includes partnerships with Queen's University and the Geological Survey of Canada. The authors also acknowledge the role of the SARPROZ© team, who graciously offered an academic license as well as extensive online support.

REFERENCES

Ao, M., Zhang, L., Shi, X., Liao, M., & Dong, J. (2019). Measurement of the three-dimensional surface deformation of the Jiaju landslide using a surface-parallel flow model. Remote Sensing Letters, 10(8), 776-785.

Azadnejad, S., Maghsoudi, Y., & Perissin, D. (2019). Investigating the effect of the physical scattering mechanism of the dual-polarization sentinel-1 data on the temporal coherence optimization results. International Journal of Remote Sensing, 40(18), 7033-7047.

Bianchini, S., Herrera, G., Mateos, R. M., Notti, D., Garcia, I., Mora, O., & Moretti, S. (2013). Landslide activity maps generation by means of persistent scatterer interferometry. Remote Sensing, 5(12), 6198-6222.

Bobrowsky, P. T., & Dominguez, M. J. (2012). Landslide susceptibility map of Canada. DOI: 10.4095/291902.

Holmes, J., Chambers, J., Wilkinson, P., Meldrum, P., Cimpoiaşu, M., Boyd, J., Huntley, D., Williamson, P., Gunn, D., Dashwood, B., & Whiteley, J. (2022). Application of petrophysical relationships to electrical resistivity models for assessing the stability of a landslide in British Columbia, Canada. Engineering Geology, 301, 106613.

Huntley, D., Bobrowsky, P., MacLeod, R., Rotheram-Clarke, D., Cocking, R., Joseph, J., Holmes, J., Sattler, K., Chambers, J., Meldrum, P., & Wilkinson, P. (2023). IPL Project 202: landslide monitoring best practices for climate-resilient railway transportation corridors in southwestern British Columbia, Canada. In Progress in Landslide Research and Technology, 1(1), 249-265. Springer International Publishing.

Huntley, D., Rotheram-Clarke, D., Pon, A., Tomaszewicz, A., Leighton, J., Cocking, R., & Joseph, J. (2021). Benchmarked RADARSAT-2, SENTINEL-1 and RADARSAT Constellation Mission Change-Detection Monitoring at North Slide, Thompson River Valley, British Columbia: ensuring a Landslide-Resilient National Railway Network. Canadian Journal of Remote Sensing, 47(4), 635-656.

Joughin I. R., Kwok, R., & Fahnestock, M. A. (1998). Interferometric estimation of three-dimensional ice-flow using ascending and descending passes. IEEE Transactions on Geoscience Remote Sensing, 36(1), 25-37.

Khoshlahjeh Azar, M., Hamedpour, A., Maghsoudi, Y., & Perissin, D. (2021). Analysis of the deformation behavior and sinkhole risk in Kerdabad, Iran using the PS-InSAR method. Remote Sensing, 13(14), 2696.

Liu, X., Zhao, C., Zhang, Q., Yin, Y., Lu, Z., Samsonov, S., Yang, C., Wang, M., & Tomás, R. (2021). Three-dimensional and long-term landslide displacement estimation by fusing C-and L-band SAR observations: A case study in Gongjue County, Tibet, China. Remote Sensing of Environment, 267, 112745.

Macciotta, R., Hendry, M., & Martin, C. D. (2016). Developing an early warning system for a very slow landslide based on displacement monitoring. Natural Hazards, 81(2), 887-907.

Macciotta, R., Hendry, M., Martin, C. D., Elwood, D., Lan, H., Huntley, D., Bobrowsky, P., Sladen, W., Bunce, C., Choi, E., & Edwards, T. (2014). Monitoring of the Ripley Landslide in the Thompson River Valley, BC. In Proceedings of the 6th Canadian Geohazards Conference, Kingston, Ontario, Canada.

Perissin, D., & Wang, T. (2011). Repeat-pass SAR interferometry with partially coherent targets. IEEE Transactions on Geoscience Remote Sensing, 50(1), 271-280.

Porter, M., Hove, J. V., Barlow, P., Froese, C., Bunce, C., Skirrow, R., Lewycky, D., & Bobrowsky, P. (2019). The estimated economic impacts of prairie landslides in western Canada. In Proceedings of the 72nd Canadian Geotechnical Society Conference. St. John's, Newfoundland and Labrador, Canada.

Porter, M., Savigny, K., Keegan, T., Bunce, C., & McKay, C. (2002). Controls on stability of the Thompson River landslides. In Proceeding of the 55th Conference of Canadian Geotechnical Society. Niagara Falls, Ontario, Canada.

Ren, K., Yao, X., Li, R., Zhou, Z., Yao, C., & Jiang, S. (2022). 3D displacement and deformation mechanism of deep-seated gravitational slope deformation revealed by InSAR: a case study in Wudongde Reservoir, Jinsha River. Landslides, 19(9), 2159-2175.

Samsonov, S., Dille, A., Dewitte, O., Kervyn, F., & d'Oreye, N. (2020). Satellite interferometry for mapping surface deformation time series in one, two and three dimensions: A new method illustrated on a slow-moving landslide. Engineering Geology, 266, 105471.

Schlögl, M., Gutjahr, K., & Fuchs, S. (2022). The challenge to use multi-temporal InSAR for landslide early warning. Natural Hazards, 112(3), 2913-2919.

Sharifi, S., Hendry, M. T., Macciotta, R., & Evans, T. (2022a). Evaluation of filtering methods for use on high-frequency measurements of landslide displacements. Natural Hazards & Earth System Sciences, 22(2), 411-430.

Sharifi, S., Macciotta, R., & Hendry, M. T. (2022b). Algorithms to enhance detection of landslide acceleration moment and time-to-failure forecast using time-series displacements. Engineering Geology, 309, 106832.

Sharifi, S., Macciotta, R., & Hendry, M., (2022c). Application of Gaussian filter to improve forecasting of landslides failure time. In Proceeding of the 75th Conference of Canadian Geotechnical Society. Calgary, Alberta, Canada.

Sharifi, S., Macciotta, R., & Hendry, M. (2021). Reduction of stochastic noise in instrumentation readings: A comparison of simple moving average and Savtizky-Golay filters. In Proceedings of the 74th Conference of Canadian Geotechnical Society. Niagara Falls, Ontario, Canada.

Sharifi, S., & Hendry, M. (2023). An improved estimation of surficial velocities obtained by MT-TOPSAR interferometry: a case study of Oldman River Dam, Alberta, Canada. Bulletin of Engineering Geology and the Environment, 82(12), 1-19.

Sharifi, S., Macciotta, R., Hendry, M., Rotheram-Clarke, D., & Huntley, D. (2023). Evaluating topography-based methods in 3D decomposition of InSAR 1D velocities obtained for translational landslides: Thompson River valley in Canada. Landslides, 1-17.

Soltanieh, A., & Macciotta, R. (2022a). Updated understanding of the Thompson River Valley landslides kinematics using satellite InSAR. Geosciences, 12(10), 359.

Soltanieh, A., & Macciotta, R. (2022b). Updated understanding of the Ripley landslide kinematics using satellite InSAR. Geosciences, 12(8), 298.

Sun, Q., Hu, J., Zhang, L., & Ding, X. (2016). Towardsslow-moving landslide monitoring by integrating multi-sensor InSAR time series datasets: The Zhouqu case study, China. Remote Sensing, 8(11), 908.

Tappenden, K. M., Wood, D. F. & Martin, C. D. (2018). Case study of the 1982 rapid reactivation of the Goddard Landslide along the Canadian Pacific Railway near Ashcroft, British Columbia. In Proceedings of the 7th Canadian Geohazards Conference, Canmore, Alberta, Canada.

Tarighat, F., Foroughnia, F., & Perissin, D. (2021). Monitoring of power towers' movement using persistent scatterer SAR interferometry in south west of Tehran. Remote Sensing, 13(3), 407.

Zhu, Y., Yao, X., Yao, L., Zhou, Z., Ren, K., Li, L., Yao, C., & Gu, Z. (2022), Identifying the mechanism of toppling deformation by InSAR: a case study in Xiluodu Reservoir, Jinsha River. Landslides, 19(10), 2311-2327.

Canadian & Cold Regions
Rail Research Conference
2024

Development of a scalable semi-quantitative washout risk assessment framework

Patrick Grover, Sterling Mitchell, & Pascal Szeftel
BGC Engineering, Toronto, ON, and Vancouver, BC, Canada

David Brown, & Trevor Evans
Canadian National Railway, System Geotechnical Engineering

ABSTRACT

A semi-quantitative risk assessment framework was developed to evaluate embankment washout risk and piloted for two Canadian National Railway subdivisions. The framework estimates risk to railway operations from embankment erosion from crossing drainage flows (i.e., washout). Risk is calculated as the impact to operations factored by the annual probability of track becoming impassable due to washout at a given location.

The leading causes of washout considered in this approach are the ones caused when drainage inflows exceed culvert outflows, or where culverts are absent. Embankment washout may initiate from internal erosion, surface erosion, mass movement at any ponding level, or overtopping. Synthetic rainfall storms were modeled to estimate inflows with annual exceedance probabilities ranging between 50% (2-year return period) and 0.2% (500-year return period) occurring over mapped drainages upstream of the railway embankment. Ponding levels behind the embankment and potential for overtopping were modeled based on culvert conveyance and ditch storage capacity for the various storms. Culvert conveyance considered the potential for culvert blockage based on upstream watershed and channel characteristics.

The probability of washout is estimated according to the vulnerability of the embankment to ponding, based on its physical characteristics. Then, track vulnerability to washout is used to estimate the probability of impassable track. Finally, the conditional probabilities and consequences are multiplied for each storm event and summed to quantify washout risk at each Site.

The assessment framework was made scalable and applicable to system-wide assessments of linear infrastructure by using automated geospatial and flow routing routines to process lidar survey data, map drainage basins, extract ditch and embankment geometries, and determine ponding levels.

The risk assessment framework was run for current and climate-adjusted rainfall storm conditions to evaluate the incremental impact of climate change on washout risk.

1 INTRODUCTION

1.1 Background

Events in recent years have demonstrated the impacts climate change and extreme weather will have on Canadian infrastructure. This has been highlighted by the November 2021 atmospheric rivers, which adversely affected all major linear infrastructure in southwestern British Columbia (BC). These extreme weather events exposed infrastructure to increased impacts from geohazards, including embankment washouts. Washouts are a form of hydraulic erosion, which involves the removal of soil particles or rock from the embankment by the action of flowing water. As such, they represent a significant risk to railway operations in Canada (e.g., Keegan, 2007).

The relationship between frequency and magnitude of extreme precipitation events is anticipated to be affected by changing climate conditions (Li et al., 2021; Gillet et al., 2022). Given the link between hydroclimatic conditions and washout hazards, the approach to washout risk management was revisited.

A literature review of washout hazard prioritization frameworks identified three primary causes which contribute to washouts: insufficient conveyance capacity, structural culvert defects, and channel erosion. Ponding water in the upstream ditch was noted as a consequence of insufficient conveyance capacity or structural culvert defects and flagged as one of the most common reasons for washout-related embankment failures (Roads and Traffic Authority of NSW, 2010). Ponding was noted to result in swift (i.e., rapid drawdown or storm event), or gradual failure of an embankment over weeks, months, or years.

1.2 Study Objectives

Starting in 2023, Canadian National Railway (CN), Transport Canada, and BGC Engineering Inc. (BGC) collaborated on a pilot study to improve the climate resiliency of the CN rail network. To accomplish this, washout risk assessment and monitoring frameworks were developed and implemented for two CN subdivisions located in northern and southern BC. The objectives of the frameworks were to:

1. Develop an inventory of Sites (defined in Section 2.2 below) where the potential for overtopping or ponding-related embankment failure was credible.
2. Complete a risk assessment of these Sites.
3. Allow CN to actively monitor the temporal variability of the washout potential by monitoring weather conditions against pre-established precipitation thresholds.

The frameworks were developed with scalability (i.e., hundreds to tens of thousands of Sites) and adaptability (i.e., can accommodate site-specific or system-wide updates) in mind without sacrificing the representation of key processes leading to embankment washout. The results of the washout risk assessment also had to be comparable to risks posed to CN operations from other hazard types to allow for development and implementation of holistic risk-reduction measures. Future developments included the potential expansion of the washout risk assessment frameworks across the CN rail network.

To emphasize the relationship between drainage inflows exceeding culvert outflows and embankment washout potential, the selected approach included a physically based, coupled hydrologic-hydraulic model simulating ponding upstream of the embankment. The results of the study are being compiled and deployed in Cambio™, a cloud-based enterprise geohazard and geo-asset management platform designed to help operators manage, assess, and interpret geohazard and geotechnical data for various types of infrastructure and manage associated risks.

This paper introduces the management of project data and outlines the Site inventorying, washout hazard assessment, and monitoring methodologies of the washout risk assessment framework.".

2 MATERIALS AND METHODS

2.1 Washout Definition

Within this assessment framework, washout was defined as internal (i.e., seepage through) or surficial (i.e., over, or across) hydraulic erosion of embankment or rail grade material resulting in degradation of the structural stability of the railway embankment. This can occur anywhere along the railway where water is directed over or through the embankment in sufficient quantities to cause erosion, provided that such flow and erosion are sustained long enough to reduce structural integrity of the embankment. If a washout is severe enough, it can result in impassable track for rail traffic due to water above the railway grade, removal of material through erosion, or failure of the underlying embankment material. It is noted that the definition of washout does not explicitly include the presence of culverts, as washout may occur at locations where no culverts are present.

Culverts were defined as a fully enclosed structure designed to pass flow through an embankment. They can be of various sizes, shapes, and material types. A culvert group was defined as adjacent or nearby culverts that convey water from the same upstream watershed. Water passing through open-bottom culverts or bridges was not evaluated as part of this scope as they are not fully enclosed and may be subject to scour. Structures that convey surface water above the track and embankment (e.g., tunnels, rock sheds) were also not evaluated.

2.2 Data Model Definitions

To support system-wide risk management of multiple geohazard types and geotechnical assets, the inventorying, risk assessment, and monitoring frameworks were designed to align within a data model structure.

The data model begins by defining an Element at Risk, which is a real-world resource, entity, or piece of infrastructure that is critical to meeting objectives, in this case the railway's objective to permit safe and effective passage of trains. The Element at Risk may be adjacent to, rest atop of, or cross constructed assets (e.g., embankments, rock cuts) or natural features (e.g., watercourses, natural slopes), which are termed Geo-assets or Natural Features, respectively. Geo-assets or Natural Features are also real-world elements and can contain multiple, one, or no credible Hazard(s) to the Element at Risk. Examples of hazard types include washout, landslide, and bank erosion.

Geo-assets, Natural Features, and their associated credible Hazard(s) are mapped as the digital intersection between their respective extents and the Element at Risk (Figure 1).

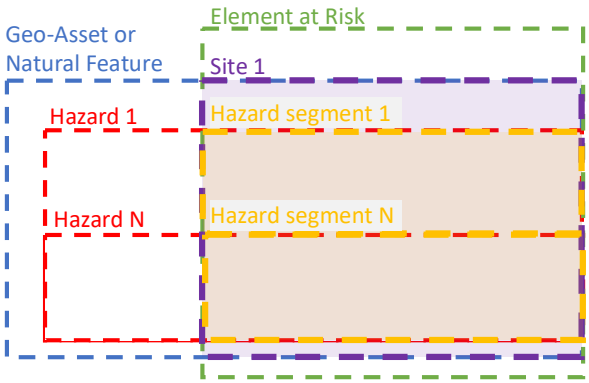

Figure 1. Visualization of the generic geohazard model. Real world elements are shown as outlines and virtual elements are shaded.

They are defined as follows:

- The intersection between a Geo-asset or Natural Feature and the Element at Risk is termed a Site and visualized as a line overlapping the element at risk.

- The intersection between Hazards originating from a Geo-Asset or Natural Feature and the Element at Risk are termed Hazard Segments, also visualized as lines.

In the case of a washout along a railway, the embankment is the Geo-asset, the integrity of which must be maintained to avoid adverse impacts to the railway (Element at Risk) objective. The Site boundaries are defined as the section of the embankment that captures drainage from a mapped watershed. The Hazard Segment(s) would be the extent where credible washout Hazard(s) exist, typically low points or culvert crossings. Within the data model, Sites, watershed, and culvert or culverts groups must always maintain a 1:1:1 relationship. A conceptual representation of the data model structure is illustrated in Figure 2.

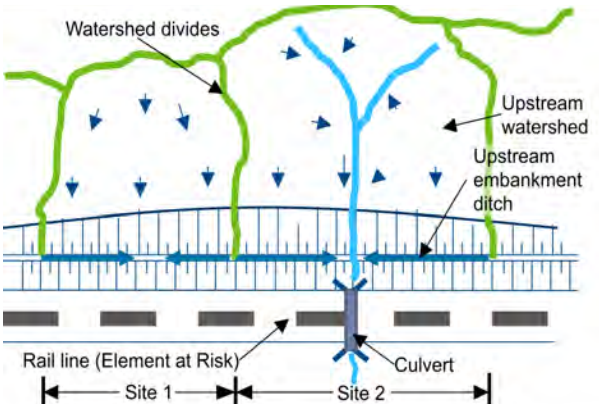

Figure 2: Conceptual model of a washout Site.

Using expert-informed algorithms partnered with engineering judgement, the risk of a given hazard segment can be assessed and prioritized alongside or combined with other geohazard segments along the railway.

This data model structure is the foundation of the Cambio platform, which was used to integrate the various data sources and summarize the results. The platform is further discussed in Section 3.2 (Results and Discussion).

2.3 Data Sources

The following key data sources were required to complete the washout risk assessment:

- A digital centreline of track alignment.
- A high-resolution terrain model, typically a bare-earth lidar digital elevation model (DEM), which captured the rail embankment and the extent of the upstream ditch.
- A culvert database detailing at a minimum, the size and location of the culverts.
- A database of bridge and tunnel crossings.
- A database of historical washout events.

These data sources were augmented by the hydrographic mapping (stream segment and watershed polygons) completed by BGC across North America and stored along with its metadata in the River Network Tools™ (RNT) geospatial database maintained by Cambio Earth Systems (Figure 3). The RNT stream network is based on the National Hydro Network (NHN) produced by Natural Resources Canada. The contributing area for each stream segment was extracted from the Shuttle Rader Topography Mission (SRTM) DEM (Van Zyl J.J., 2001).

Two earlier geohazard risk assessment frameworks developed by CN and BGC, the River Attack Track Risk Assessment System (RATRAS) and the Rockfall Hazard Risk Assessment (RHRA) by Porter (et al., 2005); and Pritchard (et al., 2005) were also reviewed.

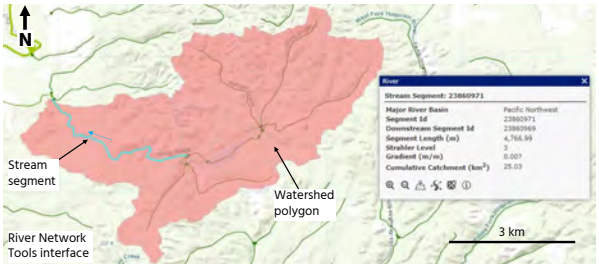

Figure 3: Watershed polygon associated with a stream segment stored in the RNT.

2.4 Washout Site Inventory

Before conducting the risk assessment, an inventory of potential washout Sites was developed. Sites were generated by intersecting the RNT watershed polygons with the railway centreline (see section 2.2). The watersheds were manually reviewed to ensure that the drainage direction was correct. The high-resolution lidar DEM was used to adjust the boundaries of the watershed as needed. Bridges and culverts were automatically assigned to each watershed and as such, a Site may have multiple conveyance structures. Each Site was assigned a starting and ending mileage along the railway based on the extents of the intersected watershed. Drainages passing over tunnels, beneath bridges, or through open-bottom culverts at track level were captured as Sites through this process but were not carried forward for washout risk assessment due to the added potential for scour. An example of the Site segmentation and inventorying is shown in Figure 4.

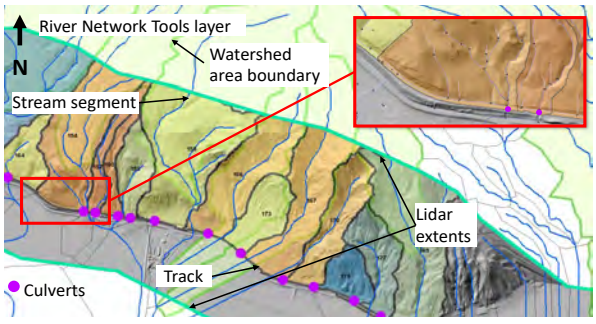

Figure 4: Washout Site inventorying workflow.

2.5 Washout Risk Assessment

2.5.1 Risk Formulation

To allow for comparison between different geohazards, a risk-based approach was chosen to assess washout Sites. The general formulation of risk estimation is defined in Equation 1.

$$Risk\ (R) = \ Hazard\ Probability\ (H) * Consequence\ (C) \quad [1]$$

Where:
R = effect of uncertainty on objects.
H = hazard probability = the likelihood of an event occurring (e.g. a washout occurring and creating impassable track).
C = Consequence = the impact of an event occurring (e.g. impassable track).

This paper focuses on the process of hazard estimation, as the formulation of consequences differs depending on the asset and its owner. For this assessment, embankment washout is the hazard caused by ponding or overtopping and potentially leading to impassable track. In this assessment, the hazard term at any given Site can be expanded to explicitly account for ponding, as shown in Equation 2.

$$R = \left(\sum_{i=1}^{n} w_i * P_{pond_i} * P_{washout|pond_i} * P_{impassable|washout_i} \right) * C \quad [2]$$

Where :
w_i is the weight associated with AEP i
$P_{pond_i}$is the annual probability of ponding occurring in the upstream ditch given a particular storm magnitude (i).
$P_{washout|pond_i}$is the conditional probability of a washout event occurring given ponding for storm magnitude (i).
$P_{impassable|washout_i}$is the conditional probability of impassable track given a washout event for storm magnitude (i).
Subscript i denotes a discrete annual exceedance probability (AEP).

The methodology for estimating the various terms of the risk equation is discussed below.

2.5.2 Probability of Ponding (P_{pond_i})

To estimate the probability of ponding, a physical modelling approach was used. Characteristics of the watershed, embankment, and the ditch at the Site were extracted through scripted GIS processes described below to allow for scalability and consistency of model results. The objective was to model flow conveyance through the upstream embankment ditch and across the embankment by estimating the inflows of the upstream watershed, the outflow via culvert(s) (if present) or overtopping, and the resulting ponding levels in the upstream ditch.

Characteristics used to parameterize the coupled hydrologic-hydraulic model at each Site are described below, first for the hydrologic model component, and then for the hydraulic model component.

Watershed geometry (e.g., area, slope, max. and min. elevations), flow path (e.g., length of longest flow path in the watershed, channel gradient), and surficial soil (e.g., USDA Curve Number) attributes were extracted for each watershed and primarily sourced from publicly available datasets. Elevation data were derived from both the high-resolution DEM and the STRM DEM (90 m resolution). Curve Number values were extracted from the GCN250 gridded dataset (Jaafar et al., 2019) and a weighted average value was determined for each watershed.

To model the flow dynamics through the upstream ditch and culvert(s) and estimate the potential for ponding or embankment overtopping at a given Site, elevations and embankment dimensions were required. This included the width, height, and side-slopes of the embankment, as well as the upstream ditch, if present. This information was obtained by automatically extracting and analyzing embankment cross sections from the high-resolution lidar DEM at the mapped culvert crossing locations. An example embankment cross section is shown in Figure 5.

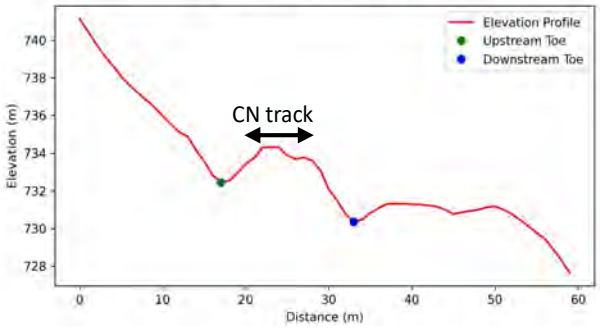

Figure 5: Example embankment cross section extracted from the high-resolution lidar DEM. Figure shown with x5 vertical exaggeration.

The high-resolution DEM was also used to estimate the storage capacity of the upstream ditch and account for potential ponding along the entire Site length. The ditch storage capacity was expressed as a stage-storage curve extracted automatically from the high-resolution lidar DEM (Figure 6) and input to the hydraulic model.

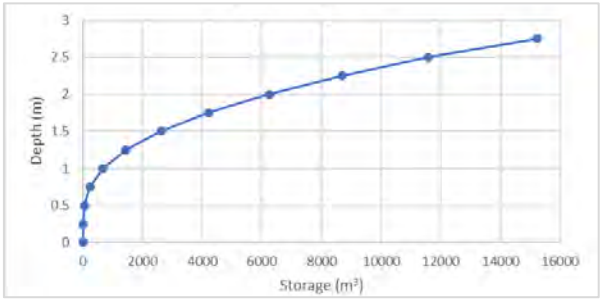

Figure 6: Stage-storage curve associated with the ditch upstream from the embankment, for a given Site.

Synthetic rainfall storm hyetographs were developed using the alternating block method (Chow et al. [1988]), taking as input intensity-duration-frequency (IDF) data (Figure 7). In this methodology, synthetic storms were created for AEPs ranging from 0.5 (2-year return period) to 0.002 (500-year return period).

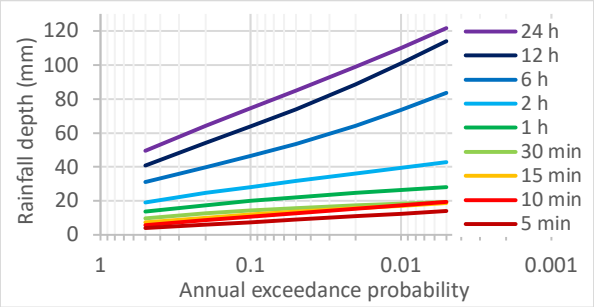

Figure 7: Sample IDF data.

Through the same methodology, climate-adjusted IDF data were used to model future conditions. The University of Western Ontario's (UWO) IDF_CC Tool Version 6.0 (Simonovic, 2015) was used to extract climate-adjusted IDF data.

For each watershed, eight synthetic rainfall storms with AEPs ranging from 0.5 to 0.002 were input to a hydrologic model that uses the watershed characteristics and storm hyetographs as input to calculate hydrographs and peak discharges (Figure 8). Modelling the watershed outflow for varying storm AEPs is necessary to account for all possible events, from low-magnitude high frequency to high magnitude low frequency. While the current framework does not account for the presence of snow on the ground and snowmelt, this is a planned future development (See Section 3.4).

The Soil Conservation Service (SCS) Curve Number loss and unit hydrograph functions were selected and implemented using the hydrologic modelling software HEC-HMS maintained by the U.S. Army Corps of Engineers (Feldman, 2000). Preparation of the input files, execution of the HEC-HMS software, and result extraction from the output files were completed automatically through scripts, thus emphasizing scalability, and reducing requirements for human intervention.

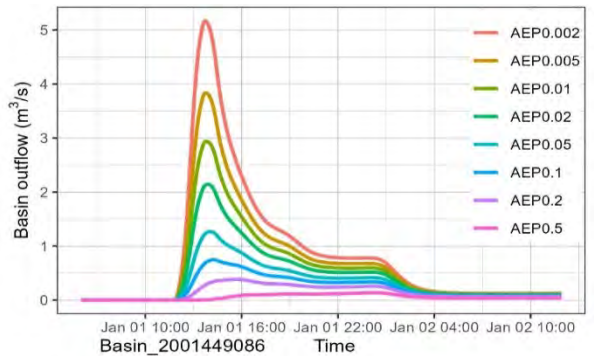

Figure 8: Watershed hydrographs resulting from the AEP 0.5 to 0.002 synthetics storm hyetographs.

The upstream ditch stage-storage curve (Figure 6) and embankment geometry (Figure 5) were also input to the coupled hydrologic-hydraulic model to calculate flow routing and evaluate ponding levels upstream of the embankment. Figure 9 illustrates flow routing through the upstream ditch and embankment culverts for AEP 0.1. For these specific Site and AEP, culvert conveyance capacity was sufficient and overtopping of the embankment was not predicted.

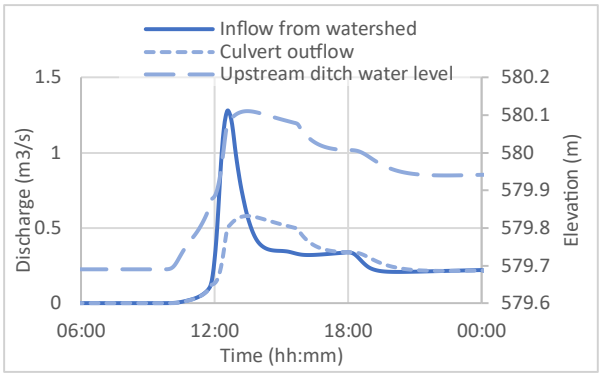

Figure 9: Flow routing through the upstream ditch (AEP 0.1).

Flow routing could then be modelled for the eight AEPs considered in the study. Figure 10 illustrate a scenario in which ponding occurs for all AEPs while embankment overtopping only occurs for AEP 0.005 and 0.002.

It is important to note that based on the characteristics of the upstream channel, storm magnitudes, and site observations, anticipated or observed culvert blockage from sediment or debris can be seamlessly accounted for in the hydraulic model. Blocked culverts are anticipated to result in elevated ponding levels due to the reduced flow conveyance capacity.

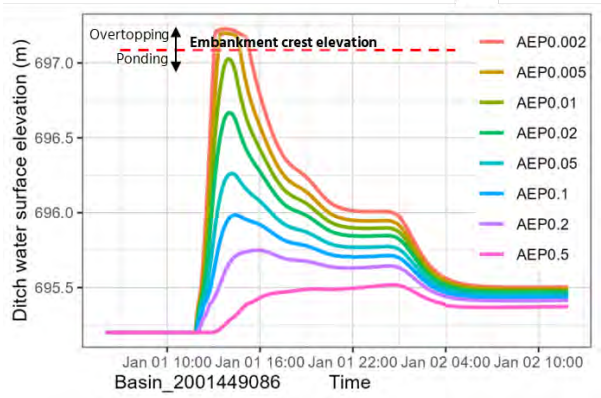

Figure 10: Water surface elevations in the upstream ditch resulting from the AEP 0.5 to 0.002 storms and inflows from the upstream watershed.

Peak water surface elevations in the upstream ditch associated with AEPs 0.5 to 0.002 were then normalized by the upstream embankment height to result in water level ratios. A ratio close to 0 corresponds to little

ponding, while a ratio of 1 or greater indicates overtopping of the embankment.

The water level ratios were mapped to base values of annual washout probability. The mapping was informed by historical washout events as well as BGC and CN engineering judgement.

2.5.3 Likelihood of Embankment Washout and Impassable Track

The base washout probabilities were then adjusted by the presence, absence, or condition of certain Site features which affect the potential for an embankment washout to occur given ponding ($P_{washout|pond}$). Such features included pre-existing signs of embankment instability and unfavourable construction material. Failure severity Site modifiers, which model the potential for the track to become impassable given a washout occurrence ($P_{impassable|washout}$) such as a damaged culvert or narrow embankment crest were then applied to each Site. As per Equation 2, P_{pond_i}, $P_{washout|pond_i}$, and $P_{impassable|washout_i}$ were weighted and summed across the eight AEPs to calculate a single annual washout probability (H) for the Site.

2.5.4 Consequence (C) and Risk (R)

While not discussed in detail in this paper, the washout risk assessment framework allows for multiple consequence and risk scenarios, such as safety, service interruption, environmental, and direct and indirect costs to be evaluated.

2.6 Washout Monitoring Framework

Based on the modelled water level ratios and Site feature modifiers, site-specific precipitation intensity and duration thresholds for embankment overtopping were defined.

For the pilot study, the system was designed to monitor precipitation and send CN automated notifications when the site-specific thresholds were exceeded. Notifications from the past 7 days are stored within the Cambio™ (see Section 3.2) dashboard which contains a map view of the precipitation data and Sites triggered by threshold exceedances (Figure 11).

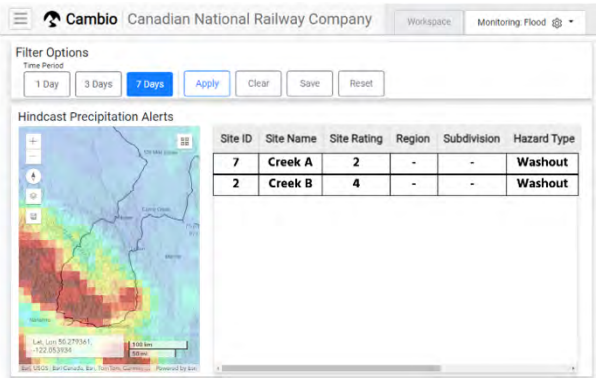

Figure 11: CN washout monitoring dashboard in Cambio.

Following the initial deployment of the monitoring framework, CN will respond to high risk notifications with follow-up ground inspections to evaluate potential washout sites. This acts as an additional way to ground truth the modelling results and further refine the assessment.

3 RESULTS AND DISUSSION

3.1 Modelling Results

The annual washout probability was calculated at the approximately 260 Sites inventoried for the northern BC subdivision (Figure 12). It is important to note that on Figure 12, the washout probability at each Site was normalized by the total washout probability and mileage was offset for the entire subdivision to preserve data anonymity. In this example, a relative washout probability of 0.001 indicates that the washout probability at the Site amounts to 0.1% of the total washout probability for the subdivision.

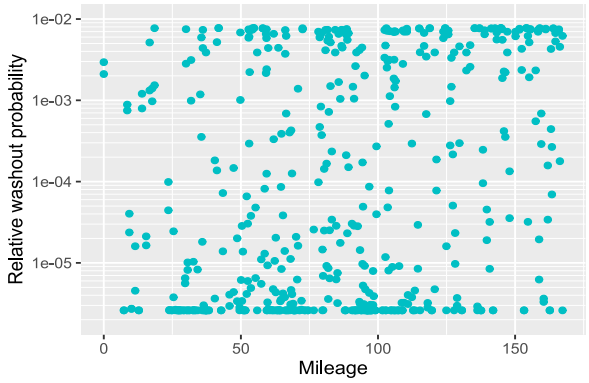

Figure 12: Relative washout probability for each Site inventoried in the northern BC subdivision.

All Sites in the inventory were then ranked according to their relative washout probability. Figure 13 shows that approximately 90% of the washout hazard for the northern BC subdivision is borne by about 55 sites (21% of the total number of Sites), an outcome that may be used to focus resources when implementing hazard- or risk-reduction strategies.

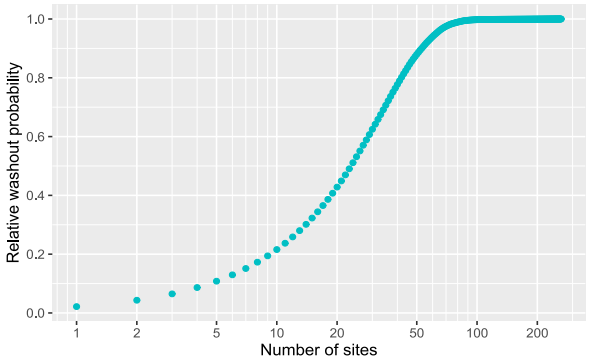

Figure 13: Cumulative relative washout probabilities for each Site inventoried in the northern BC subdivision.

The washout probabilities were then evaluated for both historical and climate-adjusted conditions. Figure 14 shows that the overall washout hazard profile of the northern BC subdivision increased between historical and climate-adjusted conditions (i.e., shift of the density towards the right). The number of Sites with a very low washout probability was reduced by 46%, while the number of Sites with a very high washout probability more than doubled between the historical and climate-adjusted scenarios. A similar outcome was reached for the southern BC subdivision (data not shown).

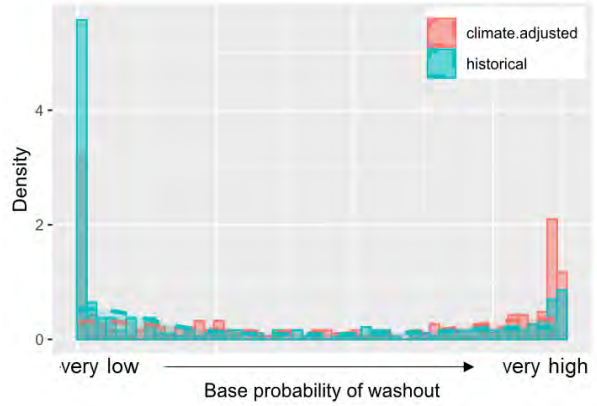

Figure 14: Distribution (density) of washout probabilities for historical and climate-adjusted conditions for the northern BC subdivision.

3.2 Cambio

The results of the washout Site inventorying, risk assessment, and monitoring dashboard are all stored within Cambio. The platform also allows for the integration of various datasets, including the culvert and bridge databases, lidar data, lidar change detection, orthoimage raster, and historical and forecast weather data (Figure 15).

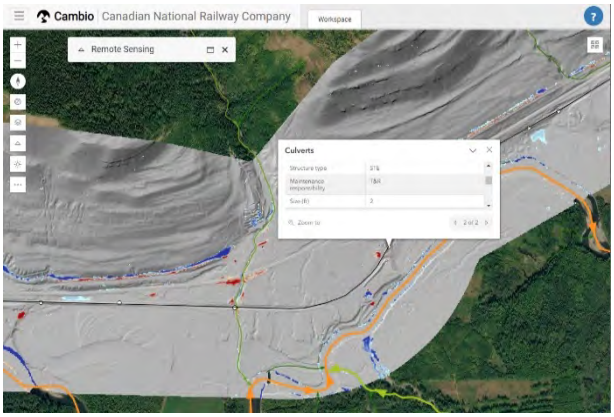

Figure 15: CN Project hosted in Cambio.

Washout inspection forms are accessible from the web or through a mobile phone or tablet application while in the field. The forms can be used to document Site conditions, record measurements, and update Site hazard and risk ratings. Files, photos, and washout events can also be added and queried based on spatial location and metadata, allowing the Cambio platform to act as a central washout hazard document repository.

3.3 Modelling Limitations

The mapped location of culverts and depth below the track are important in determining how water is conveyed through the embankment, the embankment and ditch profile, and ultimately the risk rating at a given Site. Therefore, it is critical that wherever possible the resolution of coarse DEMs and inaccurate culvert location data be improved before conducting the analysis to limit error being propagated through the modelling.

3.4 Future Developments

While the initial modelling results are expected to be refined with the integration of additional field data and the ground-truthing following precipitation threshold exceedance notifications, the framework presents several other opportunities for improvement.

Accounting for snow water equivalent and snowmelt in the IDF data and the development of synthetic precipitation storms is a planned development. This development will be paired with the ability to account for changes in a watershed landcover (e.g., wildfire) which affects both runoff and sediment yield, and the ability to account for the presence of ice in the culvert, which affect culvert conveyance capacity.

Another planned addition to the framework is the ability to model cross-watershed flow to better capture the connected nature of the hydraulic systems along the embankment. This would allow ponded water to flow not only over the embankment but also across a divide into adjacent watersheds through ditch hydraulic connectivity.

The relationship between water level ratios and base washout probabilities is expected to undergo refinements through calibration. The currently adopted exponential model appears to yield conservative results; several alternatives that potentially match the observed behaviour more closely will be tested.

The current framework only considers flow through culverts and flow over the embankment and does not consider seepage through the embankment. This likely results in increased predicted water level ratios at some Sites, notably those characterized by a relatively long mileage interval. This is a planned future development and will be implemented by either using a base value, or embankment construction parameters and materials when known.

Future improvements related to the monitoring framework would be the integration of precipitation forecast following ground-truthing and refinement of the initial notifications on observed precipitation data. This would offer the opportunity to proactively manage potential washout Sites and mitigate track outage time.

4 CONCLUSIONS

This paper presents a novel approach to predicting embankment washout hazard based on a physical model of ponding in the upstream ditch and embankment vulnerability to ponding. The washout assessment framework is scalable and can be readily applied across the entirety of CN network assuming data availability. It leverages scripting and automation to produce repeatable results.

By comparing the washout hazard and risk profiles of between historical and climate-adjusted conditions, vulnerability to climate change can be evaluated. When completed for an entire system, the climate-change vulnerability study can help rail operators identify subdivisions that are disproportionally impacted by climate change and make proactive decisions to improve the railway resiliency. Using the presented risk-based formulation, the framework also allows for the risk of washouts to be compared against and integrated with risk from other geohazard types along the same network.

While there are limitations to the current implementation of the framework in its current form, it is informed by tested guidelines, and yield results that align with the historical performance of the railway investigated in this study. Future developments and refinements are planned.

As the washout risk management program undergoes refinement and matures, the combination of the washout risk assessment and monitoring system aim to provide operational guidance to CN, to manage washout risk in the short, medium, and long-term:

- In the short term, CN will be able to actively monitor ponding and overtopping potential for washout Sites and respond promptly to mitigate outage time.
- In the medium term, CN will be able to use the washout risk ratings to proactively manage risk through targeted capital investment, and maintenance and repair budgets that result in a reduction in washout risk.
- In the long term, CN will be able to model the effects of climate change on washout risk across entire subdivisions or regions and allocate resources to effectively manage risk and resiliency in a changing climate.

The uploading of project data and assessment results, as well as the deployment of the monitoring dashboard to the Cambio platform has provided new opportunities for the work, allowing new assessments, and office and field workflows to be easily integrated.

5 ACKNOWLEDGEMENT

This work was made possible through the collaboration and funding of Transport Canada, CN, and BGC as part of the Rail Climate Change Adaptation Program (R-CCAP), a component of the Rail Safety Improvement Program. The authors would like to express appreciation for the support of the sponsors.

REFERENCES

Chow, V.T., Maidment, D.R., and Mays, L.W. (1988). Applied Hydrology. McGraw Hill, 572 p.

Colditz, R. R., Saldaña, G. L., Maeda, P., Espinoza, J. A., Tovar, C. M., Hernández, A. V., ... & Ressl, R. (2012). Generation and analysis of the 2005 land cover map for Mexico using 250 m MODIS data. Remote Sensing of Environment, 123, 541-552.

Feldman A, (2000). Hydrologic Modeling System HEC-HMS: Technical Reference Manual. U.S. Army Corps of Engineers Hydrologic Engineering Center (HEC). Davis, CA.

Gillett, N., Cannon, A., Malinina, E., Schnorbus, M., Anslow, F., Sun, Q., Kirchmeier-Young, M., Zwiers, F., Seiler, C., Zhang, X., Flato, G., Wan, H., Li, G., & Castellan, A. (2022). Human influence on the 2021 British Columbia Floods. SSRN Electronic Journal. https://doi.org/10.2139/ssrn.4025205

Jaafar, H. H., Ahmad, F. A., & El Beyrouthy, N. (2019). GCN250, new global gridded curve numbers for hydrologic modeling and design. Scientific data, 6(1), 145.

Keegan, Timothy R. (2007). Methodology for risk analysis of railway ground hazards [Doctoral thesis, University of Alberta]. University of Alberta Library. https://doi.org/10.7939/R3-1DNG-VG40

Li, C., Zwiers, F., Zhang, X., Li, G., Sun, Y., and Wehner, M. (2021). Changes in Annual Extremes of Daily Temperature and Precipitation in CMIP6 Models. Journal of Climate, 34(9), 3441-3460. https://doi.org/10.1175/JCLI-D-19-1013.1

Porter, M., Bruce, I., Pritchard, M., Keegan, T., and Abbott, B. 2005. CN River Attack Track Risk Assessment System (RATRAS). 2005 International Conference on Landslide Risk Management, Vancouver, BC, May 31 to June 2, 2005.

Pritchard, M., Porter, M., Savigny, W., Bruce, I., Oboni, F., Keegan, T., and Abbott, B. 2005. CN Rockfall Hazard Risk Management System: Experience, Enhancements, and Future Direction. 2005 International Conference on Landslide Risk Management, Vancouver, BC, May 31 to June 2, 2005.

Roads and Traffic Authority of NSW. (2010). Culvert Risk Assessment Guideline V3.02. North Sydney, N.S.W: Road and Traffic Authority of NSW.

Simonovic, S.P., A. Schardong, R. Srivastav, and D. Sandink (2015), IDF_CC Web-based Tool for Updating Intensity-Duration-Frequency Curves to Changing Climate – ver 6.5, Western University Facility for Intelligent Decision Support and Institute for Catastrophic Loss Reduction, open access https://www.idf-cc-uwo.ca.

Van Zyl, J. J. (2001). The Shuttle Radar Topography Mission (SRTM): a breakthrough in remote sensing of toography. Acta astronautica, 48(5-12), 559-565.

Canadian & Cold Regions
Rail Research Conference
2024

Investigation on the effect of hyperbolic heat condition on high strength rail steels

Stephen Okocha [1], P.-Y. Ben Jar [1], Michael Hendry [2], and Feng Yu [3]
[1] *Department of Mechanical Engineering, University of Alberta - Edmonton, Alberta, Canada*
[2] *Department of Civil and Environmental Engineering, University of Alberta - Edmonton, Alberta, Canada*
[3] *School of Mechanical Engineering and Mechanics, Ningbo University, PR China*

ABSTRACT

The increased rate of derailments of rail steels due to broken rail in temperate regions of the world like Canada has been investigated for quite some time. These areas experience a wide range of temperature changes throughout the year, having extreme temperatures as low as -50°C in the winter seasons. When brakes are applied conditionally or unconditionally, there exist a high-temperature gradient on the railhead, causing a combined effect of thermal stresses and axial stresses from the friction of the rail wheels and axial load of the train respectively. It is hypothetically suggested that such operational-environmental induced condition could contribute to reasons why unexpected rails breaks occur. This paper explores the effect and comparison of temperature and thermal strain on rail steel contributed by Fourier and non-Fourier (hyperbolic) conduction heat transfer on the deformation response. Analytical results of emergency-initiated brakes for CZ rail steel are presented at -40°C as it is seen that non-Fourier heat conduction having a wave-like model, amounted to higher temperatures than Fourier heat conduction effect thus contributing more thermal strain to the equivalent strain from mechanical and thermal loadings. Further insights show that maximum temperatures can reach closer the eutectoid temperatures, which has the possibility of affecting the microstructure due to the sudden heating and air-cooled initiated quenching at such extreme conditions especially for high tonnage and high-speed train scenarios. In the end, recommendation of reducing train speed is suggested as the safest practice to employ during extreme cold temperatures.

1 INTRODUCTION

The reliability and integrity of rail steels have been a subject of concern for several decades. This involves several efforts to improve the mechanical properties and fracture toughness of rail steels during the manufacturing process. In as much as the safety concerns have been put in place in manufacturing better rail steels, failure of these steels in terms of derailment is still a major concern. Transportation Safety Board (TSB) of Canada released its report stating that in 2020, the main-track accident rate in 2020 was 2.7 accidents per million main-track train miles, down from 3.3 in 2019 but 12% above the 10-year average of 2.4. Also, about 11 occurrences of the main-track derailments occurred from 2019-2020 according to the TSB, which were in sub-zero temperatures as seen in Table 1. These occurrences shows that there is a possibility of sub-zero temperatures contributing to the health status of main tracks. Leishman et al. (2017) also reported that derailments due to rail breaks amounts to about 3.9%. This can have more effects in cold temperatures and very high speed which is concurrent to Canada Pacific's (CP) report that advices train's maximum speed to be dropped by at least 10 miles per hour (MPH) when temperatures drops below negative 25 degrees Celsius (-25°C) and by at least 20 MPH when temperatures drop below -35°C according to the Canadian Pacific Railway Company' report (2019) accessed in the Railway age August 2019 magazine.

During extreme cold periods, the rails steel behaviour starts transiting from ductile to brittle behavior making it susceptible to fracture during applied stress at a lower strain. Hence, the impact of the mechanical loading weighs heavily on the rail steels at a lower strain according to works from Yu et al. (2015), Yu et al. (2016), Yu et al. (2017).

Table 1 Main track train derailments 2019-2020

Investigation	date	Location (close to)	Temp °C	Speed mph
R20W0025	2020-02-06	Guernsey, Saskatchewan	−18	42
R20W0031	2020-02-18	Emo, Ontario	−27	44
R20V0005	2020-01-07	Kitwanga, British Columbia	−8	35
R19W0329	2019-12-31	Beaver, Manitoba	−12	60
R19W0320	2019-12-09	Guernsey, Saskatchewan	−19	44
R19D0117	2019-11-16	Bolton-Ouest, Quebec	−10	16
R19E0150	2019-09-29	Vegreville Subdivision Chipman, Alberta	–1	41
R19E0147	2019-09-27	Blackfalds, Alberta	−1.2	22
R19W0050	2019-02-16	St. Lazare, Manitoba	−27	49
R19W0017	2019-01-22	Saskatoon, Saskatchewan	−11	31
R19V0002	2019-01-03	Partridge, British Columbia	−1	8

In addition to this, thermal stresses are also contributed to the equivalent stresses experienced on the rail steel. Ertz & Knothe (2003) reports that the sliding friction between the rail surface and the rail wheel results into contact temperature, generating heat, which initiates its contribution to the equivalent stresses. The heat generated is governed by Fourier heat conduction model supported in the works of Sobota (2014) and Faramarz & Salman (2009) that considers the rate of heat transfer through a material is proportional to the negative gradient in the temperature and to the area at right angles to that gradient, through which the heat flows. However, there is another conduction heat transfer concept known as the non-Fourier (hyperbolic) heat conduction, which proposes its occurrences when there exist a high and instantaneous temperature gradient occurring at a localized zone as depicted in the works of Chen & Akbarzadeh (2020) and Wang (2024). Chen & Akbarzadeh (2020) explains that when a material experiences a sudden change in transient and high-temperature gradient cases, the heat flux (heat per surface area) is expected to experience a phase lag in the time for heat to propagate from one point to another. This, however, insulates that the possibility of having higher heat fluxes or higher temperatures, which will result to considerations of higher equivalent stresses or stain contributed by thermal effect is possible and needs to be investigated. For the high heat flux governed by non-Fourier to be felt at the localized area of the rail steel, the speed at which the heat flux travels from the contact point are to be examined. Unlike the Fourier law which presumes that the heat flux's speed is infinite, non-Fourier law has a finite speed of propagation which yields a damped wave equation as suggested in Maurer (1969). Babaei & Chen (2010) suggests that the speed of the thermal wave strongly depends on the non-homogeneity indices in the material. Although the rail steels are considered homogenous, the microstructure of the rail steels containing different crystalline structures can initiate non-homogeneity inthe high strength rail steels, which in most cases is an alloy as seen in Okocha et al. (2023). A subject still considered for investigation.

Hence, this study involves an investigation of the contribution of non-Fourier conduction model to the equivalent strain of the rail steels as well as the temperature distribution across the rail steel. These would involve estimating the thermal speed from the contact temperature from the rail wheel and the rail surface to the width of the rail due to frictional force converted to heat energy. The study scope will be focused on the application of an emergency-initiated brake of a moving train as seen in many scenarios at sub-zero temperatures experienced in Canada (using worst-case scenario). At this scenario, both the Fourier and non-Fourier models will be investigated to see if there would be any difference in the thermal strain or equivalent strain experienced in the rail steel. The thermal effect as an addition to the constitutive governing equations for linear elastic deformation will also be looked upon using simple constitutive equations. To verify this, the test data from Yu et al. (2016) will be used where parameters of CZ rail steel were analyzed at -40°C.

Some Assumptions are made during the analysis of this work:

- No significant loss during the heat generated from contact point to point of flaw due to the thermal wave speed.
- Bending stresses contribute to the stress at the pre-existing flaw resulting to pure mode I application, which originated from manufacturing defect or rail defects because of weaker intermolecular bonds within the rail's microstructure.
- Thermal contributions to the overall strain are only by Fourier and non-Fourier heat transfers. Convection and radiation heat transfers are not considered.
- Only linear elastic deformations are considered due to the cumbersomeness of including thermal stresses/strain to plastic deformation as well as how negligible it would contribute of the equivalent stress or strain.

2 MATERIALS AND METHODS

The scenario is looked at an instant of rail beam under axial loading as depicted in Figure 1, which shows a three-dimensional (3D) illustration of the rail wheel and steel in contact. At such instant, the axial load from the train at the mid-point of the rail length of the head section creates a beam under bending stress scenario with a pre-existing flaw at the mid-point. If consideration on the rail steel to have a pre-existing flaw either from manufacturing processes or from a weaker intermolecular bond existing within the molecules of the rail steel is considered, then, the principle of localized

intensified stresses with the potential of initiating failure could occur as reported in Griffith (1921).

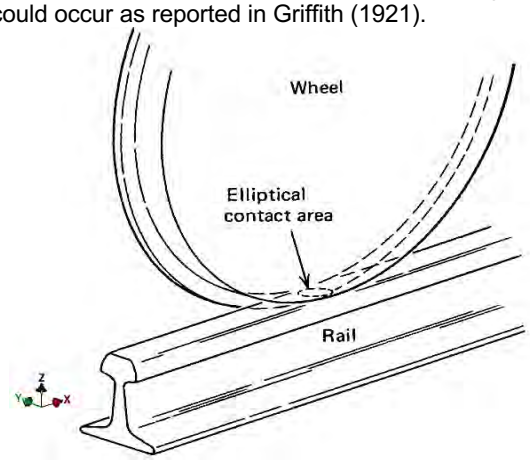

Figure 1- 3D-Rail wheel contact on rail steel

Figure 2 shows the tensile localized stresses at the flaw point. Reducing the problem to a 2-dimensional case, the mechanical loading in conjunction with the generated thermal stresses would be considered along the x-axis as an equivalent stress along the rail streel length.

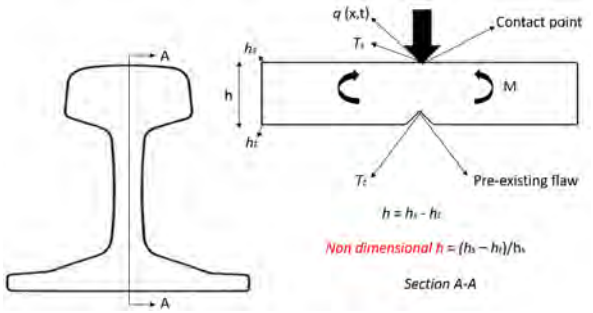

Figure 2- illustration of the loads and stresses present during contact.

From Figure 2, h_s and h_t represent the starting height and ending point respectively at which heat conduction will transmit vertically on the rail head. T_s and T_t are the starting and ending temperatures, respectively from the point of contact to the point of flaw of the rail head. q(x,t) is the heat flux as a function of location and time.

When brake is applied, the frictional force between the rail steel and the rail wheel initiates heat flux required for inducing thermal stresses. This causes a high temperature gradient, ΔT which is a difference between T_s and T_t at a very rapid rate through the height of the rail steel (h_s to h_t). This instantaneous temperature gradient causes a heat flux $q(x,t)$ and phase lag at the top surface of the rail head according to principles of non-Fourier heat conduction, which is transmitted to the point of flaw hence contributing in terms of thermal stress to the already mechanically induced localized stress. This invariably means the temperature T_t becomes the governing temperature to initiate both Fourier and non-Fourier effect. This heat flux or the fast temperature gradient is investigated using both conduction models.

2.2 Fourier and Non-Fourier heat conduction models

The heat conduction model as shown in Equation. 1 governs the heat conduction principle for the steady state condition; this relates the heat flux with the temperature gradient. However, due to the sudden change in transient and high-temperature gradient cases as suggested by Chen & Akbarzadeh (2020), a thermal relaxation time, τ_q is introduced into the Fourier law as described in Equation 2. Cattaneo (1958) and Vernotte (1958) first introduced this non-linear hyperbolic correlation to explain the finite behaviour of the thermal wave speed, C.

$$q(x,t) = -K\nabla T \quad [1]$$

$$q(x,t) + \tau_q \frac{\delta q}{\delta t}(x,t) = -K\nabla T \quad [2]$$

The thermal relaxation time creates a time delay between the $q(x,t)$ and ∇T at the fast transient condition. K is the thermal conductivity taken as a constant due to the assumed isotropic nature of the rail steels.

If the energy disseminated in the process of high ∇T across the length and height of the rail head is considered, it can be characterized by the first law of thermodynamics while the entropy effect can be considered because of the 2nd law of thermodynamics as shown in Equation 3 and Equation 4, respectively combining to contribute towards to development of the non-Fourier heat conduction process as suggested by Chen & Akbarzadeh (2020) and Babaei & Chen (2010).

$$-\nabla q(x,t) + \rho r_T = -\rho T_o \frac{\delta s}{\delta t}(x,t) \quad [3]$$

$$\rho S(x,t) = \frac{\rho C_p}{T_o}(T_{(x,t)} - T_o) \quad [4]$$

where, ρ is the density of the material, S the entropy of the material, r_T the internal heat generation within the rail steel's structure due to internal chemical activities and C_p is the specific heat capacity of the rail steel. Since there is no internal heat generation in the process ($r_T = 0$), Equation 3 and Equation 4 can be combined to give an expression relating the gradient of heat flux and temperature gradient as seen in Equation 5.

$$-\nabla.\vec{q} = \rho C_p \frac{\delta T}{\delta t} \quad [5]$$

2.3. Linear-elastic criteria

From the proposed problem in section 2.1, the localized stresses acting on a point based on classical solid mechanics principle initiates a linear elastic, and elastic-plastic deformation regimes on the rail steel. However, only elastic deformation and stresses will be considered in this study. Based on continuum mechanics, the deformation will be accompanied with a displacement in the three directions, u_x, u_y and u_z for the x-axis, y-axis and z-axis, respectively. The small finite strain based on the works of Carrera et al. (2016) can thus be estimated for each direction (precisely the x-axis in this study) as shown in Equation 6

$$E_{ij} = \frac{1}{2}\left[\frac{\delta u_i}{\delta x_j} + \frac{\delta u_j}{\delta x_i} + \sum_{k=1}^{3} \frac{\delta u_k}{\delta x_i}.\frac{\delta u_k}{\delta x_j}\right] \quad [6]$$

Since the first stage is in the regime of linear elasticity, Equation. 6 can be deduced to estimate the nine (9) infinitesimal strain by eliminating the non-linear terms. Equation. 7 can be expressed as a total of 6 equations if symmetry in the strain effect is considered.

$$\varepsilon_{xx} = \left[\frac{\delta u_x}{\delta x}\right],\ \varepsilon_{yy} = \left[\frac{\delta u_y}{\delta z}\right],\ \varepsilon_{zz} = \left[\frac{\delta z}{\delta z}\right],\ \varepsilon_{ij} = \frac{1}{2}\left[\frac{\delta u_j}{\delta xi} + \frac{\delta u_i}{\delta xj}\right] \quad [7]$$

We can deduce the displacement of the rail steel especially at a point in the continuum by integrating the strain equations respectively and applying boundary conditions for a relationship between the displacements. The compatibility equations help for the drawback of 6 strain-displacement equation for estimating only 3 displacements.

$$\frac{\delta^2 \varepsilon_{zz}}{\delta x^2} + \frac{\delta^2 \varepsilon_{xx}}{\delta z^2} = 2\frac{\delta^2 \varepsilon_{xz}}{\delta x\, \delta z} \quad [8]$$

According to hook's law, the strain and the stress can be related as depicted in Equation 9, which is a linear function of the stress as described as the *mechanical strain*:

$$\varepsilon_{ij} = \frac{1}{E}\left((1+v)\sigma_{ij} - v\sigma_{kk}\delta_{ij}\right) \quad [9]$$

where *E* is the Young's Modulus of the rail steel, *v* is the Poisson's ratio and δ_{ij} is the Kronecker delta which, a function of two variables (*i* = *j*, $\delta_{ij} = 1$ and *i* ≠ *j*, $\delta_{ij} = 0$)

In terms of stress, this can be re-written in terms as Equation. 10:

$$\sigma_{ij} = \frac{E}{(1+v)}\left[\varepsilon_{ij} + \frac{v}{(1-2v)}\delta_{ij}\varepsilon_{kk}\right] \quad [10]$$

Λ and μ are called the lame's constants which are related to the Young's Modulus and Poisson's ratio as $\lambda = \frac{vE}{(1+v)(1-2v)}$ and $\mu = \frac{E}{2(1+v)}$.

2.4 Thermal consideration

As described in section one, the kinetic energy in conjunction with the friction between the rail head and the rail wheel is converted to heat energy. As stated in earlier sections, the heat flux *q(x,t)* will be derived from the conversion from kinetic energy to heat energy which obeys the law of conservation of energy at that instant. So, considering a speed used by trains during winter periods and thus with the average mass, the kinetic energy as suggested in Faramarz & Jalalifar (2009) can be evaluated, where *m* is the mass in one rail wheel corresponding to the average weight of the train.

$$E_k = \frac{1}{2}mv^2 \quad [11]$$

According to Milošević et al. (2012), the heat power to estimate the heat flux produced per unit contact area at the radius *r* of the rail wheel is given as:

$$q(x,t) = -f_f r\omega \quad [12]$$

Where f_f is the friction force per unit contact area, ω is the angular velocity of the rail wheel.

Based on frictional analysis, f_f can be evaluated as:

$$f_f = \frac{\mu F_N}{A} \quad [13]$$

μ is the coefficient of friction, F_N average normal braking force on in one rail wheel and *A* is the contact surface area (patch) between rail steel and one rail wheel.

2.4.1 Thermo-elasticity criteria

The consideration of the thermal effect on the constitutive equations will be evaluated. For the linear elastic condition in a continuum scale, the uniform temperature increase induce a thermal strain, which is added to the mechanical strain. Eqn.14 describes the thermal strain, which is a function of the temperature gradient and the coefficient of linear thermal expansion, α^*.

$$\varepsilon_{ij}^T = \alpha^* \nabla T \quad [14]$$

Adding this to the mechanical strain re-modifies the *mechanical strain* to give the equivalent strain amounting to an equivalent stress experienced in the rail steel. Equations 9 and 10 can be re-written as Equations 15 and Equation 16 for strain and stress based models, respectively.

$$\varepsilon_{ij} = \frac{1}{E}\left((1+v)\sigma_{ij} - v\sigma_{kk}\delta_{ij}\right) + \alpha^* \nabla T \quad [15]$$

$$\sigma_{ij} = 2\mu\varepsilon_{ij} + [\lambda\varepsilon_{kk} - \alpha^*(3\lambda + 2\mu)\nabla T]\delta_{ij} \quad [16]$$

2.4.2 Thermal wave speed via non-Fourier conduction model

It is important to determine the thermal wave speed of the transient heat flux across the rail steel as this would aid in estimating the extent across the rail length at which the heat flux and/or temperature is having an influence. By combining Eqn. (1) and (2) with Eqn. (5), the temperature distribution via Fourier and non-Fourier heat conduction, respectively as shown in Equation 17 (a) and 17 (b).

$$K\nabla T_{(x,t)}^2 - \left(\rho C_p\right)\frac{\delta T}{\delta t} = 0 \quad [17a]$$

$$K\nabla T_{(x,t)}^2 + \left(\rho C_p\right)\frac{\delta T}{\delta t}\left(1 - \tau_q \frac{\delta}{\delta t}\right) = 0 \quad [17b]$$

Equation. 17 (b) can be further expressed as a wave like- equation, which the thermal wave velocity can be defined accordingly. *C* (thermal wave velocity) can be taken as $\sqrt{\frac{\varphi}{\tau_q}}$ according to the 2nd order wave equation and can be extracted from Eqn. 17c. The Fourier heat conduction is not considered as its thermal wave speed is considered *infinite*.

$$\frac{\tau_q}{\varphi}\frac{\delta^2 T}{\delta t^2} + \frac{1}{\varphi}\frac{\delta T}{\delta t} = \nabla T_{(x,t)} \quad [17c]$$

where, $\varphi = \frac{K}{\rho C_p}$, the thermal diffusivity and.

2.4.3 Boundary conditions analysis and Temperature distribution (Fourier and non-Fourier) analysis

From the equations expressed in Eqn. 17, the temperature distribution can be attained along the steel rail. Before this can be attained, boundary condition is applied over the rail steel. By using a step function, the temperature from the point of contact between the rail wheel and the rail steel to the point of the flaw is fixed but then varies along the longitudinal direction of the rail steel. A defined boundary condition can be defined as:

$$T(x,t)_{x,t=0} = T_s \qquad T(x,t)_{x=0} = T_s$$
$$T(x,t)_{x=L} = T_a$$

For the Fourier heat conduction model as expressed by Eqn. 1, this can be combined with the energy Eqn. (5) to obtain partial differential equation with temperature as a function of position and time. By using the *separation of variables* based on Fab central notes (2024), the partial differential equations (PDE) can be reduced to systems of ordinary differential equations (ODE). As an approach to achieving this, an assumption can be made that the solution will depend on space and time as a product of terms that is subject to a single coordinate. Eqn. 18 shows the final expression of the temperature distribution in space and time for Fourier heat conduction.

$$T(x,t) = T_s - (T_s - T_a)\frac{4}{\pi}\sum_{n=1}^{\infty}\frac{1}{n}exp\left[-\left(\frac{n\pi}{2L}\right)\varphi t\right]sin\left(\frac{n\pi x}{2L}\right) \quad [18]$$

n =1,3,5…… iteration terms

For the non-Fourier heat conduction, the hyperbolic model from Cattaneo (1958) and Vernotte (1958) described in Equation 17c, can be solved analytically by using a pre-assumed solution that has the two independent variables, *x* and *t* and verifying if it satisfies all boundary conditions as adopted by Choi et al. (2016).

The pre-assumed solution for the temperature distribution is taken as Equation 19(a) and then applied to Equation 17(c) to attain Equations 19(b) and 19(c)

$$T(x,t) = Ae^{ax}e^{bt} \quad [19a]$$
$$\frac{b}{C^2}^2 Ae^{ax}e^{bt} + \frac{1}{\varphi}bAe^{ax}e^{bt} = a.Ae^{ax}e^{bt} \quad [19b]$$
$$\frac{b}{C^2}^2 - \frac{1}{\varphi}b = a \quad [19c]$$

Applying the boundary conditions to obtain A and solving for b in Eqn. (19c), A, a and b can be obtained and the final expression for the temperature distribution can be obtained using mathematical processing software packages like MATLAB or Mathematica.

2.4.4 Maximum braking temperature

The estimation of the maximum temperature can be attained during a braking operation. Several researchers as recorded in Marinescu et al. (2004) estimated that the maximum temperatures for the various flux distributions are very similar to a grinding wheel and workpiece. Thus, following the suggestions of Marinescu et al. (2004), the maximum temperature can be estimated as expressed in Equation 20.

$$T_s = C_{pn}.R_w.\frac{q_{(x,t)}}{\beta}\sqrt{\frac{l_c}{\omega}} \quad [20]$$

where $\beta = \sqrt{K.\rho.C_p}$, is the thermal property of the rail steel which is a factor of the density (ρ), thermal conductivity (K) and the specific heat capacity (C_p), l_c is the length of the contact zone (proposed to be half length of major axis of the elliptical area/patch during contact), C_{pn} is taken as 1.06 is a material parameter depending on the Peclet number. R_w is the proportion of the power which enters the rail steel from the abrasion effect from the wheels taken as 0.86 as recorded in Stolarski (1990) while $q_{(x,t)}$ is the heat flux as estimated from Equations 12. This invariable means that the braking power which is a function of weight, speed and coefficient of friction can be used in estimating the maximum temperature (T_s).

3 RESULTS AND DISUSSION

Since the analysis of the deformation is to be taken as a two-dimensional case, the different parameters need to be defined and some taken as a non-dimensional case. The axial force, *P* acting from the weight of the train, plays a vital role in the mechanical parameters (stress and strain experienced by the rail steel) and then the frictional force generated at the rail surface during a brake application plays another vital role to the heat flux generated at the tip of the rail steel surface.

In other that these two parameters are efficiently defined, other properties like the rail weight per axle, the speed, coefficient of friction between rail wheel and surface need to be known to ensure a proper application of the constitutive equations. Based on literatures, these parameters for the rail operations and rail steel properties were obtained respectively.

Table 2 Rail head mechanical properties and operating conditions

Parameters	Symbol	values
Height of rail head (m)[1]	*h*	0.269
Length between ties (m)[2]	*l*	0.6096
Young's Modulus rail steel (Gpa)[3]	*E*	193
Poisson ration ()[3]	*v*	0.3
Density (Kg/m^3)[4]	ρ	7800
Specific heat capacity (J/kg K)[4]	C_p	450
Thermal conductivity (W/K m)[4]	K	50
Linear expansivity (10^{-6}) (/^{o}C)[5]	α	3.167
Nominal wheel load per axle (kN)[4]	F_N	40-150
Velocity of the rail wheel (m/s)[4]	*v*	11.11-22.22
Coefficient of friction dry condition[4]	μ	0.6
Circular contact patch, (mm)[4]	l_c	70
Contact Area (a) (mm^2)[4]	*A*	154
2nd Moment of Inertia (mm^4)[1]	I_A	3.26*10^6

1. Liberty OneSteel . 2. Louisiana Transportation Research Center
3. Yu et al. (2016) 4. Vo et al. (2014) 5. Murphy & Zhao (2014)

The thermal wave speed from the point of contact to the base of the rail head was also considered. Figure 3 looks at the reduction in the speed in contrast to Fourier's heat condition that considers C as infinity.

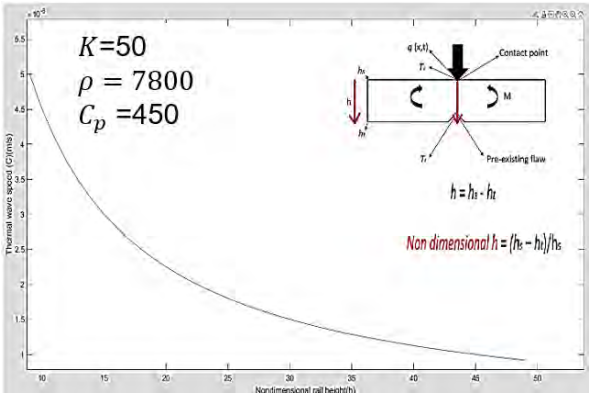

Figure 3. Thermal wave speed along rail head width

Figure 3 suggests a steep and high thermal speed closer to the contact zone which means temperature distribution is high but will reduce non-linearly across the length of the rail.

The maximum temperature that can be attained if an emergency-initiated brake is applied based on Equation 20 shows that the weight, friction and speed of the train before brake initiation are paramount to the difference in temperatures for similar speeds or masses. Figure 4 a variation of maximum temperatures for different masses and speed combinations. It is apparent that higher speed and higher tonnage produce higher *Ts* outcomes.

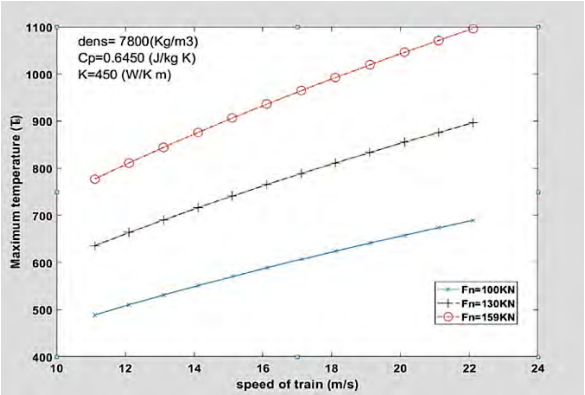

Figure 4. T_s variation with weight and speed

Figure 4 shows that even at the same speed, the duference in T_s increases with increasing tonnage. For instance, the diffeence between T_s between F_n as 100KN and 150KN repectively at 12m/s and 22m/s is laegly increased signifying there are potentiaslly more threats at higher speed and higher tonnage.

Using a T_s of 700°C and 400°C for this study, the temperature distribution along the x-axis of the rail head for both Fourier and non-Fourier heat conductions can be analyzed. Figure 5 shows the temperature distribution along the rail head.

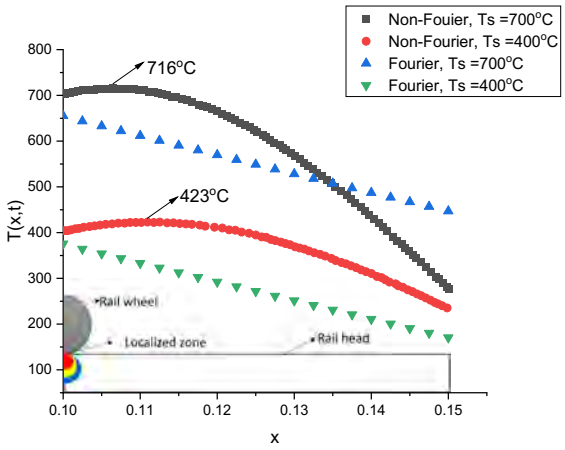

Figure 5. Temperature distribution along rail head

The figure shows that the temperature decreases from the point of heat flux generation. However, a slight increase in the temperature distribution for the non-Fourier heat conduction was seen, which tends to occur closer to the localized zone as the T_s value decreases. For the temperature distribution based on the Fourier heat conduction, a linear decrease was seen along the rail head. A max *T(x,t)* of 716°C and 423°C was observed for T_s value of 700°C and 400°C, respectively due to the time phase delay according to the non-Fourier heat equation (Equation 2), which causes a localized accumulation of heat flux.

With the description of the temperature distribution, the thermal strain part of the equivalent strain as described from Equation 14 can be estimated. The estimation requires determining the maximum *T(x,t)* value as well as the localized stresses due to the axial load on the rail head. First, the local stress is determined from the bending stress and the parameters given in Table 2 are used in attaining the mechanical stress in the elastic regime for a 2D case. With F_N as 40KN using in this study, σ_{xx} is taken as 503.01MPa, which is lower than the yielding stress as seen in Yu et al. (2016).

$$\sigma_{xx} = \frac{F_N \cdot \frac{L}{2} \cdot y}{I_A} = 503.01\text{Mpa}$$

where *y=h/2*

Applying Equation 17, ε_{xx} can be estimated with the assumption of σ_{kk} taken as a 1-D effect in the x-axis as seen in Table 3, where Fourier and non-Fourier effect were considered for an ambient temperature of -40°C.

Table 3 Equivalent strain at the localized heat zone

Heat conduction	T_s (°C)	*T(x,t)* (°C)	σ_{xx} (MPa)	ε_{xx}
Non-Fourier	700	716	503.01	0.00499
Fourier	700	622	503.01	0.00469
Non-Fourier	400	423	503.01	0.00407
Fourier	400	376	503.01	0.00392

Table 3 as an illustration, shows that more equivalent strain can be estimated for the non-Fourier heat conduction effect on the localized zone. This can cause unexpected rail breaks since the fracture strain at extreme cold temperatures decreases as seen from Yu et al. (2016).

Another challenge with the non-Fourier heat effect is that temperatures reaching as high as 716^{o}C as seen in Figure 5 are closer to the eutectic temperature of steel. At such condition air-cooled initiated quenching can occur changing the microstructure orientation due to the formation of hard secondary phases, thereby reducing the low temperature toughness or even causing distortions and cracking due to internal stress build-up.

4 CONCLUSIONS

The two different heat conduction models show temperature distribution along the rail head, providing an insight to the local effect of emergency braking during extreme cold climates. The non-Fourier heat conduction model apparently suggests that temperature build-up can occur different from the temperature at contact within the localized zone due to the time delay in its model while the Fourier heat conduction model just provides a linear decrease in temperature. This inevitably means that the equivalent strain are higher for non-Fourier heat conduction effect at the localized zone, which can contribute to unexpected fracture. However, in both cases, when T_s are very high at extreme cold temperatures, negative localized effects can occur within the rail steel's microstructure due to an air-quenched scenario occurring. Thus, this needs further study, experimentally and computationally to see the effect of air-quenching on the microstructural parameters like the grain size and interlamellar spacing and whether the non-Fourier model is captured in the experimentation outcomes. At this stage, recommendation of reducing train speed at extreme cold temperatures is the most appropriate and safest practice to employ.

5 ACKNOWLEDGEMENT

This research was made possible through the Canadian Rail Research Laboratory (www. carrl. ca). The funding for this project was provided by the Natural Sciences and Engineering Research Council of Canada (NSERC-IRC 523369-18), the Canadian National (CN) Railway, the National Research Council of Canada, and Transport Canada. Special thanks to Prof. Zengtao Chen during his lecture on Advanced Topics in Solid Mechanics I, which focused on smart materials and structures (MEC E 788).

REFERENCES

Babaei, M. H., & Chen, Z. (2010). Transient hyperbolic heat conduction in a functionally graded hollow cylinder. Journal of Thermophysics and Heat Transfer, 24(2), 325-330. https://arc.aiaa.org/doi/abs/10.2 14/1.41368

Carrera, E., Fazzolari, F. A., & Cinefra, M. (2016). Thermal stress analysis of composite beams, plates and shells: computational modelling and applications. Academic Press. https://doi.org/10.1016/B978-0-12-420066-1.00019-7.

Cattaneo, C. (1958). Sur une forme de l'equation de la chaleur eliminant la paradoxe d'une propagation instantantee. *Compt. Rendu*, *247*, 431-433.

Chen, Z., & Akbarzadeh, A. (2020). Advanced thermal stress analysis of smart materials and structures. Berlin: Springer.

FabCentral.http://fab.cba.mit.edu/classes/864.17/text/pde.pdf (accessed January 20, 2024)

Leishman, E. M., Hendry, M. T., & Martin, C. D. (2017). Canadian main track derailment trends, 2001 to 2014. Canadian Journal of Civil Engineering, 44(11), 927-934. Liberty OneSteel, Rail Track Material, http://www.libertyonesteel.com/. Accessed January, 2024

Marinescu, I. D., Rowe, W. B., Dimitrov, B., & Ohmori, H. (2012). Tribology of abrasive machining processes. William Andrew. https://doi.org/10.1016/B978-081551490-9.50007-4.

Murphy, R., & Zhao Ph D, W. (2012). Determining the Stresses in Steel Railroad-Track Rails Due to Freight Movements Using Non-Contact Laser-Speckle.

Okocha, S. I., Yu, F., Jar, P. Y. B., & Hendry, M. T. (2023). Use of a modified critical fracture strain model for fracture toughness estimation of high strength rail steels. Theoretical and Applied Fracture Mechanics, 127, 104069.

Railway Age, Easing winter's grip (2019). https://issuu.com/railwayage/docs/railway_age_digital_edition

Sobota T. (2014) Fourier's Law of Heat Conduction. In: Hetnarski R.B. (eds) Encyclopedia of Thermal Stresses. Springer, Dordrecht.

Talati, Faramarz & Jalalifar, Salman. (2009). Analysis of heat conduction in a disk brake system. Heat and Mass Transfer. 45. 1047-1059. 10.1007/s00231-009-0476-y.

Vernotte, P. (1958). Les paradoxes de la theorie continue de l'equation de la chaleur. *Comptes rendus*, *246*, 3154.

Vo, K. D., Tieu, A. K., Zhu, H. T., & Kosasih, P. B. (2014). A tool to estimate the wheel/rail contact and temperature rising under dry, wet and oily conditions. *Computers in Railways XIV: Railway Engineering Design and Optimization*, *135*, 191.

Wang, H. D. (2014). Theoretical and experimental studies on non-Fourier heat conduction based on thermomass theory. Springer Science & Business Media.

Yu, Feng & Jar, P.-Y & Hendry, Michael. (2015). Effect of temperature on deformation and fracture behaviour of high strength rail steel. Engineering Fracture Mechanics. 146. 41-55. 10.1016/j.engfracmech.2015.07.039.

Yu, Feng & Jar, P.-Y & Hendry, Michael. (2016). Critical Strain and Damage Evolution for Crack Growth From a Sharp Notch Tip of High-Strength Steel. V06AT06A029. 10.1115/PVP2016-63831.

Yu, Feng & Jar, P.-Y & Hendry, Michael. (2017). Fracture behavior at the sharp notch tip of high strength rail steels - Influence of stress triaxiality. Engineering Fracture Mechanics. 178. 10.1016/j.engfracmech.2017.04.034.

Session 5

INNOVATION AND EMERGING TECHNOLOGIES IN RAILWAY

Canadian & Cold Regions
Rail Research Conference
2024

Automated sensing data analyses for railway track gauge monitoring and defect detection

Tangjian Wei[1], Yili (Kelly) Tang[1,2,*], Xinyu Liu[1], Oliver Wang[3], Juan Hiedra Cobo[4], Mohamed Zaki Hussein[1]

[1] *Department of Civil and Environmental Engineering, University of Western Ontario (Western University), Ontario, Canada*
[2] *Department of Electrical and Computer Engineering, University of Western Ontario (Western University), Ontario, Canada*
[3] *ApoSys Technologies Inc, Ontario, Canada*
[4] *National Research Council Canada, Construction Resarch Centre, Ottawa, Canada*

ABSTRACT

Railway tracks are critical infrastructures that require continuous inspection and maintenance to ensure safety and reliability. Traditional inspections and maintenance require workers to be on-site and operate equipment to lay, maintain, and repair railway facilities. Recent advances have developed data-driven inspection methods to enhance railway maintenance safety and accuracy, such as mounting non-contact detectors and developing outlier analyses for defect detections, yet they are still scattered. This study develops automated sensing data analyses to identify, analyze and detect anomalies for railway track gauge monitoring through multi-sensing data including LiDar and GPS. Field data for this study was collected with a prototype of an electronic geometry inspection unit. Data synchronization and diagnoses from multiple sensors are conducted to match the location and time, and assess the quality of the collected data for inspection conditions such as location corrections and number of missing data. Results indicates distinguished patterns of track gauge characteristics including identification of new track, track gauge irregularity defects and rail crossings. The developed automation process to monitor track gauge conditions can provide real-time inspections and defect identification for maintenance planning and to improve operation safety.

1 INTRODUCTION

Railways are a vital component of public transportation, serving millions of people each day for travel and freight transport. Ensuring the safety and security of passengers and goods requires regular inspections of track geometry (Singh et al., 2019). Track geometry irregularities, which refer to any deviation from the prescribed minimum safety requirements for regulated standard gauge railway track, include issues such as surface (longitudinal profile) and horizontal (alignment / curvature) irregularities, gauge discrepancies, and super elevation / cross-level variations (Sharma et al., 2018). Notably, gauge irregularities can significantly reduce the lifespan of both rails and trains. They may lead to issues like derailments, excessive wear on tracks and rolling stock, and diminished ride comfort (Zheng et al., 2012). To maintain the safety and efficiency of rail operations, regular maintenance and monitoring, along with the implementation of advanced technologies, are critical for identifying and addressing gauge irregularities.

1.1 Literature review

Gauge measurement methods fall into two categories: contact inspection and non-contact measurement.

The conventional approach, manual Gauge Measurement, is a contact-based method. This technique employs tangible tools such as gauge rods and calipers. In railroad applications, a specialized ruler known as a track gauge measuring device measures the distance between the inner edges of the rails. The contact-type gauge inspection approach, noted for its high precision, has been developed and utilized extensively. However, contact-type gauge inspection systems are prone to damage due to vibrations and shocks affecting the sensors in contact with the rails. They also rely heavily on human labor and are sensitive to environmental factors, leading to slower inspection speeds (Wu et al., 2023).

As railway construction expands rapidly and train speeds and densities increase, the traditional contact mechanical measurement method falls short of current demands. This has led to the emergence of non-contact instrument measurement. Lewis (1984) introduced a method to calculate gauge by observing changes in the

light-dark interface of the rail head. This involves installing a photoelectric linear scanning device beneath a detection car, which receives reflected light from the rail head. The device calculates gauge values by monitoring changes in the light-dark interface. However, this method suffers from measurement errors and limitations due to the short lifespan of incandescent lamps used for illumination.

In recent years, computer vision has been employed for non-contact camera measurements, gaining widespread application in industrial monitoring, product inspection, and quality control (Bocciolone et al., 2007; Haigermoser et al., 2015; Tsunashima, 2008; Westeon et al., 2007). Karakose et al. (2017) described a method using a camera mounted atop a train to capture images of the current and adjacent rails. These images undergo edge and feature extraction to identify the rails. Gao (2020) explored a triangulation-based gauge measurement method using an LT3PU laser ranging sensor to collect geometric parameters at the gauge detection point. This method fits a curve equation to the collected data and the instrument, obtaining the instrument's current position value.

Recent study by Singh et al. (2019) have investigated using images from drones for track gauge measurement, and Wu et al. (2023) use the image data collected by the unmanned aerial vehicles to generate the point cloud of the railway scene. Then a hybrid segmentation algorithm based on enhanced region growth and improved alpha shape technique is used to extract tracks from chaotic scene data. And the pre-constructed railway Building Information Model used to match with the extracted railway features to determine the gauge. However, the accuracy of these methods using drones and unmanned aerial vehicles may require further enhancement.

1.2 Organization of this paper

In this paper, a gauge calculation method based on LiDAR detection is proposed and corresponding gauge patterns are analyzed. A nonlinear transformation model of the spatial attitude relationship between two LiDAR camera sensors is established to find the distance between two rails within 16 mm under the rail top tread according to the definition of gauge. The method presented in this paper has the characteristics of high stability, simple structure, fast calculation speed and high detection accuracy.

The rest of the paper is organized as follows. Section 2 introduces the track monitoring process and data structure. Section 3 explains data fusion and calibration methods. Section 4 presents the assessment and analyses of track gauge patterns based on the integrated data. Section 5 concludes the paper.

2 DATA STRUCTURE

The gauge is defined as the distance between the inner points of the left and right rails 5/8 inch (16 mm) below the top surface (Transport Canada, 2023).

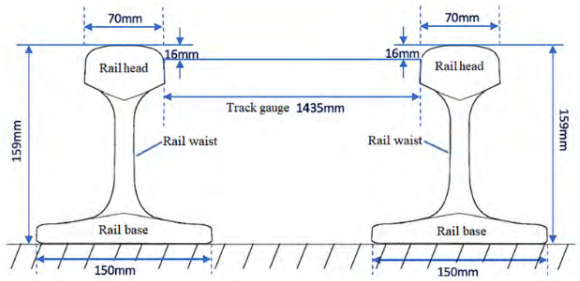

Figure 1. Definition of track gauge (Transport Canada, 2023; Wu et al., 2023)

In the experiment, two lidar sensors are used, deployed on both sides of the train bottom. One lidar sensor was facing the left track of the rail, and the other was facing the right track of the rail. The detection range was a 90-degree sector, with a nominal distance of 34cm from the lidar sensor to the top of rail,, which could precisely scan the shape of the rail. The detector detects the rail at a frequency of 100 Hz. GPS sensors are also used for time and location synchronizations.

The obtained data mainly includes the x-axis data, and z-axis data that are saved in separate files. Each set of data contains a scanning time. In the data file, there are 500 rows of data, each with 2049 columns. The first column records the date and time when the data occurred, and the data in the following 2048 columns is distance detected data by the lidar sensor. Each row of data represents data that occurred at different points in time. The data on the x-axis and z-axis are combined to form the detection point.

Figure 2 shows an example of Lidar's data, with each row representing a set of x-axis or z-axis data corresponding to different time points. The first column of the data stores the exact time point, while the other columns represent the data detected by the Lidar sensor. This includes both zero and non-zero data. The value of zero represents invalid data, indicating that no object was detected within the effective detection range. Other nonzero data represents feedback value which means lidar detecting objects. The data on the x-axis and z-axis data can be combined to obtain the points on their plane.

	0	1	2	3	4	5	6	7	8	9	...	2039	2040
0	23-06-2023 17 13 30.902937	0.0	0.0	0.0	0.0	0.0	0.0	0.0	0.0	0.0	...	-189.753905	-189.916803
1	23-06-2023 17 13 30.903567	0.0	0.0	0.0	0.0	0.0	0.0	0.0	0.0	0.0	...	-189.738031	-189.892975

Figure 2. Lidar data example

3 PROCESSING OF MEASURED DATA

To calculate the gauge of the railway track, it is necessary to convert the data to the same plane for calculation. So, the data is preprocessed based on the scanning angle and position of the lidar sensor.

For the data rotation, detecting the data on the left rail requires a 135-degree rotation, while the direction of the right and left lidar sensors is exactly opposite. Hence, the

data on the right rail needs to be rotated by -135 degrees. We use formulas (1), (2), and (3) for rotation to convert data on the x and y axes.

$$\theta = \frac{degree}{180} \cdot \pi \quad [1]$$

$$x = x' \cdot \cos\theta - z' \cdot \sin\theta \quad [2]$$

$$z = x' \cdot \sin\theta + z' \cdot \cos\theta \quad [3]$$

Then, based on the positions of the two lidar sensors, the data of the x and z axes are translated. According to formula (4), the corresponding data of the x-axis is added with the required displacement value of the x-axis. According to formula (5), the data of the z-axis is added with the value of the z-axis displacement as shown in Figure 2.

$$x = x + x_{displacement} \quad [4]$$

$$z = z + z_{displacement} \quad [5]$$

Finally, the gauge is calculated using two points 16 millimeters below the top of rail to determine the distance between the tracks. Firstly, the positions of the highest points on the left and right sides of the rail surface are calculated to obtain their coordinates, subtract 16 millimeters from the z-axis of the two coordinates, and then find the corresponding value on the x-axis. At this point, the coordinates of the two points are obtained, and the distance between the two points is calculated using the Euclidean distance formula (6). The calculated distance will be the corresponding gauge.

$$d = \sqrt{(x_1 - x_2)^2 + (z_1 - z_2)^2} \quad [6]$$

All correct points and calculated gauges will be visualized to obtain Figure 3.

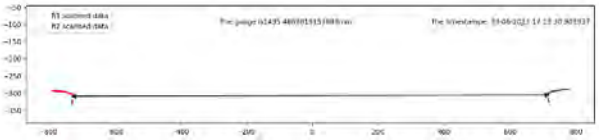

Figure 3. Railway visualization

4 GAUGE ANALYSIS

4.1 Data collection

We used our prototype monitoring equipment to collect data for a railway segment with length of 183 miles (294.4 km). With the 2 LiDAR sensors, which are nominally installed symmetrically with the same but opposite angle of 38.2° respect to the vertical, we collected the x-axis and z-axis data information of 8973 points. Formula (6) is used to obtain the gauge information about these points. Part of the data information is shown in Table 1 below.

Table 1. Partial collection point data information

Points	mileage	point1_x	point1_y	point2_x	point2_y	gauge
1	326.0873	-694.5991382	-321.4129962	742.8202511	-326.4089803	1415.428071
2	326.0873	-694.4466345	-321.5990836	740.091905	-326.5474327	1412.547074
3	326.0873	-694.553117	-321.3648018	741.6496305	-326.3401955	1414.211366
4	326.0873	-694.4220628	-321.3909143	741.488303	-326.3827606	1413.919043
5	326.0873	-694.7525243	-321.3503645	741.6245898	-326.2996911	1414.385641
6	326.0875	-690.153398	-325.2658539	731.5436602	-330.1754732	1399.705536
7	326.0875	-689.9463232	-325.3868756	731.6069818	-330.2837832	1399.561739
8	326.0875	-718.10044	-349.536117	730.989093	-353.3479901	1427.094547
9	326.0875	-717.8003467	-349.6514971	731.3053086	-351.5474571	1427.106896
10	326.0875	-717.7178711	-349.4920112	731.5999251	-353.4384587	1427.323169

4.2 Gauge pattern analysis

Gauge values of 8973 points collected above are shown in the following Figure 4. It can be seen from this figure that the gauge of most points is around 1435mm, which indicates that the gauge of most points is in line with the standard gauge requirements; In addition, there were some fluctuations in the gauge of the initial points, and some fluctuations in the gauge values occurred at points 4700 to 5000, 7700 to 8100, and 8300 to 8400. In order to further analyze the gauge fluctuation of these points, gauge diagrams are drawn for the above areas respectively, as shown in Figures 5 to 8.

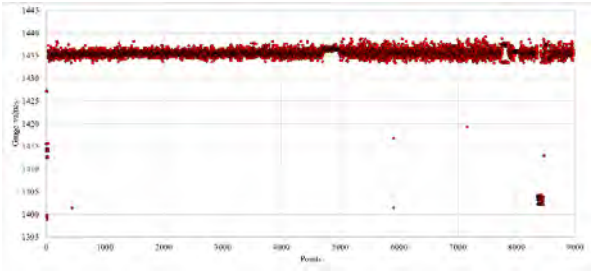

Figure. 4. Gauge information of all points

Figure 5 below shows the gauge information from point 1 to point 100. It can be seen from the figure that the gauge values from point 1 to point 35 fluctuates frequently, and the fluctuations are concentrated around 1400mm, 1415mm and 1427mm. At the same time, it can be seen from Figure 4 that after point 35, the gauge stabilized around 1435mm, which may be because the data acquisition system was unstable just when it started, or certain vibration was generated when it was just started, resulting in fluctuations in the gauge. It is suggested that a certain buffer time should be given to the system initialization in the follow-up data acquisition and measurement.

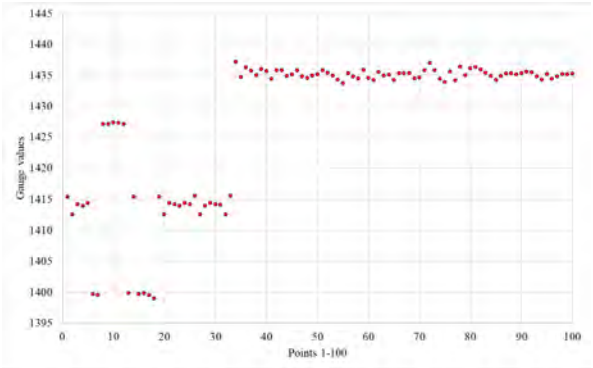

Figure. 5. Gauge information of points 1-100

Figure 6 shows the gauge value information from point 4501 to point 5300. As it can be seen from the figure, the gauge of point 4720 to point 4950 is slightly greater than 1435mm. At the same time, compared with the surrounding area, the variability of the gauge in this section is relatively small. In general, the gauge fluctuation in other areas is slightly larger than in this section.

There are two possible reasons for the gauge of the section from point 4720 to point 4950 to be slightly larger than that of the surrounding area: 1) there may be a rail wear or deformation in the section, resulting in a slightly larger gauge; 2) Or the rail track has been updated in the area, and the gauge of new track is slightly larger than the surrounding area. As for the specific cause of the above condition, it is necessary to obtain additional data like maintenance information or on-site verification to verify the reason.

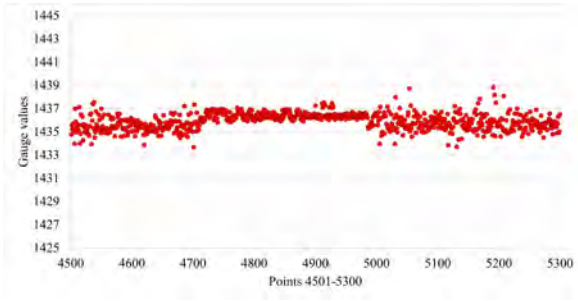

Figure. 6. Gauge information of points 4501-5300

Figure 7 shows the gauge value information from point 7501 to point 8300. In this figure, there are two sections with variable gauge values: the gauge from point 7750 to point 7880 fluctuates between 1433mm and 1437mm; The concentration of point 7950 to point 8060 is 1436mm and the concentration degree is significantly higher than that of the surrounding area. The first abnormal section (points 7750-7880) may be caused by equipment such as railway line crossings or switches, and the second abnormal section (points 7950-8060) may be caused by rail wear.

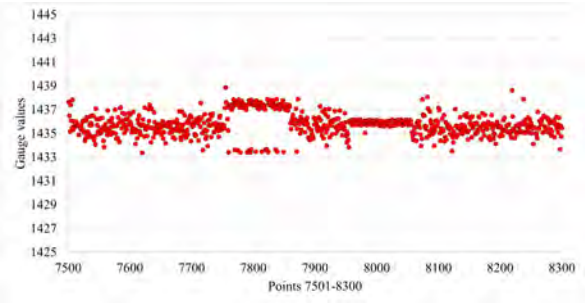

Figure. 7. Gauge information of points 7501-8300

Figure 8 temporarily shows the last abnormal gauge section. It can be seen from Figure 8 that the gauge of the section from point 8355 to point 8455 fluctuates from 1402mm to 1437mm, while the gauge from point 8355 to point 8410 and from point 8420 to point 8455 is about 30mm lower than the standard gauge. The resulting smaller gauge may be caused by line crossing, and the specific reasons can be further verified by on-site verification or other data source information (such as picture source information).

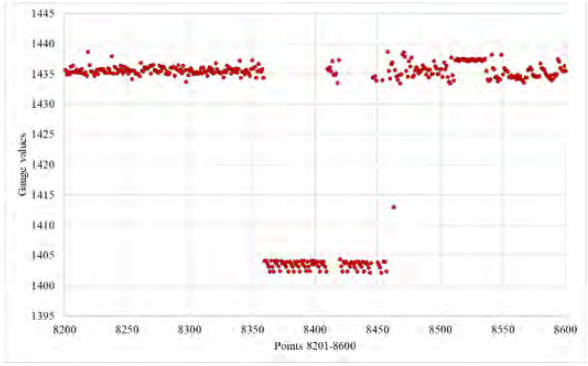

Figure. 8. Gauge information of points 8201-8600

5 SUMMARY

This study develops rail track monitoring and gauge analysis method to calibrate track gauge conditions and identify gauge characteristics for maintenance and rail operation management. Sensing techniques are used including LiDars and GPS for an automated process to collect and calibrate the rail track gauges. There are also limitations of the LiDar techniques where the measurement accuracy can be affected by weather, physical obstructions and calibrations. Results indicate a variety of differentiated patterns are identified including new track, defects and railway crossings which can provide informative references for operators to quantify the rail track conditions. The developed methods also open new avenues for railway maintenance and monitoring including defect development monitoring and maintenance schedule optimizations. Future studies can also focus on rail track wears and dynamic defect monitoring.

6 ACKNOWLEDGEMENT

The authors wish to thank the editors and anonymous reviewers. This study is supported by the Natural Sciences and Engineering Research Council of Canada (ALLRP 586566) and Mitacs (IT36952). Also thanks to ApoSys Technologies Inc. and the National Research Council of Canada - Construction Research Centre.

REFERENCES

Bocciolone, M., Caprioli, A., Cigada, A., Collina, A., 2007. A measurement system for quick rail inspection and effective track maintenance strategy. *Mechanical Systems and Signal Processing* 21, 1242-1254.

Gao, A.C.X.L.L., 2020. Research on track gauge measurement system based on sensor. *Intelligent Computer and Applications* 02, 5.

Haigermoser, A., Luber, B., Rauh, J., Gräfe, G., 2015. Road and track irregularities: measurement, assessment and simulation. *Vehicle System Dynamics* 53, 878-957.

Karakose, M., Yaman, O., Baygin, M., Murat, K., Akin, E.J.I.J.o.M.E., Research, R., 2017. A new computer vision based method for rail track detection and fault diagnosis in railways. 6, 22-17.

Lewis, R., 1984. Track-recording techniques used on British Rail, *IEE Proceedings B (Electric Power Applications)*. IET, pp. 73-81.

Sharma, S., Cui, Y., He, Q., Mohammadi, R., Li, Z., 2018. Data-driven optimization of railway maintenance for track geometry. *Transportation Research Part C: Emerging Technologies* 90, 34-58.

Singh, A.K., Swarup, A., Agarwal, A., Singh, D., 2019. Vision based rail track extraction and monitoring through drone imagery. *ICT Express* 5, 250-255.
Transport Canada, 2023. Rules Respecting Track Safety.

Tsunashima, H., 2008. Condition monitoring of railway tracks using in-service vehicles: development of probe system for track condition monitoring. *Japanese railway engineering* 48.

Westeon, P.F., Ling, C.S., Roberts, C., Goodman, C.J., Li, P., Goodall, R.M., 2007. Monitoring vertical track irregularity from in-service railway vehicles. *Proceedings of the Institution of Mechanical Engineers, Part F: Journal of Rail and Rapid Transit* 221, 75-88.

Wu, J., Peng, L., Sheng, W., Wang, C.C., Sun, J., 2023. Track gauge measurement based on model matching using UAV image. *Automation in Construction* 155, 105070.

Zheng, S., Chai, X., An, X., Li, L., 2012. Railway track gauge inspection method based on computer vision, *IEEE International Conference on Mechatronics and Automation*, pp. 1292-1296.

Canadian & Cold Regions
Rail Research Conference
2024

Comparative investigation of field measured Insertion Loss of railway track with FEM and 1-DOF theoretical models

M. Hassan Esmaeili[1], Reza Mousapour[2], Yazdan. M. Haft-Cheshmeh[3]
[1,3]Department of Railway Engineering and Transportation Planning, Faculty of Civil Engineering and Transportation, University of Isfahan, Isfahan, Iran
[2]Department of Civil and Environmental Engineering - University of Alberta, Edmonton, Alberta, Canada

ABSTRACT

In railway operations, the excessive vibration is likely to affect infrastructures, passengers, or surrounding environment. Therefore, it is important to design a reliable vibration mitigation measure (VMM) for track system. The effectiveness of VMM is quantified using insertion loss (IL), which is defined as the level of the vibration reduced in every center frequency as the consequence of using VMM. A higher value of IL indicates more reduction capabilities of the track. To estimate the IL value of a track system, various methods are employed, including finite element (FE) and field measurement techniques. There exists a gap in the technical literature for comparing these methodologies. This paper aims to address this gap by measuring the IL of track in the field compared with corresponding values obtained from FE and one-degree of freedom (1-DOF) model. The study demonstrates that IL values predicted by FEM and 1-DOF are under-estimated in frequencies less than 30 Hz, while it is overestimated in frequencies more than 64 Hz (From 30 to 64 Hz the IL values are similar). In frequencies more than 64 Hz where the theoretical models overestimate the IL values (The differences reaches to 26 decibels), the design of VMM could be controversial, especially in the marginal values of the IL.

1 Introduction

Insertion loss (IL) is an important parameter for showing the vibration reduction capabilities of the railway track (Costa et al., 2012; Diego et al., 2017; Kraśkiewicz et al., 2018; Kraskiewicz et al., 2021; Quagliata et al., 2018; Sol-Sánchez et al., 2015; Zbiciak et al., 2021). This parameter is used to evaluate the effectiveness of vibration mitigation measures (VMM) for railway tracks, expressing the reduction/amplification values in decibel versus frequency (Di Meglio & Wang, 2000; He et al., 2021; Kaewunruen et al., 2018). Therefore, it is now a distinguishing parameter in the design phase of projects when various VMM's like floating slab mat (Sol-Sánchez et al., 2015), high resilient fasteners (Sadeghi et al., 2020) and mass spring systems (interface "Using High-Performance Mass-Spring Systems to Reduce Noise and Vibration in Track") are intended to be used in railway projects (Ngamkhanong & Kaewunruen, 2020; Pandrol, 2014).

A review of literature shows that there are various methods for approximating IL values in railway track systems including: laboratory measurement (45673-1, 2010; 45673-2, 1995; 45673-3, 2004; Bolmsvik & Linderholt, 2015; Di Meglio & Wang, 2000), field measurement with artificial excitation (Barlow & Asia-Pacific, 2004; Bolmsvik & Linderholt, 2015), field measurement with train excitation (Kraśkiewicz et al., 2023), and theoretical methods like one degree of freedom (1-DOF) (Barlow & Asia-Pacific, 2004; Rantatalo & Xin, 2013) or FEM modeling (Isolgomma, 1972). There is sometimes considerable difference in IL values derived from these approaches which may considerably affect vibration design of railway track system. Therefore, it is needed to know how much various techniques are different when used to derive the IL of one VMM. This is addressed in the current work.

In order to have an estimate of the amount of difference between IL derived from various techniques, the values of IL are measured in a railway track under operation and is compared with corresponding values derived from FEM and 1-DOF model of railway track system. Measurements are done in a Metro system located in Shiraz metro with typical slab track system floated on an elastomer layer made from polyurethane.

2 Field measurement of insertion loss

The IL values are measured in Shiraz metro line 2. The properties of the site are presented in Table 1. The IL is measured while the train passed with the speed varying from 10 km/h to 40 km/h. The track structure is Rehda-2000 (Mundrey, 2010). Slab track system is floated on elastomer mat made from polyurethane. The track substructure is lean concrete with average thickness of 60 cm, rested on the reinforced concrete of the tunnel lining

with the thickness of 40 cm. Figure 1 showed the schematic view of metro line structure.

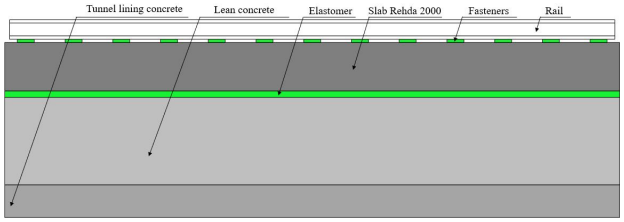

Figure 1. Typical cross section of metro line structure

Table 1: Characteristic of field for IL measurement

Item	Specification
Test location	Shiraz Metro Line 2, UTM coordinate: X:29.61013, Y:52.52109
Rail	UIC54E1
Fastener	Vossloh W14 with resilient rubber pads
Slab track	Rehda-2000 (Di-block sleepers, thickness: 400 mm)
Elastomer	Full support elastomer mat, thickness 25mm
Train	Five car Metro train, passing speed: 10 to 40 km/h, Axle load: 13.5-ton, dimensional properties showed in Fig. 2.

The train used in the test is a five-car metro train manufactured in CRRC Nanjing Puzhen Co (CHU et al.). The geometrical characteristic of the train is presented in Figure 2.

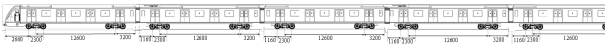

Figure 2. Dimensional characteristics of five-car metro train used for measurements of IL

In order to measure the IL, the track is instrumented in four locations including on the ground level (ST04), on the rail (ST03), slab (ST02), and close to the slab (ST01). A view of instrumented points on the ground and on the track, level is presented in Figure 3.

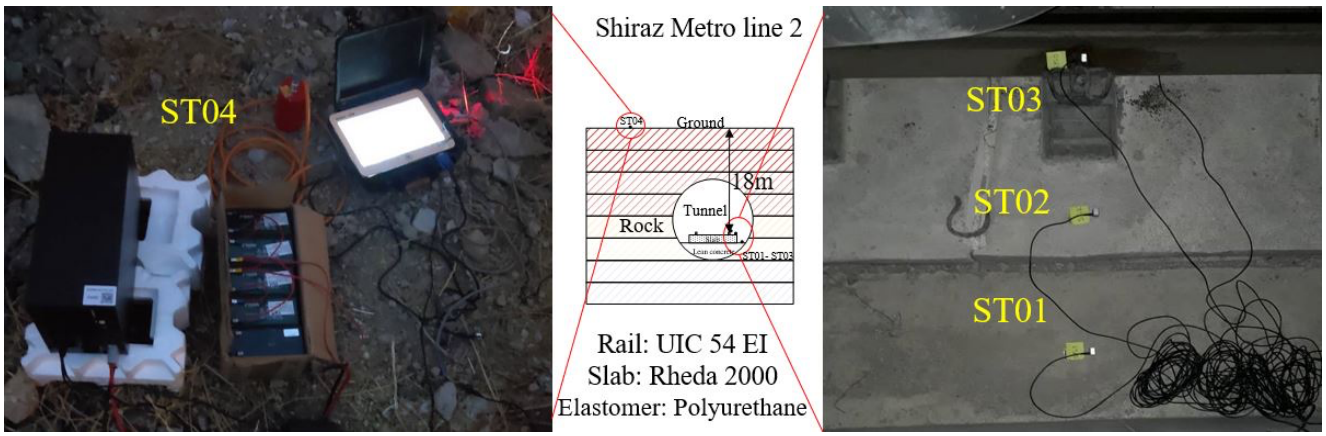

Figure 3. Track and ground instrumentation setup for measurement of insertion loss in Shiraz Metro Line 2

3 Numerical estimation of insertion loss

In order to theoretically calculate the IL from FEM model, a two-dimensional Finite Element Model (FEM) of track/tunnel and soil system is developed in the ABAQUS software (Figure 4). The two-dimensional plane-strain model of the slab track structure is then used to derive the values of IL in every pass of train with various speeds. The whole model consists of definition of geometry, material properties, loading conditions, meshing and boundaries explained as follows:

3.1. Geometrical properties of the model

The model of train-track and soil is a 100×30 meters' rectangle with to circular TBM tunnels at the center. The dimensions is showed that is sufficient for simulation of the railway wave propagation problems (Manual, 2012). The large dimensions of the model along with the thickness and width of the soil layers avoids the vibration waves to reflect from the boundaries which may cause error in the results of the model. Infinite elements are also placed at the boundaries of the model to properly simulate the real conditions of the waves coinciding the boundaries of the model. A view of the model developed in this work is presented in Figure 4.

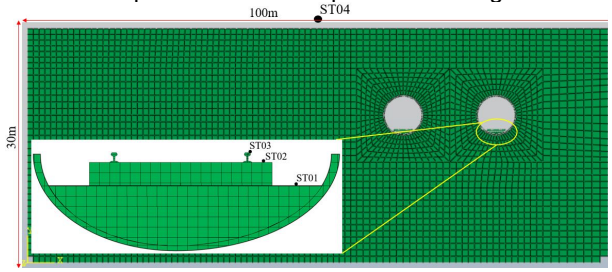

Figure 4. Two-dimensional model of train-track-tunnel and ground system used to calculate insertion loss

The properties of each element considered in the FE simulations is listed in Table 2. These parameters are taken from documents of the Shiraz Metro (Hegza, 2017). As mentioned in this table, the behavior of all materials is considered to be linear elastic witch matches to the real mechanical behavior of the materials. Note that considering the very low value of strains generated from rail vibrations, the stress-strain relation of all materials remains in the linear region.

Table 2: Material parameters used in the FE model of train-track-tunnel and soil system

Item	Material	Elastic Modulus (MPa)	Poison ratio	Density (kg/m^3)	Damping ratio
Soil	Rock	2500	0.37	1900	0.04
Tunnel lining	Concrete	17000	0.25	2400	0.01
Lean concrete	Concrete	25000	0.25	2800	0.01
Concrete slab	Concrete	25000	0.25	2800	0.01
Elastomer	Polyurethane	0.55	0.35	130	0.103
Rail pad	Natural rubber	20	0.3	1100	0.075
Rail	Steel	210000	0.3	7850	0.007

One important parameter in modeling the whole system is material damping, which is simulated here using well known Rayleigh-damping model (Ma et al., 2016). In this method, the damping matrices is proportional to both mass and stiffness matrices (Cui et al., 2021) written by:

$$[C]=\alpha[M]+\beta[K] \qquad [1]$$

where, [*M*], [*K*] and [*C*] are mass, stiffness and damping matrices, respectively. *α* and *β* are damping coefficients of materials taken based on the method explained in (Cui et al., 2021; Ma et al., 2016).

3.2. Boundary conditions and train load

In order to satisfy the right radiation condition of the vibration waves coinciding the boundaries of the model, two approaches are addressed in the literature; first: To place tangent and normal spring and dashpots at the boundaries (Connolly et al., 2013); second: Using infinite elements at the boundaries (Connolly et al., 2013). In current research infinite elements are defined at lateral sides of the model. In addition, roller supports were used at the bottom of the model, which have freedom in the horizontal direction and is fixed in the vertical direction.

The train load also could be considered in two ways; first: to insert a sequence of load time histories in the model (Sadeghi & Esmaeili, 2017); second: Transient load of the train is modeled using DIOAD subroutine (Connolly et al., 2013). DIOAD subroutine is used in this work. In this subroutine the location of every single wheel load on the rail (*P*) is calculated using the following equation:

$$P = X - (Vt - \frac{L}{2}) \qquad [2]$$

In which *L* is the length of Hertz contact ellipse in m, *V* is the train speed in m/s, *t* is time passed from the start of the run expressed in s, and *X* is the X-coordinate of the wheel initial position on the rail.

4 DOF model of insertion loss

1-DOF model of track system is a handy tool that companies usually use it to derive the value of the IL (Getzner, 2015). The schematic view of the model is presented in Figure 5. As showed, the model consists of a mass, (the summation masses of the rail, slab and wheel), a dashpot (Corresponded to the damping values of the elastomer), and spring (Corresponded to the values of the stiffness of the elastomer). The frequency dependent *IL* could then be calculated using the following equation:

$$IL = 20\times\log(\frac{[1-TR]}{[1-TR_R]}) \qquad [3]$$

Where *TR* is the transmissibility of the system (maximum load in the base to the values of the load exerted to the mass (f_{max} (t)) of the system), when the elastomer is used in the track. *TR* is calculated using the following Equation:

$$TR = \frac{f_{\max}(t)}{P_0} = \frac{1}{\sqrt{(1-\beta^2)^2+(2\times\xi\beta)^2}}\times[1+(2\times\xi\beta)^2]^{1/2} \qquad [4]$$

TR_{ref} is the value of the *TR* where no elastomer is used in the track. β is the ratio of input frequency to the natural frequency of the system, and ξ is the damping ratio of the elastomer.

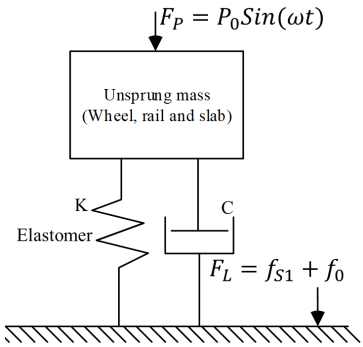

Figure 5. 1-DOF model of track system used in insertion loss calculation

5 Result of theoretical model and field measurements

Time and frequency domain of measured vibrations compared with the corresponding values derived from FEM is presented in Figure 6. As showed, the pick vibrations of every wheel passing the track is obviously reflected in the time domain signal. It is also showed that the frequency content of the vibrations is occurred in the center frequency of 64 Hz. It is showed that the result of field and model has acceptable agreement.

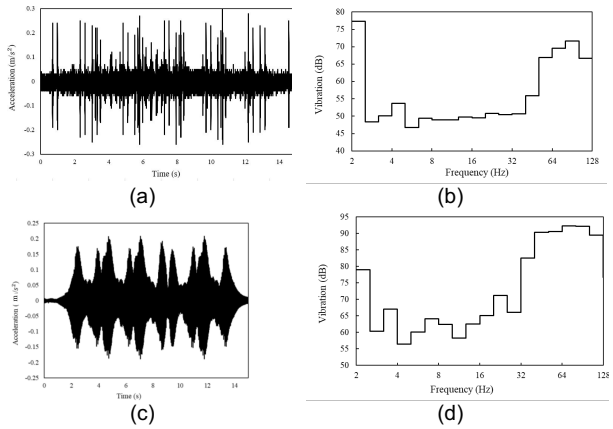

Figure 6. Time and frequency domain of measured vibrations at ST01 compared with FEM (a) time domain of field measurement in the tunnel, (b) frequency domain of field measurement in the tunnel, (c) time domain of FEM in the tunnel and (d) frequency domain of FEM in the tunnel

The values of IL measurements compared with FEM at the train passing with the speed of 35 km/h is presented in Figure 7. As showed, the track system is capable to reduce the vibrations up to 40 dB, depending on the frequency.

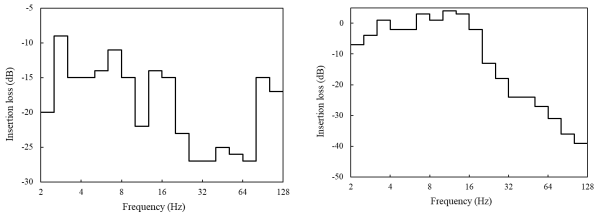

Figure 7. Insertion loss measurement compared with the results of FEM analysis for points located in the tunnel (a) Field measurement and (b) FEM, Train speed: 35 km/h

6 Discussion

The values of IL derived from filed measurements, FEM model and 1-DOF is summarized in Figure 8. According to this figure, based on the difference between measurements and theoretical models (FEM and 1DOF), the graphs could be compared in three frequency regions, say 1-32 Hz, 32-64 Hz and 64-110 Hz. In 1-32 Hz region, the theoretical models underestimate the IL values compared with measurement. From 32 to 64 Hz, theoretical models match measurement results. The 64 to 110 Hz is the region where the IL derived from theoretical models is overestimated.

In 1-32 Hz region, the theoretical models underestimate the IL values compared with measurement. This means that the capability of the real VMM is expected to be more than what has reported in the design phase. In other word, the VMM works beyond what is estimated in the design phase of the railway project. Moreover, from the figure, the theoretical calculations show that the vibrations are intensified in the vicinity of 8 Hz, while the results of the measurement do not show such a phenomenon.

In the region of 32 to 64 Hz, the results of the theoretical approaches match with the measurements, which could be considered as the region where the simulations could be directly related to those of the measurements.

The findings of this work shows that region of 64 to 110 Hz is crucial in the design phase of railway track, because the theoretical models give more credit to the VMM. As showed in Figure 8, the theoretical models have estimated much more values of IL compared to the amount each VMM is able to cover in reality. Therefore, the designer should be aware when considers the reduction of the vibrations in the frequency range of 64 to 110 Hz. Maybe a factor of safety could be considered in this region.

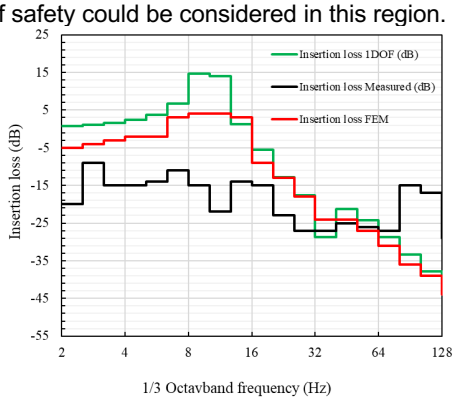

Figure 8. Insertion loss values derived from filed measurements compared with the results of theoretical models (i.e., 1-DOF and FEM)

7 Conclusion

Theoretical and experimental methods used for calculating insertion loss (IL) of railway track systems are compared in this work. IL is defined as the capability of vibration mitigating measures (VMM) to reduce railway vibrations. The IL values directly measured in a Metro line is compared with the corresponding values of two well-known theoretical approaches i.e. A 1-DOF track model and finite element model of the slab track system. According to the IL values derived from theoretical models and filed measurement, following conclusions are derived:

1. The values of the IL estimated by theoretical models from 1 to 32 Hz are less than the corresponding values derived from the field. This means that, the VMM is expected to be more efficient in practice in reducing the vibrations. Moreover, the theoretical calculations show that the vibrations are intensified in the vicinity of 8 Hz, while the results of the measurement do not show amplification of the vibrations.
2. In the frequency range of 32 to 64 Hz, the theoretical models have IL values similar to those measured in the field.
3. From the frequency range of 64 to 110 Hz, there should be specific considerations in the design of VMM, because the theoretical methods

overestimate the vibration reduction capability of the track system. The theoretical models have estimated up to 26 decibels more reduction for VMM. This could be a challenging issue specially when the vibrations are to be reduced close to sensitive building/equipment. In this region it is suggested to consider a factor of safety when the design of VMM is intended.

8 Acknowledgement

Our gratitude is given to the Shiraz Urban Railway Organization (SURO), for their support during field measurements. This research was undertaken in the Department of Railway Engineering and Transportation Planning, Faculty of Civil Engineering and Transportation, University of Isfahan,

REFERENCES

C. Kraskiewicz, A. Zbiciak, K. Wasilewski, and A. Al Sabouni-Zawadzka, “Laboratory Tests and Analyses of the Level of Vibration Suppression of Prototype under Ballast Mats (UBM) in the Ballasted Track Systems,” Materials (Basel), vol. 14, no. 2, Jan 9, 2021.

M. Sol-Sánchez, F. Moreno-Navarro, and M. C. Rubio-Gámez, “The use of elastic elements in railway tracks: A state of the art review,” Construction and building materials, vol. 75, pp. 293-305, 2015.

A. Zbiciak, C. Kraśkiewicz, S. Dudziak, A. Al-Sabouni-Zawadzka, and J. Pełczyński, “An accurate method for fast assessment of under slab mats (USM) performance in ballastless track structures,” Construction and Building Materials, vol. 300, pp. 123953, 2021.

C. Kraśkiewicz, A. Zbiciak, W. Oleksiewicz, and W. Karwowski, “Static and dynamic parameters of railway tracks retrofitted with under sleeper pads,” Archives of Civil Engineering, vol. 64, no. 4/II, 2018.

P. A. Costa, R. Calçada, and A. S. Cardoso, “Ballast mats for the reduction of railway traffic vibrations. Numerical study,” Soil Dynamics and Earthquake Engineering, vol. 42, pp. 137-150, 2012.

S. Diego, J. Casado, I. Carrascal, D. Ferreño, J. Cardona, and R. Arcos, “Numerical and experimental characterization of the mechanical behavior of a new recycled elastomer for vibration isolation in railway applications,” Construction and Building Materials, vol. 134, pp. 18-31, 2017.

A. Quagliata, M. Ahearn, E. Boeker, C. Roof, L. Meister, and H. Singleton, Transit noise and vibration impact assessment manual, 2018.

A. Di Meglio, and L. S. Wang, “A variational method for identification of viscoelastic parameters from experimental data,” The Journal of the Acoustical Society of America, vol. 108, no. 6, pp. 2746-2753, 2000.

W. He, C. Zou, Y. Pang, and X. Wang, “Environmental noise and vibration characteristics of rubber-spring floating slab track,” Environmental Science and Pollution Research, vol. 28, no. 11, pp. 13671-13689, 2021.

S. Kaewunruen, C. Ngamkhanong, M. Papaelias, and C. Roberts, “Wet/dry influence on behaviors of closed-cell polymeric cross-linked foams under static, dynamic and impact loads,” Construction and Building Materials, vol. 187, pp. 1092-1102, 2018.

J. Sadeghi, M. Seyedkazemi, and A. Khajehdezfuly, “Nonlinear simulation of vertical behavior of railway fastening system,” Engineering Structures, vol. 209, pp. 110340, 2020.

A. h. i. c. a. interface “Using High-Performance Mass-Spring Systems to Reduce Noise and Vibration in Track”.

C. Ngamkhanong, and S. Kaewunruen, “Effects of under sleeper pads on dynamic responses of railway prestressed concrete sleepers subjected to high intensity impact loads,” Engineering Structures, vol. 214, pp. 110604, 2020.

Pandrol Co., "Track report,", Delachaux Group SA, 2014.

Å. Bolmsvik, and A. Linderholt, “Damping elastomers for wooden constructions–Dynamic properties,” Wood Material Science & Engineering, vol. 10, no. 3, pp. 245-255, 2015.

DIN. 45673-3, "Messtechnische Ermittlung der Einfügungsdämmung in eingebautem Zustand (Prüfaufbau und Betriebsgleis) bei Ersatzanregung," Part 3, 2004.

DIN. 45673-2, "Vibration measurement associated with railway traffic systems," Part 2, 1995.

DIN. 45673-1, "Terms And Definitions, Classification, Test Procedures,"Part 1, 2010.

S. C. Barlow, and P. Asia-Pacific, "Field measurements of slab track vibration to demonstrate the insertion loss of low stiffness rail fasteners." pp. 23-30.

C. Kraśkiewicz, A. Zbiciak, J. Pełczyński, and A. Al Sabouni-Zawadzka, “Experimental and numerical testing of prototypical under ballast mats (UBMs) produced from deconstructed tires–The effect of mat thickness,” Construction and Building Materials, vol. 369, pp. 130559, 2023.

M. Rantatalo, and T. Xin, “Review of countermeasures and regulations for railway induced ground vibrations in tunnels,” Luleå University of Technology & Luleå Railway Research Center, 2013.

Isolgomma. "https://www.isolgomma.com/railway-antivibration-solution/railway-anti-vibration-mats/," https://www.isolgomma.com/railway-antivibration-solution/railway-anti-vibration-mats/.

J. Mundrey, “Tracking for high-speed trains in india,” RITES Journal, vol. 7, pp. 1-16, 2010.

Y.-p. CHU, S.-l. LIU, X.-g. MA, L. ZHANG, and W. TIAN, “Intelligent Assembly Technology of Railway Vehicle Bogies.”

ABAQUS user guide manual, “Transient modal dynamic analysis,” Section 6.3.7, 2011.

Hegza, Pavement design The middle part of the metro line of Shiraz, 2017.

M. Ma, W. Liu, C. Qian, G. Deng, and Y. Li, “Study of the train-induced vibration impact on a historic Bell Tower above two spatially overlapping metro lines,” Soil Dynamics and Earthquake Engineering, vol. 81, pp. 58-74, 2016.

X. Cui, Z. He, B. Huang, Y. Chen, Z. Du, and W. Qi, “Study on the effects of wheel-rail friction self-excited vibration and feedback vibration of corrugated irregularity on rail corrugation,” Wear, vol. 477, pp. 203854, 2021.

D. Connolly, A. Giannopoulos, and M. Forde, “Numerical modelling of ground borne vibrations from high speed rail lines on embankments,” Soil Dynamics and Earthquake Engineering, vol. 46, pp. 13-19, 2013.

J. Sadeghi, and M. H. Esmaeili, “Safe distance of cultural and historical buildings from subway lines,” Soil dynamics and earthquake engineering, vol. 96, pp. 89-103, 2017.

Getzner Co., "Mass spring system", Jürgen Rainalter, 2023.

Canadian & Cold Regions
Rail Research Conference
2024

A quantitative evaluation of the impact of railway track characteristics on the magnitude of dynamic loads

Danial Behnia & Michael T. Hendry
Department of Civil and Environmental Engineering, University of Alberta, Edmonton, Alberta, Canada

ABSTRACT

The main purpose of this research is to investigate the influence of various track characteristics on the magnitude of dynamic loads in terms of dynamic load factor (ϕ). The ϕ value is crucial for analyzing, designing, and selecting rail steel and cross-sectional (weight) characteristics. An extensive trial on a 340 km Canadian Prairies track section, operated by a North American Class 1 freight railway, utilized a train-mounted system with the instrumented wheelset (IWS) and MRail measurement systems. The study utilized continuous measurements along the entire track, including tangent sections, curves, bridges, grade crossings, and switches. The evaluation of observable track characteristics reveals significant influences on dynamic load ranges and ϕ values, particularly pronounced in non-tangent tracks such as curves, switches, crossings, and bridges. New ϕ equations are developed for tangent and non-tangent tracks (including bridges, grade crossings, curves, and switches). Track surface variations significantly impact ϕ values, leading to a 15-36% increase in dynamic load magnitudes, deviating from prevalent design practices. Assessing subgrade track stiffness conditions demonstrates a critical association with observable increases in ϕ values, potentially increasing dynamic load magnitudes by 20-30%. In curved sections, heightened subgrade track stiffness may increase dynamic loads in the lower rail, especially in tracks with average to poor conditions. An investigation into transition directions indicates that transitions from soft-to-stiff conditions amplify dynamic loads, while stiff-to-soft transitions attenuate them. This analysis emphasizes the contribution of subgrade track conditions to the effectiveness of transition direction influence. These quantitative insights provide an opportunity to optimize maintenance schedules promptly, preventing rail breaks.

1 INTRODUCTION

In Canada, rail breaks and failures of track components are the leading causes of train derailments (Leishman et al., 2017). These derailments tend to happen at faster train speeds than other causes, making them higher in energy and resulting in a greater number of cars derailing. This also makes the cars' contents more likely to be released. Given the ongoing rail failures, revisiting our understanding of the magnitude of dynamic loads exerted on the rail is valuable. This is crucial for ensuring the safety of train operations and preventing accidents caused by rail malfunctions and fractures.

From the track structure point of view, the dynamic train-track interaction is influenced by two major factors: changes in track geometry and variations in track subgrade stiffness (Sussman et al., 2001; Lundqvist & Dahlberg, 2005; Dahlberg, 2010). The former refers to the three-dimensional spatial orientation of railway tracks (Selig & Waters, 1994; Hyslip, 2002; Li et al., 2016), while the latter refers to the stiffness of the foundation beneath the track. These factors contribute to the increasing and fluctuating nature of the dynamic interaction between trains and tracks. The track structures, such as bridges, grade crossings, and switches, also affect the dynamic loads along the track. The impact of track structures on the magnitude of dynamic loads along the track is not fully understood.

The dynamic load factor (ϕ) is an important parameter in railway design as it provides a measure of the dynamic loads experienced by the track. The ϕ value in railway engineering refers to the ratio between the vertical wheel-to-rail loads generated by a moving train (dynamic loads, P_d) and the static loads (P_s) resulting from the weight of the rail car and its contents (Equation [1]) Peters, 2010; Sadeghi, 2012; Van Dyk et al., 2017; AREMA, 2021). This factor is often calculated as a function of train speed. Engineers commonly use the ϕ values and the evaluated dynamic loads in designing track structures or the selection of rail steel and cross-sections (weight) (Peters, 2010; Sadeghi, 2012; AREMA, 2021). The ϕ equations vary from simple linear train speed functions to more complex ones considering wheel diameters, track modulus, and empirical factors.

$$\phi = P_d / P_s \quad [1]$$

Research on train-track dynamic interaction has a long history and remains a critical area of study in railway dynamics and design. However, despite the significance

of track structures, geometry, and subgrade stiffness, there is a significant gap in the understanding of how these factors impact the magnitude of dynamic loads experienced along the track. One limitation with the current understanding of dynamic load magnitudes along the track is that they have been evaluated based on measured dynamic loads from trains as they pass over an instrumented section of track (Dybala & Radkowski, 2013; Van Dyk et al., 2017; Yu & Hendry, 2019). This method captures the variety of loads from different rolling stock types (locomotives and a variety of cars), axle loads, and wheel conditions, but it only represents a specific type of well-maintained straight track, which might not reflect the typical or most extreme conditions for generating dynamic loads.

This study utilized three primary datasets collected from a 340 km section of a North American Class 1 freight railway line. The datasets include the instrumented wheelset (IWS), MRail system, and track surface geometry measurements. The IWS and MRail systems captured vertical dynamic loads and vertical track deflection (VTD) while moving, offering insights into dynamic load variations across diverse track conditions and assets (such as bridges, grade crossings, curves, and switches) at operational train speeds on a Class 1 freight railway main line. However, they are limited to loads from a single car with a specific suspension type, wheel diameter, and static load. The research also investigates track surface changes, specifically focusing on rail surface variations. This focus is driven by the established relationship between rolling contact fatigue (RCF), variations in the rail surface, and wheel-rail dynamic excitation.

This paper presents the IWS, MRail, and rail surface data sets along the section of track studied, statistical distributions of considered parameters, a comparison of ϕ values derived from the IWS measurements to the most common ones for North American freight railways (AREMA 2021). The ϕ values are evaluated versus train speed for differing track conditions, and track assets (tangent, curved, bridges, grade crossings, and switches) to develop ϕ equations. Then, impacts of the track surface roughness and track subgrade conditions are evaluated against the developed equations and the AREMA values. The data is also evaluated within the range of speeds permissible on North American classes of track (1 through 4).

2 MATERIALS AND METHODS

The data for this study was collected from a 340 km (212 miles) section of track operated by a North American Class 1 freight railway through the Canadian Prairies. This section of the track is part of a high-traffic subdivision and facilitates the transportation of annual freight loads exceeding 50 million gross tonnes (MGT). The evaluated rail track includes more than 30 bridges, one tunnel, 100 grade crossings, and 50 switches. Approximately 230 km of the track is straight, while around 83 km is curved. The rail is continuously welded and is supported primarily by concrete ties.

Specialized rail vehicles are used to regularly monitor track geometry in Canadian freight railways. These vehicles traverse the network and take measurements every 0.305 m (1 ft.) along the track. As mentioned earlier, the rail surface is one of the critical parameters in track geometry measurements that can play an important role in wheel/rail dynamic interactions and rolling contact fatigue (RCF). It is defined as the vertical deviation of the rail from a straight-line reference chord (62 ft.) projected onto the vertical plane. The rail surface is typically characterized by two parameters: hump (i.e., lifted zone; positive values) and dip (i.e., fall-off or depression zone; negative values). For this study, these measurements resulted in a track geometry database containing more than 1.23×10^6 rail surface measurements.

The IWS and MRail data were collected from the instrumentation mounted on a 15.8 m (52 ft) gondola car loaded with gravel weighing 1175 kN (264 kips). One end of the instrumented car was fitted with IWS and MRail systems (Figure 1). These systems measured dynamic load magnitudes at the wheel-rail interface and vertical track deflection (*VTD*).

The IWS data was collected during four passes of the study site, with trains traveling in both directions, between July and August 2015 at speeds of up to 95 km/h (59 mph). The MRail data utilized in this investigation were recorded during two passes in the same direction in July 2015, with a maximum operational train speed of 82 km/h (51 mph). These measurements were taken while the car was in revenue service, as part of a freight train, without control over the type or weight of adjacent cars or the travel speed. Such limitations are common when studying Class 1 North American freight railway tracks.

Figure 1. Photograph the train-mounted system with instrumented wheelset (IWS) and MRail systems installed on the Gondola railcar to collect the data used for this study (image credit: Michael T. Hendry).

3 PRESENTATION OF RESULTS

Figure 2 presents the distribution of the magnitude of measured vertical dynamic loads by track type (tangent and curve) and features (switch, crossing, and bridge) derived from all four IWS wheels and across all four passes. There is a significant variation in the data obtained for each track type: tangent track accounted for 69.9% of the collected data, curves accounted for 24.7%, bridges accounted for 1.6%, grade crossings accounted for 2.2%, and switches accounted for 1.6%. The statistical values representing these distributions are presented in Table 1. These distributions are naturally normal, with mean and median values close to the static load (144 kN), as shown in Table 1. Among the various track types, tangent sections exhibit the narrowest distribution and the fewest extreme values [Figure 2(a)]; this is followed by the curved track and bridges with very similar distributions [Figure 2(b)], and grade crossings and switches with similar distributions.

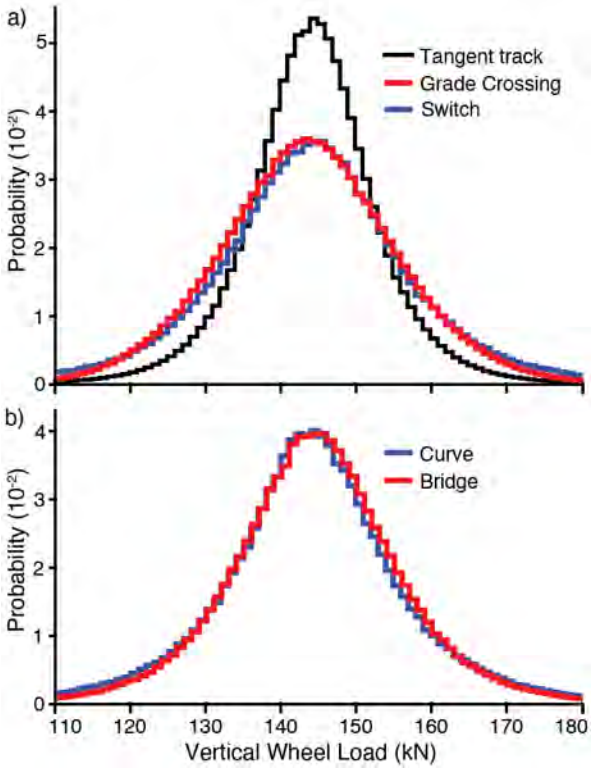

Figure 2. Probability distributions of vertical load measurements from the IWS: (a) on tangent track, grade crossings, and switches; and (b) on curves and bridges. Note that data includes all four instrumented wheels and all four passes (*after* Behnia et al., 2022).

The evaluation of rail surface measurements concerning different track features, as illustrated in Figure 3, reveals that the measurements follow a normal distribution. The similarity in the shapes of the distributions for tangent and curve tracks indicates that the rail surface conditions are statistically similar in these two track features. Other track assets exhibit similar distribution patterns, including grade crossings, bridges, and switches. The mean values of rail surface measurements across different categories exhibit consistent uniformity and are approximately zero. Grade crossings and switches exhibit notably higher maximum values than other track elements. Specifically, grade crossings demonstrate the highest standard deviation in rail surface fluctuations. However, the most substantial overall variations in rail surface deviations are observed in track assets, namely bridges, grade crossings, and switches.

Table 1. Statistical measures from probability distributions of dynamic vertical load measurements from the IWSs (*after* Behnia et al. (2022)).

Type	μ (kN)	Median (kN)	σ (kN)	Maximum (kN)
All	143.9	144.1	11.3	384.4
Tangent track	143.9	144.2	10.9	384.4
Curved section	143.7	143.6	12.2	292.8
Bridge	144.6	144.6	12.4	288.9
Grade crossing	144.2	144.1	13.1	264.2
Switch	144.1	144.1	14.4	302.5

Note: Data includes all four instrumented wheels, and all four passes; μ= mean; and σ=standard deviation.

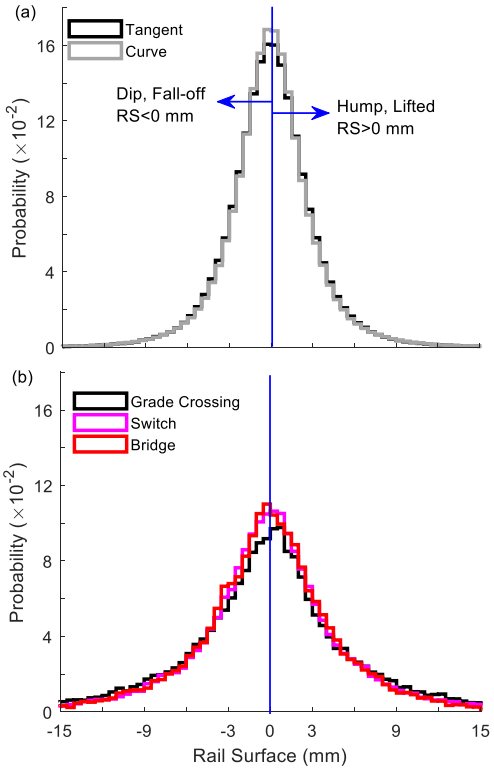

Figure 3. Probability distributions of track geometry measurements (available datasets) from the track geometry car: (a) rail surface on tangent and curve tracks; and (b) rail surface on grade crossings, switches, and bridges.

To evaluate the impact of subgrade track stiffness (VTD_{sub}) on dynamic load magnitudes, the MRail

measurements were used to obtain vertical track deflection (*VTD*) values. The vertical track deflection (*VTD*) data underwent a filtering process to characterize subgrade stiffness. Thus, the initial phase involved calculating VTD_{sub} values. Roghani and Hendry (2016) outlined a methodology for gauging subgrade and embankment stiffness (VTD_{sub}) via *VTD* measurements. This process was designed to eliminate noise of lower wavelengths, which could be attributed to structural conditions and imperfections on the track surface (Roghani & Hendry, 2016). A moving average filter was employed for its straightforward application and effectiveness in noise reduction while retaining step responses (Smith, 1997) (Equation [2]). The objective of this procedure was to attenuate the effects of surface anomalies and defects, thereby reducing the potential for noise within the collected data. The moving average technique was applied at consistent intervals of 20 meters, as this interval was determined to provide optimal resolution for detecting subgrade characteristics (Roghani & Hendry, 2017). Variations in subgrade track stiffness, denoted as ΔVTD_{sub}, are quantified by calculating the secant slope of the vertical track deflection with respect to the subgrade (VTD_{sub}) over a given distance (d) (Roghani & Hendry, 2017). This distance represents the length of the track under consideration. The secant slope is determined by the absolute value of the rate of change of VTD_{sub} concerning the distance, as expressed in (Equation [3]).

$$VTD_{sub}(i) = \frac{0.305}{L}\sum_{-L/(2)(0.305)}^{L/(2)(0.305)} VTD[i+j] \quad [2]$$

$$\Delta VTD_{subR}(x_i) = VTD_{sub}(x_i + d/2) - VTD_{sub}(x_i - d/2)/_d \quad [3]$$

Figure 4 displays the probability distributions of VTD_{sub} measurements. Roghani and Hendry (2017) categorized subgrade track conditions into three classifications based on AREMA (2021) thresholds: *'good'* (VTD_{sub}≤ 3.1 mm), *'average'* (3.1 <VTD_{sub}≤ 4.4 mm), and *'poor'* (VTD_{sub}> 4.4 mm), which are demarcated by vertical blue lines in the figure. Figure 4(a) compares the statistical distributions for tangent and curved tracks, revealing their similarity. A detailed analysis of the curved sections indicates that most data points are from the high (outer) rail, often associated with better (*'good'*) track conditions. The observed trend in the distribution of curve section data (i.e., high and low rails) suggests that poor track conditions can lead to increased dynamic loads on the low (inner) rail. In contrast, Figure 4(b) shows consistent statistical distribution patterns for bridges, grade crossings, and switches, demonstrating uniformity in VTD_{sub} measurements across these diverse track structures.

Variations in subgrade track stiffness, denoted as ΔVTD_{subR}, play a crucial role in the dynamic behavior of rail tracks. A positive ΔVTD_{subR} (Δ>0) signifies a transition from a stiff to a soft state, while a negative ΔVTD_{subR} (Δ<0) indicates a shift from a soft to a stiff state. Our study of tangent sections shows that a soft-to-stiff transition tends to increase the dynamic load magnitude, while a stiff-to-soft transition decreases it. Figure 5 presents the probability distributions of ΔVTD_{subR} across various track structures, including tangent sections, curves, grade crossings, bridges, and switches. As depicted in Figure 5(a), the distributions for tangent tracks and curves are similar, suggesting similar behavior in these track sections. Both tangent and curve section distributions are symmetric, indicating that the majority of the stiffness variations are concentrated around the mean (μ~0). However, the curve section has a slightly broader spread than the tangent track, indicating a higher standard deviation or variability in subgrade track stiffness for curve sections. Figure 5(b) demonstrates that grade crossings, bridges, and switches share comparable distribution patterns. Their probability distributions are symmetric and centered around the mean (μ~0), but they have a wider spread compared to tangent and curve sections, indicating greater variability in stiffness changes for these structures.

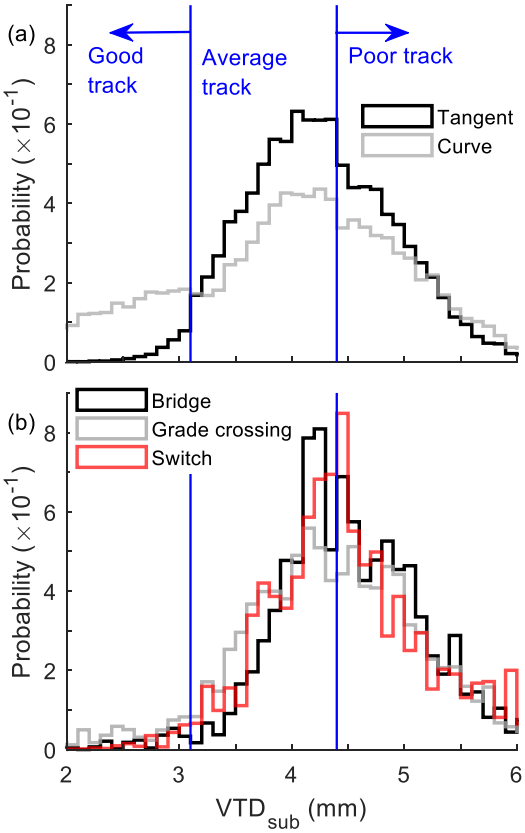

Figure 4. Probability distributions of VTD_{sub} measurements from the MRail system: (a) on tangent and curve sections; and (b) on bridges, grade crossings, and switches. The data are from both rails and both passes. The graph is segregated into three sections by blue lines, indicating good (VTD_{sub}≤3.1), average (3.1<VTD_{sub}≤4.4), and poor (VTD_{sub}>4.4) tracks.

4 DISCUSSION

The ϕ equations are generated using the upper envelope of measured dynamic loads, such that they can be used as design loads. Using the maximum measured dynamic loads from the IWS system results in very high ϕ values (>2.6), significantly higher than predicted by any of the

other ϕ equations (within the range of train speeds for which measurements at which IWS measurements were obtained. These outlier values must be excluded, and many methods exist to do so (ASTM, 2021). Some of the existing ϕ equations were generated by using 3σ, or the 99.9th percentile, as an upper value exclusive of outliers (Sadeghi & Barati, 2010), and this threshold is used within this analysis due to this precedence. An alternative method for the removal of outliers recommended by ASTM (2021) is the Grubbs' test, which is effective for data sets with near-normal distributions (Grubbs, 1969; Pearson, 2005) (Figure 3). The Grubbs' test determines a Grubbs' value (G) at which μ is the mean value of the sample, σ is the standard deviation, x_i is the value of the i^{th} element of the data set (Equation [4]).

$$G = \frac{max_{i=1,\dots,n}|x_i - \mu|}{\sigma} \quad [4]$$

The current investigation considered the provided equation by AREMA (Equation [5]) used to estimate ϕ values to evaluate how the considered track characteristics influence the magnitude of dynamic load (in terms of ϕ) since this is the most prevalent and accepted ϕ value within the field.

$$\phi = 1 + 5.21\frac{S}{D} \quad [5]$$

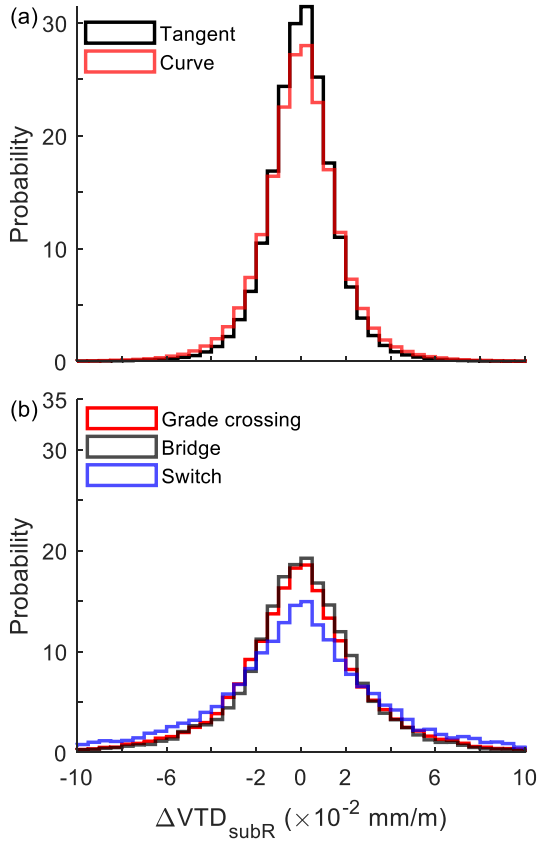

Figure 5. Probability distributions of variations in subgrade track stiffness, in terms of ΔVTD_{sub}, based on measurements from the MRail system for: (a) tangent track and curve sections; and (b) bridges, grade crossings, and switches. Note: the data includes both rails and both passes.

This study evaluates three key factors contributing to variations and increasing dynamic interaction at the wheel/rail interface: observable track structures, surface roughness, and subgrade track stiffness. The subsequent sections will individually assess the impact of these parameters on the magnitude of dynamic loads.

4.1 Quantifying the Effect of Observable Track Structures

Regarding the similar statistical distributions of the measurements collected for grade crossings, switches, curves, and bridges (as shown in Figure 2), all of these non-tangent track data were grouped together. In contrast, the tangent track exhibited a narrower distribution, indicating a distinct behavior. Consequently, the data was categorized into two groups: tangent and non-tangent. Quadratic equations were then fitted to the ϕ values, derived using the Grubbs' test, for both groups. These equations delineate the potential range of ϕ values that tangent and non-tangent sections may encounter in service.

$$\phi_{Tan} = 3 \times 10^{-5}S^2 + 1.4 \times 10^{-3}S + 1.19 \quad [6]$$

$$\phi_{NTan} = 3 \times 10^{-5}S^2 + 2.5 \times 10^{-3}S + 1.27 \quad [7]$$

Figure 6 compares the estimated ϕ values by AREMA (2021) and Behnia et al. (2022) for both tangent and non-tangent tracks. The equations provided in this study, based on IWS measurements, consistently indicate higher ϕ values than those suggested by AREMA across all speed ranges. This comparison implies that the AREMA model might underestimate the dynamic load factor, even for tangent tracks, when compared to the model proposed by Behnia et al. (2022)- in this study. In tangent sections, the disparities between these models become more apparent, particularly at lower speeds. In non-tangent sections, the AREMA model significantly underestimates the dynamic load magnitude, which could have profound implications for track design and maintenance.

4.2 Quantifying the Effect of Track Surface Roughness

Rail surface measurements are divided into two categories: humps, with positive deviations, and dips, with negative deviations. Since these measurements typically follow a normal distribution centered around zero, this study focuses on the absolute values of rail surface deviations, represented as |RP|. It was necessary to align datasets to assess the impact of rail surface changes on vertical load magnitudes. Track geometry was recorded every 0.3 meters, while load measurements varied with speed and were taken at 0.005-second intervals. A window length of 20 meters was chosen for analysis based on maintenance practices and previous studies, with a 95% overlap ratio determined to be optimal for quality results. This research primarily examines the |RP|max in each section.

The previous section demonstrated through statistical analysis that dynamic load intensity can be categorized into tangent and non-tangent tracks. The similarity between rail surface changes in curves and tangent tracks and load variations in curves and track assets necessitated the separation of curves as a distinct

category. Consequently, data were sorted into tangent track, curve track, and track assets.

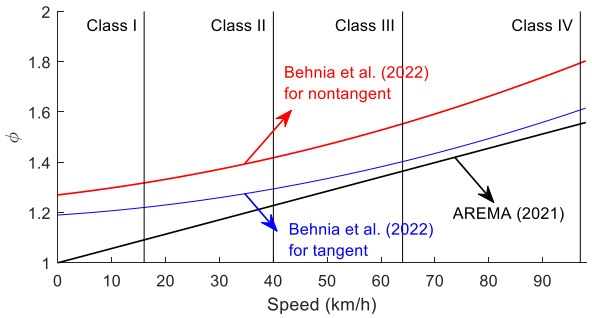

Figure 6. Comparison of estimated dynamic load factor values by AREMA (2021) and Behnia et al. (2022) (developed separately for tangent and nontangent tracks).

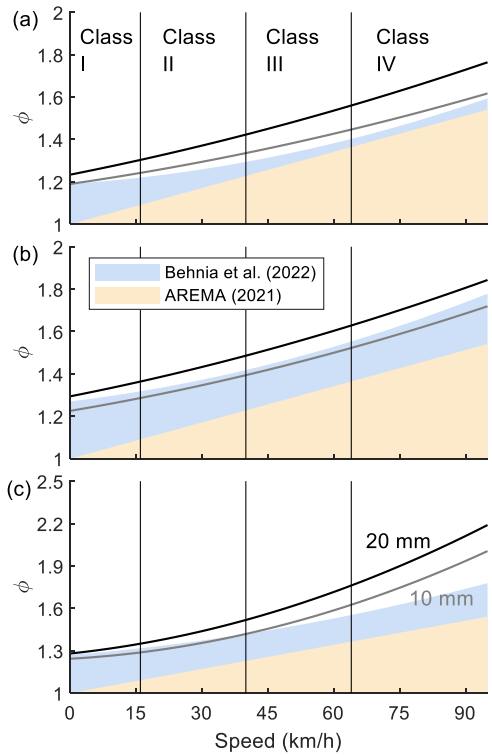

Figure 7. Comparison of estimated values by AREMA (2021) and Behnia et al. (2022) and fitted lines regarding the considering scenarios (i.e., $|RP|_{max} < 10\,mm$, $|RP|_{max} < 20\,mm$, and $|RP|_{max} < 24\,mm$) for rail surface in: (a) tangent track, (b) curve, and (c) track assets (i.e., grade crossings, bridges, and switches).

Two scenarios were defined based on rail surface conditions: a high-frequency range (<10mm) and an upper bound of the typical range (<20mm). Figure 7 compares these scenarios with AREMA (2021) and Behnia et al. (2022) (i.e., the provided equations in the previous section). In tangent tracks, AREMA's values were 20% lower than the upper bound line, while Behnia et al. reported a 15% discrepancy. For high-speed trains (class 4) on track assets, such as grade crossings, bridges, and switches, the observed values exceeded the estimates by 50% for AREMA and 30% for Behnia et al. This understanding has significant implications for the design and maintenance of railway tracks, as underestimating dynamic loads could lead to insufficient infrastructure robustness and increased wear or failure rates.

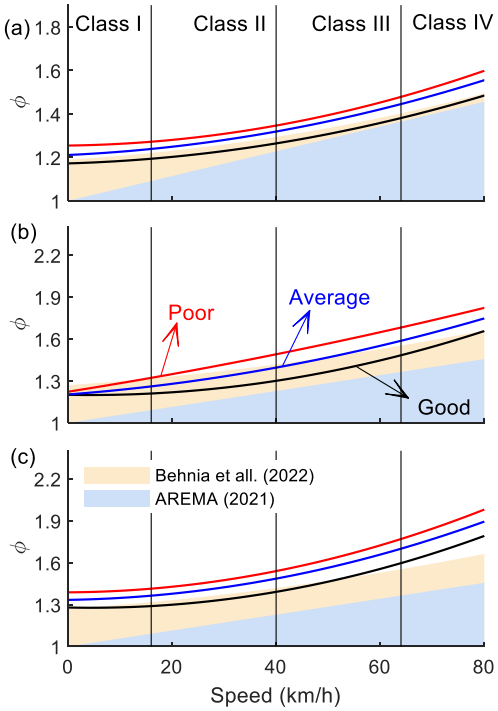

Figure 8. Comparison of estimated ϕ values by AREMA (2021) and Behnia et al. (2022) based on the subgrade track stiffness conditions (i.e., good, average, and poor tracks) in: (a) tangent track; (b) curve; and (c) track assets (inclusive of grade crossings, bridges, and switches).

4.3 Quantifying the Effect of Subgrade Stiffness Conditions

The statistical properties of dynamic loads and VTD_{sub} measurements necessitate a classification into three distinct categories: tangent track, curve, and track assets (including grade crossings, bridges, and switches). This classification is crucial for setting a specific threshold value, which is used to evaluate the impact of VTD_{sub} on the magnitude of dynamic loads. Based on the available dataset and observed statistical distributions, a threshold value of $\phi \geq 1.1$ is deemed suitable for subsequent evaluations.

To better understand the impact of subgrade conditions, trendlines are fitted to the data under three scenarios: good, average, and poor subgrade conditions. Figure 8 shows the nonlinear trendlines fitted onto available data, considering different track characteristics and subgrade conditions. These trendlines reveal that poor subgrade sections exceed

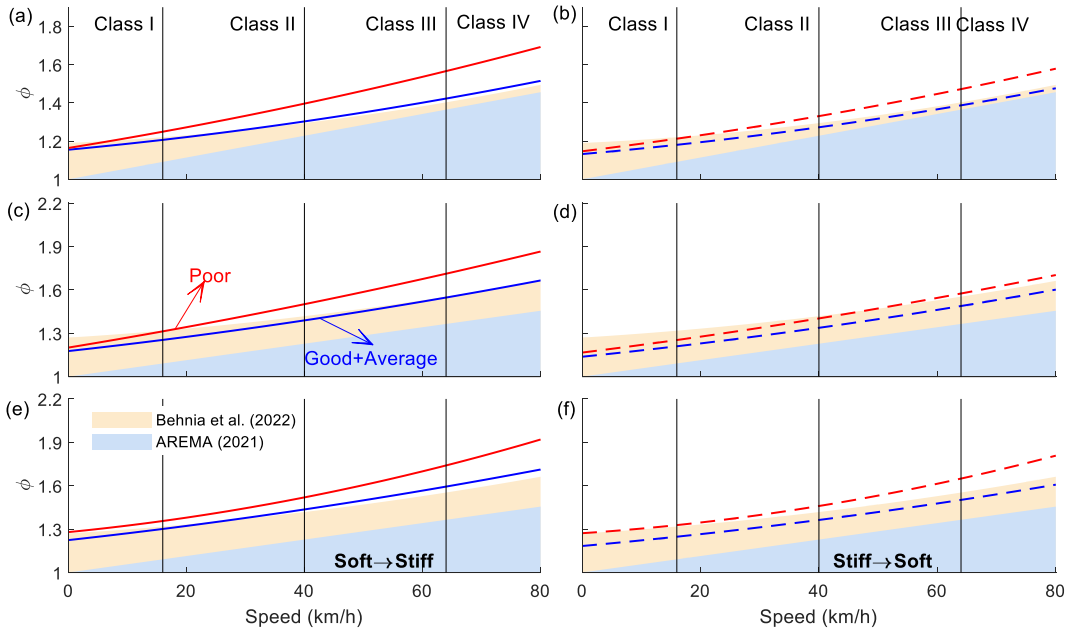

Figure 9. Comparison of estimated ϕ values by AREMA (2021) and Behnia et al. (2022) based on the subgrade track stiffness conditions (i.e., good-average and poor tracks) and transition directions in: (a,b) tangent track; (c,d) curve; and (e,f) track assets (inclusive of grade crossings, bridges, and switches). Note: (a), (c), and (e) are related to soft-to-stiff transition, and (b), (d), and (f) are related to stiff-to-soft transition. Soft-to-stiff transitions are indicated by solid lines, while stiff-to-soft transitions are represented by dashed lines.

previous estimates by AREMA (2021) and Behnia et al. (2022). The most critical areas, surpassing these estimates by about 50% and 30%, respectively, are higher speeds and track assets. Higher speeds show a 20% and 40% discrepancy in average conditions with Behnia et al. (2022) and AREMA (2021), respectively. The most significant differences are observed in track assets such as grade crossings, bridges, and switches.

4.4 Quantifying the Effect of Transition Directions

Statistical properties of dynamic loads and ΔVTD_{sub} measurements allowed for effectively categorizing the data into three distinct groups: tangent track, curve, and track assets (including grade crossings, bridges, and switches). The threshold value for further evaluations, $\phi \geq 1.1$, was determined based on the available dataset and the observed statistical distributions of dynamic load magnitudes.

The available datasets were divided into two groups based on track subgrade conditions: good-average condition and poor condition. This division was made concerning the percentage representation of different transition directions (i.e., soft-to-stiff and stiff-to-soft) within the designated classifications. Figure 9 presents trendlines fitted to the available data, considering different track characteristics and subgrade conditions. These trendlines provide quantitative insight into dynamic load magnitudes compared to previously developed equations for North American railways. The fitted trendlines revealed that in good-average conditions, the differences between transition directions in tangent and non-tangent tracks were 5% and 10%, respectively. These differences increased to 10% and 15% in poor subgrade conditions.

5 CONCLUSIONS

The research presented a quantitative evaluation of railway track characteristics on the magnitude of dynamic loads in terms of dynamic load factor (ϕ). A distinctive aspect of this research lies in its departure from instrumented track sections, opting for continuous measurements across a 340 km in-service track, providing insights into dynamic loads under diverse conditions. The findings underscore the significant influence of these factors on the magnitude of dynamic loads, particularly in non-tangent sections of the track. The study also developed equations to represent the dynamic load factor (ϕ) in terms of speed, providing a method to quantify the observed variation.

The research further highlights the significant influence of track surface roughness and subgrade stiffness variations on dynamic loads, revealing magnitudes that exceed previous estimations. The study also investigates the effects of transition directions on dynamic load magnitudes, revealing that soft-to-stiff transitions amplify dynamic loads while stiff-to-soft transitions attenuate them. The findings underscore the importance of considering these factors in railway engineering, as they inform decisions related to track design, material selection, and overall system safety. The research contributes to the field by providing quantitative insights into the effect of various track features on the magnitude of dynamic loads, thereby

enabling the optimization of maintenance schedules and strategies for enhanced safety and efficiency of the railway network. While this research offers valuable contibutions, it is crucial not to forget the limitations stemming from the measurement conditions, such as single railcar and limited track segment. The authors, therefore, suggest that additional research is necessary to establish dynamic load ranges that account for both track conditions and variations in car type and condition.

6 ACKNOWLEDGEMENT

The authors would like to thank the Canadian National Railway for their support and facilitation of this project. Specifically, Tom Edwards for facilitating the collection of these data sets. This research was made possible through the Canadian Rail Research Laboratory (*www.carrl.ca*). Funding was provided by the Natural Sciences and Engineering Research Council of Canada (NSERCIRC 523369-18), Canadian National Railway and Transport Canada.

REFERENCES

AREMA (American Railway Engineering and Maintenance of Way Association). (2021). Manual for railway engineering. Lanham, MD: AREMA.

ASTM. (2021). “Standard practice for dealing with outlying observations.” ASTM E178-02. West Conshohocken, PA: ASTM.

Behnia, D., Hendry, M.T., Haji Abdulrazagh, P. and Wahba, A., (2022). “Railway Dynamic Load Factors Developed from Instrumented Wheelset Measurements.” *Journal of Transportation Engineering, Part A: Systems*, 148(7), p.04022042. https://doi.org/10.1061/JTEPBS.0000685.

Dahlberg, T. (2010, March). Railway Track Stiffness Variations-Consequences and Countermeasures. *International Journal of Civil Engineering*, Vol. 8, No. 1.

Dybala, J., and S. Radkowski. (2013). “Reduction of Doppler effect for the needs of wayside condition monitoring system of railway vehicles.” *Journal of Mechanical Systems and Signal Processing*, 38 (1): 125–136. https://doi.org/10.1016/j .ymssp.2012.03.003.

Grubbs, F. E. (1969). “Procedures for detecting outlying observations in samples.” *Technometrics,* 11 (1): 1–21. https://doi.org/10.1080 /00401706.1969.10490657.

Hyslip, J.P. 2002. Fractal analysis of geometry data for railway track condition assessment. PhD, University of Massachusetts Amherst, ProQuest Dissertations and Theses.

Leishman, E. M., M. T. Hendry, and C. D. Martin. 2017. “Canadian main track derailment trends, 2001 to 2014.” *Canadian Journal of Civil Engineering*, 44 (11):927–934. https://doi.org/10.1139/cjce-2017-0076.

Li, D., Hyslip, J.P., Sussmann, T.R., and Chrismer, S.M. (2016). *Railway geotechnics*, Taylor & Francis Group LLC, Boca Raton, FL, USA.

Lundqvist, A., & Dahlberg, T. (2005). Railway track stiffness variation-consequences and countermeasures. In: 19th IAVSD Symposium of Dynamics of Vehicles on Roads and Tracks, Milano, August 29-Seprember 2, 2005. Department of Mechanical Engineering, Politecnico di Milano.

Pearson, R. K. (2005). Mining imperfect data: Dealing with contamination and incomplete records. Philadelphia, PA: Society for Industrial and Applied Mathematics.

Peters N. (2010). “CN Railway Engineering Course.” Retrieved from McGill University Civil Engineering Graduate Studies class.

Roghani, A., & Hendry, M. T. (2016). “Continuous vertical track deflection measurements to map subgrade condition along a railway line: Methodology and case studies.” *Journal of Transportation Engineering*, 142(12), 04016059.

Roghani, A., and Hendry, M. T. (2017). “Quantifying the impact of subgrade stiffness on track quality and the development of geometry defects.” *Journal of Transportation Engineering, Part A: Systems*, 143(7), 04017029.

Sadeghi, J. (2012). “New advances in analysis and design of railway track system.” Journal of Reliability Engineering and System Safety. 30 (3): 75–100.

Sadeghi, J., and Barati, P. (2010). “Improvements of conventional methods in railway track analysis and design.” Canadian Journal of Civil Engineering, 37(5), 675-683.

Selig, E.T. and Waters, J.M. 1994. Track geotechnology and substructure management. Thomas Telford Ltd., London.

Smith, S. W. (1997). “The scientist and engineer’s guide to digital signal processing.” California Technical Publication, San Diego.

Sussman, T. R., Ebersöhn, W., & Selig, E. T. (2001). Fundamental nonlinear track load-deflection behavior for condition evaluation. *Transportation Research Record*, 1742(1), 61-67.

Van Dyk, B. J., Edwards, J. R., Dersch, M. S., Ruppert Jr, C. J., and Barkan, C. P. (2017). “Evaluation of dynamic and impact wheel load factors and their application in design processes.” *Proceedings of the Institution of Mechanical Engineers, Part F: Journal of Rail and Rapid Transit*, 231(1), 33-43.

Yu, F., & Hendry, M. T. (2019). “A new strain gauge configuration on the rail web to decouple the wheel–rail lateral contact force from wayside measurement.” *Proceedings of the Institution of Mechanical Engineers, Part F: Journal of Rail and Rapid Transit*, 233(9), 951-960.

Session 6

COLD REGIONS ENGINEERING

Canadian & Cold Regions
Rail Research Conference
2024

Investigation of tie plate icing/ice jacking

Yin Gao, & Dingqing Li
MxV Rail, Pueblo, Colorado, USA

ABSTRACT

Snow and ice can create hazards with regard to the safety and integrity of train operations and rail infrastructure. Because tie plate icing (also referred to as ice jacking) has resulted in past train derailments, this hazard needs to be thoroughly investigated and closely monitored. Tie plate icing occurs when ice builds up between the base of the rail and the tie plate. The ice buildup may cause the rail to sit vertically above the shoulder of the tie plate, thereby reducing resistance to lateral rail movement.

Under the sponsorship of Transport Canada, MxV Rail investigated and documented observations of tie plate icing/ice jacking during field inspection trips to three railroads in cold weather conditions. Tie plate icing is possible any time snowfall accumulates around the base of the rail and tie plates but, it can be difficult to identify. Snow/ice buildup around the rail base, snow cracking due to rail movement, as well as changes in track gage and rail cant can be typical indications of tie plate icing occurrences. MxV Rail's research effort also included 1) a railroad survey to collect the industry's experience with tie plate icing, 2) a track panel testing program, and 3) numerical simulations to further understand the effects of tie plate icing on track gage strength and evaluate possible remediation methods.

1 INTRODUCTION

Tie plate icing occurs when ice builds up between the base of the rail and the tie plate. The ice buildup may cause the rail to sit vertically above the shoulder of the tie plate, leaving the spike fasteners as the primary means of providing resistance to lateral rail motion. Figure 1 shows the ice buildup lifting the rail and raising the spikes.

Figure 1. Ice buildup on tie plate.

Tie plate icing is possible any time snowfall accumulates around the base of the rail and tie plates. According to the investigation by Canadian National Railway (CN 2020), when the track is in a condition where the rail pumps up and down, the motion creates a void under the rail and sucks snow around the base of the rail into the void (Figure 2). The snow in the void is then compacted and transformed into a layer of ice under the rail, lifting the base of the rail above the shoulder of the tie plate and placing the primary source of lateral restraint on the spike fasteners. The spikes are not able to withstand the lateral loading, and they will eventually wear down, break, or fall out under load. Once the spikes fail, the rail will then push outward, allowing the wheels to fall between the rails.

The Transportation Safety Board (TSB) of Canada reported two train derailments due to snow and ice buildup below a rail. Both locations were on curves. Wide gage was found, but no urgent or near urgent defects were noted. The two locations had cut spike fastening systems with standard tie plates. The weather reports for the accident areas included several freeze-thaw cycles, and tie plate icing was found at both locations. The reports concluded that the development of tie plate icing was due to a combination of the weather conditions and the track conditions (TSB 2011 and TSB 2020).

Reports from both locations also indicated that frequent pumping locations, such as joints, curves, turnouts, diamonds, road crossings, bridge approaches, etc., could be areas of concern. Poor tie conditions or ballast fouling could also contribute to ice buildup along the base of the rail (CN 2020).

To date, both the formation and development of tie plate icing have not been fully investigated or understood. The effect of environmental and track

conditions needs to be studied further to understand how these conditions contribute to the issue. In addition to a summary of railroad survey results, this study includes information from field inspections that were combined with experimental testing and numerical modeling and performed to investigate and improve the understanding of the tie plate icing issue and create better focus for future studies.

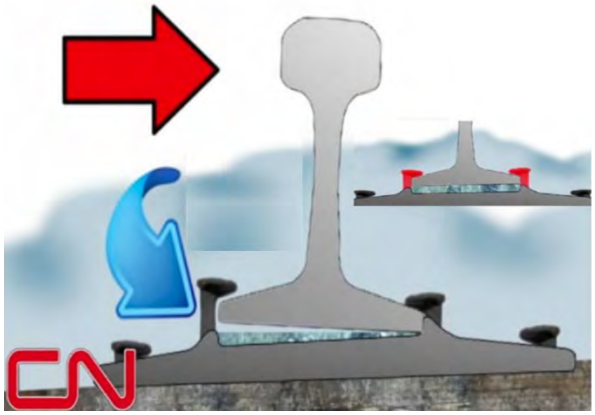

Figure 2. Development of ice buildup under the rail (CN 2020).

2 RAILROAD SURVEY

MxV Rail designed and distributed a survey to collect information on individual working experiences with tie plate icing in North America. The survey included eleven questions regarding each railroad's experience with the identification of and remediation methods for tie plate icing. Survey responses were kept anonymous, and a total of eleven responses were received. Most respondents (9 out of 11) experienced tie plate icing and track issues caused by tie plate icing. According to the survey, tie plate icing can occur anywhere on a railroad track (Figure 3). The responses comprised all the selective typical areas of concern. Three answers in "Other" included "All tracks," "Tangent tracks," and "Tunnels."

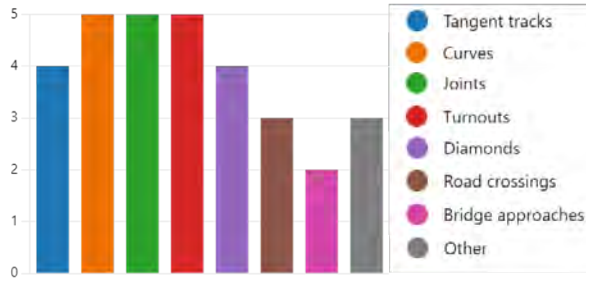

Figure 3. Survey responses highlighting typical areas of concern of tie plate icing.

Poor ballast drainage and rail pumping were the most common track conditions chosen regarding when tie plate icing occurred (Figure 4). Two respondents mentioned frost heave as another track condition. In addition, even though the condition "Tracks with high rail neutral temperature" was not selected in this survey, one Class 1 railroad stated that it experienced tie plate icing on those tracks during the Phase I study.

Figure 4. Survey responses indicating track conditions when tie plating icing is found.

Based on the survey results, the two most common ways to address the effect of tie plate icing were speed reduction and the manual removal of ice/snow. In general, reactive actions were taken to remediate tie plate icing, most likely due to the nature of tie plate icing. Tie plate icing is extremely dependent on localized conditions (both track and weather), and the location of the icing occurrence can be difficult to predict.

3 FIELD INVESTIGATION

Three cold season inspection trips were taken to make observations and document tie plate icing conditions at sites of interest where tie plate icing had occurred in the past. The three sites of interest were on three different railroads: two sites in Canada (one on Canadian Pacific Kansas City (CPKC) and one on CN) and one site in the United States (Genesee & Wyoming). Both weather conditions and site and track characteristics (rail size, tie type and condition, fastening type and condition, track curvature, drainage condition, etc.) were documented at each location. During the trips, lateral track strength measurements were taken for some locations with gaps between tie plates and rails. Other locations generally had great lateral track gage strength with minimum gage widening. Engineers from MxV Rail also spoke with local track managers/roadmasters and gathered information about the maintenance practices and inspection methods related to the tie plate icing issue.

3.1 Trip 1: Fergus Falls, MN, USA

The first location was a Class III railroad operating 64 miles of track between Moorhead, Minnesota (MN), USA and Fergus Falls, MN, USA with some short branch lines near Fergus Falls. The gross rail load of cars on this railroad was typically 286,000 pounds. Several grade crossings with a history of tie plate icing were identified by the hosting railroad and inspected on February 16 and 17, 2022.

On February 16, the inspection was performed at a grade crossing on a tangent track in Fergus Falls, MN (46.2802042, -96.0668825). The hosting railroad identified this location as the best potential site for tie plate icing since the area was a low track spot, and the

track did not have good drainage. The rail size was 115 pound/yard, and the fastening system was made up of 14” plates with two rail spikes. The speed limit of the inspection site was 10 miles per hour. The inspection trip began around 9:30 a.m. CST. The weather was sunny at the beginning and slightly snowy in the afternoon. The temperature varied from 11°F to 26°F during the day. The grade crossing was covered by snow/ice (Figure 5).

Figure 5. Grade crossing at 46.2802042, -96.0668825.

The top 3–5” of snow were easy to remove, but the mixture of snow and dirt was packed solid near the bottom of the rail web (red circle in Figure 6). Since the grade crossing was at a low spot and near a busy in-town highway, muddy ballast with very poor drainage was found at the location. The frozen dirt and ice around the rail seat area made it difficult to dig to the bottom of the rail and tie plate. Only one rail seat area was fully exposed for inspection.

The minimum gap between tie plates and rails is required for railroad tracks. However, a 0.2” gap was found between the bottom of the rail and the tie plate on the one exposed rail seat (Figure 7), but there was no ice and dirt underneath the rail. Since the shoulder of the tie plate was 7/16” tall, the rail base was measured about halfway up the tie plate shoulder.

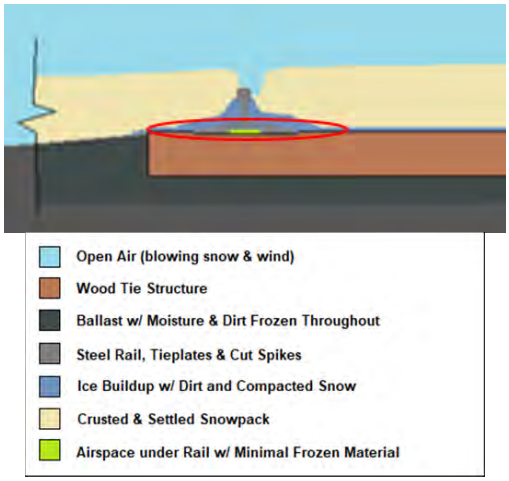

Figure 6. Track conditions of the grade crossing.

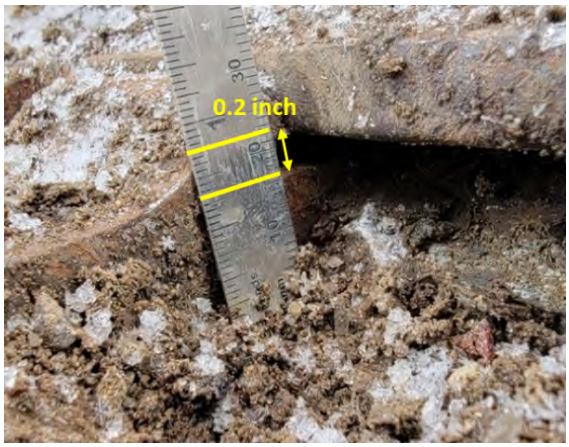

Figure 7. A 0.2” gap found at one rail seat.

Lateral track loading fixture (LTLF) measurements were taken on every third tie in that area, four ties total. The load was applied on the rail web only. When a 9,000-pound gage widening load was applied, the gage for the four ties only increased 1/32 or 1/16”. The ice, frozen dirt, and ballast contributed to the track stability and strength of the track.

Another grade crossing (46.3381161, -96.1666634) outside the town was inspected on the second day. This grade crossing was on a tangent track and had better track conditions than the previously inspected location (e.g., relatively new ties, clean ballast, and good drainage). The snow and ice were removed relatively easily compared to the previous location, and approximately twelve rail seats were exposed and inspected. Ice buildup was observed between the high spikes and the top surface of tie plates (Figure 8). This observation confirmed that ice can build up in fastening system gaps if certain conditions were met. While the exact mechanism is still unknown, one hypothesis, per the local track manager, is that ice can build up in the fastening system gaps if melted snow and ice are able to drip down under the rail seat and refreeze.

Figure 8. Grade Crossing at 46.3381161, -96.1666634.

3.2 Trip 2: White River, ON, Canada

During the second trip, the MxV Rail team visited multiple locations in the White River and Heron Bay Subdivisions of White River, Ontario, Canada to observe tie plate icing. Out of eight inspected locations, only one location had tie plate icing where the rail was lifted above the tie plate shoulder. Other locations generally showed minimal icing.

Compared to the locations without tie plate icing, the problematic location generally had worse track conditions. As shown in Figure 9, the location with tie plate icing had missing anchors, degraded wood ties, and fouled ballast. The gaps between rails and tie plates were measured with a ruler and are listed in Table 1. The bottom of the rail at several ties (Tie #4, 5, 6, 7) was above the tie plate shoulder on both sides. However, since the cut spikes in these locations were still in place, the track gage strength was not reduced.

Table 1. Gaps between rails and tie plates.

Tie	Field Side of Rail (inch)	Gage Side of Rail (inch)
1	12/32	13/32
2	11/32	15/32
3	10/32	14/32
4	16/32	21/32
5	17/32	20/32
6	19/32	23/32
7	17/32	17/32
8	13/32	14/32

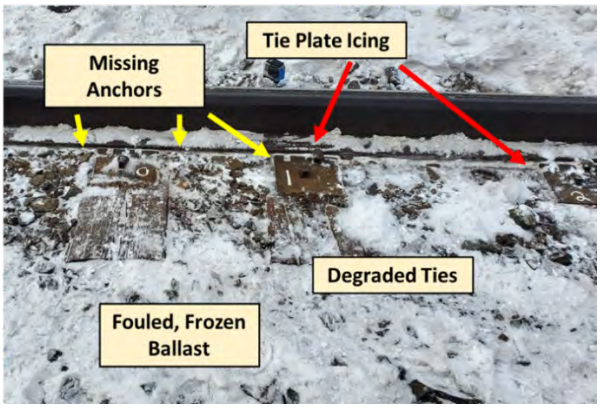

Figure 9. Location with tie plate icing in Heron Bay Sub.

Based on the hosting railroad's experience, problematic locations are often associated with the following conditions:

- Snow covered
- Higher-degree curves
- High RNT (rail neutral temperature)
- Poor anchoring
- Tie degradation
- Fouled ballast

The hosting railroad also mentioned that it does not need very low temperatures or heavy snowfalls to form tie plate icing. The hypothesis is that snow gets trapped in any gaps between the rail and the tie plate. Then, rail movement, especially on the outside rail in curves, packs down snow/ice in layers until the rail is jacked above the tie plate shoulder. When the track is covered with snow, it is difficult to identify problematic locations. One possible indication of tie plate icing that can be seen during a visual inspection is "cauliflowering," i.e., cracked/moved snow or ice near the rail base, indicating rail movement (Figure 10).

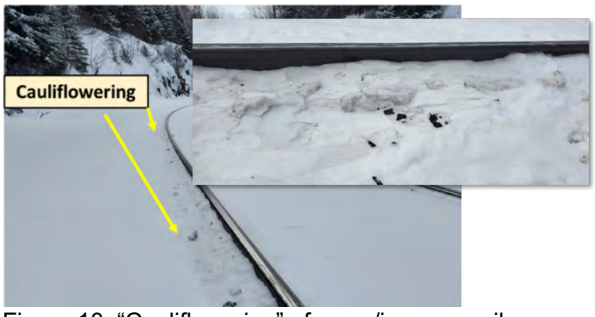

Figure 10. "Cauliflowering" of snow/ice near rail.

3.3 Trip 3: Winnipeg, MB, Canada

On the third trip, the team inspected multiple track locations in the River Subdivision near Winnipeg, Manitoba, Canada. No ice jacking was observed at any of the eight inspected locations. The tracks were frozen and did not show any track gage strength reduction.

Representatives from the hosting railroad stated that ice jacking is possible any time snow accumulates around the base of the rail and tie plates and can occur anywhere the rail is not tightly seated in the tie plate. Problematic locations are often associated with snow cover, high-degree curves, and poor tie and fastener conditions. The hosting railroad representatives also mentioned "black marbling" as an indicator of potential areas of ice jacking and rail movement around the rail base area (Figure 10).

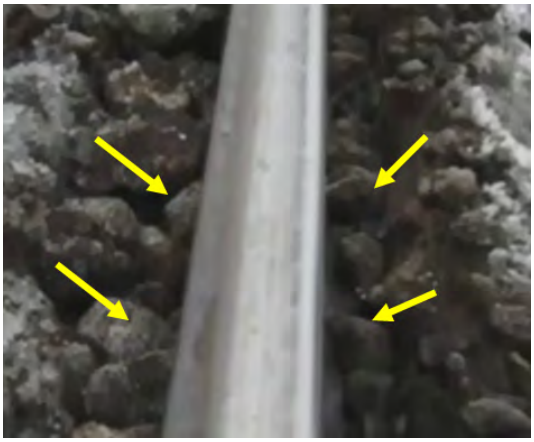
Figure 10. "Black Marbling".

3.4 Summary of Field Investigations

Based on the experiences during the three field investigations, researchers found it difficult to identify the problem with snow cover. Also, because tie plate icing locations often move around depending on where the ties are in the tie degradation cycle, finding a location with ice jacking relies on the experience of the railroad employees, but there is no guaranteed method that will identify tie plate icing. Tie plate icing is believed to be caused by a combined effect of track conditions and weather conditions. The track conditions will cause the rail to not seal tightly to the tie plate, allowing the weather conditions to fill the gap with snow or ice.

Based on the discussions with the railroads, at least two conditions could cause tie plate icing: rail jacked by snow and rail jacked by ice (Figure 11). The first condition is created by snow getting blown against the bottom of the rail and then getting packed layer by layer to jack up the rail. The second condition is caused by weather conditions that create freeze-thaw cycles where snow/ice melts and becomes trapped in the gap between the bottom of the rail and tie plate before freezing again. Ice jacking is often associated with poor drainage.

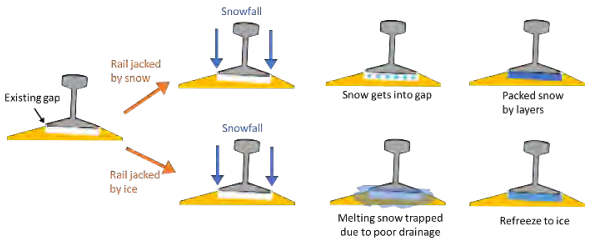

Figure 11. Two conditions for tie plate icing.

4 TRACK PANEL TEST

The main purposes of the track panel test were 1) to simulate tie plate icing in a controlled environment and 2) to validate the computer model. It is important to validate the model before expanding the modeling effort to simulate other cases. The following test scenarios were performed during the track panel test:

- Installing shims on multiple ties to simulate tie plate icing on consecutive ties.
- Adjusting shim thickness to simulate different levels of tie plate icing severity.
- Removing spikes to simulate broken/missing spikes.

4.1 Test Setup

A 32-tie track panel was built on a flat, open space (Figure 12). The panel was constructed with 14" standard AREMA plates, a four-cut-spike pattern, new wood ties, and AREMA 136 RE rail. The ties were numbered from 1 to 32 and spaced 19.5" apart.

Figure 12. Track panel test setup.

Two smooth-surface steel shims measuring 6"×7.5"×0.5" and 6"×7.5"×0.25", respectively, were used to mimic the condition of an actual snow surface and simulate different tie plate icing situations (Figure 13). The shoulder of a tie plate is 7/16" tall. Therefore, the 0.25"-thick steel shim simulated mild tie plate icing (rail base below tie plate shoulder), and the 0.5"-thick steel shim simulated severe tie plate icing (rail base is above tie plate shoulder). The track conditions simulated by steel shims were similar to what was documented during the field trips.

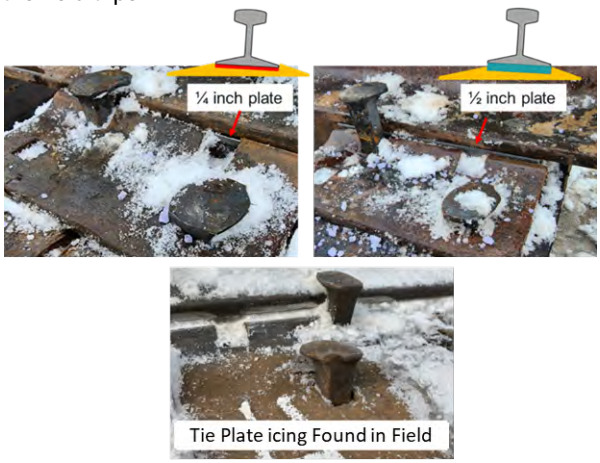

Figure 13. Steel shims used to simulate tie plate icing.

The lateral track gage strength was quantified using a LTLF. Track gage widening was measured at both the rail head and the rail web. The track was loaded by an incremental gage widening load of 0, 1, 2, 3, 4 kips. The track gage at a 4-kip load was the focus in the following analysis.

4.2 Test Matrix

The test cases were designed to adjust the conditions of the middle five ties: Ties 14, 15, 16, 17, and 18. The following factors were considered in the test design:

- Baseline test – No steel shims installed.
- Severity of tie plate icing: 1/2" or 1/4" steel shims.
- Number of ties having tie plate icing: One tie, three ties, or five ties.
- Missing spikes: only remove field side rail spikes on Tie #16.
- Number of rails having tie plate icing: One rail or two rails.

The test matrix was generated based on the above factors. Table 2 covers the first four factors. The same test cases (Case 2 to Case 14) were conducted for both one rail and two rails (number of rails having tie plate icing).

Table 2. Test matrix (MS: Missing spike).

Case #	Tie 14	Tie 15	Tie 16	Tie 17	Tie 18
Case 1: baseline					
Case 2			1/4"		
Case 3			1/2"		
Case 4		1/4"	1/4"	1/4"	
Case 5		1/4"	1/2"	1/4"	
Case 6		1/2"		1/2"	
Case 7	1/4"	1/4"	1/4"	1/4"	1/4"
Case 8	1/4"	1/4"	1/2"	1/4"	1/4"
Case 9	1/4"	1/2"	1/2"	1/2"	1/4"
Case 10	1/2"	1/2"	1/2"	1/2"	1/2"
Case 11 (MS)	1/4"	1/4"	1/4"	1/4"	1/4"
Case 12 (MS)	1/4"	1/4"	1/2"	1/4"	1/4"
Case 13 (MS)	1/4"	1/2"	1/2"	1/2"	1/4"
Case 14 (MS)	1/2"	1/2"	1/2"	1/2"	1/2"

4.3 Test Results

The gage widening values at the highest gage widening load (4 kips) were plotted for each test case. Figures 14 and 15 present the test results documenting the gage widening when simulated tie plate icing on one rail and both rails, respectively. Due to the complexity of track components in an actual track panel, such as spike orientation, initial position of rail, etc., the trend of gage widening can be complicated.

Five ties with 1/2" steel shims produced 0.310" and 0.333" gage widening for one rail and both rails, respectively. Removing a field side rail spike on Tie #16 would increase the gage widening but not by much (usually less than 10 percent). The highest gage widening was measured at 0.380" in Case 14 (both rails), and this amount was a 10 percent increase from Case 10.

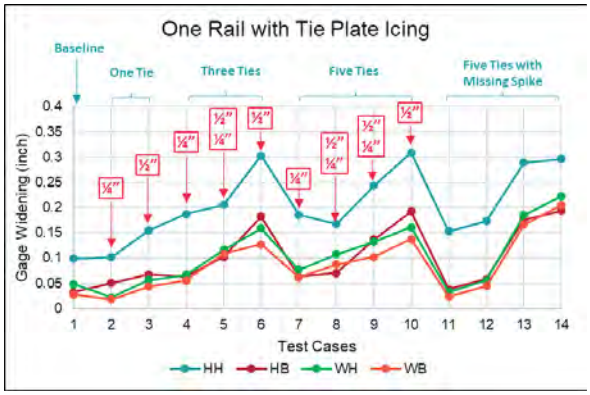

Figure 14. Gage widening for different cases when tie plate icing occurs only on one side of rail.

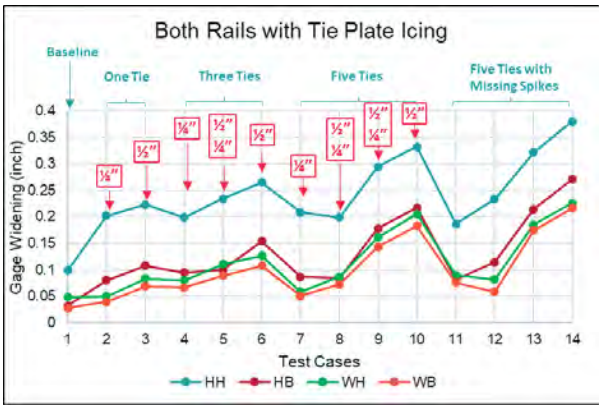

Figure 15. Gage widening for different cases when tie plate icing occurs on both rails.

4.4 Takeaways

The major findings from the track panel test are summarized below:

- Baseline (without tie plate icing) had the strongest gage strength.
- Typically, gage widening increased as the number of ties simulating tie plate icing and the severity of tie plate icing increased.
- 1/4" steel shims caused 0.2" gage widening (0.1" for the baseline case), regardless of the number of ties with tie plate icing. Using 1/2" steel shims further increased gage widening up to 0.19" compared to corresponding 1/4" steel shim cases. Track strength did not change significantly from one rail to both rails with simulated tie plate icing, indicating that if tie plate icing occurs, track strength will be reduced similarly no matter if it occurs on one rail or both rails.
- Missing one field-side rail spike did not result in an obvious reduction in track strength. Cases with more missing spikes were simulated by the numerical model in Section 5.
- The gage widening test load was maximized at 4 kips in the track panel test, resulting in a maximum 0.38" gage widening. The actual train operation environment can have a lateral load or gage widening load several times higher than 4 kips. Therefore, tie plate icing can indeed generate train operation safety concerns.

5 NUMERICAL SIMULATION OF TIE PLATE ICING

Numerical modeling was conducted using Ansys® Workbench™ to assess the influence of tie plate icing on track performance, primarily on gage strength. The modeling efforts characterized the effects of various parameters on track strength and integrity. The simulated parameters included 1) the number of ties having tie plate icing, 2) the number of missing spikes, 3) new and degraded wood ties, and 4) rail longitudinal forces.

The model used for tie plate icing simulation had eighteen ties with 14" plates and cut spikes, the same as the track panel test. The contact types for rails/spikes,

rails/tie plates, plates/spikes, and tie plates/ties were set as frictional contacts. The coefficient of friction was set at 0.4 for the frictional contacts used in the model. Spikes and ties were set to be bonded. The plate element type was a solid tetrahedron element (sizing: 0.5"), and the rail, spikes, and ties were a solid hexahedra element, with sizes 0.78", 0.2", and 4", respectively. The total nodes and elements of the model were 1,076,067 and 381,512, respectively. The two rails were constrained at both ends to simulate the condition of continuous rails, i.e., rails that should not move much longitudinally due to the loading conditions in this study. All the track components were assumed to be elastic. In addition, the gage widening load in the simulation was 4 kips. The track panel tests showed the widened gage was not critical when the rail base is still below the tie plate shoulder. Therefore, only the cases with severe tie plate icing (worst scenario: rail base above the tie plate shoulder) were simulated.

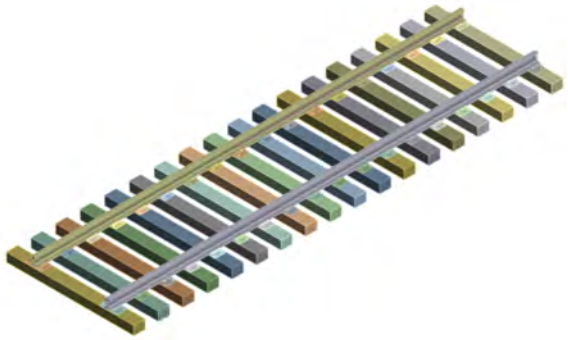

Figure 16. Finite element model for tie plate icing.

5.1 Model Validation

Tie plate icing simulated by 1/2" steel shims (rail base above tie plate shoulder) was the extreme case during the track panel test. Therefore, Cases 3, 6, 10, and 14 (for one rail and both rails), as well as the baseline case, were used to validate the model. Table 3 shows the comparison of test results and simulation results. Most of the simulation cases matched the actual tests within 10 percent. Two cases had over a 30 percent difference, possibly due to the initial setup (initial positions of track components) during that test. Overall, the trend and magnitude of the simulation results were reasonable. Figure 13 and Figure 14 plot the test cases and corresponding simulation cases for a visualized comparison.

Table 3. Model validation.

Test Case	Gage Widening (Test)		Gage Widening (Model)		Difference (%)	
	HH (in.)	WB (in.)	HH (in.)	WB (in.)	HH	WB
Baseline	0.099	0.028	0.102	0.027	3%	-4%
One 1/2" shim, one rail	0.154	0.043	0.145	0.045	-6%	5%
Three 1/2" shims, one rail	0.303	0.128	0.210	0.086	-31%	-33%
Five 1/2" shims, one rail	0.310	0.138	0.305	0.163	-2%	18%
Five 1/2" shims, one rail, one missing spike	0.297	0.205	0.315	0.181	6%	-12%
One 1/2" shim, two rails	0.223	0.067	0.190	0.065	-15%	-3%
Three 1/2" shims, two rails	0.266	0.110	0.260	0.108	-2%	-2%
Five 1/2" shims, two rails	0.333	0.183	0.359	0.195	8%	7%
Five 1/2" shims, two rails, two missing spikes	0.380	0.216	0.372	0.213	-2%	-1%

5.2 Number of Consecutive Ties

Due to testing safety concerns, the number of consecutive ties with tie plate icing and the number of missing spikes were limited in the track panel test. The model, however, did not have the same limitations, and the MxV Rail researchers increased the tie plate icing severity by adding more ties with tie plate icing and more missing spikes.

Cases 15, 16, and 17 were simulated to have seven, nine, and eleven consecutive ties experiencing tie plate icing. No missing spikes were simulated in these three cases. The gage widening values at the rail head for these three cases were: 0.359", 0.401", and 0.427" for one rail with tie plate icing (Figure 17) and 0.398", 0.431", and 0.452" for both rails (Figure 18). The increase rate of widened gage slowed after five ties with tie plate icing, indicating that the effect of the number of ties with tie plate icing decreased when the number reached five ties.

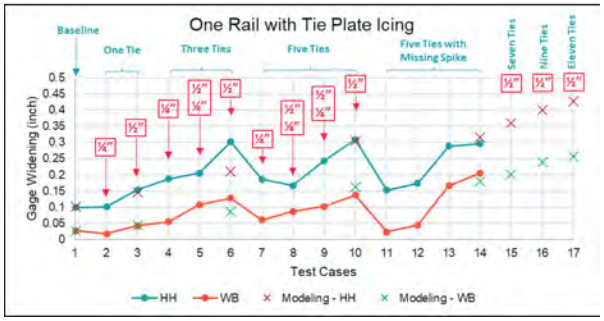

Figure 17. Test and simulation cases for one rail with tie plate icing

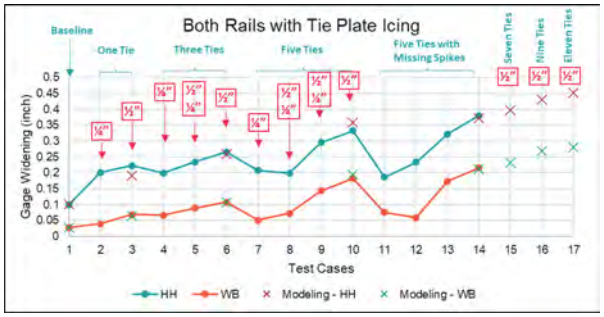

Figure 18. Test and simulation cases for two rails with tie plate icing

In addition, simulations of three scenarios of ties with tie plate icing were performed:

- Tie plate icing on every other tie.
- Three consecutive ties with tie plate icing with one tie without tie plate icing in between.
- Five consecutive ties with tie plate icing with one tie without tie plate icing in between.

The gage widening values had a minimal difference (<1 percent) compared to Cases 3, 6, and 10 (one tie, three ties, and five ties having tie plate icing, respectively), indicating that the number of consecutive ties having tie plate icing dominated the widened gage.

5.3 Missing Spikes

Case 16 (nine ties with tie plate icing) was selected for investigating the effect of missing spikes. Since field-side rail spikes are the key spikes used to restrain the rail lateral movement, those spikes were removed to simulate the missing spike cases (Figure 19). The lateral load was applied at the middle tie of the nine consecutive ties. Missing spike cases involve five scenarios:

- One spike missing on the middle tie
- Three spikes missing (removed two rail spikes on the ties adjacent to the middle tie)
- Five spikes missing
- Seven spikes missing
- Nine spikes missing

The widened gages generated by missing spikes at the rail head by the head-applied load (HH) for each case were plotted in Figure 20. As can be seen, the widened track changed relatively slowly from no missing spike to three missing spikes. The rate of change increased with five or more missing spikes. Understandably, a significant amount of lateral load could still be carried by the field-side rail spikes on adjacent ties in cases with one or three missing spikes. However, in cases with more consecutive missing spikes, a longer piece of rail lost lateral support from spikes, causing more lateral rail bending and gage widening.

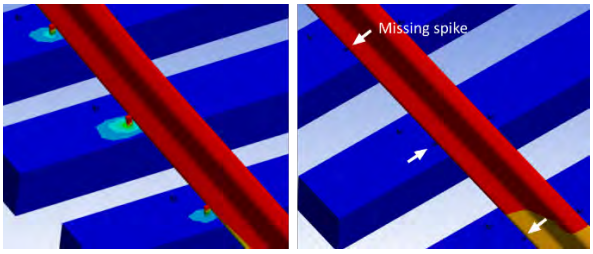

Figure 19. Schematic of missing field-side rail spikes

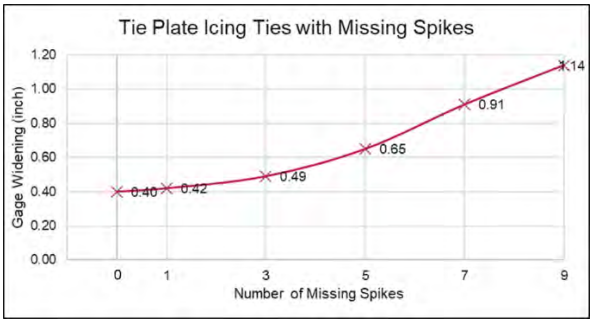

Figure 20. Effect of missing spikes

It is worth noting that the gage widening load in the simulation cases was 4 kips. This load could easily be much higher in a curve or under other vehicle/track conditions. The model used was elastic, therefore, the gage widening values would be two to three times greater for the simulated cases if the load level is doubled or tripled, meaning the widened gage could be higher than 1" (the maximum allowable gage widening for Class 4 and 5 track by Transport Canada). In reality, some track components (e.g., spikes) might have failed due to high lateral displacement, which would worsen the track conditions.

5.4 Tie Degradation

In the model, new solid-sawn hardwood ties with a tie modulus of 1,700 ksi were considered for the tie material. However, wood ties will degrade over time due to weathering, decay, and dynamic load. A tie modulus of 400 ksi was used to simulate a degraded tie condition. Gage widening at both the rail head and the rail base was simulated using the reduced wood tie modulus. A widened gage increase that varied from 11 to 15 percent was recorded for various simulated cases (Figure 21).

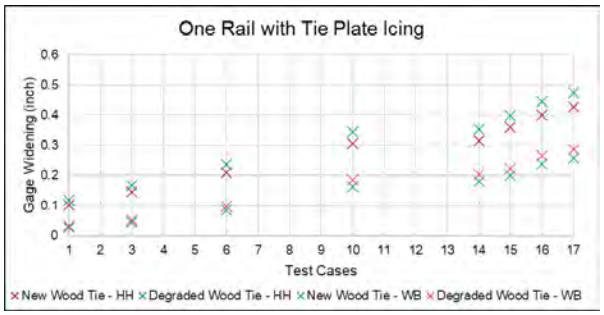

(a)

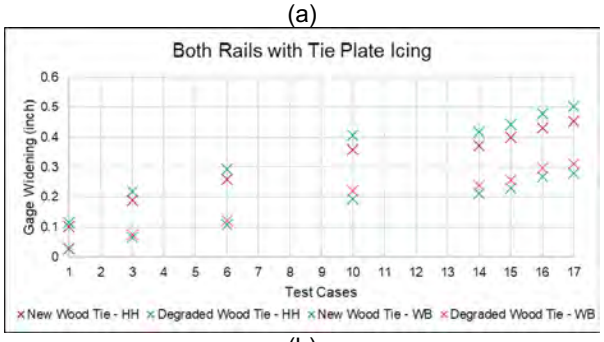

(b)

Figure 21. Effect of wood tie degradation

5.5 Rail Longitudinal Forces

Either a braking/tractive effort or the rail temperature can generate longitudinal forces in rails. The rail longitudinal forces combined with the lateral load may exacerbate the gage widening caused only by the lateral load. In the simulation, rail longitudinal forces were applied on both rails just outside the ties that have tie plate icing (Figure 22). A rail longitudinal force of 10 kips is considered a typical value generated by locomotives when accelerating or braking, and this force was used for the simulation. Approximately 0.1" to 0.2" gage widening was added to the rail head displacement (Figure 23).

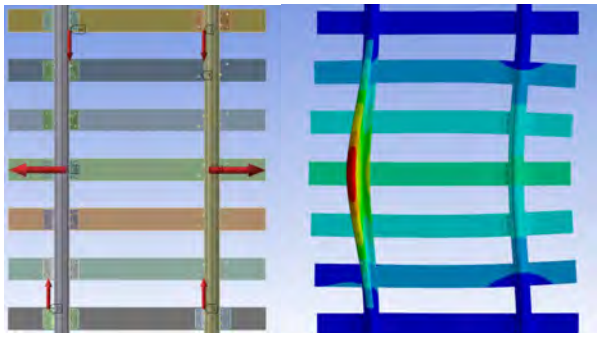

Figure 22. Rail longitudinal forces setup in the model

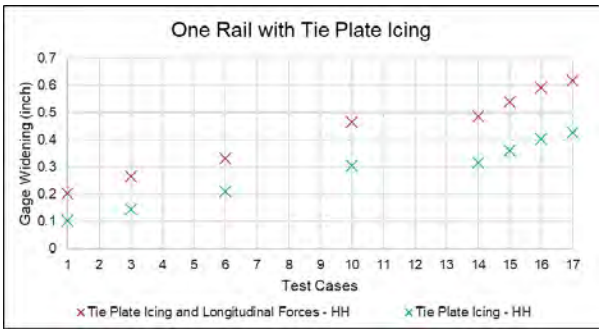

Figure 23. Effect of rail longitudinal forces

6 CONCLUSIONS AND FUTURE RESEARCH RECOMMENDATIONS

MxV Rail performed field inspections of locations for three railroads to investigate the tie plate icing issue. Further, MxV Rail designed a railroad survey to collect the industry's experience on tie plate icing. The survey showed that tie plate icing can occur anywhere on a track, and visual inspection and manual removal are the usual ways to deal with the tie plate icing issue.

Further, MxV Rail used a track panel test and a numerical simulation to investigate the track gage strength with the occurrence of tie plate icing. The test findings included the following:

- Track gage strength was highly correlated with the number of ties simulating tie plate icing and the severity of tie plate icing (rail base above or below tie plate shoulder). The largest widened gage recorded was 0.38" when both rails had five consecutive ties simulating tie plate icing and missing field-side rail spikes.
- The baseline case had 0.1" gage widening. Adding 1/4" steel shims caused 0.2" gage widening regardless of the number of ties having tie plate icing (up to five ties in this test). When increasing the severity of tie plate icing by replacing 1/4" shims with 1/2" shims, gage widening could increase up to 0.19" compared to corresponding 1/4" steel shim cases.
- Simulated tie plate icing that occurred on only one rail or both rails did not have a significant difference in track gage strength.
- One missing field-side rail spike did not result in an obvious reduction in track strength.

The results from the track panel test were then used to validate a computer model that had an eighteen-tie track panel. The modeled track gage widening matched the trend and magnitude measured in the track panel tests. The validated model was used to investigate the effect of tie plate icing. The findings from the model include:

- The number of consecutive ties with tie plate icing varied from 0 to 11. None of the simulated cases exceed 1" gage widening (Class 4 and 5 track according to Rules Respecting Track Safety, Transport Canada) under a 4-kip gage widening load (used in track panel test). However, a higher gage

widening load could cause gage widening above the rules of track gage.
- The number of missing field side rail spikes varied from 0 to 9 in the model. The model showed that missing spikes could substantially increase the gage widening if there were more than five missing spikes. When the number of missing spikes was nine, the simulated gage widening was above 1".
- Degraded ties (low tie modulus) showed an 11–15 percent increase in gage widening for various simulated cases.
- Rail longitudinal forces can cause an extra 0.1" to 0.2" gage widening when a 10-kip longitudinal force was applied on the rails.

6.1 Guidelines for Identification and Mitigation

The most important factor for “Ties with tie plate icing” is the presence of a gap between the rail base and the tie plate of that tie. “Gap” management would be key in the identification and mitigation of the tie plate icing issue. To identify potential areas that could cause a gap, the following actions are recommended:

- Locate high spikes and missing spikes, especially when consecutive high spikes and missing spikes are found.
- Observe black marbling/cauliflowering when snow covers the track.
- Take vertical track deflection or track cant measurements to identify rail pumping.

For mitigation, the following methods are recommended:

- To minimize the gap between the rail base and tie plate, use a gage lock type of screw spike at rail spike position on a standard plate or curve block plates/elastic fasteners every fourth tie (or depending on railroad’s requirement) in areas that are prone to have tie plate icing.
- Replace or fix missing spikes and high spikes before winter.
- Improve ballast drainage in areas prone to tie plate icing.

Future work should include testing the effectiveness of potential mitigation methods. If track geometry and weather data for the areas of concern can be obtained, an analysis of track geometry change, especially rail cant, track gage, base gage (if available) would be beneficial to identify tie plate icing in early stage. Also, asymmetric/uneven ice buildup may cause the rail to be rolled inward or outward. The rail roll could change the wheel/rail (W/R) contact geometry and change the vehicle steering and W/R forces, which, in turn, could exacerbate any gage widening problems. Additionally, researchers could examine the likelihood of tie plate icing in frost heave regions to understand the correlation between frost heave and tie plate icing.

7 ACKNOWLEDGEMENT

Authors would like to thank the inspection and testing support from host railroads and survey participants from various railroad-related organizations. Additionally, authors would like to thank Transport Canada for the funding support for the research presented in this paper.

REFERENCES

Canadian National Railway. (2020). Engineering Safety Flash, Derailment Prevention.

Transportation Safety Board of Canada (2011). Railway Investigation Report R11V0057: Main-track train derailment.

Transportation Safety Board of Canada (2020). Railway Transportation Safety Investigation Report R20W0031: Main-track train derailment.

Canadian & Cold Regions
Rail Research Conference
2024

Effects of cold temperature on ultrasonic rail flaw testing

Survesh Shrestha, Anish Poudel
MxV Rail, Pueblo, Colorado, USA

Glenn Washer
Department of Civil and Environmental Engineering – University of Missouri, Columbia, Missouri, USA

ABSTRACT

Under the sponsorship of Transport Canada, MxV Rail investigated the effects of extreme cold temperature on the performance of ultrasonic testing (UT) for rail defect inspections. The non-contact UT experiments were conducted using a chiller bath inside an ultrasonic immersion tank, and the contact UT experiments were conducted using a cold chamber. The UT parameters such as ultrasonic velocity and density in rail steel and different fluids (couplants) were determined experimentally. Changes in the refraction angle for shear waves were also measured. Additionally, ultrasonic beam modeling and simulation were conducted using CIVA UT to assess ultrasonic beam field responses for the ultrasonic velocities and densities determined for different cold temperatures. The 45- and 70-degree refraction angles showed a decreasing linear trend with decreasing temperature. This refraction angle shift can cause the beam to miss the targeted inspection zone and defects. Thus, conducting hi-rail ultrasonic system calibration at cold temperatures is advisable when performing testing at cold temperature.

The UT was also conducted using rails with internal fatigue defects at cold temperature and a UT system with a roller search unit (RSU) similar to the ones used in rail inspection vehicles. Calibration was performed using a rail specimen with a 3.175 mm side-drilled hole (SDH). The results showed that the signal amplitudes from the defective rail samples improved when the system was calibrated at the inspection temperature compared to the signal amplitudes obtained when calibrated at room temperature. In addition, MxV Rail compared the signal amplitudes from the SDH in the calibration specimen at different temperatures and observed a significant decrease in the signal amplitude at -40°C compared to the room temperature signal.

1 INTRODUCTION

Due to extreme winter weather conditions, Canadian railroads face several challenges, such as increased safety risks and component failure. Problems such as broken rails occur more frequently in the winter, thereby increasing the frequency of track inspections (Ladubec & Magel 2011). Minor defects or anomalies can initialize internal rail cracks that can grow with accumulated train tonnage (Garcia & Jeong 2003, Orringer et al. 1986, Banerjee & Morrison 2019). Due to the significant decrease in rail temperature from the rail neutral temperature in extreme cold conditions, rails experience high tensile forces (Ladubec & Magel 2011) that may cause failure at weak spots, such as the internal fatigue defects in the rails and welds.

Periodic rail inspections are vital for smooth railroad operations. North American railroads rely vastly on ultrasonic testing (UT) non-destructive evaluation (NDE) technologies to monitor rail health. However, due to the extreme winter weather conditions, it is very challenging to conduct these rail inspections.

The primary objective of this research was to investigate and understand the effects of cold temperature on ultrasonic rail flaw testing capabilities. The research focuses on ultrasonic testing in rail samples at extreme cold temperatures. First, the ultrasonic parameters, such as ultrasonic velocities in rail steel and different coupling fluids, as well as the density of the fluids at cold temperatures, were determined using contact and non-contact UT approaches. Then, ultrasonic beam modeling and simulation in rails was conducted to study the ultrasonic beam field responses at different cold temperatures. Finally, the effect of cold temperature on ultrasonic signals was studied using rail samples with internal fatigue defects.

1.1 Ultrasonic Rail Flaw Testing Technology

The in-motion UT technology incorporated in a hi-rail inspection vehicle uses roller search units (RSU) to scan and detect rail defects. An RSU is a liquid-filled membrane (tire) that houses piezoelectric ultrasonic transducers oriented at different angles. Figure 1 shows

a typical RSU configuration running on a rail. The different-colored lines represent the ultrasonic signal path from the different transducers. Although the ultrasonic signal paths are shown as single lines, each line represents an array of the ultrasonic beams transmitted and received. Table 1 lists the different transducer orientations typically used in RSUs for detecting different rail defects.

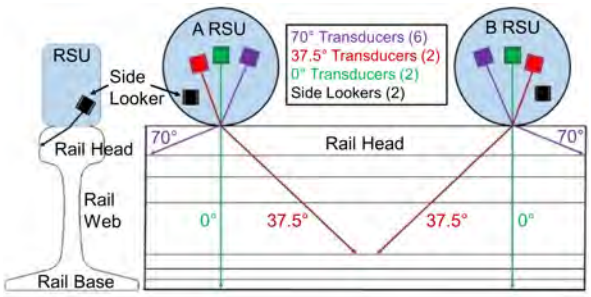

Figure 1. Ultrasonic transducers configurations in RSUs (Poudel et al. 2019).

Table 1. Transducer orientation and targeted rail flaw types (Poudel et al. 2019).

Transducer Orientations	Target Flaw Types
0-degree	Flaws oriented horizontally - shells, horizontal split head (HSH), split web
37.5- or 45-degree	Bolt hole cracks, web defects
70-degree	Transverse defects (TDs), vertical split heads (VSH), weld defects (porosity, inclusions, etc.)

1.2 Ultrasonic Parameters

The RSU material and fluid are selected to minimize the acoustic impedance mismatch. Acoustic impedance (Z) is a physical material property that depends on the density (ρ) and acoustic velocity (C) of the material and can be calculated using Equation 1 (Rose 2014).

$$Z = \rho C \qquad [1]$$

The RSUs are typically filled with fluids (antifreeze/water mix) that have minimal ultrasonic velocity variation with temperature to minimize the variation of the ultrasonic refracted angle in the test piece with temperature. The use of couplants also allows for the effective transmission of the ultrasonic signal into the rail steel and back to the transducers.

Since the RSU material and fluid's acoustic velocity depends on the material's stiffness and density, the ambient temperature should also be considered while conducting ultrasonic inspection. Equation 2 shows the dependance of ultrasonic velocities on temperature (Rose 2014).

$$C_L = \sqrt{\frac{K}{\rho}} \; and \; C_S = \sqrt{\frac{G}{\rho}} \qquad [2]$$

In Equation 2, C_L and C_S are the longitudinal and shear wave velocities; K is the bulk modulus; and G is the shear modulus. Since the volume changes with temperature, density also varies with temperature. Based on Equation 2, it can be understood that sound waves travel faster through media with high stiffness and lower density. The velocity of sound wave can also be calculated by using Equation 3.

$$C = \frac{2d}{t} \qquad [3]$$

In Equation 3, d is the one-way distance traveled by the ultrasonic wave, and t is the transit time of the ultrasonic wave. An ultrasonic wave passing through an interface between two materials at an oblique angle produces both reflected and refracted waves. Due to the different acoustic velocities, refraction occurs in the second material (Figure 2).

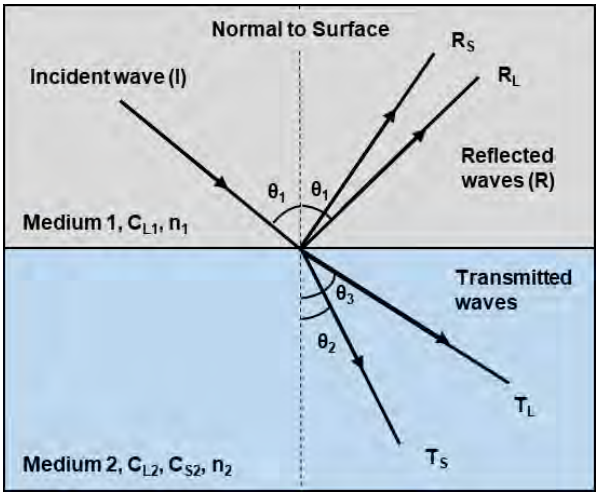

Figure 2. Mode conversion at interface for longitudinal wave incidence (Poudel et al. 2022).

2 MATERIALS AND METHODS

2.1 Determination of Ultrasonic Parameters

This preliminary study determined some parameters for ultrasonic testing, such as ultrasonic velocities in rail steel and different coupling fluids at freezing temperatures (0°C to approximately -38°C). The densities of the fluids (couplants) were also determined at those temperatures.

Two different experimental setups, contact and non-contact, were designed, and tests were conducted in static conditions to measure the ultrasonic parameters. The contact UT approach was used to measure the ultrasonic velocity in rail steel. Similarly, the non-contact UT approach was used to measure ultrasonic velocity and density in the fluids and the angle of refraction in the rail steel.

For the contact approach, a test sample machined from the head of a 136 RE rail with a 3.175 mm diameter through hole was used to conduct the velocity measurements (Figure 3).

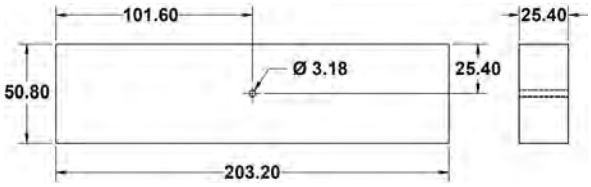

Figure 3. Engineering drawing of the test sample used in the contact UT approach (units in mm).

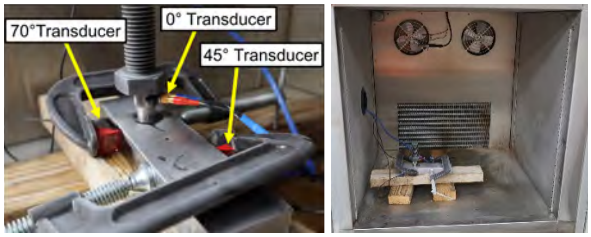

Figure 4. Test setup for ultrasonic velocity measurements in rail steel using contact UT approach.

Figure 4 shows the test setup using an environmental cold chamber. The measurements were conducted using both longitudinal wave (L-wave: 0-degree) and shear wave (S-wave: 45- and 70-degree) transducers held in position with a weight (bolt) and clamps, respectively. The transducers were connected to an Olympus Epoch 600 flaw detector to measure the ultrasonic signal amplitudes. EchoPure^{TM} gel was used as a couplant and a thermocouple was attached to the sample surface to monitor the sample temperature. The lowest temperature achieved was -38°C.

The ultrasonic velocity was calculated using Equation 3. In the case of L-wave, the sample width was used as the value of d, whereas, in case of S-wave, the distance between probe index point and through hole was used as the value of d.

For the non-contact UT, a calibration specimen machined from the head and web area of a 136RE rail was used (Figure 5). A delay line transducer was used to conduct measurements. The test setup consisted of a chiller bath placed inside an ultrasonic immersion tank (Figure 6). The specimen was placed inside an aluminum container within the chiller bath because air bubbles were getting trapped in the liquid in the chiller bath. The air bubbles caused the ultrasonic waves to scatter, thereby reducing the energy in the ultrasonic waves significantly. With the chiller, the lowest temperature achieved was -37°C.

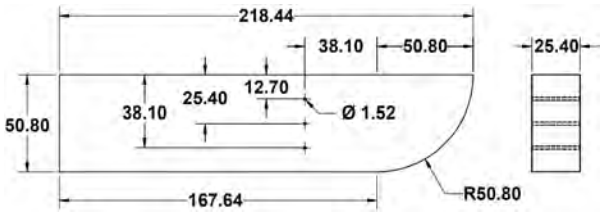

Figure 5. Engineering drawing of the calibration specimen used in non-contact UT approach (units in mm).

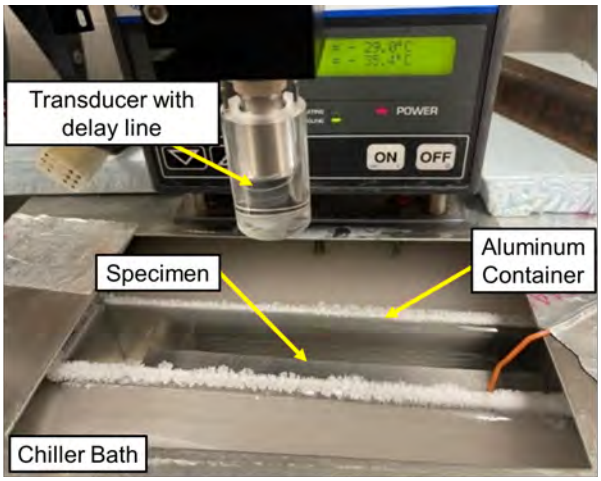

Figure 6. Test setup for ultrasonic velocity measurements in rail steel and coupling fluids using non-contact UT approach.

The fluids considered for ultrasonic velocity and density measurements include glycol, ultrasonic couplant (EchoPure^{TM} gel), and different glycol/water concentrations (80/20 and 50/50 mix). The fluid density was measured using the changes in volumes of the liquids at different temperatures in graduated cylinders. The cylinders were placed in the chiller bath to cool the fluids and then removed temporarily from the bath to record the volume for the given temperature. In addition to the velocity and density measurements, the changes in the refraction angles of S-waves due to the temperature change were also measured using the non-contact UT approach.

2.2 Ultrasonic Beam Modeling and Simulation

Ultrasonic beam modeling and simulation in rails were performed using CIVA UT to assess the ultrasonic beam field responses for the range of ultrasonic velocities and densities determined at different cold temperatures. A three-dimensional (3D) model of a 136RE rail section was used for this study. The ultrasonic parameters used were 1) 0, 37.5, and 70-degree refraction angles, 2) a single element, flat focusing, immersion type probe, and 3) a 25 mm water path. The frequencies for the 0, 37.5, and 70-degree refraction angle settings were 3.5, 2.25, and 2.25 MHz, respectively. Material properties and ultrasonic velocities for rail steel and fluids determined from the experiments described in section 2.1 were used for the simulation, and the study was conducted at room temperature (22°C) and two extreme cold temperatures (-20°C and -30°C).

2.3 Effect of cold temperature on ultrasonic signal

This study was conducted to simulate ultrasonic rail flaw testing in extreme winter revenue service type scenarios. The tests were conducted in a controlled environment inside an environmental chamber (cold room) with an internal floor area of 2.74 m x 2.74 m at temperatures ranging from 0°C to -40°C.

The rail sample used for this test had two closely located internal transverse defects (TDs) that had

occurred naturally from years of service. A TD is a type of internal fatigue defect oriented along a rail's transverse (or cross-sectional) plane. For this study, the TDs were labeled as TD 1 and TD 2.

A UT system with an RSU, also known as a walking stick, was used for testing. A 70-degree transducer in the RSU was used with an Olympus Epoch 600 flaw detector to measure the ultrasonic signal amplitudes from the defects in the rail sample. The couplant used for the testing was a 50/50 mix of propylene glycol and water. Propylene glycol has a melting point of -60°C and acts as an antifreeze that helps facilitate testing in temperatures below 0°C.

Figure 7. A walking stick with RSU connected to an Olympus Epoch 600 flaw detector.

The UT system was calibrated using two identical rail calibration specimens. Each specimen had a 3.175 mm diameter side-drilled hole (SDH), 12.7 mm below top of the rail head (Figure 8). One of the calibration rail specimens was placed in the lab at room temperature, and the other calibration rail specimen was placed in the cold room alongside the rail sample (Figure 9).

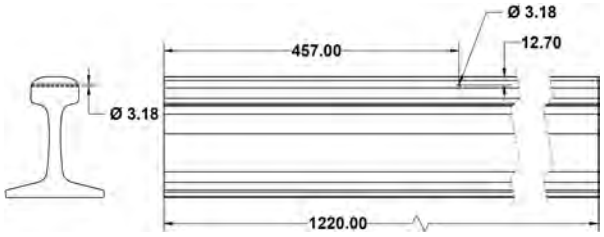

Figure 8. Engineering drawing of the calibration rail specimen (units in mm).

Initially, before conducting the cold temperature tests, the baseline measurements from TDs were recorded at room temperature with the RSU calibrated at room temperature. Then, the tests were conducted at cold temperatures between 0°C to -40°C with the measurements taken at every 5°C interval. The RSU was first calibrated at room temperature, and the signal amplitudes from the TDs were measured at the inspection temperature. Then, the RSU was calibrated at the inspection temperature, and the signal amplitudes from the TDs were measured again. The two data sets were used to study the signal amplitude changes resulting from the UT system calibration at room temperature versus the inspection temperature.

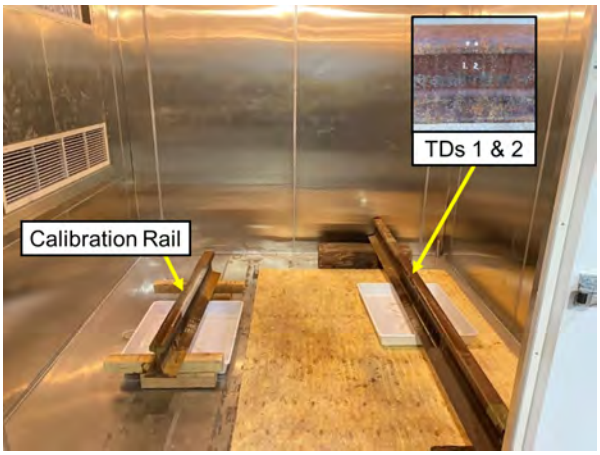

Figure 9. Test setup inside the environmental chamber with the rail sample containing TDs on the right, and calibration rail specimen for cold temperature calibration on the left.

3 RESULTS AND DISUSSION

3.1 Ultrasonic Parameters

The L-wave and S-wave velocities were initially calculated at room temperature and verified with the known values for carbon steel. Then, the velocities were calculated at temperatures from -18°C to approximately -38°C. The experiment was repeated five times. Then, the average velocity was calculated for each temperature group.

The changes in L-wave velocities with decreasing temperatures are shown in the plot in Figure 10. A slight increase in the velocity was observed as the temperature decreased. The difference in velocities between room temperature and -38°C is 13 m/s, which correlates to a 0.22 percent increase from the velocity at room temperature to the velocity at -38°C.

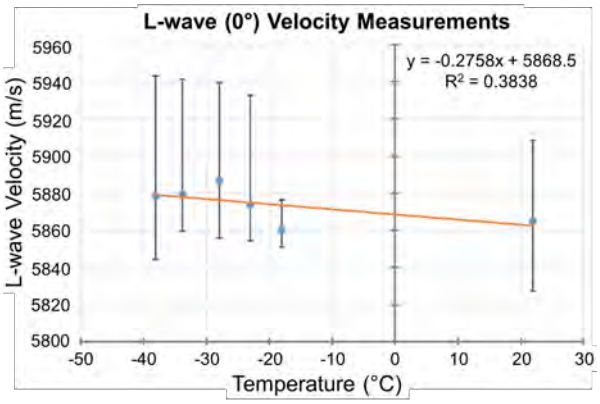

Figure 10. L-wave velocity measurements in rail steel at different temperatures using contact UT.

Figure 11 and Figure 12 show the plots for the changes in 45-degree and 70-degree S-wave velocities with changing temperatures. The difference in 45-degree S-wave velocities at room temperature and -38°C corresponds to a 2.61 percent increase in velocity from room temperature to -38°C. Similarly, the increase in 70-degree S-wave velocity between room temperature and -38°C was 1.65 percent.

Data scattering was observed during most of the velocity measurements. The data scattering in these velocity measurements may be the result of amplitude shifts (erratic readings) in the recorded A-scans or due to the changes in piezoelectric crystal properties due to prolonged exposure to the lower temperature. Despite the data scattering, the trends from temperature change can still be observed and analyzed statistically.

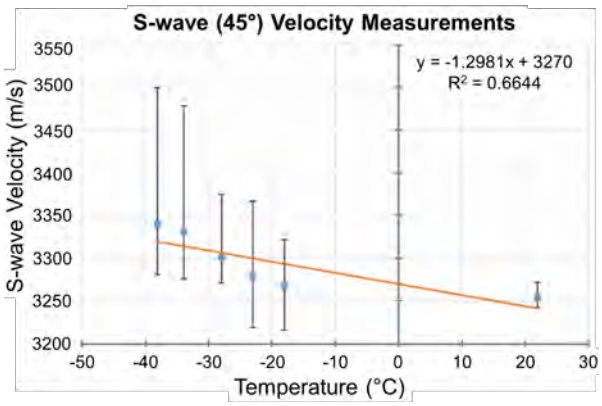

Figure 11. S-wave (45-degree) velocity measurements in rail steel at different temperatures using contact UT.

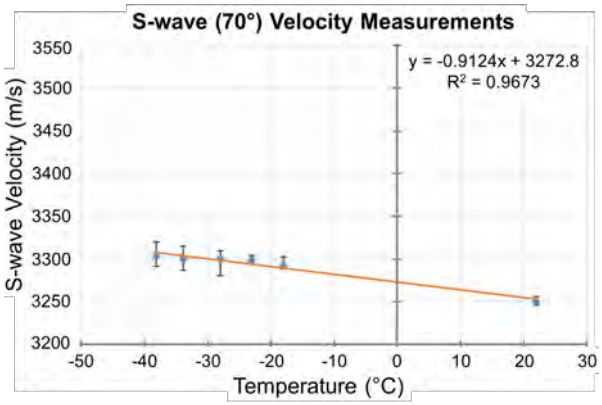

Figure 12. S-wave (70-degree) velocity measurements in rail steel at different temperatures using contact UT.

The L-wave velocities for different fluids (glycol, glycol/water mix, and EchoPure™ gel) were measured at different temperatures using a non-contact UT approach. Figure 13 shows the plot of L-wave velocity measurements for these fluids at different temperatures. The measurements showed that the ultrasonic velocities for these fluids increased with the decreasing temperatures. Among all the fluids considered for this study, the 50/50 glycol/water mix had the highest ultrasonic velocity values at all tested temperatures.

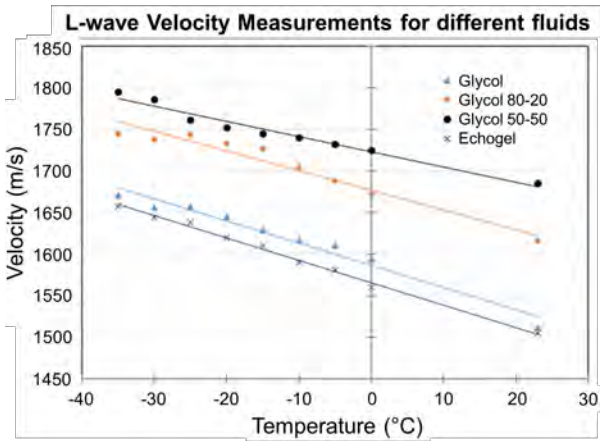

Figure 13. L-wave velocity measurements for different fluids at different temperatures using non-contact UT.

Similarly, the density measurements showed that the densities of the different fluids increased as the temperatures decreased. The density measurements for the different fluids are shown in the plot in Figure 14.

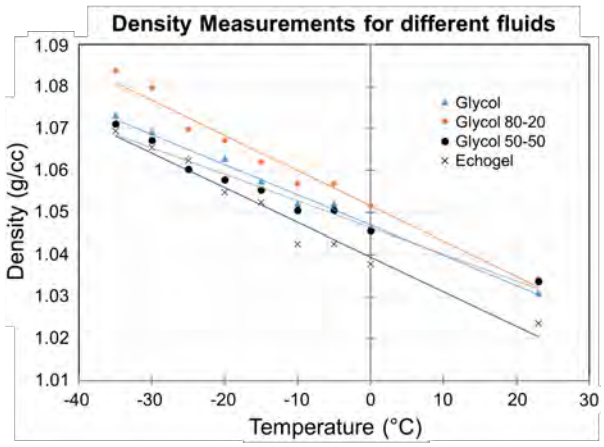

Figure 14. Density measurements for different fluids at different temperatures.

The non-contact UT setup was also used to study the deviations in the refraction angles of 45-degree and 70-degree S-waves due to the temperature change. The procedure was adequate for a 45-degree S-wave but proved problematic for 70-degree S-wave due to ultrasonic signal losses in the immersion liquid as temperatures decreased. The angle of refraction was found to vary with temperature as shown in Figure 15. The refraction angle measured at 44.61 degrees at room temperature had decreased to 40.4 degrees at -30°C, meaning defects could be missed during inspection in frigid temperatures due to the deviation in refraction angle.

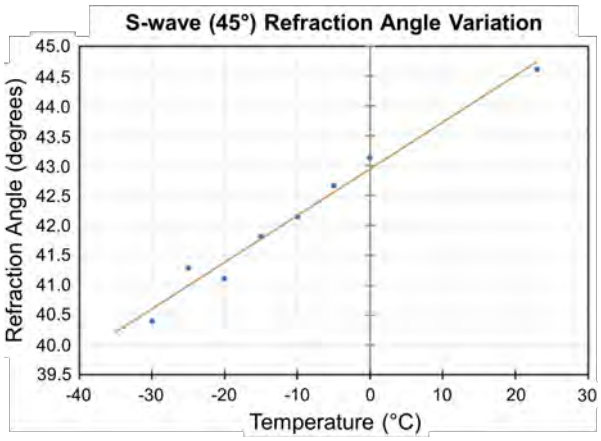

Figure 15. S-wave (45-degree) refraction angle variations at different temperatures using non-contact UT.

3.2 UT Beam Modeling and Simulation

The velocity of sound waves in different materials governs the angle of refraction when a wave is transmitted from one material to another. Table 2 summarizes the angle of refraction calculated for different temperatures. The refraction angle for the water/steel interface was also calculated as a baseline for comparison under different scenarios. Figure 16 shows the plot of these results. In both cases of refraction angles (45 and 70-degree), the refraction angle decreased linearly with the decrease in temperature.

Table 2. Refraction angle changes in fluid/steel interface as a result of temperature change.

Mediums	Incident Angle (degrees)	Refraction Angle (degrees)
Water/Steel (22°C)	18.95	45.00
Glycol/Steel (22°C)	18.95	40.19
Glycol/Steel (-20°C)	18.95	37.16
Glycol/Steel (-30°C)	18.95	36.92
Water/Steel (22°C)	25.56	70.00
Glycol/Steel (22°C)	25.56	60.28
Glycol/Steel (-20°C)	25.56	53.38
Glycol/Steel (-30°C)	25.56	52.97

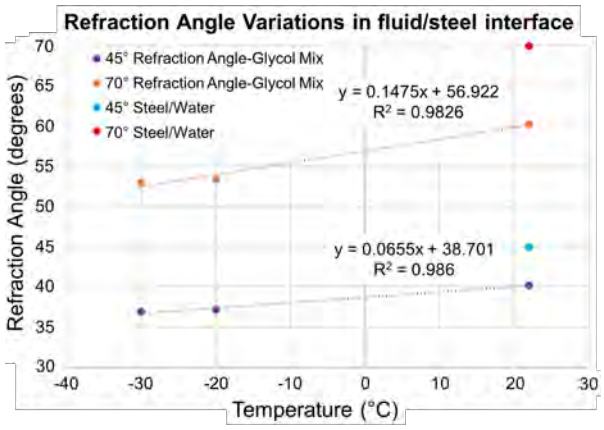

Figure 16. Refraction angle variations in fluid/steel interface as a result of temperature change.

The change in the angle of refraction can shift the beam away from the targeted inspection zone, which, in turn, could cause the beam to miss defects in that zone during the inspection process. Therefore, performing hi-rail ultrasonic system calibration at cold temperatures while testing at cold temperatures is highly recommended.

Inspection simulations were also performed for a rail model embedded with an internal defect for different temperatures using a 70-degree transducer. The modeled defect was a 13 mm diameter transverse fissure (TF) defect located at the center of the rail head at a depth of 13 mm with an orientation of 10 degrees. Scanning for this simulation was performed along the longitudinal direction of the rail model at a 1 mm step. The ray tracing results for this simulation are shown in Figure 17. The simulation results showed that the rays hit the TF defect only in the water/steel simulation case. In all other cases, the flaw was missed entirely and, therefore, undetected due to the change in the refraction angle.

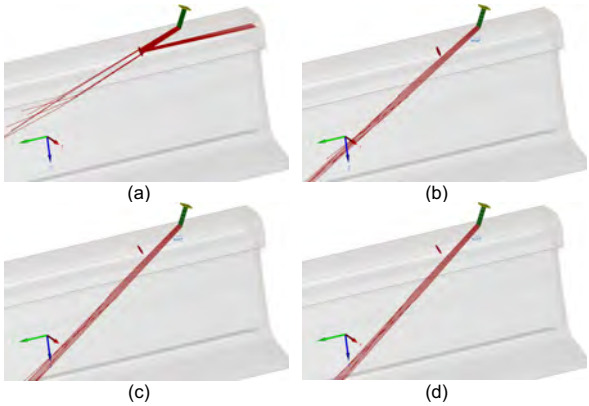

Figure 17. 70-degree S-wave beam ray-tracing result for TF in rail steel: (a) water/steel at 22°C; (b) glycol mix/rail steel at 22°C; (c) glycol mix/rail steel at -20°C; (d) glycol mix/rail steel at -30°C.

3.3 Effect of cold temperature on ultrasonic signal

The ultrasonic signal amplitudes from the 3.175 mm SDH in the calibration rail specimen were measured at room temperature (21°C) and at every 5°C interval between 0°C to -40°C to study the effect of extreme cold temperatures on the ultrasonic signal. The signal amplitudes from the SDH were plotted as shown in Figure 18, and a linear decreasing trend in the signal amplitude with the decreasing temperature was observed. There was a significant decrease in the ultrasonic signal from the SDH at -40°C compared to room temperature. The signal amplitude dropped from 80 percent at room temperature to 36 percent at -40°C.

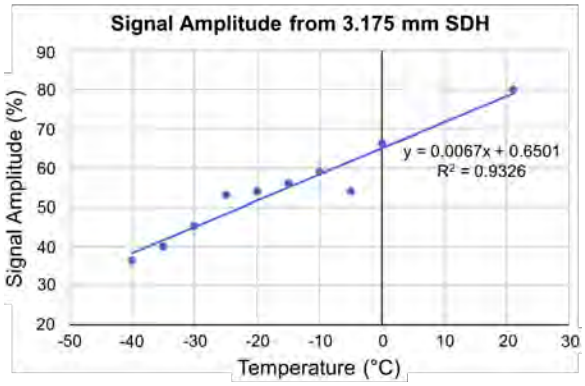

Figure 18. Signal amplitude measurements for 3.175 mm SDH in calibration rail specimen at different temperatures.

There can be challenges during defect detection due to the effects of extreme cold temperature on ultrasonic signals. To minimize these effects, in this study, the ultrasonic signal amplitude measurements for TD 1 and TD 2 were conducted once with the UT system calibrated at room temperature and again with the system calibrated at the actual inspection temperatures. Figures 19 and 20 show the comparisons of the results obtained from experiments conducted with the UT system calibrated at room temperature and inspection temperatures for TD 1 and TD 2, respectively. The results show that signal amplitudes from both defects improved to some degree after calibrating the inspection system at the actual inspection temperatures.

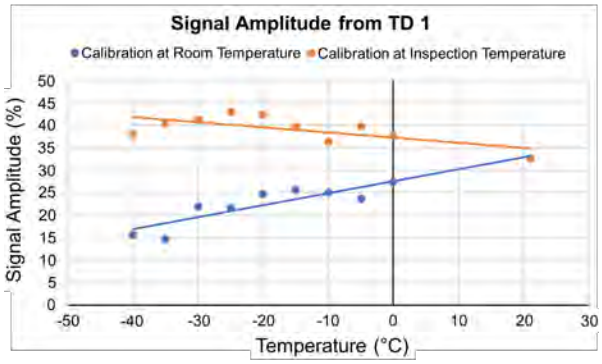

Figure 19. Comparison of signal amplitudes for TD 1 before and after calibrating the UT system at the inspection temperatures.

The maximum increase (by 26 percent) in the signal amplitudes from room temperature calibration to actual inspection temperature calibration for TD 1 was observed at -35°C, while the signal amplitude increased by 22 percent at -40°C. Similarly, a 14 percent increase in the signal amplitudes was observed at -40°C for TD 2.

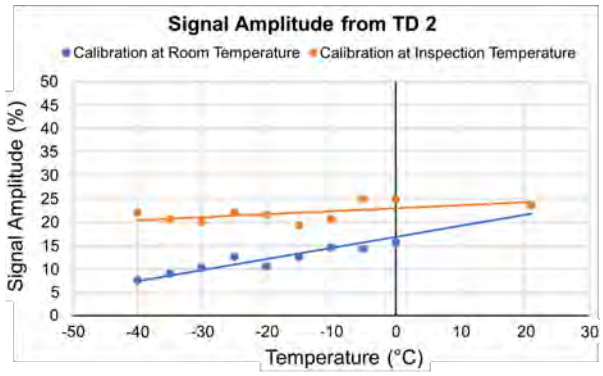

Figure 20. Comparison of signal amplitudes for TD 2 before and after calibrating the UT system at the inspection temperatures.

4 CONCLUSIONS

Extreme cold weather conditions bring many operational challenges to the railroad industry. Conducting rail inspections in extreme winter conditions is also very challenging. This research was conducted to study the effects of extreme cold temperatures on ultrasonic rail flaw testing capabilities.

The L-wave and S-wave velocities in the rail steel and the different fluids increased as the temperature decreased. The density of the fluids also increased as the temperature decreased. The angle of refraction of the S-waves decreased linearly with the decreasing temperature. Similar results were also obtained from the UT beam modeling and simulation. The changes in the angle of refraction can shift the beam away from the targeted inspection zone causing the beam to miss defects in that zone during the inspection process.

Thus, it is advisable to calibrate the hi-rail ultrasonic system at cold temperature while performing testing at cold temperature. It was observed from the tests conducted using the rail samples with transverse defects that calibrating the UT system at the actual inspection temperature when inspecting at cold temperatures helped improve the signal amplitude obtained from the defects.

5 ACKNOWLEDGEMENT

The authors would like to thank Transport Canada for providing funding to conduct the work reported in this paper.

REFERENCES

Banerjee, A., & Morrison, K. (2019). Fatigue Crack Growth Rate Properties of Rail Steels and Their Influence on Rail Life. Technology Digest, TD19-008. AAR/TTCI, Pueblo, CO.

Garcia, G., & Jeong, D. Y. (2003). Rail Defect Growth Under Heavy Axle Loads. Railway Track and Structures, Simmons-Boardman Publishing Corporation, New York, NY, pp. 17–19.

Ladubec, C., & Magel, E. (2011). Winter railroading in Canada: A review of track and rolling stock challenges. International Heavy Haul Association Conference, IHHA 2011, June 19-22, Calgary, Alberta, Canada, Collection / Collection: NRC Publications Archive / Archives des publications du CNRC.

Orringer, O., Morris, J. M., & Jeong, D. Y. (1986). Detail Fracture Growth in Rails: Test Results. Theoretical and Applied Fracture Mechanics, 5(2), pp. 63–95.

Poudel, A., Lindeman, B., & Wilson, R. (2019). Current Practices of Rail Inspection Using Ultrasonic Methods: A Review. Materials Evaluation, 77(7), pp. 870–883.

Poudel, A., Shrestha, S., Lindeman, B., & Washer, G. (2022). Ultrasonic Rail Flaw Testing Parameters in Extreme Cold Temperature. Proprietary report for Transport Canada, P-22-018, Pueblo, CO: MxV Rail.

Rose, J. L. (2014). Ultrasonic Guided Waves in Solid Media. Cambridge: Cambridge University Press. DOI:10.1017/CBO9781107273610.

Canadian & Cold Regions
Rail Research Conference
2024

Performance-based design principles in cold regions: Key requirements for addressing climate challenges on Canadian railways

Reza Mousapour
Department of Civil & Environmental Engineering – University of Alberta, Edmonton, Alberta, Canada

Payman Yousefi Mojir
WSP, Toronto, Ontario, Canada

ABSTRACT

Comprehensive design standards establish design specifications to meet the specific regional requirements from the initial design phase through construction. The 'Prescribed design' section explicitly defines all design components, simplifies design processes, reduces costs, and defines the required time in design standards. While the advantages of such an efficient approach are evident, there are inherent limitations. The 'Prescribed design' approach may not consider all the detailed specifications required for customized designs to meet regional needs. These additional simplifications may also result in over/underestimating design requirements in several scenarios. In cold regions, severe environmental conditions that can impact the performance of track components may not be sufficiently addressed. This paper provides an overview of North America's current railway track design standards and conducts a comparative analysis between these standards and the adaptive performance-based design approach.

1 INTRODUCTION

In North America, with a particular focus on Canada's cold regions, the extensive railway network is a crucial artery for freight and passenger transport. This network is governed by various entities, including Transport Canada, Canadian National Railway (CN), and Canadian Pacific Railway (CP). These companies use standards set by organizations such as the Federal Railroad Administration (FRA) and the American Railway Engineering and Maintenance-of-Way Association (AREMA). These guidelines have traditionally been developed assuming stable climatic conditions, which is required to consider the challenges of climate change. To address the risks posed by climate change and extreme weather to Canada's rail network.

The escalating impacts of climate change, marked by extreme temperature fluctuations in Canada's cold regions (Flannigan, M. et al. 2005), present significant challenges for railway infrastructure. The increasing frequency and severity of weather events highlight the urgent need for the railway industry to reassess the resilience and adequacy of current standards. Railway operators need to update their codes and practices with climate-resilient frameworks to withstand such unpredictable effects.

It must be considered that the railway tracks in Canadian cold regions, traditionally designed based on historical climate data, now face unexpected temperature variations. These variations are causing significant stress on the railway infrastructure, especially causing fatigue within the rail and track structure. This situation underscores the need to critically reassess current maintenance and inspection practices for the tracks and rolling stock to ensure they can withstand these new climatic conditions. However, more research is needed on the effects of climate-induced temperature variations on railway infrastructure in these areas.

Transport Canada has introduced the "Rail Climate Change Adaptation Program (R-CCAP)" as part of the Rail Safety Improvement Program. This program is dedicated to researching, developing, and implementing innovative technologies and approaches to identify climate change risks and mitigate extreme weather impacts on the Canadian rail sector (Transport Canada. 2016).

This paper addresses the significant gap in general understanding of the impact of climate change-induced temperature variations on railway infrastructure in Canadian cold regions. It aims to enhance North American railway standards by addressing climate change challenges through a comprehensive review of existing standards, employing a performance-based design approach. The study will review established practices worldwide to propose necessary adjustments to the current climatic conditions. It also seeks resources needed to conduct comprehensive full-scale tests that precisely simulate and address these evolving conditions.

2 IMPACT OF CLIMATE CHANGE ON RAILWAY INFRASTRUCTURE

Addressing the multifaceted challenge of climate change on railway infrastructure requires a comprehensive understanding and strategic approach to ensure the resilience and sustainability of rail systems.

Studies have identified various effects of climate change, including rail buckling, flooding, electrical equipment failure, bridge scour, ground settlement and increased susceptibility to extreme weather events, which can disrupt rail operations and incur substantial financial costs for repairs and maintenance (Kostianaia et al., 2021; Garmabaki et al., 2021). Palin et al. (2021) conducted a comprehensive analysis of climate change implications for railway infrastructure, emphasizing the increased frequency and intensity of extreme weather events and their potential impacts on railway systems. The study considers critical weather-related risks, including flooding, landslides, high temperatures, and storms, discussing the importance of transitioning from traditional risk assessment methods to ones that accommodate the deep uncertainties presented by climate change (Palin et al., 2021).

Numerous studies have examined the challenges arising from climate change and their effect on the infrastructures. While some of these studies offer insights from specific case studies, it may not be feasible to review them in detail. However, it would be more effective to review them generally to identify challenges and suggested mitigation approaches. Sa'adin et al. explore the risks of climate change concerning the Singapore-Malaysia High-Speed Rail System, pointing out that severe weather conditions, such as high temperatures, can lead to asset system failure, degraded operation, and delays in train services. They addressed the issues that cause storms, floods, and landslides and how they risk the railway infrastructure and the High-Speed Rail System operation in those regions (Sa'adin et al., 2016). In another study, Kellermann et al. discussed the changing frequencies of meteorological extremes, including very intensive rainfall, heavy snowfall, and heat waves that cause damage to the infrastructure and pose challenges in regular rail operations in Austria. They predict an increase in extreme rainfall and heatwave events, while heavy snowfall is expected to decrease as the future pattern (Kellermann et al., 2016).

Some studies addressed the effect of climate change on railway track components, focusing on different aspects, such as materials that have been used. Dikanski et al. (2017) explore the impact of climate change on railway bridge structures by focusing on bridge scour. They addressed climate change factors such as increased rainfall intensity and frequency, leading to higher river flows and greater scour risk (Dikanski et al., 2017). Kaewunruen et al. (2019) investigate the impact of extreme climate conditions on the topology and durability of railway-prestressed concrete sleepers, evaluating how extreme temperatures and humidity affect the creep and shrinkage behaviours of the sleeper's serviceability. They evaluate the significant role of environmental conditions, particularly temperature and humidity, in the time-dependent behaviour of these sleepers (Kaewunruen et al., 2019).

On the other hand, considering current climate change trends, Canada faces unavoidable warming trends, notably marked by an increase in warm days during the wintertime. This suggests that in the coming years, the number of days experiencing extreme temperature fluctuations will rise (Zhang et al., 2019), which is expected to result in many issues, including the risk of temperature fatigue failure in existing railway tracks. Figure 1 represents future projections for freezing degree days for high emission scenarios in the short and long term.

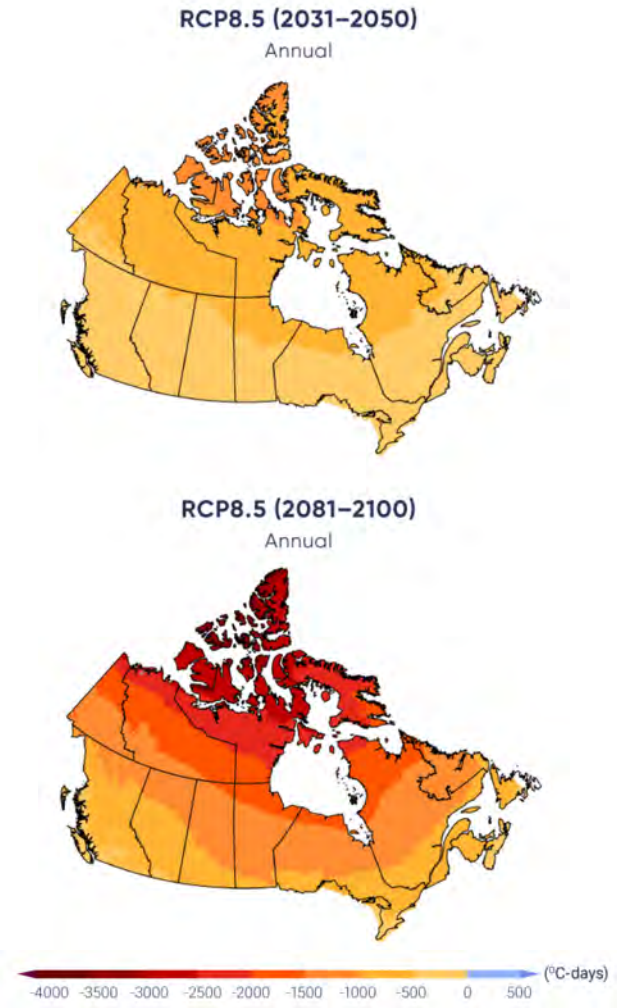

Figure 1. Future projections for freezing degree days for high emission scenarios in the short-term (2031-2050) and long-term (2081-2100). (Zhang et al., 2019).

Given the challenges encountered by existing railway systems in cold regions, various studies have been conducted to address the current issues related to the infrastructure. Roghani et al. provide valuable insights into the evolving challenges in cold regions by focusing on freeze-thaw cycles (FTCs) on railway tracks driven by climate change. They discussed that increased FTCs, as a direct consequence of warmer and drier winters, cause track surface deformation and geometry degradation

(Roghani et al., 2021). Mirzanamadi et al. discussed Sweden's railway system's challenges, including temperature-induced rail buckling and issues with frozen soil (Mirzanamadi et al., 2024). The studies emphasize the significance of implementing regular maintenance and measures as a proactive approach to ensure operational stability amid fluctuating environmental conditions.

These studies highlight the need to integrate climate adaptation strategies from the initial design phase of railway construction to effectively mitigate the challenges posed by climate change and ensure the long-term resilience of rail systems. In the case of existing railway tracks, it becomes imperative to develop customized proactive approaches based on the specific track conditions and the challenges posed by climate change. Revising existing codes, standards, and manuals is essential to ensure the adaptation of railway infrastructure to changing climate conditions and to guarantee its safety and resilience in harsh environmental circumstances.

3 CHALLENGES OF PRESCRIBED DESIGN IN COLD REGIONS

A general review of current railway standards and manuals, such as AREMA and Go Transit, reveals several challenges in the prescribed design for cold regions, particularly under the extreme cold weather conditions experienced in parts of Canada.

3.1 Extremely low temperatures

The current standards fall short in addressing the operational resilience and functionality of railway infrastructure at extremely low temperatures, such as those reaching -50ºC. This oversight underscores the necessity for standards that ensure infrastructure reliability under such harsh conditions.

3.2 Snow and ice management

Effective management of snow and ice is inadequately covered by the existing standards. Improved guidance on snow removal and de-icing strategies is essential to mitigate operational disruptions and enhance safety during extreme cold weather.

3.3 Climate change adaptation

As climate change leads to more frequent and severe weather conditions, it is imperative that railway standards are revised to reflect these new environmental challenges accurately. Climate change is making extreme weather more intense, which requires the design and maintenance standards to reflect it and suggest adaptation approaches. This adaptation is critical for ensuring the long-term resilience of railway infrastructure.

3.4 Material selection and design for cold weather

The provided manual and standards, while detailing maintenance procedures, lacks specific guidelines on the selection and design of track materials capable of withstanding very cold temperatures. This gap points to a pressing need for enhanced resilience under severe climatic conditions.

3.5 Durability and material testing:

The existing standards just test construction materials such as steel down to -25ºC, leaving a significant gap in evaluating these material's performance in severe conditions in cold regions. It raises concerns about the potential for material brittleness and failure, highlighting the urgent need for standards to mandate durability testing in more extreme cold conditions. Furthermore, the standards need to effectively address the contraction and expansion of materials caused by extreme temperature fluctuations. This is crucial for preventing structural issues such as track buckling and joint failures, which can compromise safety and efficiency.

3.6 Design of electrical and mechanical components

The current standards do not provide sufficient design considerations for electrical and mechanical components, like signalling systems, to function reliably in low temperatures. This lack of guidance could increase the risk of system failures during critical times.

These limitations show the current railway manual and standards should be updated to address the challenges of extreme cold weather and the broader impacts of climate change. It is vital for ensuring the resilience, safety, and efficiency of the North American railway network in cold regions.

4 PERFORMANCE-BASED DESIGN APPROACH

The traditional perspective design approach focuses on the means to develop a design and involves applying codes/standards to design an engineering element. Performance-Based Design (PBD) in engineering is a methodology that focuses on designing structures to meet specific performance requirements under various conditions, such as earthquakes, wind, or fire (Easa S. M. et al., 2019). PBD aims to ensure infrastructures can withstand environmental stresses while maintaining functionality, resilience, and sustainability. In the context of railway engineering, the performance goals are considered based on requirements rather than just adhering to existing standards and manuals. This approach is imperative in the context of climate change, where the resilience and adaptability of infrastructure are paramount.

Several studies consider the PBD approach in infrastructure design and maintenance. Liu et al. (2019) introduce a comprehensive PBD framework for high-speed railway suspension bridges, focusing on structural integrity, operational performance, and public safety. This study highlights the need for accurate design considerations, such as cable force adjustments and the integration of dampers, to ensure the bridge's functionality and safety under dynamic loads, reinforcing the railway system's resilience to environmental stresses (Liu et al., 2019). In another study, Micheli et al. (2019) explored the

integration of damping systems in wind-excited tall buildings that meet immediate performance criteria and optimize long-term economic and environmental impacts (Micheli et al., 2019). Similar studies show that by focusing on performance targets rather than prescriptive measures, PBD allows for innovative solutions that address both present and future challenges, ensuring the long-term viability of infrastructure over changing environmental and operational demands.

PBD emphasizes designing railway systems to withstand the dynamic challenges posed by environmental changes. It involves considering future climatic scenarios and ensuring that infrastructure such as tracks, bridges, and maintenance vehicles can endure and function under altered conditions. The infrastructure properties must adjust throughout the different phases of their life cycle, including design, operation, and maintenance (Thaduri A. et al., 2021). Considering climate change in PBD involves evaluating the impact of extreme temperatures, increased precipitation, flooding, and other climatic factors on railway infrastructure. Strategies for adaptation include advanced monitoring and early warning systems, innovative engineering techniques, and integrating climate considerations into design and maintenance (Agbehadji E. et al., 2023). The use of innovative materials and technologies is also regarded as an adaptation approach.

Genovese et al. (2017) investigate using new composite materials in railway vehicles to enhance energy efficiency and meet environmental standards. It represents where the PBD approach, including long-term sustainability and adaptability, drives the selection of materials (Genovese et al. 2017). Furthermore, implementing the PBD approach aligns with addressing environmental sustainability and infrastructure element adaptation to changing environmental conditions. Baluch (2019) emphasizes the need to consider climate change in designing and constructing new railway lines, focusing on reducing energy consumption and environmental impacts (Baluch, 2019).

It is crucial to ensure that infrastructures remain resilient and functional in changing environmental conditions. Sustainability and adaptability are integral components of the Performance-Based Design (PBD) approach, which emphasizes the importance of designing infrastructure that is both environmentally sustainable and capable of adapting to future changes. Performance-based design (PBD) in the railway industry represents a forward-thinking strategy by integrating climate change considerations and innovative technologies and prioritizing sustainable, resilient, and adaptable infrastructure. By adopting Performance-Based Design (PBD), railway systems can effectively address current needs while considering and preparing for future requirements and challenges. Overall, this approach addresses current needs while anticipating future requirements and challenges.

5 INTEGRATING PERFORMANCE-BASED DESIGN IN EUROPEAN RAILWAY STANDARDS

The EN standards in the railway sector are an example of implementing Performance-Based Design (PBD) principles, particularly in evaluating railway components such as fastening systems and ties under real-world loading and climate conditions. These standards provide a framework for assessing the overall performance of railway systems, considering environmental factors and long-term sustainability. Here's an insight into how this works:

5.1 System-Wide Assessment Under Real Conditions

The railway application EN standards, such as those for fastening systems (EN 13146 – Railway applications), and concrete ties (EN 13230 – Railway applications), emphasize testing these components under real-case conditions, highlighting the importance of climate variations. For instance, EN 13146- Part 5 outlines procedures to determine the electrical resistance of fastening systems in wet conditions, simulates scenarios such as heavy rainfall or flooding, and assesses the durability of these systems under severe environmental impacts. Also, EN 13146- Part 6 specifies test methods for fastening systems—the effect of severe environmental conditions.

5.2 Life Cycle Cost Analysis in Project Design

The total life-cycle cost (LCC) is defined as the sum of construction costs, inspection and maintenance costs, and serviceability failure costs, all adjusted to their future values, providing a comprehensive financial analysis from construction to the end of a structure's lifespan (Micheli, L. et al. 2019). The EN standard series facilitates a comprehensive analysis of the lifecycle costs of different railway components. By evaluating products under actual climate conditions, project designers can decide which materials and designs offer the best value and sustainability over the long term. This is where the PBD approach helps designers and operators consider real-world infrastructure conditions, including technical and financial aspects. For instance, when ties are selected according to EN 13230, considering climate factors, the decision may result in options that, although initially more costly, offer enhanced longevity and decreased maintenance expenses in particular environmental circumstances.

5.3 Ensuring Sustainability and Adaptability

Given the increasing complexity of climate change and the unpredictability of its future patterns, it requires the standard and manuals for an approach that considers current needs and anticipates future performance needs to design adaptable and resilient infrastructure. EN standards emphasize real-case testing and comprehensive analysis of whole-system performance to ensure infrastructure sustainability and resilience. In this context, the railway section of the EN standard series stands as an example of the PBD approach. It involves real-case testing of components and considering climate impacts, along with conducting life cycle cost analysis to ensure long-term sustainability. This approach ensures

that railway infrastructure remains resilient and adaptable to future environmental challenges.

6 FUTURE REQUIREMENTS AND INSIGHTS FOR PERFORMANCE-BASED DESIGN APPROACH IN NORTHERN AMERICA AND COLD REGIONS

North American Railway standards and manuals are required to address challenges arising from extreme cold weather conditions, snow and ice management, and climate change adaptation. Furthermore, inadequate design considerations for electrical and mechanical components and lack of proper guidance for material selection and durability testing for cold climates highlighted the need for updated standards to consider the infrastructure resilience, safety, and efficiency amid changing environmental conditions. Here's a list of the essential tools and facilities needed:

6.1 Climate Adaptation Testing Facilities - Simulation Chamber

A simulation chamber can assist with addressing the challenges of extreme cold weather and climate change and serves as the Climate Adaptation Testing facility. The test facilities' dimensions require allowing full-sized railway sections and components to be tested, ensuring realistic testing environments. It should feature the capability of a broad temperature range, from -50°C to +60°C, to simulate various extreme weather conditions, and be equipped with advanced humidity control systems to accurately mimic different climatic scenarios, including conditions of freezing rain, heavy snow, and high humidity. Swiss Federal Railways (SBB) has a climate chamber testing laboratory (Figure 2), that offers services for testing railway components under various environmental conditions. It simulates precise temperature and humidity control, ranging from +60°C to -33°C, facilitated by innovative systems such as cold air generation and distribution. With efficient insulation and circulation units, the chamber ensures minimal temperature differences (SBB Passenger Traffic Operations, 2019).

Figure 2. Testing laboratory Climate chamber. (Adopted from SBB Testing laboratory/climate chamber Brochure, 2019).

The National Research Council of Canada (NRC) offers a climatic testing facility, for assessing the performance of vehicles, rail cars, and components across various conditions (National Research Council of Canada, 2023). It needs to be modified to provide the opportunity to conduct full tests on railway track sections and their components in real-world situations. This facility enables the simulation of different scenarios to evaluate adaptation methodologies, revise existing standards, and develop localized manuals tailored to Canadian railway conditions.

6.2 Dynamic Load Testing Equipment

The Dynamic Testing Equipment must have a robust load capacity to replicate the real-scale forces and dynamic impacts seen on railway tracks, along a rail section. Furthermore, it should offer the versatility to simulate various dynamic load types, including vertical, lateral, and longitudinal forces, to ensure a comprehensive evaluation of track resilience and safety. It can address the current inadequacies in the documents about the track structure and components' behaviours under extreme weather conditions. This equipment enables a comprehensive assessment of infrastructure durability and helps implement adaptation methodologies to enhance the resilience, safety, and efficiency of railway infrastructures.

TÜV SÜD offers facilities to conduct dynamic testing on railway tracks under train loads, allowing for rigorous evaluation of track components and structures under various stress conditions (TÜV Rail Vehicle and Component Testing). Having such facilities, the Canadian Railway can simulate real-world scenarios, including those involving extreme weather conditions, contributing to the development of more resilient railway infrastructure in cold regions.

6.3 Electrical Resistance Measurement Tools and Fatigue Testing Equipment

Evaluating electrical and mechanical components in extreme temperatures through the test procedure and tools appropriate for that purpose is crucial to addressing their design requirements effectively. Electrical resistance measurement tools, along with vibration and fatigue testing systems, can accurately assess the performance and durability of track components. The EN 13146-5:2012 standard provides laboratory testing methods to determine the electrical resistance of fastening systems under wet conditions, which is crucial for ensuring the proper functioning of signalling systems in railway infrastructure (Vranešić, K., et al., 2023). However, studies and research must be provided to evaluate the fastening system's electrical resistance in extreme weather conditions. Figure 3 shows a sample for electrical resistance testing and the test equipment.

On the other hand, the fatigue test is essential for assessing the performance and durability of rail fastening systems under varying load conditions. Studies have evaluated different fastening systems under cyclic loads with a broad range of vibration frequencies to evaluate their behaviour over time. However, it's vital to conduct fatigue tests under diverse weather and temperature conditions to propose adjustments in standards and manuals considering climate change and regional requirements.

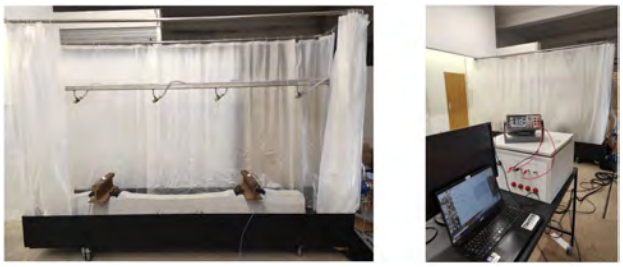

Figure 3. Electrical Resistance test sample and test equipment (Vranešić, K. et al., 2023).

6.4 Advanced Material Resilience Testing Equipment

Advanced material tests are essential to adequately address the requirement for selecting the materials appropriate for North American railways in extreme weather conditions. Here are some of the tests that are required for the cold regions:

6.4.1 Frost Heave Test Equipment

Frost heave, triggered by freezing temperatures causing soil expansion, can lead to structural damage and drainage issues. It is influenced by soil type, water content, and temperature severity. BS 812-124 provides a procedure for testing the frost resistance of material commonly used in road construction (BSI Group, 2009). This test involves compacting a cylindrical sample to a specified water content and density, followed by exposure to freezing temperatures. This test evaluates the potential of soil to undergo expansion due to the formation of ice lenses within its structure.

6.4.2 Freeze-Thaw Cycle Test

Due to climate change, the frequency of freeze-thaw cycles (FTC) has increased, and it is recognized that this impacts the stability, safety, and efficiency of railway tracks. ASTM C666/C666M-15 (2024) provides guidelines for conducting concrete freeze-thaw tests to evaluate concrete's resistance to rapid freezing and thawing, especially for Northern American regions. While the test method is explained for concrete components in railway tracks, it's essential to consider that the freeze-thaw phenomenon also affects other track structure and its components. Roghani (2021), conducted a study analyzing the track geometry measurements over one year after the completion of the thaw seasons, which suggested a significant degradation in track profile and alignment. Even though winters were warmer and drier, more frequent freeze-thaw cycles led to heightened frost heave and track roughness, resulting in notable damage to the track profile and alignment (Roghani, A., 2021).

6.4.3 Corrosion Resistance and Chemical Compatibility Test

These tests are critical for ensuring the durability of railway tracks in cold regions, as the use of de-icing chemicals and salts can significantly increase the risk of metal component corrosion and material degradation. These tests are essential for selecting materials that can withstand such harsh environmental conditions without compromising the structural integrity and safety of the railway system. The material testing standards, such as ASTM B117 for salt spray testing, offer relevant test guidelines to generate relative corrosion resistance data for metals and coated metals exposed to standardized corrosive environments.

7 CONCLUSION

Climate change poses significant challenges to railway tracks in cold regions, requiring a comprehensive review of current standards and manuals to ensure they are flexible and adaptable to changing conditions. This paper aims to address the needs of railway track operators who are responding to changing conditions in cold regions. It emphasizes shifting towards a performance-based design (PBD) approach. This method focuses on determining necessary modifications and adaptations based on performance outcomes, allowing for adjustments according to current needs. It will improve resilience and sustainability and enhance the safety and efficiency of railway tracks while they are dealing with challenges due to climate change.

Adopting PBD in North American railway standards requires integrating advanced simulation tools, climate adaptation testing facilities, and other advanced testing equipment to ensure a comprehensive evaluation of the infrastructure adaptation requirements. Those advanced simulators, which mimic various environmental conditions, would enable detailed assessment of materials, components, and overall track performance under extreme weather scenarios. The comprehensive testing and resulting performance outcomes help suggest climate adaptation strategies that can then be incorporated into updated manuals and regulations.

This approach requires collaboration among researchers, industry stakeholders, and regulatory bodies. These parties can update standards and guidelines to incorporate the latest scientific insights and technological advancements in regard to cold regions. This collaboration leverages ongoing research and innovation in materials science, structural engineering, and climate science to refine and advance the PBD approach. It ensures the development of railway infrastructure that is efficient, sustainable, and resilient to evolving environmental conditions. Furthermore, this approach is expected to bring economic benefits for the railway organizations. Although initial costs may increase due to modifications and improvements, long-term savings are ensured through reduced maintenance expenses and increased operational efficiency.

In conclusion, integrating performance-based design principles into North American railway standards represents a forward-thinking approach to infrastructure resilience, sustainability, and climate change adaptation. It is imperative for the railway industry to adopt this approach to effectively address the challenges posed by severe climate conditions. By considering performance outcomes and leveraging advanced testing and simulation technologies, North American railways can ensure safety,

reliability, and efficiency in the face of unpredictable climate change challenges.

REFERENCES

Zhang, X.; Flato, G.; Kirchmeier-Young, M.; et al. (2019). Bush, E.; Lemmen, D.S. (eds.). "Changes in Temperature and Precipitation Across Canada]; Chapter 4" Canada's Changing Climate Report.

Agbehadji, I. E., Schütte, S., Masinde, M., Botai, J., & Mabhaudhi, T. (2023). Climate Risks Resilience Development: A Bibliometric Analysis of Climate-Related Early Warning Systems in Southern Africa. Climate.

ASTM International. ASTM C666/C666M-15: Standard Test Method for Resistance of Concrete to Rapid Freezing and Thawing. Retrieved from https://www.astm.org/c0666_c0666m-15.html

Bałuch, H. (2019). Climate change and energy consumption–examples associated with railway construction. Problemy Kolejnictwa, (183), 77-82.

Easa, S. M., Yan, W. Y. (2019). Performance-based analysis in civil engineering: Overview of applications. Infrastructures, 4(2), 28.

Flannigan, M. D., Logan, K. A., Amiro, B. D., Skinner, W. R., Stocks, B. J. (2005). Future area burned in Canada. Climatic change, 72(1-2), 1-16.

Garmabaki, A., Thaduri, A., Famurewa, S., Kumar, U. (2021). Adapting Railway Maintenance to Climate Change. In Sustainability (Vol. 13, No. 24, Article 13856).

Genovese, A., Russo, M., & Strano, S. (2017). Mechanical characterization and modeling of an innovative composite material for railway applications. Proceedings of the Institution of Mechanical Engineers, Part L: Journal of Materials: Design and Applications, 231(1-2), 122-130.

Kellermann, P., Bubeck, P., Kundela, G., Dosio, A., Thieken, A. H. (2016). Frequency analysis of critical meteorological conditions in a changing climate—assessing future implications for railway transportation in Austria. Climate, 4(2), 25.

Kostianaia, E., Kostianoy, A., Scheglov, M., Karelov, A. I., Vasileisky, A. (2021). Impact of Regional Climate Change on the Infrastructure and Operability of Railway Transport. In Transport and Telecommunication Journal.

Li, D., Kaewunruen, S. (2019). Effect of Extreme Climate on Topology of Railway Prestressed Concrete Sleepers. In Climate (Vol. 7, No. 1, Article 17).

LIU, X., GUO, H., ZHAO, X., SU, P., GAO, M. (2019). Performance-Based Design Research on a Long-Span High-Speed Railway Suspension Bridge.

Micheli, L., Alipour, A., Laflamme, S., & Sarkar, P. (2019). Performance-based design with life-cycle cost assessment for damping systems integrated in wind excited tall buildings. Engineering Structures, 195, 438-451.

Mirzanamadi, R., Nyberg, E., Torstensson, P., Andersson-Sköld, Y. (2024). Lateral Track Buckling in Sweden: Insights from Operators and Infrastructure Managers. CivilEng, 5(1), 136-149.

National Research Council of Canada (NRC). "Climatic Testing Research Facility." National Research Council of Canada. [https://nrc.canada.ca/en/research-development/nrc-facilities/climatic-testing-research-facility]. Accessed 14 Jan. 2024.

Palin, E. J., Stipanovic Oslakovic, I., Gavin, K., & Quinn, A. (2021). Implications of climate change for railway infrastructure. Wiley Interdisciplinary Reviews: Climate Change, 12(5), e728.

Rail Vehicle and Component Testing, www.tuvsud.com/en-us/industries/infrastructure-and-rail/rail/rail-vehicle-and-component-testing. Accessed 14 Jan. 2024.

Roghani, A. (2021). Quantifying the effect of freeze-thaw cycles on track surface deformation and degradation of railway track geometry; Case study. Transportation Geotechnics, 30, 100601.

Roghani, Alireza. "Quantifying the effect of freeze-thaw cycles on track surface deformation and degradation of railway track geometry; Case study." Transportation Geotechnics 30 (2021): 100601.

Sa'adin, S. L. B., Kaewunruen, S., Jaroszweski, D. (2016). Risks of climate change with respect to the Singapore-Malaysia high speed rail system. Climate, 4(4), 65.

SBB Passenger Traffic Operations. (2019). Testing laboratory/climate chamber. SBB AG. https://www.sbb.ch/en/climate-chamber

Thaduri, A., Garmabaki, A., & Kumar, U. (2021). Impact of climate change on railway operation and maintenance in Sweden: A State-of-the-art review. Maintenance, Reliability and Condition Monitoring (MRCM), 1(2), 52-70.

Transport Canada. (2016). Climate Change Adaptation for Railways. Retrieved from: https://tc.canada.ca/en/programs/funding-programs/rail-climate-change-adaptation-program

Vranešić, K., Haladin, I., Lakušić, S., & Burnać, K. (2023). Convenient Procedure for Measuring the Electrical Resistance of Fastening Systems in Urban Railway Tracks. Energies, 16(4), 1990.

Canadian & Cold Regions
Rail Research Conference
2024

Efficacy of geocell modulus in reducing dynamic load factor on railway track subjected to freeze-thaw

Arghya Chatterjee, & Sanat Pokharel
Stratum Logics, Acheson, Alberta, Canada

Marc Breault
Paradox Access Solution, Acheson, Alberta, Canada

ABSTRACT

For a reliable railway track operation in cold climate, an effective load transfer mechanism from ballast and sub-ballast layers is required so that the vibration, bearing capacity of sub-soil, and the track settlement problems that ultimately cause track failure are minimized for safe operations. The railway traffic load transferred to the embankment is calculated as the effective static load scaled up by a dynamic load factor (DLF) that accounts for the impacts from variable velocity and deceleration from breaking. While some design methodologies proportion the DLF to the design velocity of the train, other research indicate the influence of track modulus is important. In cold climate regions, where the ground is subject to freeze-thaw cycles, there is a tendency to lose the effective stiffness of the railway embankment during thawing inviting higher DLF. This increase in DLF from the decrease in supporting soil modulus with time is not accounted for in current design practices. Additionally, the variance of stiffness along the track does call for higher DLF. Geosynthetic soil reinforcement not only increases the track modulus multifold, but as indicated in recent research, it also minimizes the loss of layer modulus caused by freeze-thaw cycles by at least 34%. Thus, effectively reducing the design DLF value and its uncertainty. This paper establishes guidelines in consideration for the DLF for rail track embankments reinforced with high-modulus geocell subject to freeze-thaw cycles. The geocell reinforcement also minimizes the uncertainty of stiffness variance and reduces the loss of track modulus. The theoretical study completed through this paper shows that the DLF can be reduced by at least 6.3% (at 40 kmph velocity with concrete ties) with the use of high-strength polymeric geocell reinforcement and the increase of DLF with thaw-softening is minimized significantly. A case of design implementation has also been discussed.

1 INTRODUCTION

While designing railway tracks, track foundations and other load transfer components the design layer thicknesses heavily depend on the effective load transferred into each member. A simplified approach in estimating the dynamic load is converting it into equivalent static load. This conversion is done by multiplying the load with Dynamic Load Factor (DLF). Scaled-up DLF accounts for the causes behind this dynamic load such as track undulations, track joints, dip angle, can't deficiency at curves, variance in track modulus. Track foundation design methods developed by Li and Selig (1998) utilize the DLF for calculating equivalent static load. Van Dyk et al. (2017) summarized and compared the different approaches currently used in the evaluation of DLFs. One of the commonly used formulations for evaluating DLF is the one developed by Talbot presented in AREMA (American Railway Engineering and Maintenance-of-Way Association, 2012). This DLF calculation method considers the design velocity of the train and the diameter of the wheel. Other methods like the one developed by the Washington Metropolitan Area Transit Authority (Prause, 1974) and Sadeghi (Sadeghi, 2010) have developed empirical relations to calculate the DLF based on the design velocity of the train only. While velocity does play a key role, these methods do not consider the importance of track modulus. Velocity can amplify the effect of track modulus leading to a higher DLF. In cases like cold climate regions where freeze-thaw action negatively affects the supporting soil modulus, the assumption of neglecting foundation soil strength in DLF is over-simplification which may lead to design deficiencies. Some recent experimental (Behnia, 2022) and numerical (Anh Dung, 2020) studies done on DLF developed new statistical correlations and highlighted the importance of required further studies. Roustaei (2021) has shown that the variance in frost depth with climate change can be a challenge in the near

future for rail subgrade and embankment strengths, particularly with thaw softening. The methodologies recommended for design by Indian Railways (Srinivasan, 1969) do indirectly account for the supporting soil strength in calculating DLF by considering track modulus (equation 1). Doyle (1980) attempted to algebraically combine the Talbot equation (equation 2) and the Indian Railways standard into equation 3. This helped with the inclusion of the diameter of the train wheel (D), along with the track modulus (U). It is observed that Doyle (1980) is slightly conservative for a typical 36-inch (914mm) diameter wheel.

$$\varphi = 1 + \frac{V}{3 * \sqrt{U}} \quad [1]$$

$$\varphi = 1 + \frac{33 * V}{100 * D} \quad [2]$$

$$\varphi = 1 + \frac{15 * V}{D * \sqrt{U}} \quad [3]$$

where, φ is the calculated DLF, V is the velocity of the train (in mph; 1mph = 1.609kmph) and U is the track modulus (psi, 1MN/m/m = 145.038psi) and D is the diameter of the wheel (in; 1in = 25.4mm).

Selig and Li (1994) in their detailed study on track modulus established that one of the key parameters influencing track modulus is the subgrade strength. Cai et al. (1994) tried to develop mechanistic methods for developing the relation with the entire supporting soil along with subgrade for estimating the track modulus. Ultimately, it cannot be denied that the track modulus is a function of the supporting embankment and the effective subgrade modulus. Thus, accounting for the track modulus in the calculation of DLF also accounts for the strength of the supporting soil.

Loss of modulus within the embankment and the subgrade by freeze-thaw cycles, varying water level, lateral spreading of ballast and sub-ballast, and other reasons affect the track modulus. A variance of stiffness along the driving direction can invite additional impacts and thus lead to higher dynamic forces. These forces in turn overload the embankment, leading to an increased demand for maintenance and in some extreme cases early failure of tracks. The current design methodologies neglect this variance of foundation soil strength in calculating DLF by assuming same modulus for embankment and subgrade over the entire design life. Cai et al. (1994) while trying to establish a theory for track modulus calculation, mentioned that track modulus shall vary based on freeze-thaw (F-T) cycles. Local influence with the presence of water and improper drainage can worsen the condition and lead to relative stiffness issues. Mian et al. (2021) using lab experiment has shown that multiple cycles of freeze-thaw can lead to the reduction of stiffness and ultimate bearing capacity of granular backfill material by 80%. This fluctuation of embankment strength does affect the track modulus and leads to an uncertainty in the design value for DLF. Mian H. (2020) discusses that the use of high-strength Novel Polymeric Alloy (NPA) geocell can preserve the strength loss by at least 34%. Initial results from full scale field application in NPA geocell reinforced pavement, subject to free-thaw cycles, showed the potential on preservation of higher load distribution angle as compared to unreinforced sections Mian H.'s (2023). Thus, reducing the uncertainty of DLF calculation. This paper establishes guidelines in consideration for the DLF for rail track embankments reinforced with high-modulus polymeric geocell subjected to freeze-thaw cycles.

2 METHODOLOGY

The correlations developed by Cai et al. (1994) have been reproduced to link the embankment stiffness with track modulus. There are several simplified approaches discussed in the same paper. However, for ease of application and looking into the practical application aspect, the resultant graph (in Figure 1) with three different kinds of tie cases has been used. Concrete ties are typically used in conjunction with rubber pads. Rubber pads are usually high-density polyethylene (HDPE) or ethylene-vinyl acetate (EVA) or some other variety of grooved synthetic rubber (SYN). Based on the stiffness of the pad, the composite stiffness (k_v) of the tie varies largely. For example, a Canadian National (CN) 55A category concrete tie (180mm x 230mm x 2600mm) with an EVA pad placed at every 600mm can have k_v around 107MN/m/m while the same with SYN can be around 84MN/m/m and a wooden tie of somewhat similar dimension (210mm x 240mm x 2500mm) would have an effective stiffness of around 63MN/m/m. In Figure 1, it is observed that as the tie gets stiffer the importance of the supporting soil stiffness increases. The relation between the track modulus and the supporting soil stiffness can be represented using polynomial equations of second order (equation 4). The coefficient for the equation varies based on the stiffness of the rail ties.

For the given three types of ties, the coefficients of the best-fit polynomial equations in Figure 1, are plotted with respect to k_v in Figure 2. For design application, if a different tie configuration is used the resultant k_v will have to be calculated independently and the relevant coefficient for the polynomial relation (equation 4) between k_s and U can be derived from Figure 2. Once the coefficients A' and B are known, the track modulus (U) can be derived for a specific supporting soil modulus (k_s) using equation 4.

Instead of developing a new correlation for DLF as a function of track modulus, current established and accepted design methodologies by Indian Railways and Doyle (1980) have been used for the current study. Once the track modulus is known for the specific supporting soil modulus the DLF can be computed using equation 1 or equation 3. A full-scale study is however, recommended for the future to have more reliable and optimized relations.

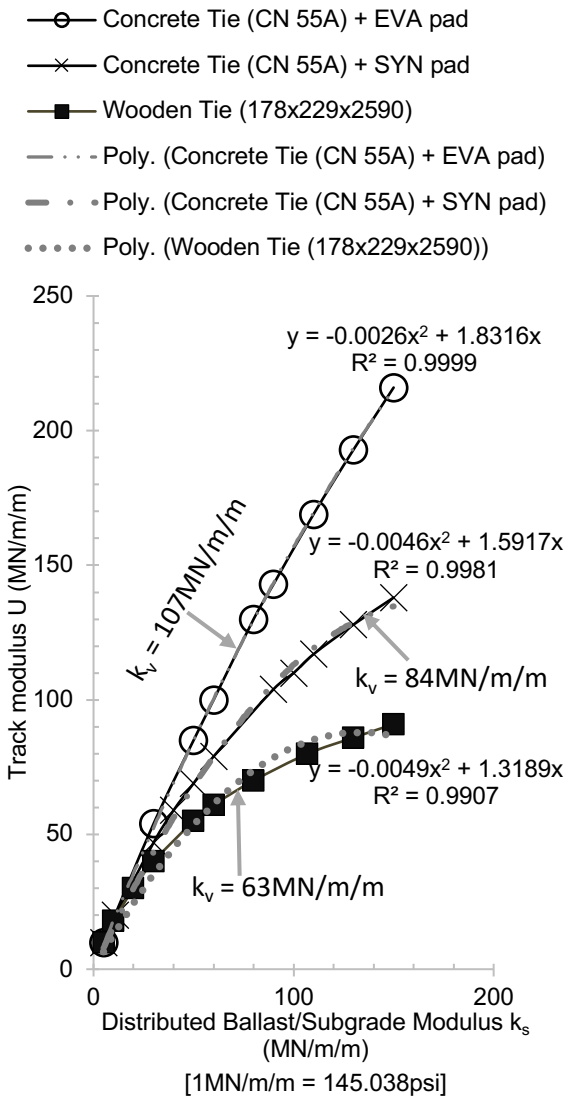

[1MN/m/m = 145.038psi]

Figure 1. Relation between track modulus with supporting soil stiffness for various tie stiffness (original correlations reproduced from Cai et al. (1994) with added mathematical relations)

$$U = \frac{-(k_s)^2}{1000} * A' + k_s * B \quad [4]$$

where, k_s is the composite stiffness of the embankment and the subgrade and *A'* and *B* are the dimensionless parameters derived from Figure 2.

As mentioned before (Mian et al. 2021), soil can lose 80% of its mechanical strength (stiffness and bearing capacity) over five freeze-thaw cycles. Using the calculation methodologies discussed above, this reduction of soil strength increases the DLF from 41% to 44% based on the type of tie used for a design velocity of 75mph (121kmph). Even for tracks with relatively slower design velocity, like loops for loading and unloading grains having a design velocity of 25mph (40kmph), the DLF increases in the range of 18% to 20%. Thus, the loss of supporting soil strength must be considered in estimating the DLF.

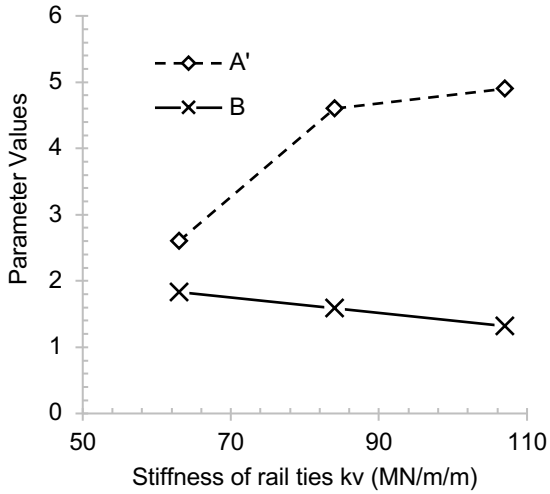

Figure 2. Parameter approximation based on tie stiffness for track modulus calculation

Nimbalkar (2012) through several case studies and literature reviews identified the importance of using geocells and maintaining the supporting soil strength for the long-term performance of rail tracks. Though the observations align with the current study on DLF, nothing in particular on DLF was identified in that research. The study summarized the current practices on design with geocell for rail embankments, identifying the potential for modulus improvement and risk elimination with other long-term uncertain parameters like varying water levels. It must be noted that the loss of supporting soil strength can also lead to issues with settlement, bearing capacity loss, etc., however for the current scope of the study, the focus is on DLF only. The use of soil reinforcement, particularly NPA geocell, increases the soil modulus from 2.5 to 5 times, as reported by multiple research (Saride, et al. 2022; Kief et al. 2011; Pokharel et al. 2018). Chatterjee et al. 2023) explained the mechanism of how such modulus improvements are achieved and maintained over the long term through high modulus geocell. This use of high strength/modulus geocell reinforcement can be seen as a multi-level advantage in the long-term performance of the design. Firstly, the initial strength provided is higher. For example, with a design velocity of 75mph (121kmph), using a modulus improvement factor of 3, the DLF reduction can range between 12% to 15% based on the stiffness of the sleepers considered in the study above. For an even higher modulus improvement factor of 5, this reduction can scale up to 25% at 125mph (201kmph) design velocity with concrete sleepers. Secondly, soil reinforcement can reduce the loss of supporting soil strength. Mian et al. (2020) reported that the use of NPA geocell can reduce the loss of strength in the order of 35% over several freeze-thaw cycles as compared to conventional unreinforced sections. This can minimize the risk of underestimating the DLF in the long-term

performance of the track. Thus, to compare the effective modulus improvement factor over the long term, it can be stated that the unreinforced section starts with a modulus factor of 1.0, and then over the freeze-thaw loss of 80%, it reduces to 0.2. Whereas NPA geocell starts with a minimum modulus improvement factor of 3.0 and then with 35% less loss (loss rate = 80% -35% = 45%) of strength, it results in a modulus improvement factor of 1.45 (3*0.45). This long-term modulus improvement factor effectively reduces the DLF by at least 6%, as compared to increasing by 41% for the unreinforced design (considering the design velocity of 8 kmph).

3 DESIGN IMPLEMENTATION

At Kargil Moose Jaw in Saskatchewan, Canada, the loop track used for loading grains needed high maintenance for relative settlement and track alignment issues (Figure 3). This was particularly prevalent at track joints and where the train changed velocity like at turns and close to the loading-unloading point. Amongst several reasons for the poor performance of the track, the most critical one observed was the lack of proper ditching, fine migration from sub-grade and varying water levels leading to the loss of embankment stiffness. Figure 4 shows the subgrade that is susceptible to strength loss from freeze-thaw effects. The estimated strength for the exposed subgrade was around 1% CBR (California Bearing Ratio). Though no record of previous subgrade preparation was available, it can be stated that with varying seasonal water level and temperature, the sub-grade also faced some strength loss. Adding a layer of geotextile for separation was an identified necessity. This reduction of the modulus of the base layer leads to the increase of applied pressure at the subgrade-sub-ballast interface than what it was theoretically designed for. Subsequently, worsening the condition with an amplified DLF. The track was rated for an effective design velocity of 25 miles per hour with wooden ties (178mm x 230mm x 2590mm) at every 475mm. Using the methodology discussed above without any reinforcement, it was estimated that the loss of subgrade stiffness should have accounted for at least a 7% increase in DLF. From φ=1.19 for no adjustment on supporting soil stiffness loss, to φ = 1.26 for roughly 50% loss of the soil modulus).

The seasonal loss was prevented using a geocell of pocket size 210mm x 245mm and 150mm high. The presence of woven geotextile under geocell reduced the risk of sub-ballast contamination. Class 1 category crushed rock ballast (Canadian National Engineering Specifications for Industrial Tracks, Appendix A, 2019), having <1% fines (passing 0.75mm sieve) and 70-90% passing 50mm sieve was used. The sub-ballast used was Type 33 sand with less than 15% fines (passing 0.75mm sieve), as per the specifications of Saskatchewan Highway and Transportation (September 2004). The ballast and sub-ballast thickness were 250mm and 225mm respectively. It was possible to use sand owing to the confinement effect of geocell proving the necessary strength. The effect of reinforcement reduces with a larger pocket size and thus, the optimum cell pocket size was selected. Geocell material was selected to be high strength (tensile strength of 22kN/m with dynamic stiffness modulus of 800MPa at $+30^0$C) for optimum performance. The selected design with the sandy infill having around 15% fines for sub-ballast provided roughly 3 times effective modulus improvement over a conventional structure.

Figure 5 shows the schematic of the load-bearing section. The profile was designed to maintain a positive drainage and not to drain the water into the vicinity track. This modulus improvement with NPA geocell also opened the opportunity to reduce DLF by roughly 5.5% (φ=1.12). Considering the combined effect of the stiffness loss that was prevented with the improved modulus, the net change in DLF considered was 12.5%. This reduction of 12.5% load is reciprocated into an embankment fill reduction of at least 10% for the same bearing at the subgrade interface.

Figure 3. Track alignment issues

Figure 4. Subgrade susceptible to strength loss with freeze-thaw

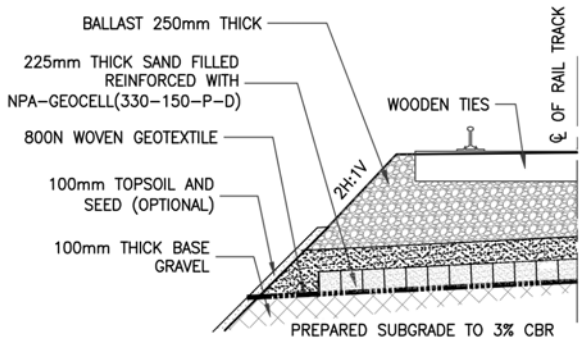

Figure 5. NPA geocell design

4 RESULTS AND DISCUSSION

Velocity plays an essential role in DLF, so based on the developed methodology discussed above, it was essential to test how the supporting soil would impact DLF over a varying range of velocities. In Figure 6 and Figure 7, two specific cases for typical rail ties were chosen. The tie systems were assumed to be placed 600mm apart. It can be assumed that the unreinforced embankment right after completion of construction, which is yet to face any loss of modulus, has a factor of 1.0. Factor 0.5 is used for a modulus loss of around 50% over several freeze-thaw cycles. The loss of supporting soil strength can happen over time in non-freeze-thaw cases as well. For example, varying water levels, fines migration, and lateral spreading can all lead to loss of strength. Factors 2 to 4 have been assumed based on the effective improvement provided by NPA geocell soil reinforcement after potential long-term strength loss.

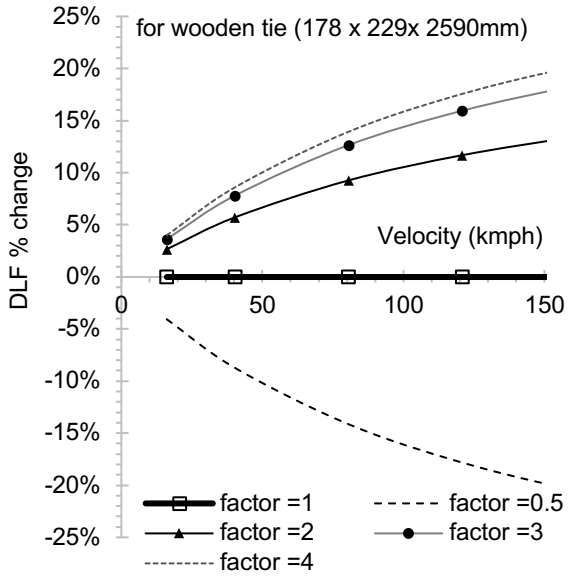

Figure 6. Change in DLF for various modulus improvement factors in the case of wooden ties.

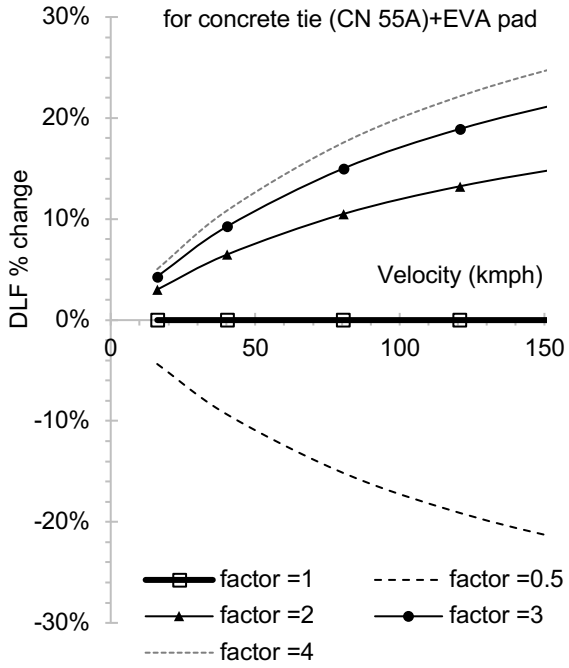

Figure 7. Change in DLF for various modulus improvement factors in case of concrete ties (+EVA pads)

As shown in Figure 6 and Figure 7, the loss of supporting soil strength can massively increase DLF, particularly for tracks designed for high-velocity rails. At 100 miles per hour, in the case of a wooden tie, the loss of 50% strength demands a DLF increase of 16.1%. However, the same case with an effective 3-factor improvement reduces DLF by 14.4%. When the design velocity is reduced to 25mph (=40kmph), with potential for strength loss the DLF needs to increase by 5.9%,

whereas when the ground is improved by an effective factor of 2 with NPA geocell reinforcement, DLF can be reduced by 3.9%. From Figure 6 and Figure 7, it must also be noted that an efficient design must focus more on the protection of the strength loss and a slight increase in effective modulus. The change in DLF reduction percentage is not as significant when the effective modulus improvement factor is increased from 3 to 4, as compared to an increase from 1 to 2.

Figure 8 and Figure 9 represent a simplified model where the percentage change in DLF can be calculated based on the long-term effective soil modulus for the concrete and wooden ties. In Figure 5, focusing on the design velocity of 75mph (121kmph), with the long-term reduced effective modulus being at 60% of the original design modulus, DLF needs to be increased by 10%. However, with the use of soil improvement and retaining an effective modulus of 2.5 times the theoretical unreinforced modulus the DLF reduction is roughly 11%. Thus, an overall effective DLF reduction of 21% is possible with improved soil with NPA geocell reinforcement.

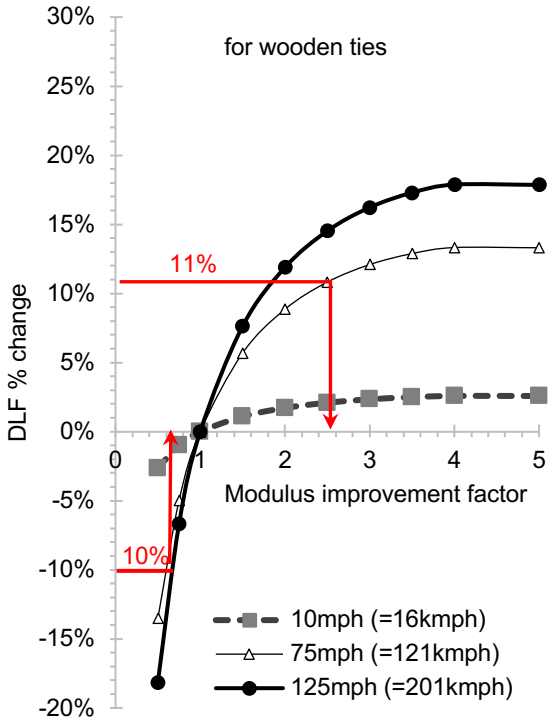

Figure 8. Percentage change in DLF with improved soil modulus for wooden ties

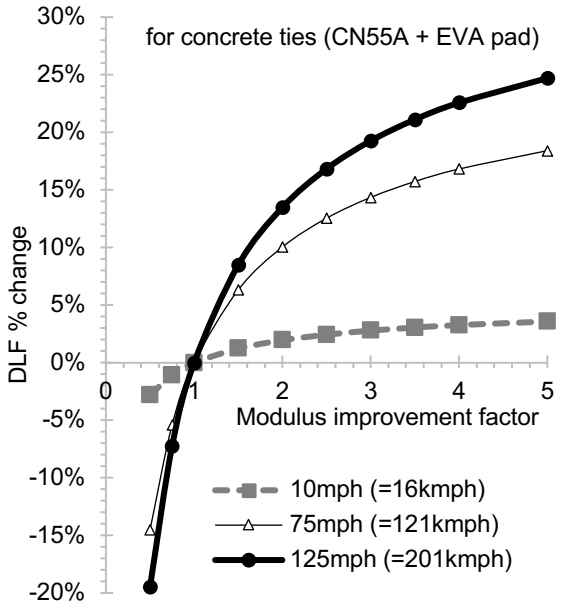

Figure 9. Percentage change in DLF with scaling soil modulus for concrete ties (CN55A + EVA pad)

Comparing Figure 8 and Figure 9, it can be stated that at higher modulus improvement and higher design velocities, the reduction of DLF is more prominent. Reduction of overall load and particularly the dynamic factor has a significant impact on achieving optimum design for the rail tracks and stable embankment. It must also be noted that with higher stiffness of rail ties, the DLF factor adjustment is more prominent.

The results discussed as part of this study are limited to currently available literature and rail track design standards. Most of these are limited to lab-based experiments only. Although a practical example is discussed here, it must be noted that for application in practical design using the suggested DLF adjustment methodology, more practical validation with full-scale experiment is recommended. There are very limited studies available on the dynamic advantages of using geocell for rail embankment. The effect of soil reinforcement on DLF, particularly for cold climate areas can be amplified significantly with the modified elastic vibration parameters of a reinforced embankment. Pokharel and Breault (2020) implemented high modulus geocell reinforcement design on permafrost zones and other soft soil zones susceptible to strength loss over freeze-thaw cycles. The DLF modification methodology was not available during the design phase. However, the fact that the design worked successfully over more than six years, whereas the vicinity areas without soil reinforcement struggled with maintenance, shows that there is a potential for DLF adjustment considerations in future cold climate designs.

The example discussed showed successful design implementation, the construction was completed in May 2021. Figure 10 shows the compacted base for laying woven geotextile (Figure 11). Figure 12 shows the high strength geocell being stretched.

Figure 10. Base prepared for laying woven geotextile

Figure 11. Woven geotextile layer

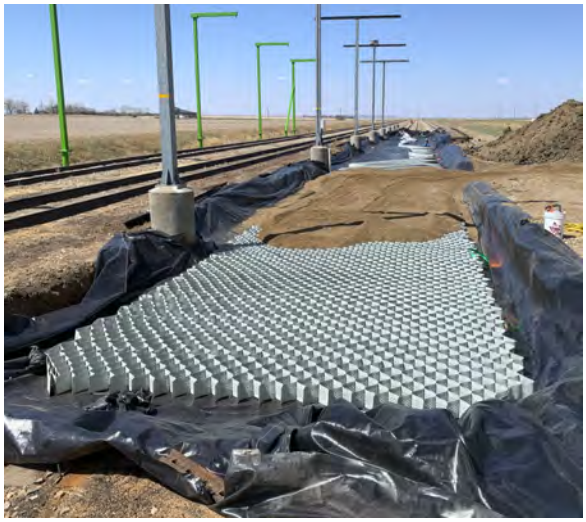

Figure 12. Stretching geocell as per design section and using sand (<15% fines) as infill material

The methodology of DLF adjustment was implemented conservatively as there was no other lab-based results to validate the theoretical development. At certain locations sub-cut of a maximum of 400mm was necessary to match the track grade to the existing. The site has been under regular monitoring and observation for over two years. No settlement, lateral spreading, ballast contamination from the vicinity-standing-water or any other issue have been observed. Figure 13 shows the track one year after construction, prior first track-surfacing. It can be stated that the high modulus geocell has the potential for further optimizing the design, particularly under the effect of rail vibrations. However, that demands more research and validation.

Figure 13. Performance a year after construction

5 CONCLUSIONS

Calculation of DLF plays a key role in rail track design. Though in most available standards the DLF calculation depends on rail design velocity, there can be other important parameters that significantly influence the DLF like track modulus. Particularly areas where the supporting soil is subject to a seasonal strength loss with freeze-thaw or varying water levels or otherwise. On the other side, the advent of soil reinforcement with advanced technologies like NPA geocell has opened avenues for optimizing the DLF. Through the current theoretical study and the implemented design, a methodology has been developed where this DLF adjustment can be computed. The methodology has been simplified on a case-specific basis for ease of application and finding the safe range of DLF that can optimize the design. For future studies, carrying out full-scale lab experiments is recommended. It must also be noted that the presence of high modulus geocell, reduced the strength loss of the embankment. Thus, proportionally reducing deformation, enhancing the track geometry, reducing the maintenance cycles to lessen operational disruptions.

REFERENCES

Van Dyk BJ, Edwards JR, Dersch MS, Ruppert CJ, Barkan CP. (2017) Evaluation of dynamic and impact wheel load factors and their application in design processes. Proceedings of the Institution of Mechanical Engineers, Part F: Journal of Rail and Rapid Transit. 2017;231(1):33-43. doi:10.1177/0954409715619454

AREMA Manual for Railway Engineering. American Railway Engineering and Maintenance-of-Way Association. s.n., 2012.

Prause, R. H. and Meacham H.C. (1974) Assessment of Design Tools and Criteria for Urban Rail Track Structures. Department of Transportation: Urban Mass Transportation Administration.

Sadeghi, J. and P. Barati. (2010) Evaluation of conventional methods in Analysis and Design of Railway Track System. In International Journal of Civil Engineering, Vol. 8, p. 46.

Roustaei, M., Hendry, M. T., Roghani, A. (2021). Effect of climate change on frost penetration depth in the subgrade soil beneath railway tracks: case study. First Canadian & cold regions rail research conference. 9-10 November 2021, Virtual Event.

Behnia D., Hendry M.T., Haji Abdulrazagh P., Wahba A. (2022) Railway Dynamic Load Factors Developed from Instrumented Wheelset Measurements. Journal of Transportation Engineering, Part A: Systems. 2022 Jul 1;148(7):04022042.

Anh Dung T., Van Tham M., Xuan Quy D., The Truyen T., Van Ky P., Hai Ha L. (2020) Numerical and experimental study of the dynamic factor of the dynamic load on the urban railway. Journal of the Mechanical Behavior of Materials. 2020 Dec 31;29(1):195-202.

Li, D., Selig, E.T. (1998) Method for railroad track foundation design. II: Applications. Journal of Geotechnical and Geo-environmental Engineering 124(4), 323-329.

Srinivasan, M. Modern Permanent Way. (1969) Somaiya Publications Pvt. Ltd., Mumbai, India.

Doyle, N. F. (1980) Railway Track Design: A Review of Current Practice. BHP Melbourne Research 301 Laboratories, Bureau of Transport Economics, 1980

Selig, E.T., Li, D. (1994). Track modulus: its meaning and factors influencing it. Transportation Research Record.

Cai, Z., Raymond, G.P., & Bathurst, R.J. (1994). Estimate of static track modulus using elastic foundation models. Transportation Research Record.

Mian H., Lin C., Pokharel S.K. (2021) Freeze–thaw effects on the mechanical behavior of geocell-reinforced sands from element and model tests. International Journal of Geosynthetics and Ground Engineering. 2021 Jun;7(2):40.

Mian, H., Lin, C., Pokharel, S.K., Tura, A., Mukhopadhyaya, P. (2020). Model tests of freeze-thaw behavior of geocell-reinforced soils. Geotextiles and Geomembranes. 49. 10.1016/j.geotexmem.2020.12.003.

Nimbalkar, S., Indraratna, B., Dash, S.K., Christie, D. (2012) Improved Performance of Railway Ballast under Impact Loads Using Shock Mats. Journal of Geotechnical and Geo-environmental Engineering 138(3), 281-294 (2012).

Saride, S., Baadiga, R., Balunaini, U., & Madhira, M. R. (2022). Modulus improvement factor-based design coefficients for geogrid- and geocell-reinforced bases. Journal of Transportation Engineering, Part B: Pavements,148(3). https://doi.org/10.1061/jpeodx.0000380

Kief O., Rajagopal K., Veeraragavan A., Chandramouli S. (2011) Modulus improvement factor for geocell-reinforced bases. Geosynthetics India. 2011 Sep-11.

Pokharel, S., Han, J., Leshchinsky, D., & Parsons, R. (2018). Experimental evaluation of Geocell-reinforced bases under repeated loading. International Journal of Pavement Research and Technology, 11(2), 114–127. https://doi.org/10.1016/j.ijprt.2017.03.007

Chatterjee A., Pokharel S.K., Breault M. (2023). Polymeric Alloy Geocell Reinforced Design for a Heavily Loaded Gravel Pad with Restricted Fill Thickness. Industrial Fabrics Association International Conference (IFAI / ATA), Kansas City, USA.

Pokharel S.K., Breault M. (2020). High-strength polymeric geocell-reinforced railway line repair in degraded permafrost condition. Industrial Fabrics Association International (IFAI / ATA), Indianapolis, USA.

Canadian National Engineering Specifications for Industrial Tracks, Appendix A (January 31, 2019). Office of chief engineer structures, design, and construction.

Saskatchewan Highway and Transportation. Section 3500 Specification for base aggregate and base mix (September 2004). Government of Saskatchewan.

Mian, H., Jiming L., Cheng L., Pokharel S., Dagenais T., Chatterjee A., (2023) Field experimental investigation of geosynthetics-stabilized bases in Sturgeon County, Alberta. GeoSaskatoon Conference 2023. Saskatoon, Saskatchewan, Canada.

Session 7

INNOVATION AND EMERGING TECHNOLOGIES IN RAILWAY

Canadian & Cold Regions
Rail Research Conference
2024

Rail monitoring system

John Wallace
Tensar, Alpharetta, GA, USA

ABSTRACT

Traditional methods utilized to inspect and plan rail ballast and subgrade maintenance tend to be periodic with weeks or months delay between inspections and are focused mainly on what can be observed via visual inspection or track geometry. While these methods provide good information, they don't always reflect the current state of the ballast and subgrade which can vary considerably due to climate conditions and other variables. Near "real time" information on track health can be valuable in detecting issues early as well as understanding if a problem area needs immediate attention. A new type of sensing system has been developed which utilizes multiple components to analyze the track condition and provide data in near "real time". The system uses embedded sensors and an IoT and Analytics platform to detect and report the current status. These sensors are combined with other data sources to create a "sensor fusion" effect which, when analyzed together as a complete system, can interpret the data and provide key insights about the overall condition of the track. These insights which reflect current track conditions can provide operators with the ability to implement a proactive, data driven maintenance strategy and optimize budgets. This paper will describe the various components of the system as well as review data and results from field tests.

1 INTRODUCTION

Passenger and freight rail is a critical part of the overall transportation infrastructure. Climate change has created a new urgency for rail usage which includes ensuring adequate maintenance is performed on the track structure in a timely manner. The Rail track supporting structure generally consists of a layer of sub ballast and ballast placed over the subgrade. This structure provides support to the ties and rails and helps to ensure the safe operation of the railway. Degradation can occur in the structure due to traffic and environmental conditions. This degradation occasionally requires some type of maintenance to return the structure to full health and ensure the structure is able to support the rail traffic in a safe manner. Knowing when and where to perform these maintenance activities can be challenging. Operators usually rely on some type of inspection of the structure to determine maintenance needs.

Inspection techniques to assess the condition of the rail structure and the need for maintenance fall into two categories: Visual or Automated. Automated inspection techniques include the use of Track Geometry Cars, Ground Penetrating Radar and similar techniques (Fontual et al. 2016) which can generate useful data but are performed periodically which means the track health could have changed since the last scan and the data may not represent the current condition of the track. The frequency of the automated inspections can vary with the type and use of the track but generally occur at least one time per year (APTA 2017). For longer term maintenance planning the current condition of the track structure may not be of major concern. However, in known problem areas or areas where emergency maintenance may be required, knowing the current, near real-time status of the track structure is especially important. The goal of this research is to develop a new type of monitoring system which can provide near real time information about the current state of the rail track structure. This information could be used as an input to a condition-based maintenance program to pinpoint areas of concern as well as highlight areas where an immediate repair is needed.

This paper discusses the design of the system as well as initial results from early field trials. Additional data collection and analysis is ongoing.

2 MATERIALS AND METHODS

Rail track structure generally consists of a sub ballast and ballast on top of the subgrade which form the supporting structure for the rail track. Depending on subgrade conditions, a layer of geogrid can be added to increase the support structure as shown in figure 1. Performance of the rail track depends on how well the supporting structure manages the loading from train traffic. Over time, repetitive loading from traffic as well as weather conditions can affect the substructure and the ability to safely support traffic. Excess moisture (accelerated by Climate Change) in particular can weaken the subgrade and create weak areas which must be addressed.

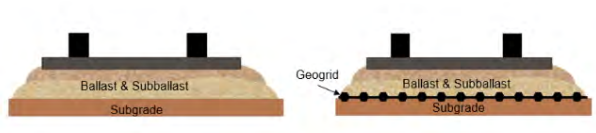

Figure 1. Track Configuration

As a train travels over a section of rail track, some small momentary deflection or displacements of the track structure occurs. For well supported track, the amount of the deflection is small (1-2 mm) but can vary considerably depending on the condition of the supporting substructure. The amount of deflection is related to the stiffness of the substructure with a greater deflection occurring for a soft supporting structure which is associated with poor performance and a need for maintenance (Powrie & Le Pen 2016). Measurement of the deflection which occurs under a load can be a useful parameter to determine overall substructure health, especially when this measured parameter can be trended over longer time periods to assess changes from a baseline measurement.

2.1 System Description

As noted above, the goal of this research is to develop a new type of monitoring system which can provide near real time information about the current state of the rail track structure. In order to accomplish this, several components are needed, not only to capture the value of the parameters of interest but to store and transport the data to a cloud-based platform for analysis. The following paragraphs describe each of the components.

2.1.1 Sensing

Different sensing methods have been evaluated during the project. Strain gauges were initially used as a sensing method. The strain gauges were mounted on the rail as shown in figure 2. While the gauges can measure small amounts of strain during rail traffic, they are somewhat difficult to install as they need to be mounted on the rail itself and protected from any moisture or other environmental damage.

Figure 2. Strain gauges on rail

In addition, the data can be somewhat difficult to interpret in noisy electrical environments due to the very small signal levels. The original intent in using strain gauges was to combine the strain measurements from the different gauges and calculate an approximation for the track modulus which could be trended over time to look for changes that would indicate the need for maintenance. Obtaining a consistent calculation for the track modulus in the presence of noise as noted above proved challenging and not reliable enough to identify issues which would require maintenance. Because of the difficulty in mounting the strain gauges as well as the lack of consistency in the modulus calculation a review of other sensing technologies was performed. It was found that accelerometers could be used when proper analysis techniques were applied. Accelerometers measure the acceleration the sensor experiences by a force imparted on the sensor body and is usually represented in units of “g’s” (the acceleration due to gravity ~ 9.81 m/sec^2). A Triaxial Micro-electromechanical system (MEMS) accelerometer (model 4030 supplied by TE Connectivity) was chosen for the field trials. The accelerometer produces an analog voltage which is proportional to the acceleration experienced by each axis. The model 4030 has a rugged housing and is sealed which provides good protection in the rugged environment that the sensor needs to operate in. The sensor was mounted in a small enclosure which was then attached to the rail tie. Mounting the enclosure to the tie is relatively simple and provided a very effective way to measure the acceleration of the track structure. Figure 3 shows the accelerometer package mounted to a tie at the field trial site.

Figure 3. Accelerometer mounted on tie

2.1.2 Capturing & Logging Data

As noted above, the accelerometer produces an analog signal which must be recorded by a data logger. For field trials, a National Instruments (NI) data acquisition system (DAQ) was used along with an

embedded PC. The acceleration data is sampled at 200 Hz. In order to reduce the amount of accelerometer data that needs to be saved and uploaded, data from a single strain gauge mounted on the rail is continuously monitored. When the strain data exceeds a pre-determined threshold (which indicates rail traffic is occurring) data from the accelerometer is saved to disk. The data capture algorithm looks for relatively large changes in the strain levels and does not suffer from the challenges noted above with interpreting the strain gauge data. A batch upload of the saved accelerometer data to the IoT platform occurs periodically.

2.1.3 Cellular Gateway & IoT Platform

A cellular gateway & IoT Platform provide the ability to send the data from the PC to a remote server. The gateway and DAQ were mounted in an enclosure which also contained a solar panel and battery to power the system. The enclosure was mounted on the wayside of the track as shown in figure 4.

Figure 4- DAQ and Gateway enclosure

2.2 Measurement Techniques

In theory, displacement can be obtained from acceleration by integrating the acceleration data once to obtain velocity and integrating a second time to obtain displacement. In practice, care must be taken to ensure that noise is minimized to reduce errors that accumulate as a result of the integrations. Micro-electromechanical systems (MEMS) technologies are present in many different types of sensors including the accelerometer chosen for the field trials. The technology incorporates a combination of electronics and miniaturized moving parts to provide the desired sensed parameter (acceleration in our case) (Miline et. al 2016).

The accelerometers mounted on the rail ties provide a signal which is proportional to the instantaneous acceleration the tie is experiencing due to train loading. As noted earlier, the deflections (or displacement) of the rail track under loading can be utilized to assess the health of the rail track. After the acceleration data from the DAQ is pushed to the cloud-based server, it must be converted into a usable value. The following steps are performed to convert the acceleration data to a displacement value.

2.2.1 Signal conversion

The accelerometer used for the field trial produces a voltage output which is proportional to acceleration experienced by each axis of the sensor. The voltage signal must be scaled appropriately to convert the voltage into a “g” value. In the case of the Model 4030 accelerometer, +/- 2g is the full range value which corresponds to a voltage reading of 0.5 volts (-2g) to 4.5 volts (+2g) with 2.5 volts representing 0g.

2.2.2 Filtering to remove gravity effect

The second step in the process is to filter the data. The Model 4030 is a DC coupled device meaning it can be used to capture stationary acceleration such as gravity. In this application, the presence of gravity in the signal is not desired and must be filtered out. This is accomplished by applying a high pass filter on the data which effectively removes the gravity component of the acceleration signal.

2.2.3 Calculating displacement

In order to reduce the noise present in the signal, a low pass filter is used before integration of the acceleration signal occurs. After the noise is removed, trapezoidal integration is performed on the acceleration data to obtain velocity. A second integration operation is then performed on the velocity to obtain the displacement.

3 RESULTS AND DISUSSION

The system has been installed on a railway to test the ability to collect acceleration data and convert to displacement data. The test site was located near Birmingham, AL USA on a rail line which is used to transport coal to a power plant. The traffic on the line is consistent with coal cars being the only traffic. The goal is to monitor the track over time and identify changes in the long-term trend of the calculated displacement value which would indicate some change in the response of the track structure and the potential need for some type of maintenance. While the test is still in process, the initial results are promising.

Figure 5 shows the result of the displacement calculation for one wheel passing over the tie (y axis is

mm and x axis is time). Note how the calculated value returns nearly to the starting position as expected. The small residual error is likely due to the noise from the accelerometer which is magnified by the double integration process. Displacement calculations such as this could be performed over an extended time period and trend analysis techniques utilized to determine if excessive movement of the rail track is occurring which could indicate the need for some type of maintenance to be performed.

For this field trial, the accelerometer is mounted to the tie and not the rail. While there would likely be some difference in the data if the accelerometer were mounted on the rail, in practice, it would be difficult to mount the accelerometer to the rail and one of the objectives was to develop a system that was relatively easy to install and minimize track down time. Assuming the rail is attached to the tie in a sufficient manner, the movement of the tie should be a good proxy for the movement of the rail.

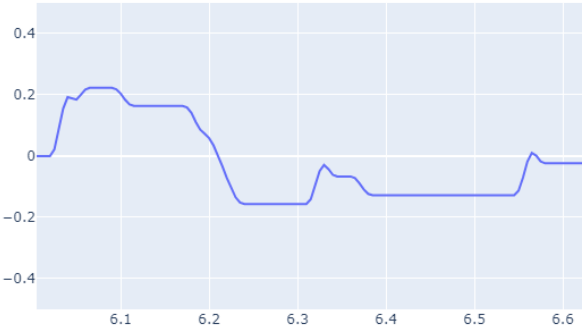

Figure 5. Displacement calculation

4 CONCLUSIONS

This paper describes a rail monitoring system that can be used for continuous monitoring of the rail track structure. The system utilizes relatively low-cost MEMS accelerometers mounted on rail ties as the sensing element. Initial results from the field test are promising and show that displacement calculations, when filtered and analyzed over time, could indicate when maintenance should be performed. The existing field trial was installed at a location where the rail traffic was known and consistent which supports the use of trend analysis to determine changes in the track structure. Variations in the type, loading and speed of the traffic will have an effect on the calculations. Also, note that this study focused on measuring the movement of the tie only and does not take into account other components which could adversely affect track performance. It is anticipated that further research will need to be completed to factor these variations into the analysis.

5 ACKNOWLEDGEMENT

The author wishes to acknowledge the support of Tensar for providing equipment, Row 58 LLC for providing graphics development and Southern Company Electric Rail for providing a field test site.

REFERENCES

American Public Transportation Association (APTA). 2017. “Rail Transit Track Inspection and Maintenance.” APTA RT-FS-S-002-02, Rev. 1

Fontual, et al., (2016). “Railways Track Characterization Using Ground Penetrating Radar.” *Procedia Engineering*, Volume 143,

Milne, et al., (2016) “Proving MEMS Technologies for Smarter Railway Infrastructure.” *Procedia Engineering*, Volume 143

Powrie, W. & Le Pen, L. (2016). “A Guide to Track Stiffness”. Produced by the Cross Industry Track Stiffness Working Group

Canadian & Cold Regions
Rail Research Conference
2024

Advanced technology in railway track monitoring using the GPR Technique: A Review

Farhad Kooban[1], Aleksandra Radlińska[1], Reza Mousapour[2], & Maryam Saraei[3]
[1]*Department of Civil and Environmental Engineering, Penn State University, Pennsylvania, USA*
[2]*Department of Civil and Environmental Engineering, University of Alberta, Edmonton, Alberta, Canada*
[3]*Department of Railway Engineering, Iran University of Science and Technology, Tehran, Iran*

ABSTRACT

Subsurface evaluation of railway tracks is crucial for safe operation, as it allows for the early detection and remediation of potential structural weaknesses or defects that could lead to accidents or derailments. Ground Penetrating Radar (GPR) is an electromagnetic survey technique as advanced non-destructive technology (NDT) that can be used to monitor railway tracks. This technology is well-suited for railway applications due to the sub-layered composition of the track, which includes ties, ballast, sub-ballast, and subgrade regions. It can detect defects such as ballast pockets, fouled ballast, poor drainage, and subgrade settlement. The paper reviews recent works on advanced technology and interpretations of GPR data collected for different layers. Further, this paper demonstrates the current techniques for using synthetic modeling to calibrate real-world GPR data, enhancing accuracy in identifying subsurface features like ballast conditions and structural anomalies and applying various algorithms to refine GPR data analysis. These include Support Vector Machine (SVM) for classifying railway ballast types, Fuzzy C-means, and Generalized Regression Neural Networks for high-accuracy defect classification. Deep learning techniques, particularly Convolutional Neural Networks (CNNs) and Recurrent Neural Networks (RNNs) are also highlighted for their effectiveness in recognizing patterns associated with defects in GPR images. The article specifically focuses on the development of a Convolutional Recurrent Neural Network (CRNN) model, which combines CNN and RNN architectures for efficient processing of GPR data. This model demonstrates enhanced detection capabilities and faster processing compared to traditional object detection models like Faster R-CNN.

1 INTRODUCTION

Rail transportation is a compelling alternative to road transport, offering superior efficiency in key areas like energy consumption, CO2 emissions, system capacity, and safety (Alexander 2012). However, railway tracks are susceptible to internal defects that can worsen over time, leading to significant deterioration. This deterioration includes issues ballast fouling voids beneath sleepers, washouts, subgrade diseases (Liu et al. 2023), moisture levels in ballast and ballast beds, water cavities due to drainage problems, and locations with insufficient bearing capacity (e.g., ballast pockets). These issues can compromise track safety and performance. To address these concerns, conducting regular and thorough inspections to monitor the internal condition of tracks is crucial. Given that these problems often form within the underground structure, which is invisible to the naked eye, current inspection methods rely on observing surface manifestations, such as rail corrugation (Esmaeili 2014), white spots which is like limestone powder on tracks (Sysyn, et al. 2020 & Mostofinejad et al. 2021) or mud pumping (Figure 1). In contrast, non-destructive testing methods offer viable alternatives. These methods enable the evaluation of subsurface conditions without causing harm to the structure, making them safer and more practical for routine inspections. A variety of non-destructive testing techniques are available for assessing the subsurface condition of transportation infrastructure, including analyzing vibration trends and detecting abnormal vibrations (Sui et al. 2023).

Figure 1. White spots of ballast breakdown (left) (Sysyn, et al. 2020) and Mud pumping induced by ballast fouling (right) (Nurmikolu et. Al (2013)

However, these techniques sometimes lack the accuracy needed to identify problems beneath the track structure.

Among various non-destructive testing methods, Ground Penetrating Radar (GPR) is particularly effective for railway track inspections (Solla et al. 2021). First used in the 1990s for the detection of railway infrastructure issues, GPR initially employed ground-mounted antennas. Subsequent advancements led to the adoption of high-frequency horn antennas, which facilitate non-contact testing and enable faster data acquisition (Liu et al. 2023). GPR is an electromagnetic method that images the subsurface using radar pulses. It operates by sending a high-frequency electromagnetic signal into the ground via a transmitting antenna. When this signal encounters different materials or interfaces within the subsurface, such as between ballast, sub-ballast, and the subgrade (Feld 2017; Casas et al. 2009), part of the signal is reflected back to the surface and captured by a receiving antenna (Figure *2*). The time taken for the signal to return, and the strength of the reflected signal provide information about the depth and nature of the subsurface features (Al-Qadi et al. 2008).

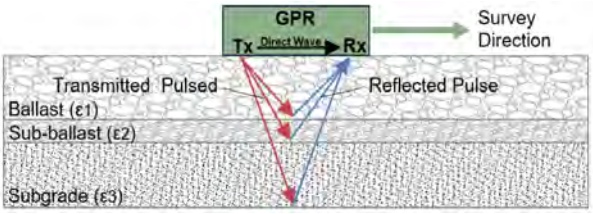

Figure 2. Schematic diagram of a GPR survey shows how reflected waves, as they move beneath the surface, travel at different velocities depending on the dielectric permittivity (ε) of the materials they come across

GPR's effectiveness in railway track inspection stems from its ability to detect variations in material composition, moisture content, and structural anomalies. This makes it invaluable for identifying common railway track defects such as ballast fouling, voids beneath sleepers, washouts, subgrade diseases (Liu et al. 2023), moisture levels in ballast and ballast beds, water cavities due to drainage problems, and locations with insufficient bearing capacity (e.g., ballast pockets). However, challenges arise in interpreting GPR data in high-conductivity materials (e.g., clay soils) and heterogeneous conditions (e.g., rocky beds).

The presence of wet beds or elevated moisture levels in railway track beds, especially in cold regions, can significantly impact railway infrastructure and safety. Excessive moisture in the subgrade can cause various issues, including subsidence and mud pumping (Cheng et al. 2022). Moreover, moisture within the track bed can reduce the subgrade's bearing capacity. When the ground becomes saturated, its strength and stiffness are compromised, potentially leading to track settling or shifting. This issue is particularly acute in areas with clayey soils, which are more prone to moisture content fluctuations.

Early detection through GPR provides crucial data for the maintenance and repair of the subgrade, offering valuable insights into its condition and informing necessary interventions (Cheng et al. 2022). The vehicle mounted GPR device enables rapid and efficient non-destructive inspections of the subgrade's data without interrupting train operations, as shown in Figure *3*.

Figure 3. Data collection setup of two 500 MHz antennas and one 800 MHz antenna for GPR test on railway track beds

2 A REVIEW OF GPR PRINCIPLES

Ground penetrating radar (GPR) is an imaging technique that operates by measuring reflected electromagnetic (EM) waves (Annan 2009; Travassos et al. 2017). It utilizes radar pulses in the ultra or very high frequencies (UHF/VHF) of the microwave portion of the radio spectrum.

The GPR system includes a transmitting di-pole antenna that emits EM pulses into the ground and a receiving di-pole antenna that records changes in the reflected signal over time. These reflections primarily occur at interfaces between materials with differing dielectric properties. The thickness of a surveyed layer is determined by using the time difference measured between the reflected pulses at its boundaries. This measurement is combined with the layer's known dielectric properties, as outlined in Equation 1 (Kahil et al. 2023):

$$d_i = \frac{c \times t_i}{2\sqrt{\varepsilon_{r,i}}} \quad [1]$$

where d_i the thickness of a surveyed layer, t_i the two-way reflection time, c the speed of light and $\varepsilon_{r,i}$ the relative dielectric constant of the medium.

It is crucial to understand that even minor variations in dielectric impedance, such as small-scale heterogeneities, can result in faint or barely noticeable responses in GPR readings. These variations

significantly impact the signal's energy as it propagates, primarily due to scattering phenomena. Notably, the extent of these scattering losses is closely tied to the frequency of the radar pulses; the losses increase with higher pulse frequencies (O'Neill, K., 1999; De Bold 2015). These interface reflections produce responses that are instrumental in deducing underground structural profiles.

This principle is exemplified in Figure *4*, which juxtaposes a railway profile (depicted on the left) against a typical radar line scan response profile (shown in the middle). When multiple scans are combined, they create an integrated underground radar profile (displayed on the right). The layered analysis capability of GPR makes it exceptionally suitable for railway applications, offering the advantage of high-speed data collection.

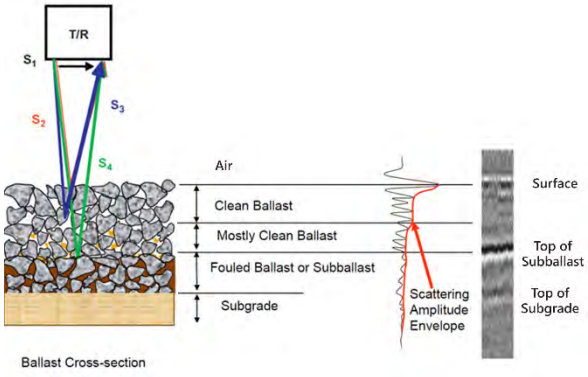

Figure 4. Cross section and A-scan from of a single GPR profile of track layers (adopted from De Bold et al. 2015 & Sui et al. 2023)

GPR technology has demonstrated the capability to estimate the thickness of the ballast and subballast layers with a precision of approximately 3 centimeters (Hugenschmidt 2000). Moreover, it offers some proficiency in determining the extent of subsoil penetration into the ballast layer.

A key property that GPR relies on is dielectric permittivity, which primarily governs the speed of electromagnetic wave propagation through a material, as illustrated in Figure 5. This property is influenced by several factors, including material density, water content, and the type of material. Variations in dielectric permittivity within subsurface materials, as depicted in Figure 5, are critical for GPR's ability to detect subsurface interfaces and anomalies.

Understanding material characteristics is fundamental for professionals working with Ground Penetrating Radar (GPR). Variations in dielectric permittivity significantly impact the accuracy and interpretation of GPR data, playing a crucial role in the success and efficacy of subsurface investigations (Narayanan et al. 2004). It has been observed that fouled ballast possesses a higher dielectric constant compared to clean ballast. This increase is attributed to the presence of contaminants such as moisture, fine particles, and organic matter, which augment its capacity to store electrical energy. These impurities reduce the air voids within the ballast and enhance water retention, thereby contributing to a higher overall dielectric constant detectable by GPR (Anbazhagan et al. 2016).

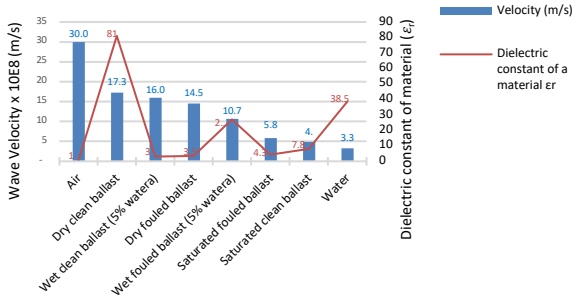

Figure 5. Electromagnetic properties of common materials in ballast layer (De Bold et al. 2015)

Interpreting GPR data involves various formats, each providing unique insights into subsurface features, as illustrated in Figure 6. An A-scan in GPR is a fundamental data form that displays signal strength over time at a single point, useful for identifying individual reflectors and their depths. A B-scan, created by stacking A-scans along a line, provides a 2D cross-sectional view of the subsurface, revealing layers, interfaces, and buried objects. A C-scan, which combines parallel B-scans across an area, offers a 3D plan view of subsurface features, aiding in mapping their extent and distribution. A T-scan, extracting data at a specific depth from B-scans, yields a focused 2D horizontal slice of the subsurface. The selection of a GPR interpretation format is dependent on the specific application and the information required (Kingsuwannaphong et al. 2021).

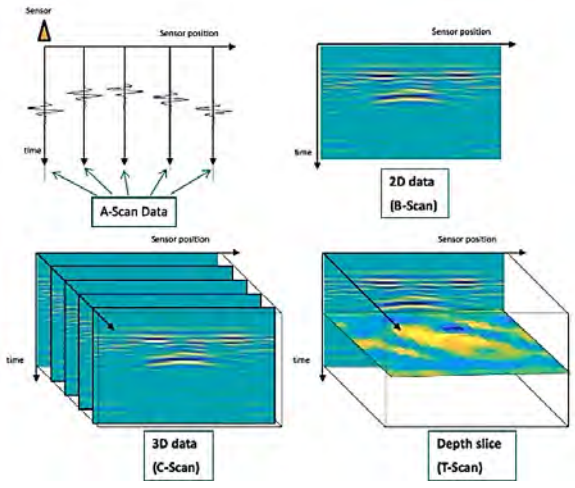

Figure 6. Different forms of GPR interpretation (Kingsuwannaphong et al. 2021)

A series of typical GPR B-scan images depicting various defect types is presented in Figure 7. These images are

instrumental in identifying and analyzing subgrade defects, with each type exhibiting distinct features in GPR profiles. Analysis of these images facilitates the recognition and characterization of different defect types, essential for the assessment and maintenance of railway subgrades (Liu et al. 2023).

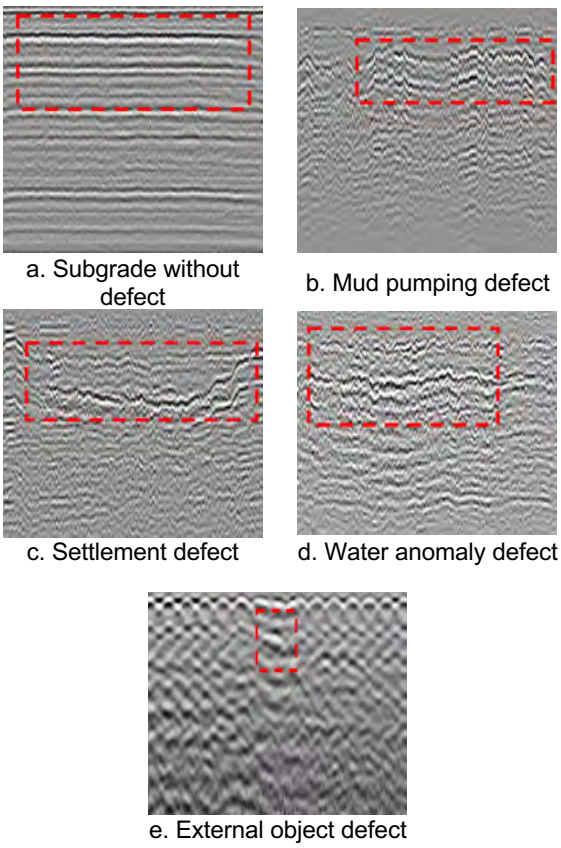

a. Subgrade without defect

b. Mud pumping defect

c. Settlement defect

d. Water anomaly defect

e. External object defect

Figure 7. B-scan images of different types of defects in railway subgrades (*Liu, et al. 2023)*

In Figure 7.a, a clear lamellar structure is evident, characterized by a continuous and straight in-phase axis, resulting in uniform reflected energy. In contrast, Figure 7.b shows a disordered, discontinuous, and low-frequency strong reflection pattern, resembling the shape of a mountain peak or a straw hat. Figure 7.c displays a reflection in the settlement radar image, characterized by a notable bending of the in-phase axis and a downward offset in depth. Figure 7.d illustrates signal attenuation, with strong reflected energy at the top surface and the presence of multiple exit waves (Liu et al. 2023). Lastly, Figure 7.e also demonstrates signal attenuation, with strong reflected energy indicating the location of a metallic object, such as a steel pipe.

This paper explores the integration of simulation techniques in ballasted railway tracks and the application of machine learning (ML) models for the precise inspection of various defects, such as cavities, in the process of advanced railway track monitoring using Ground Penetrating Radar (GPR). Key aspects of this technique include identifying the position, depth, and size of defects. Developing a highly accurate machine learning model necessitates a considerable volume of training data, which should encompass a wide range of technical conditions. Acquiring such a dataset from real-world test measurements represents a significant challenge.

The research conducted by Kingsuwannaphong et al. (2021) is pivotal in this context, as it investigates the use of high-accuracy simulation models to generate the required dataset. These simulation models present a substantial advantage by markedly reducing the time required for both the setup and execution of measurements. This efficiency can considerably shorten the data collection timeline, potentially reducing it from years to mere weeks.

3 METHODOLOGY

3.1 Simulation of a Ballasted Railway Track and GPR Test

The use of simulation models is instrumental in calibrating real-world Ground Penetrating Radar (GPR) equipment and validating survey techniques. By comparing actual GPR survey data with simulated models, engineers can more accurately predict the subsurface conditions of railway tracks, thus facilitating more effective maintenance planning (Öztürk et al. 2010). Synthetic modeling of a railway track using GPR involves creating computer-based models that simulate GPR responses under various trackbed conditions. This process is vital for interpreting real-world GPR data with higher accuracy and for identifying and characterizing subsurface features such as ballast condition, moisture content, and the presence of structural anomalies.

Synthetic modeling leads to a better understanding of GPR responses, proving particularly effective in assessing ballast conditions, which exhibit distinct responses based on the extent of fouling, largely due to variations in void size (Barrett et al., 2019). While much of the literature assumes uniform ballast breakdown throughout the ballast layer, it is recognized that ballast contamination often exhibits significant stratification. For instance, in cases where there is a transition between clean ballast and highly fouled ballast, particularly when fouling is stratified, a distinct reflection indicating a boundary layer can be observed in a radargram. This reflection is primarily due to a shift in the effective dielectric constant. However, when this contrast is minimal or the transition from clean to fouled ballast is gradual, the boundary may be less discernible, appearing in the radargram as a change in the degree of scattering (Couchman et al. 2023).

Research involving the creation of synthetic radargrams aims to qualitatively mimic the complex radargrams typically acquired during real surveys. These synthetic radargrams help explore how various trackbed conditions influence GPR responses. To generate these, an open-source electromagnetic simulation software, gprMax, was employed by researchers such as Warren et al. (2016), Couchman et

al. (2023), Chomdee et al. (2021), Liu et al. (2020), and Scanlan et al. (2018).

In these studies, gprMax was used to produce radargrams based on trackbed models with predetermined electrical properties. For more complex materials like ballast, external generation was used, with geometries and electrical characteristics imported into gprMax. The ballast layers were generated to reflect realistic particle size distributions (PSDs) and void space ratios, varying according to the PSD used.

Earlier attempts to create ballast models for both mechanical and electromagnetic simulations have employed various approaches. Some electromagnetic models used simplistic 2D particle shapes, such as irregular polygons, without a specific PSD. Others, like Benedetto et al. (2020), incorporated PSD but simplified particle shapes to circles. Striving for more realistic particle shapes, Kingsuwannaphong et al. (2021) used Blender, an open-source graphics software, with a rock generator plugin to create 3D ballast particles that closely resemble real gravel. This approach also incorporated a fouled ballast model by using an effective medium approach within the void spaces (Figure 8). The particle sizes used in their study closely matched industry-standard clean ballast (31.5–63 mm) as defined by Boler et al. (2014) and maintained aspect ratios in accordance with AREMA No. 24 and EN13450 standards. Moreover, Kingsuwannaphong et al. (2021) conducted real GPR measurements with the same ballast size and layer thicknesses for model verification.

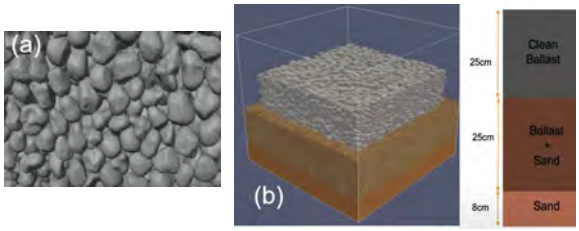

Figure 8. (a). Gravel model and (b). Simulated model of fouled ballast (FDB) (Kingsuwannaphong et al. 2021)

After simulating the GPR test in gprMAX, a comparison of the GPR results of the simulated gravel model with actual measurements shows a high degree of similarity, as expected.

3.2 Application of Machine Learning (ML) Techniques

Machine learning techniques significantly enhance the efficiency and reliability of GPR testing in railway track inspection by automating and improving data analysis. ML algorithms refine GPR data processing, enhancing clarity and reducing noise, thus facilitating better interpretation of subsurface conditions (Kahil et al. 2023). The evolution of GPR-based subgrade defect identification has transitioned from relying on manually designed features to employing ML for classification. For instance, a Support Vector Machine (SVM) approach has been utilized to classify railway ballast types by analyzing amplitude spectral characteristics at frequency inflection points. Another study extracted two-dimensional signal features, such as energy, variance, and histogram statistical features, to develop an SVM-based model for recognizing subgrade defects.

A method involving the division of radargrams into blocks for feature extraction, followed by the use of Fuzzy C-means and Generalized Regression Neural Network algorithms, resulted in high classification accuracies for different defect types (Liu et al. 2023).

Deep learning (DL), a significant advancement in ML (Shomal Zadeh et al. 2023), has been particularly effective in analyzing GPR data for infrastructure health monitoring. Convolutional Neural Networks (CNNs), a DL technique, can be trained to recognize patterns associated with defects in GPR images, thereby swiftly identifying potential issues in railway infrastructure. CNNs are proficient in learning data structure information and dependencies, which enhances target recognition and classification. Besaw et al. (2015) demonstrated high-precision subsurface anomaly identification using CNNs to classify hazardous explosives from GPR data.

Other studies have employed advanced neural network models like YOLO (You Only Look Once) and Cascade R-CNN for detecting mud-pumping defects and subsidence with considerable accuracy (Liu et al. 2023).

YOLO models use a single CNN to simultaneously predict multiple bounding boxes and class probabilities for those boxes. It is known for its speed and accuracy, making it suitable for applications that require real-time pattern recognition images (Li et al et al. 2020). Cascade R-CNN is also an advanced pattern detection framework that improves upon the traditional R-CNN by using a multi-stage approach. While CNNs excel in feature extraction, they have limitations in processing time-series GPR data. This gap is filled by Recurrent Neural Networks (RNNs), capable of learning time-series correlations and dependencies in the data (Tong et al. 2020).

Combining CNN and RNN structures for feature extraction has proven effective, as demonstrated in human re-identification research. The Convolutional Gated Recurrent Neural Network (CGRNN), which combines CNNs for feature extraction with bidirectional gated recurrent units (BGRUs) to learn long-term patterns, has shown enhanced recognition accuracy (Xu et al. 2017).

Liu et al. (2023) combined CNN and RNN for GPR detection of subgrade diseases and anomalies. Their study focused on applying deep neural networks (DNN) for the detection of subgrade defects using raw GPR data. They introduced an innovative DNN model that utilized a multi-layered one-dimensional CNN to autonomously extract feature functions from signal channel waveforms, resulting in a model with fewer parameters and faster processing times compared to previous DNN models using two-dimensional CNNs. Additionally, they incorporated a multi-layer RNN to handle multiple channel features from the CNN, aligning the model more closely with B-scan data. The design of their CNN-RNN (CRNN) model was outlined, and its performance was showcased using manually labeled B-

scan data. Their findings indicated that the CRNN achieved comparable accuracy to Faster R-CNN, albeit at a higher speed and with a smaller model size. Faster R-CNN is an advanced object detection neural network that enhances detection speed and accuracy by utilizing a Region Proposal Network (RPN) to identify object locations. This network takes advantage of the strengths of both CNN and RNN, capturing complex patterns and dependencies in the GPR data, making it a powerful tool for detecting railway subgrade conditions and evaluating the presence of defects.

4 RESULTS AND DISCUSSION

The work of Kingsuwannaphong et al. (2021) highlighted the difficulty of visually detecting fouling in ballast due to the lack of clear distinctions between Fouled Ballast Data (FDB) and Clean Ballast Data (CDB). This finding underscores the importance of effective detection techniques and precise simulation models in this domain. In their study, a rough estimate of the subgrade interface (sand) location is marked by a red dashed line at approximately 9ns, while the boundary between clean and fouled ballast is denoted by a yellow dashed line around 6ns. Despite efforts to accurately replicate the simulation model, the position of this boundary in the measurements appears slightly shallower (Figure 9). This discrepancy could be due to minor differences in the overall permittivity of the stones compared to those used in the simulation.

These findings indicate that the complex scattering effects caused by ballast present challenges in establishing its visual boundaries, thereby emphasizing the need for the application of advanced machine learning (ML) methods.

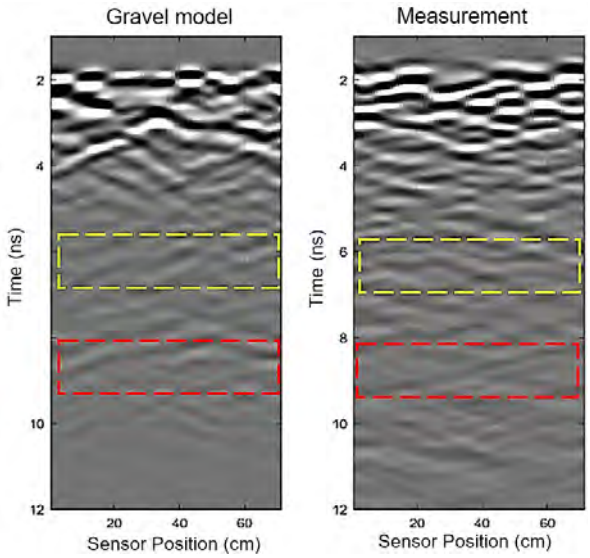

Figure 9. B-Scan comparison between simulated (left) and measured (right) models (Kingsuwannaphong et al. 2021)

Liu et al. (2023) demonstrated through experimental results and a literature survey that four network models – CNN, RNN, CRNN, and Faster R-CNN – each have their respective advantages and disadvantages. The CNN is proficient in extracting deep features from GPR waveforms and reduces storage needs but lacks the capability to process time-series data effectively. The RNN, with its chained architecture, considers both current input and the output of its predecessor network but struggles with gradient issues and nonlinear activation functions. The CRNN model offers the advantages of lightweight, fast inference, and simplicity in handling GPR data, yet it faces limitations in terms of sample size, data imbalance, and lower accuracy. On the other hand, Faster R-CNN delivers high recognition accuracy and has readily available source code, but its model training process is relatively slow. Each model has its specific niche, with its suitability depending on particular requirements and constraints in different scenarios.

5 CONCLUSIONS

The innovative application of Ground Penetrating Radar (GPR) in railway track inspection, particularly through the use of simulated models and machine learning (ML), marks a significant advancement in railway infrastructure maintenance and safety. The process of simulating a ballasted railway track and conducting GPR tests, as outlined in this research, underscores the potential of synthetic modeling in accurately predicting the subsurface conditions of tracks, which is crucial for effective maintenance planning. The employment of synthetic modeling, as demonstrated in this study, is instrumental in creating computer-based models that simulate GPR responses under various trackbed conditions, thereby aiding in the precise identification and characterization of subsurface features such as ballast condition, moisture content, and structural anomalies. A notable aspect of this approach is the use of gprMax, an open-source electromagnetic simulation software. gprMax has been pivotal in generating synthetic radargrams that closely mimic real-world scenarios. These radargrams, created with predefined electrical properties and realistic particle size distributions, provide a robust platform for understanding how various trackbed conditions influence GPR responses. The ability of gprMax to produce detailed and accurate simulations has proven invaluable, particularly in providing data for training ML models. This capability is crucial because a significant volume of high-quality data is essential for developing accurate and efficient ML models for railway track inspection. The comparative analysis of GPR results from the gprMax-simulated gravel model with actual measurements further validates the effectiveness of this approach. The close similarity between the simulated and real-world data not only confirms the reliability of the simulation models but also highlights the potential of gprMax in offering a practical and efficient solution for data generation in ML applications.

The Convolutional Recurrent Neural Network (CRNN) represents a groundbreaking model in Ground Penetrating Radar (GPR) anomaly detection, integrating

the strengths of Convolutional Neural Network (CNN) and Recurrent Neural Network (RNN) architectures. This model is distinctively designed to process both longitudinal and transverse aspects of GPR data efficiently, obviating the need for transforming data into images. Such a design results in a model that is not only compact but also highly efficient, exhibiting faster processing capabilities than object detection models like Faster R-CNN.

Although the CRNN generally performs on par with its counterparts, it tends to identify more minor anomalies at the boundaries of larger anomalies and occasionally faces challenges in accurately determining starting positions of anomalies. In practical applications, this lightweight model is advantageous as it conserves computational resources by directly processing raw GPR data. This direct approach eliminates the need for image conversion or extensive post-processing for anomaly localization, offering potential for even faster processing with adequate training.

However, the model's primary limitation lies in its focus on anomaly detection; it requires additional data to enhance its classification accuracy, particularly when dealing with complex, real-world data scenarios. Therefore, while the CRNN model marks a significant advancement in GPR data analysis, further refinement and training with diverse datasets are necessary to fully realize its potential in practical applications.

REFERENCES

Al-Qadi, I. L., Xie, W, Roberts, R., (2008). Time-Frequency Approach for Ground Penetrating Radar Data Analysis to Assess Railroad Ballast Condition. Research in Non-destructive Evaluation, 19(4):219-237. DOI: 10.1080/09349840802015107.

Alexander, P.E. (2012). Rail Transportation Energy Efficiency-Oriented Technologies. 787-791. DOI: 10.1115/JRC2012-74130.

Anbazhagan, P., Dixit, P. S. N., & Bharatha, T. P. (2016). Identification of type and degree of railway ballast fouling using ground coupled GPR antennas. Journal of Applied Geophysics, 126, 183–190. DOI: 10.1016/j.jappgeo.2016.01.018.

Annan, A. P. (2009). Electromagnetic principles of ground penetrating radar. Ground penetrating radar: theory and applications, 1, 1-37.

Barrett, B., Day, H., Gascoyne, J. & Eriksen, A. (2019) Understanding the capabilities of GPR for the measurement of ballast fouling conditions. Journal of Applied Geophysics, 169, 183–198.

Besaw, L. E., & Stimac, P. J. (2015). Deep convolutional neural networks for classifying GPR B-scans. In S. S. Bishop & J. C. Isaacs (Eds.), SPIE Proceedings. SPIE. https://doi.org/10.1117/12.2176250.

Boler, H., Qian, Y., & Tutumluer, E. (2014). Influence of Size and Shape Properties of Railroad Ballast on Aggregate Packing: Statistical Analysis. Transportation Research Record, 2448(1), 94-104. https://doi.org/10.3141/2448-12.

Casas, A., Pinto, V., Rivero, L., (2009). Fundamental of ground penetrating radar in environmental and engineering applications. Annals of Geophysics, 43(6):1091-1103. DOI: 10.4401/AG-3689.

Cheng, Y., Li, T., Du, C., Liu, J., Zhang, X., & Zhang, W. (2022). Study on grading evaluation of moisture content in subgrade bed of high-speed railway based on ground penetrating radar technology. Second International Conference on Testing Technology and Automation Engineering (TTAE 2022). https://doi.org/10.1117/12.2660578.

Chomdee, P., Boonpoonga, A., & Lertwiriyaprapa, T. (2021). Study on the detection of object buried under railway by using clutter removal technique. 2021 Research, Invention, and Innovation Congress: Innovation Electricals and Electronics (RI2C), Bangkok, Thailand, DOI: 10.1109/RI2C51727.2021.9559774.

Couchman, M.J., Barrett, B., & Eriksen, A. (2023). Synthetic modelling of railway trackbed for improved understanding of ground penetrating radar responses due to varying conditions. Near Surface Geophysics. DOI:10.1002/nsg.12272.

De Bold, R., O'Connor, G., Morrissey, J.P., Forde, M.C. (2015). Benchmarking large scale GPR experiments on railway ballast, Journal of Construction and Building Materials, Volume 92, Pages 31-42, ISSN 0950-0618, https://doi.org/10.1016/j.conbuildmat.2014.09.036.

Esmaeili, M., Mosayebi, S. A., & Kooban, F. (2014). Effect of Rail Corrugation on the Amount of Train Induced Vibrations Near a Historical Building. Journal of Advances in Railway Engineering, (Vol. 2, No. 2, pp. 73-84).

Feld, R., (2017). Advantages of Electromagnetic Interferometry Applied to Ground-Penetrating Radar: Non-Destructive Inspection and Characterization of the Subsurface Without Transmitting Anything. DOI: 10.4233/UUID:384BF6BE-42DF-4FBA-BBA0-0648C7A52E24.

Hugenschmidt, J. (2000). Railway track inspection using GPR. Journal of Applied Geophysics, 43(2-4), 147-155.

Kahil, N. S., Tempe, V., Yeferni, A., Calon, N., Benkhelfallah, Z., Annag, I., & Mbongo, G. (2023). Automatic analysis of railway ground penetrating radar: Using signal processing and machine learning approaches to assess railroad track substructure. Transportation Research Procedia, 72, 3008–3015. https://doi.org/10.1016/j.trpro.2023.11.848.

Kingsuwannaphong, T., Bräu, C., Rümmler, S., Rial, F., & Heberling, D. (2021). Realistic railway ballast FDTD simulations for ground penetrating radar railway track inspection. 11th International Workshop on Advanced Ground Penetrating Radar (IWAGPR).

Liu, H., Wang, Sh. J., Jing, G., Yu, Z., Guo, Y., (2023). Combined CNN and RNN Neural Networks for GPR Detection of Railway Subgrade Diseases. Sensors, 23(12):5383-5383. DOI: 10.3390/s23125383.

Liu, S., Lu, Q., Li, H., & Wang, Y. (2020). Estimation of moisture content in railway subgrade by ground penetrating radar. Remote Sensing, 12(18), 2912. https://doi.org/10.3390/rs12182912.

Li, Y., Zhen, Z., Luo, Y., & Zhi, Q. (2020). Real-Time Pattern-Recognition of GPR Images with YOLO v3 Implemented by Tensorflow. Sensors, 20(22), 6476. https://doi.org/10.3390/s20226476

Mostofinejad, D., Khademolmomenin, M., & Tayebani, B. (2021). Evaluating durability parameters of concrete containing limestone powder and slag under bacterial remediation. Journal of Building Engineering, 40, 102312. https://doi.org/10.1016/j.jobe.2021.102312

Narayanan, R. M., Jakub, J. W., Li, D., & Elias, S. E. G. (2004). Railroad track modulus estimation using ground penetrating radar measurements. NDT & E International, 37(2), 141–151. DOI:10.1016/j.ndteint.2003.05.003.

Nurmikolu, A., & Guthrie, W. S. (2013). Factors affecting the performance of railway track substructures in seasonally cold climates. ISCORD 2013. https://doi.org/10.1061/9780784412978.063.

O'Neill, K., (1999). Radar sensing of thin surface layers and near-surface buried objects. IEEE Transactions on Geoscience and Remote Sensing, 38(1):480-495. DOI: 10.1109/36.823943.

Öztürk, C., Drahor, M. G., (2010). Synthetic GPR modelling studies on shallow geological properties and its comparison with the real data. 1-4. DOI: 10.1109/ICGPR.2010.5550215.

Scanlan, K. M., Hendry, M. T., Martin, C. D., & Schmitt, D. R. (2018). Evaluating the sensitivity of low-frequency ground-penetrating radar attributes to estimate ballast fines in the presence of variable track foundations through simulation. Proceedings of the Institution of Mechanical Engineers, Part F: Journal of Rail and Rapid Transit, 232(4), 1168–1181. https://doi.org/10.1177/0954409717710408.

Shomal Zadeh, S., Aalipour Birgani, S., Khorshidi, M., & Kooban, F. (2023). Concrete Surface Crack Detection with Convolutional-based Deep Learning Models. International Journal of Novel Research in Civil Structural and Earth Sciences, 10, 25–35. https://doi.org/10.5281/zenodo.10061654.

Solla, M., Vega, P.G., Fontul, S., (2021). A review of GPR application on transport infrastructures: Troubleshooting and best practices. Remote Sensing, 13(4):672-. DOI: 10.3390/RS13040672.

Sui, X., Leng, Z., Wang, S. (2023) Machine learning-based detection of transportation infrastructure internal defects using ground-penetrating radar: a state-of-the-art review, Journal of Intelligent Transportation Infrastructure, Volume 2, liad004, https://doi.org/10.1093/iti/liad004.

Sysyn, M., Nabochenko, O., & Kovalchuk, V. (2020). Experimental investigation of the dynamic behavior of railway track with Sleeper Voids. Railway Engineering Science, 28(3), 290–304. https://doi.org/10.1007/s40534-020-00217-8.

Tong, Z., Gao, J., & Yuan, D. (2020). Advances of deep learning applications in ground-penetrating radar: A survey. Construction and Building Materials, 258(120371), 120371. https://doi.org/10.1016/j.conbuildmat.2020.120371.

The American Railway Engineering and Maintenance-of-way Association: AREMA No. 24 Standards.
The European standards: EN13450-2013, Aggregates for railway ballast Grading D to F.

Travassos, X. L., Pantoja, M. F., (2017). Ground Penetrating Radar. 987-1023. DOI: 10.1007/978-3-319-30050-4_9-1.

Warren, C., Giannopoulos, A., & Giannakis, I. (2016). gprMax: Open-source software to simulate electromagnetic wave propagation for Ground Penetrating Radar, Computer Physics Communications, 209, 163-170, 10.1016/j.cpc.2016.08.020.

Xu, Y., Kong, Q., Huang, Q., Wang, W., Plumbley, M.D. (2017). Convolutional gated recurrent neural network incorporating spatial features for audio tagging. In Proceedings of the 2017 International Joint Conference on Neural Networks (IJCNN), Anchorage, AK, USA, 14–19 May 2017; pp. 3461–3466.

Canadian & Cold Regions
Rail Research Conference
2024

Automating track inspection through using an instrumented hi-rail truck

Alireza Roghani, Taufiq Rahman, Samy Metari, Abdelhamid Mammeri, & Sylvie Chenier
National Research Council of Canada, Ottawa, ON, Canada

ABSTRACT

Utilizing inspection technologies has demonstrated efficacy in monitoring railway tracks and enhancing the overall safety of railway operations. The introduction of automated track geometry measurement systems and their consequential impact on reducing geometry-related derailments underscores the significance of technological adaptation in the railway sector. Maintaining safe track conditions under future climate projections requires more frequent inspections, and consequently track down time. However, the growing demand for rail transportation and supply chain constraints require railway operators to increase the number of trains along their network, consequently limiting the time available for comprehensive track inspection. In response to this multifaceted challenge, railways are actively exploring emerging technologies and embracing automation to facilitate more frequent inspections, thereby enhancing operational efficiencies while upholding safety standards. Addressing this imperative, the National Research Council of Canada (NRC) has undertaken the development of a prototype instrumented hi-rail truck designed to automate select track inspection activities currently reliant on human visual inspections. Equipped with an array of sensors featuring diverse sensing modalities and a range of perspectives, this instrumented truck generates digital representations of the track and its surrounding environment. The resulting digital models, in conjunction with artificial intelligence algorithms, enable the spatial and temporal identification of certain track issues. This short paper provides an overview of the NRC's instrumented hi-rail truck, including both the software and hardware components, the opportunities it presents to supplement/replace specific aspects of visual inspections, and some results from its deployment under actual field conditions.

1 INTRODUCTION

Railway companies strive to employ diverse measurement technologies for track inspection to ensure a safe operating condition for trains. Despite the widespread adoption of advanced technologies, visual inspection of the track remains a regulatory imperative. The frequency of these visual inspections varies, ranging from one per month to two per week, depending on factors such as track classification and annual tonnage, as outlined in existing regulations (Transport Canada, 2021a).

The visual inspection process faces several challenges, making it labor-intensive, tedious, and prone to errors influenced by human factors. This is primarily attributed to the subjective nature of human evaluation and manual record-keeping, compromising the consistency of the identification of potential problems. Additionally, the existing process lacks the capability to quantify and monitor the progression of issues, hindering proactive identification. The prolonged track downtime demanded by the present inspection procedures adversely impacts train schedules, leading to decreased efficiency in railway operations. Furthermore, the current inspection process may prove inadequate in coping with the anticipated increase in weather-related issues under future climatic conditions. Addressing these limitations is crucial for enhancing the overall effectiveness, safety, and adaptability of the railway inspection procedures.

Recent advancements in perception technologies, both hardware and software elements, have introduced new opportunities for enhancing track inspection procedures. The accessibility of high-resolution sensors with various sensing modalities, along with the affordability of powerful on-board computers for real-time data processing on mobile platforms, has significantly transformed the landscape. This technological progress has opened new avenues for improving the efficiency and accuracy of track inspection processes. The deployment of these advanced sensors, along with robust computing capabilities, holds the potential to revolutionize the way railway tracks are monitored, offering a more cost-effective approach to ensure safety and performance in rail operations.

Since 2019, NRC has been actively working on the development of an instrumented hi-rail truck tailored to augment traditional visual inspections (Roghani et al., 2022a and b, Arroyo Mora et al., 2023). This endeavor involves a comprehensive exploration of optimal hardware solutions and the development of requisite software and algorithms for efficient data processing. This short paper provides a brief overview of the ongoing progress in implementing the instrumented hi-rail truck and its potential contributions to track inspection methodologies. The discussion will touch upon the key

aspects of hardware selection, software development, and algorithmic advancements.

2 INSTRUMENTED HI RAIL TRUCK

NRC's hi-rail truck (Figure *1*) is instrumented with a suite of sensors and auxiliary components to develop a complete data acquisition (DAQ) system that can acquire environmental data in different sensing modalities and multispectral bandwidths.

The DAQ system is comprised of two units that are located on the roof and on the back of the truck. The system on the roof features one LiDAR, two RGB cameras, and two Infrared cameras, capturing images from each side of the track; while the system on the back features one LiDAR and one downward camera which provides a view of the track. The DAQ also includes IMU, GNSS, and CAN-bus. In addition to these sensors, two high-capacity computers are deployed inside the hi-rail truck to host the supporting software and to facilitate the data acquisition task.

Figure 1. NRC's instrumented hi-rail truck

Except for the IMU, all other sensors installed on the hi-rail truck operate on electromagnetic signals from different spectra (radio waves, visible light, and infrared light). The LiDAR, RGB cameras and infrared cameras provide raw data that could be processed to monitor various features on track or within the right-of-way, and the IMU and the GNSS receivers are used to determine local and positioning information for the other sensor streams.

A software stack hosted on the in-vehicle computer and based on the Robot Operating System (ROS) was developed to facilitate data acquisition and real-time visualization. It includes vendor-supplied and custom drivers to translate binary sensor data into ROS messages. It also included nodes that captured these published ROS messages to save to the local storage of the computer in ROSBAG format for each message. The recorded data in the ROSBAG format can be replayed with accurate time deltas to provide a convenient pipeline for rapid prototyping of data processing algorithms. This provides an opportunity for track engineers to view data later as if they are inspecting the track from a hi-rail truck in the field.

The data processing tasks are very resource intensive and involve the following steps: (1) reading binary files from local/cloud storage, (2) de-serializing the binary sensor data into appropriate formats, and (3) evaluating perception algorithms on the formatted data, etc. All these steps require high GPU, CPU and memory resources. The large volume of acquired data poses a challenge for processing using the available computing capacities.

3 RESULTS AND DISUSSION

The NRC has been proactively engaged in advancing the capabilities of the instrumented hi-rail truck, exploring novel applications. The truck has exhibited successful applications in mapping surface water area and elevation within the track right-of-way (ROW). This capability enhances the truck's utility by providing valuable insights into the water dynamics along the railway tracks. Furthermore, the instrumented hi-rail truck has demonstrated effectiveness in mapping vegetation along a railway line. This application contributes to the overall monitoring and maintenance strategy by offering detailed information about the vegetation profile within the track ROW.

3.1 Mapping surface water area

Water levels in close proximity to railway tracks have a significant impact on train safety. With the anticipated rise in both the frequency and severity of extreme weather events due to climate change, there is an urgent need to bolster the resilience of transportation infrastructure, particularly railways. In response to this expectation, the NRC has explored the potential use of its instrumented hi-rail truck for advanced water detection and inspection near railway tracks.

The system underwent testing on two Canadian railroads to evaluate its proficiency in mapping surface water areas and elevation within the ROW. Utilizing images from both infrared and RGB cameras, an algorithm was trained to autonomously identify the presence of water within the ROW. Subsequently, a Structure from Motion (SfM) procedure was employed to ascertain the elevation difference between the water

surface and the track. This approach facilitates the detection of changes in water elevation over time, providing valuable information for track inspectors as an early indicator of potential issues.

Figure 2a and b show how the surface water at the outlet of a culvert appears in infrared and RGB images taken from the hi-rail truck. Using images from RGB cameras, a 3D point cloud of the scene is generated using SfM techniques. Figure 2d shows a different view for the same area, including the track segment, illustrating how the elevation difference can be measured between water surface and a reference point, such as top of rail.

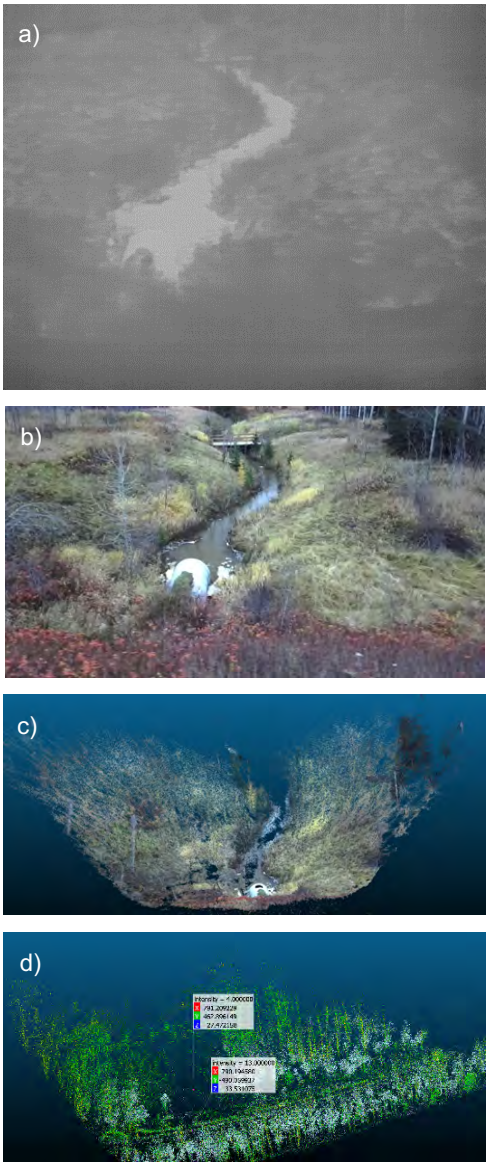

Figure 2. Water presence at the outlet of a culvert located under a rail track in an (a) infrared, (b) RGB images, and (c) 3D map generated by the SfM algorithm, (d) demonstrating calculation of water level from top of rail

3.2 Vegetation management at grade crossings

The safety of rail operations over grade crossings is a critical issue for Canada's railway industry. Accidents at grade crossing represents approximately one third of all fatalities and half of all serious injuries from railway accidents (Transport Canada, 2021b). Effective vegetation management near grade crossings is crucial for ensuring safe and secure train operations, as well as safeguarding the public and personnel. Inadequate vegetation control can lead to compromised sightlines at public crossings, increasing the risk of accidents.

Transport Canada sets the minimum requirement for the clear sightline area around each crossing. These sightlines must, at the minimum, provide crossing users with sufficient time to see and react to an oncoming train, from both the 'approach' and 'stop' positions. Sightlines clear area must be preserved by prohibiting the construction of buildings or structures, or the placement of objects that would obstruct the sightlines

The NRC's instrumented hi-rail truck offers a distinctive advantage with its capability to generate 3D maps of the track environment. These maps provide detailed insights into vegetation presence along the rail line, offering valuable information on sightline obstructions such as the height of potential hazard trees, and their proximity to the track. This automated approach, in comparison with the current visual inspections conducted by track inspectors, provides a more efficient means of quantifying the situation and allows for tracking changes over time.

Integration of measurements from scanning LiDARs and Inertial Measurement Unit (IMU) data is employed to create a 3D map of scanned locations through Simultaneous Localization and Mapping (SLAM) techniques. Utilizing two LiDARs positioned on the roof and back units enhances the precision of the 3D map, enabling its application in various railway inspection tasks.

Figure 3a shows a single LiDAR scan acquired within the track environment, and Figure 3b demonstrates a dense 3D point cloud representation of the track surroundings near a farm crossing. Following the acquisition of these maps, integration with Global Navigation Satellite System (GNSS) data collected by the hi-rail instrumentation facilitates the generation of a geo-referenced 3D map encompassing grades and farm crossings. Railway operators typically possess approximate GNSS coordinates for these crossings, allowing for automated identification within the generated 3D maps by referencing existing databases. Once the crossing locations are identified, the volume that is required to be free of obstructions can be determined in the 3D maps. Within these volumes, it is trivial to localize point cloud clusters above the track surface. Volumetric analysis of these clusters provides a mean to ascertain whether sightline obstructions are present. The geo-references videos from the cameras on the hi-rail truck can be replayed if further inspection is desired. These problem areas can then be scheduled for remedial actions.

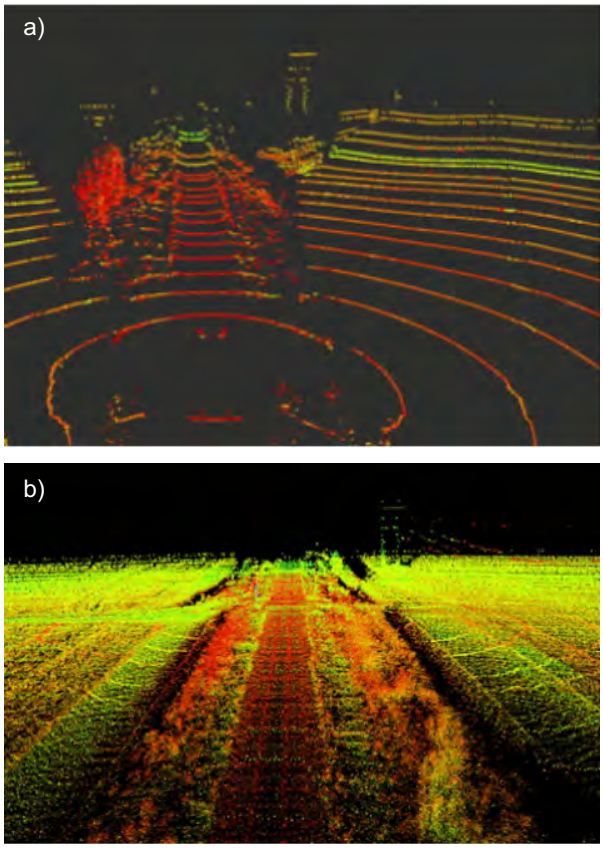

Figure 3. (a) A single LiDAR scan, (b) multiple LiDAR were registered together to create a 3D map of a farm-crossing.

4 CONCLUSIONS

This paper emphasized the crucial role of advanced technologies in enhancing the safety and efficiency of railway operations. The use of advanced sensors on mobile platforms has the potential to revolutionize track inspection processes, addressing challenges posed by climate impacts, increased rail traffic, and supply chain constraints. The preliminary results of hi-rail truck, equipped with sensors and advanced algorithms, suggested promising solution to address these challenges.

The practical applications of the hi-rail truck, demonstrated through successful mapping of surface water areas and vegetation along railway lines, showcase its potential in enhancing current track visual inspections. Going beyond traditional visual inspections, the truck offers an automated and detailed approach to identify issues within ROW. The discussions on water mapping and vegetation management not only showcase the truck's effectiveness but also its adaptability in enhancing safety protocols.

Looking forward, ongoing efforts to develop and optimize the hi-rail truck's hardware and software are underway. The integration of LiDAR, GNSS, and visual data streams provide a comprehensive approach to monitor and manage railway environments. As the industry continues to embrace emerging technologies, the instrumented hi-rail truck can find further applications, contributing to the ongoing evolution of railway track inspection practices.

5 ACKNOWLEDGEMENT

The research presented in this paper has been carried out within the framework of multiple projects generously funded by various organizations. The authors extend their gratitude to the Transport Canada Innovation Center, VIA Rail Canada, Ontario Northland Railway, and the Resilient Ground Transportation Program at NRC for their support. Special acknowledgment is also extended to Daniel Singh Cheema, Thomas Davies, and Ehsan Raei for their valuable contributions to different facets of this work.

REFERENCES

Arroyo-Mora, Juan Pablo, Margaret Kalacska, Alireza Roghani, and Oliver Lucanus. 2023. "Assessment of UAS Photogrammetry and Planet Imagery for Monitoring Water Levels around Railway Tracks" Drones 7, no. 9: 553. https://doi.org/10.3390/drones7090553

Tarek, O (2016). The Federal Railroad Administration's LiDAR-Based Automated Grade Crossing Survey System: Research Results. Federal Railroad Administration, Washingtin D.C. US.

Roghani, A. et, al (2022a). Emerging Technologies for Monitoring and Managing Water Levels around Railway Tracks, Phase II-Stage II, National Research Council Canada, Ottawa, Canada.

Roghani, A. Mammeri, H., Siddiqui, A. (2022b). Proceedings of the Canadian & Cold Regions Rail Research Conference 2021, pp. 106-114, 2021-11-09.

Transport Canada, (2021a). Rules Respecting Track Safety.

Transport Canada, (2021b). https://www.canada.ca/en/transport-canada/news/2021/06/proposed-amendments-to-the-grade-crossings-regulations-will-help-focus-efforts-to-improve-safety-at-grade-crossings.html, Accessed on January 2022.

Session 8

RENEWABLE POWER SOLUTIONS & INNOVATION AND EMERGING TECHNOLOGIES IN RAILWAY

Canadian & Cold Regions
Rail Research Conference
2024

A comparative life cycle sustainability analysis of hydrogen-powered and diesel locomotives

Lizette Correa-Carrillo, Kasun Hewage, Faran Razi & Rehan Sadiq
Life Cycle Management Laboratory (LCML), School of Engineering – University of British Columbia, Kelowna, British Columbia, Canada

ABSTRACT

The transportation sector contributes to nearly one-fourth of the total emissions in Canada. There is a growing interest worldwide in investigating and piloting the use of hydrogen to decarbonize the transportation sector. As a prominent global hydrogen producer, Canada possesses abundant resources to achieve the net zero emissions goal. This study offers a comprehensive assessment of the overall sustainability performance of hydrogen-powered locomotives from a life cycle perspective. It investigates the economic and environmental impacts of integrating hydrogen technology into conventional diesel railway locomotives while considering five different hydrogen production pathways: water electrolysis, steam methane reforming, and coal gasification, with and without carbon capture utilization and storage technology. The comparative life cycle analysis underscores the substantial influence of refurbishing components on the economic viability of hydrogen locomotives. Regarding the environmental impacts, it is crucial to note that incorporating carbon capture utilization and storage technology for hydrogen production significantly contributes to environmental benefits compared to diesel locomotives. Notably, among the five different hydrogen production scenarios analyzed, only the steam methane reforming process with carbon capture utilization and storage pathway emerges as the most sustainable alternative to diesel, resulting in a potential 20% emissions reduction. The insights garnered from this study promise long-term emission reductions and establish a competitive cost-effective alternative to achieve the net zero emissions goal in Canada's railway industry.

1 INTRODUCTION

The United Nations Framework Convention on Climate Change (UNFCCC) seeks to tackle climate change and stabilize atmospheric greenhouse gas (GHG) emissions to prevent harmful interference with the climate system (Environment Canada, 2022). To align with these goals, global efforts are required. In this regard, Canada has pledged to reduce its GHG emissions by 40-45% below 2005 levels by 2030 and achieve net-zero emissions by 2050 (Environment and Climate Change Canada, 2023).

The Canadian transportation sector emerged as the second-largest contributor to the national GHG emissions, comprising 22% of the total reported emissions in 2021 among all economic sectors (Environment and Climate Change Canada, 2023). Moreover, GHG emissions from the transportation sector exhibited a consistent annual increase from 1990 to 2021. Of the overall 27% growth during this period, the primary contributors were heavy-duty trucks and passenger light trucks (Environment and Climate Change Canada, 2023).

In contrast, railway transport is recognized as one of the most energy-efficient modes of transportation (International Energy Agency, 2019). Despite handling substantial traffic, the railway sector contributes to just about 4% of emissions from the transportation sector (Railway Association of Canada, 2023). Consequently, it stands out as an environmentally friendly option among the various transportation modes.

The emissions from railway locomotives primarily result from diesel combustion. Consequently, efforts have been directed towards exploring clean technologies to decarbonize the railway sector. In Canada, alternative propulsion systems such as hydrogen and electric locomotives have undergone analysis and testing (Railway Association of Canada, 2023). Moreover, hybrid locomotives incorporating both battery and hydrogen technologies are regarded as the most promising option for the future of railway locomotives (Ahsan et al., 2023).

Hydrogen emerges as a promising solution for mitigating carbon emissions on diesel rail routes, especially when implementing electrification is challenging, and the distances surpass the capabilities of battery electric trains (International Energy Agency, 2019). Hydrogen serves as an energy carrier through its reaction with oxygen to produce electricity in a fuel cell (*Hydrogen Basics*, n.d.). Additionally, it offers the advantage of being a carbon-free fuel when used in a fuel cell, as it generates no emissions but water vapour at the point of use (Natural Resources Canada, 2020). However, hydrogen is not naturally available in a free

state; on the contrary, it requires substantial energy input for its production, storage, and delivery stages (Ahmadi & Kjeang, 2015).

Hydrogen can be generated through various methods and feedstocks, including water electrolysis, Steam Methane Reforming (SMR), or coal gasification from various feedstocks such as water and electricity, natural gas, crude oil, and biomass, among others. The selection of the production methods and energy sources contributes to the overall carbon intensity of hydrogen (Natural Resources Canada, 2020). When contemplating using fossil fuels in hydrogen production, incorporating Carbon Capture Utilization and Storage (CCUS) technology can yield low carbon intensity hydrogen. With its considerable potential, Canada stands at the forefront of advancing hydrogen generation and CCUS, offering significant opportunities to substantially reduce GHG emissions (Razi & Dincer, 2022).

To attain the 2050 net-zero targets, examining hydrogen technology in the railway sector is imperative. Thus, this study seeks to conduct a comprehensive comparative analysis between conventional diesel and hydrogen-powered locomotives, considering various hydrogen production pathways and feedstocks specifically tailored to the characteristics of Canada and its energy sources. The comparative analysis encompasses environmental and economic impacts linked to retrofitting conventional diesel locomotives with hydrogen technology. The goal is to provide a sustainability analysis with a life cycle perspective, covering different stages of the locomotive's life, from the refurbishing of required components to its end-of-life stage.

The Life Cycle Assessment (LCA) methodology is a globally employed tool for assessing and comprehending the impacts linked with products throughout their lifespan (ISO, 2006a). This study provides a thorough comparison of the potential economic and environmental impacts throughout the various locomotive life stages and propulsion technologies.

The approach considered in this study has been widely used in the transportation sector to provide comparative assessments of various fuels or propulsion technologies for passenger vehicles (Ahmadi & Kjeang, 2015; Bekel & Pauliuk, 2019; Chester et al., 2010; Candelaresi et al., 2021; Lu et al., 2022; Miotti et al., 2017), in the aviation transport (Bicer & Dincer, 2017; Siddiqui & Dincer, 2021) and marine applications (Bicer & Dincer, 2018; Bilgili, 2021).

In the railway sector, most of the comparative life cycle assessment studies have been performed for diesel, electric and natural gas propulsion systems (Stodolsky et al., 1998; M. V. Chester & Horvath, 2009; M. Chester & Horvath, 2012; M. Chester et al., 2013). Regarding the role of hydrogen in the railway sector, Haseli et al., (2008) presented a comparative assessment of hydrogen technology in the railway sector, focusing on environmental aspects. Their study compared diesel, electric, and hydrogen locomotives, highlighting potential environmental benefits based on the impacts of locomotive components and operation. However, it is essential to note that their analysis lacked consideration of the end-of-life phase, and there is no comprehensive comparison of cost implications for the different propulsion systems.

This study uses a life cycle perspective to present a comprehensive assessment of the economic and environmental impacts associated with both hydrogen and diesel propulsion systems. The overarching goal is to thoroughly compare each system's potential advantages and drawbacks, ultimately contributing to the decarbonization objectives within the railway sector.

2 MATERIALS AND METHODS

The study employs a life cycle methodology to assess the environmental and economic implications of introducing a retrofitted hydrogen-powered railway locomotive, comparing it with a conventional diesel locomotive operation in Canada. This assessment adheres to ISO 14050, which outlines the life cycle assessment framework, including its key phases: goal and scope definition, inventory analysis, impact assessment, and interpretation (ISO, 2006b). These phases are detailed and defined within the subsequent sections of this study.

2.1 Goal and scope definition

The goal and scope of the study are consistent for both environmental and economic analyses. Its primary aim is to estimate the emissions and costs associated with implementing hydrogen technology in Canada's railway sector. The evaluation compares five distinct hydrogen production pathways among each other and with diesel fuel. The functional unit is defined as a locomotive with an average daily travel distance of 300 km and a lifespan of 20 years.

The analyses encompass three crucial life cycle phases for the hydrogen-powered locomotive: refurbishing, operation, and end-of-life. The refurbishing phase estimates the impacts associated with critical components essential for retrofitting the locomotive. These components include the fuel cell, battery pack, and hydrogen storage tanks. In the case of the diesel locomotive scenario, the evaluation focuses solely on the operational phase, as no retrofitting components are involved. The key inputs and outputs assessed within the system are depicted in the system boundary illustrated in Figure 1.

The operational phase analyzes the production and utilization of hydrogen and diesel throughout the locomotive's entire lifespan. Five different hydrogen production pathways are analyzed to offer a comprehensive overview of the diverse alternatives within hydrogen technology. These pathways include water electrolysis powered with the Canadian average electricity mix, SMR with and without CCUS, and coal gasification with and without CCUS.

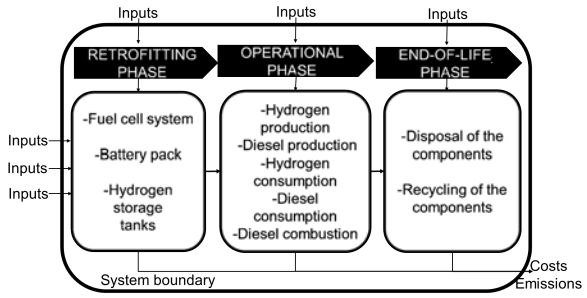

Figure 1. System boundary for comparative locomotive life cycle analyses

The final phase pertains to the end-of-life, focusing on the refurbishing components' disposal, recycling, or salvage value when the locomotive reaches the end of its operational life.

The analysis excludes the maintenance phase of the locomotive. This decision is grounded in the understanding that the examined retrofitting components would not require replacement over the locomotive's 20-year lifespan.

2.2 Life cycle inventory

The analysis of locomotive characteristics drew inspiration from the Frankfurt - Hamburg case study conducted by Ruf et al., (2019). This choice was guided by the similarities between the Frankfurt - Hamburg railway line and the conditions prevalent on a typical Canadian railway line, encompassing factors such as extreme weather conditions and rigorous operation. This mainline locomotive design includes a 689-kilowatt fuel cell, an 890-kilowatt-hour battery capacity, and hydrogen tanks capable of storing 765 kilograms of compressed hydrogen. This configuration is designed to deliver an average power output of 1,350 kilowatts while consuming an average of 0.82 kilograms per kilometer traveled.

The life cycle costing analysis aims to furnish cost data sourced from the prevailing market conditions in Canada, America, or globally. When specific cost data is not accessible from the market, the analysis incorporates information obtained from published literature.

The materials and quantities for the environmental life cycle inventory are sourced from the study conducted by Miotti et al., (2017). These values are subsequently scaled up to match the quantities pertinent to the characteristics of the locomotive system under consideration.

The refurbishing components are modelled using SimaPro software to determine the emissions generated during the refurbishing and end-of-life phases. The ecoinvent database is utilized to acquire the necessary data for the modelling process.

During the operation phase, the emissions produced within the fuel production stage are estimated using the GHGenius model. GHGenius is a tool Natural Resources Canada provides that calculates life cycle emissions based on historical data for various fuels and feedstocks, including hydrogen and diesel.

2.3 Life cycle impact assessment

A life cycle costing model is created to determine the cost per kilometre for the locomotive, considering diesel and various hydrogen production pathways and feedstocks. In this model, the unit price of fuel in Canada is estimated according to the prices illustrated in Table 1, where the diesel's and the compressed hydrogen's unit prices are estimated based on the average market prices in refuelling stations in British Columbia and the rest from published literature.

Table 1. Diesel and hydrogen prices at the refueling station

Fuel		Prod. ($/kg)	Transport ($/kg)	Price at refuelling station ($/l or $/kg)
Diesel		-	-	1.8
H_2	Water electrolysis	-	-	12.8
	SMR with CCUS	2.3	5.0	7.2
	SMR without CCUS	1.7	5.0	6.7
	Coal with CCUS	2.4	5.0	7.4
	Coal without CCUS	1. 8	5.0	6.7

Data obtained from British Columbia Utilities Commission, (2023), HTEC, (2023), Olateju & Kumar, (2013), and Olateju & Kumar, (2011)

The environmental impact assessment stage is elaborated with the ReCiPe 2016 v1.1 method. The global warming category is selected to obtain the total emissions in kg CO_2 equivalent from the refurbishing components for further analysis.

3 RESULTS AND DISCUSSION

The estimated life cycle costs and environmental life cycle emissions are presented separately to facilitate a detailed discussion on various life cycle stages, hydrogen production pathways, and their individual contributions to the overall results. Finally, a life cycle cost-emission comparison is provided, offering a comprehensive assessment of hydrogen technology's application in Canada's railway sector.

3.1 Life cycle cost assessment

While estimating the life cycle cost of hydrogen locomotives, the refurbishing and end-of-life phases are assumed to be uniform across all analyzed hydrogen production pathways. This assumption is based on the premise that the fuel cell, battery pack, and hydrogen storage tanks retain consistent characteristics. Conversely, the operational phase differs depending on the chosen hydrogen production pathway.

As illustrated in Figure 2, the operational phase emerges as the primary contributor to the overall life

cycle cost, with the hydrogen production cost playing a pivotal role.

The production cost of hydrogen from different pathways is influenced by technical and economic factors, encompassing feedstock costs, capital costs, and operating costs (Natural Resources Canada, 2020).

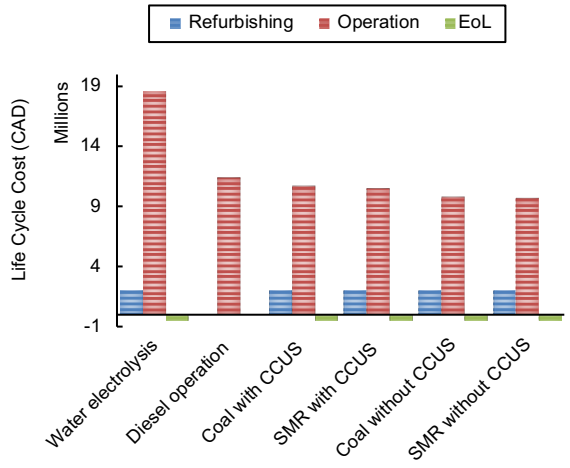

Figure 2. Comparison of locomotive life cycle cost between diesel and hydrogen fuel obtained from various pathways

The end-of-life phase is depicted on the negative side of the axis due to the inclusion of salvage value attributed to the remaining lifespan of the fuel cell and battery pack of the locomotive at the end of its operational life.

The life cycle cost analysis reveals that the scenario involving a hydrogen-powered locomotive, with hydrogen produced through water electrolysis, stands out as the most expensive among various hydrogen production pathways, almost doubling the life cycle costs obtained from the SMR and Coal without the CCUS scenarios.

Conversely, costs associated with a diesel locomotive demonstrate a similar trajectory to the life costs of the hydrogen locomotive, particularly in scenarios where fossil fuels are employed for hydrogen production. The operation costs of the diesel locomotive resulted in $11.4 million and a range of $9.7-10.7 million for the hydrogen locomotive from SMR and Coal scenarios. This result reveals that hydrogen locomotive operation may be cost-competitive compared to diesel ones. However, when analyzing the investment required to retrofit the locomotive to incorporate the hydrogen technology, the life cycle cost of the hydrogen locomotive increases, resulting in a range of $11.2-12.2 million.

Hence, despite apparent similarities in operating expenses in the comparison between diesel and hydrogen locomotives, it is crucial to emphasize that refurbishing and end-of-life costs significantly influence the overall investment considerations. Therefore, a meticulous analysis of resource optimization becomes imperative to minimize investment costs in hydrogen locomotives, primarily attributed to components such as hydrogen fuel cells, batteries, and hydrogen storage technology. These reductions would minimize the difference in life cycle cost between hydrogen and diesel locomotives.

3.2 Environmental life cycle assessment

The locomotive's environmental life cycle assessment results reveal that the operation phase contributes the most to the total emissions, as shown in Figure 3. In contrast, although the emissions stemming from the refurbishing components are relatively minor compared to the significant impact of the operational phase, their collective contribution to the total locomotive life cycle emissions is approximately 1 ton.

During the operation phase of the diesel locomotive, emissions result from fuel production and the combustion process of diesel within the locomotive. This combustion process is a notable contributor to the overall emissions during the operation phase. Specifically, the diesel locomotive engine emits 2.99 kg of CO_2-eq per litre of diesel consumed (Environment Canada, 2022).

Conversely, when hydrogen is utilized via the fuel cell technology in the locomotive, the only resulting by-product is water vapour. This distinctive characteristic classifies hydrogen locomotives as having zero emissions during their utilization stage. Consequently, the operation phase of hydrogen locomotives entirely depends on the hydrogen production stage.

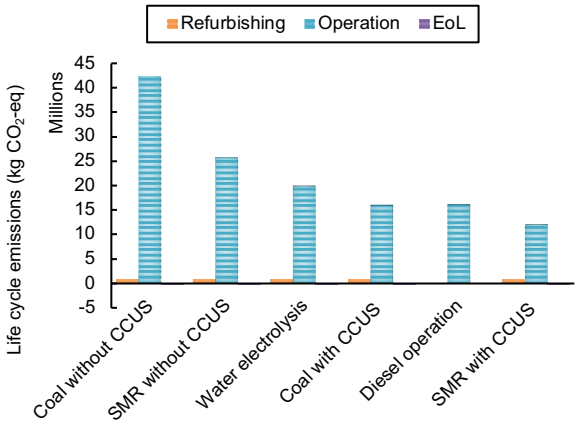

Figure 3. Comparison of locomotive life cycle emissions between diesel and hydrogen fuel obtained from various pathways

Overall, the environmental impact of the hydrogen locomotive, whether utilizing hydrogen from coal with or without CCUS, water electrolysis, or SMR without CCUS, is potentially more harmful than that of the diesel locomotive. This difference mainly comes from the emissions primarily generated from various feedstocks and energy sources during the hydrogen production process.

For instance, water electrolysis is almost a net-zero emission method when combined with emission-free electricity sources like renewable energy (Natural Resources Canada, 2020). Nevertheless, when hydrogen is generated using electricity from the Canadian grid mix, the life cycle emissions of hydrogen surpass those of diesel by nearly 5 tonnes of CO_2-eq. These emissions are attributed to the composition of the Canadian grid mix, which consists of 60% from hydro sources and 40% from various sources like natural gas, coal, biomass, petroleum, nuclear, wind, and solar (Canada Energy Regulator, 2023).

The locomotive that utilizes hydrogen from SMR with CCUS emerges as the only preferable option compared to diesel in terms of life cycle emissions. This underscores the significance of incorporating CCUS technology into the hydrogen production process, as it becomes the determining factor in evaluating whether the alternative is considered more beneficial than diesel utilization, having the potential to mitigate up to 3 tonnes of GHG emissions over the lifespan of the locomotive.

3.3 Life cycle sustainability analysis

Integrating environmental and economic life cycle analyses achieves a more thorough assessment. The relationship between these two aspects underscores the significance of exploring alternatives that offer environmental benefits and the importance of identifying economically viable alternatives for society.

The total distance normalizes the total life cycle costs and emissions travelled considered during the locomotive's operation, presenting the results in a more simplified manner, as illustrated in Figure 4.

The life cycle cost per kilometre is consistent across most scenarios, ranging from $5.1-5.6, except for water electrolysis, which rises to nearly $9.2 per km. Regarding life cycle emissions, there is a significant variation among the scenarios. Water electrolysis, diesel, SMR, and coal with CCUS range from 5.9-9.5 kg of CO_2-eq, whereas SMR and coal without CCUS result in 12.2 and 19.7 kg of CO_2-eq, respectively.

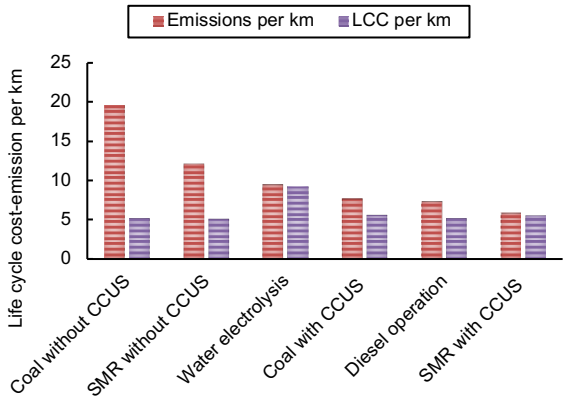

Figure 4. Comparison of locomotive life cycle cost-emissions per km between diesel and hydrogen fuel obtained from various pathways

The hydrogen locomotive using hydrogen from coal without CCUS emerges as the most environmentally harmful option among all the hydrogen and diesel scenarios. Conversely, it is the least expensive alternative. Furthermore, when comparing coal to SMR without CCUS, the life cycle cost per kilometre is quite similar. However, emissions produced with the SMR method are nearly 40% lower than in the coal scenario.

Likewise, the life cycle cost per kilometre for the water electrolysis scenario surpasses that of diesel, coal with CCUS, and SMR with CCUS. This positions water electrolysis as a less economically favourable alternative under the conditions examined. The diesel scenario is a preferable alternative to coal, SMR without CCUS, and water electrolysis in terms of costs and emissions. In contrast, coal and SMR with CCUS exhibit comparable life cycle costs but have the potential to equalize or reduce life cycle emissions.

4 CONCLUSIONS

Hydrogen-powered locomotives represent a potential solution for decarbonizing the railway sector. The study assesses a retrofitted hydrogen locomotive's life cycle costs and emissions across various production pathways and feedstocks. This environmental and economic evaluation is then compared to that of a conventional diesel locomotive, yielding the following key findings:

- While the refurbishing components may not significantly contribute to the overall life cycle emissions, their cost implications can be pivotal in determining whether hydrogen locomotives are perceived as a more economical alternative to diesel locomotives.
- Including CCUS technology is a crucial factor that can significantly influence whether the hydrogen locomotive offers advantages compared to the diesel locomotive.
- The water electrolysis scenario resulted in the most expensive alternative at $9.2 per km, with nearly 30% of additional emissions compared to diesel. These emissions are primarily attributed to the high energy intensity of the method, exacerbated by the Canadian grid mix.
- The hydrogen locomotive emerges as a more sustainable alternative to the diesel locomotive, particularly when considering the SMR with the CCUS pathway. This pathway results in a notable 20% reduction in emissions, accompanied by a modest cost increment of only 6% compared to diesel.

Hydrogen technology still needs to be developed; consequently, comprehensive data for its application in the railway sector is not widely available. Several assumptions must be made considering the data published from the passenger vehicle applications. Moreover, in the railway sector, passenger and freight rail transportation exhibit distinct characteristics that require further study to gather reliable data, which could enhance the accuracy of results.

Additionally, it is crucial to emphasize that these findings are contingent upon the characteristics of the analyzed region, as the choice of electricity source for hydrogen production significantly impacts both cost and emissions. Given that this study encompasses the entire Canadian region, it is crucial to underscore the substantial variation in electricity sources from one province to another.

5 ACKNOWLEDGEMENT

The authors would like to express appreciation for the financial support provided by the Transport Canada Grant of Dr. Kasun Hewage (AWD-020944).

REFERENCES

Ahmadi, P., & Kjeang, E. (2015). Comparative life cycle assessment of hydrogen fuel cell passenger vehicles in different Canadian provinces. International Journal of Hydrogen Energy, 40(38), 12905–12917. https://doi.org/10.1016/j.ijhydene.2015.07.147

Ahsan, N., Hewage, K., Razi, F., Hussain, S. A., & Sadiq, R. (2023). A critical review of sustainable rail technologies based on environmental, economic, social, and technical perspectives to achieve net zero emissions. Renewable and Sustainable Energy Reviews, 185, 113621. https://doi.org/10.1016/j.rser.2023.113621

Bekel, K., & Pauliuk, S. (2019). Prospective cost and environmental impact assessment of battery and fuel cell electric vehicles in Germany. The International Journal of Life Cycle Assessment, 24(12), 2220–2237. https://doi.org/10.1007/s11367-019-01640-8

Bicer, Y., & Dincer, I. (2017). Life cycle evaluation of hydrogen and other potential fuels for aircrafts. International Journal of Hydrogen Energy, 42(16), 10722–10738. https://doi.org/10.1016/j.ijhydene.2016.12.119

Bicer, Y., & Dincer, I. (2018). Clean fuel options with hydrogen for sea transportation: A life cycle approach. International Journal of Hydrogen Energy, 43(2), 1179–1193. https://doi.org/10.1016/j.ijhydene.2017.10.157

Bilgili, L. (2021). Comparative assessment of alternative marine fuels in life cycle perspective. Renewable and Sustainable Energy Reviews, 144, 110985. https://doi.org/10.1016/j.rser.2021.110985

British Columbia Utilities Commission. (2023). Home Page—Gas Prices BC. Gas Prices BC. https://www.gaspricesbc.ca/

Canada Energy Regulator. (2023). CER – Provincial and Territorial Energy Profiles – Canada. https://www.cer-rec.gc.ca/en/data-analysis/energy-markets/provincial-territorial-energy-profiles/provincial-territorial-energy-profiles-canada.html#wb-tphp

Candelaresi, D., Valente, A., Iribarren, D., Dufour, J., & Spazzafumo, G. (2021). Comparative life cycle assessment of hydrogen-fuelled passenger cars. International Journal of Hydrogen Energy, 46(72), 35961–35973. https://doi.org/10.1016/j.ijhydene.2021.01.034

Chester, M., & Horvath, A. (2012). High-speed rail with emerging automobiles and aircraft can reduce environmental impacts in California's future. Environmental Research Letters, 7(3), 034012. https://doi.org/10.1088/1748-9326/7/3/034012

Chester, M., Pincetl, S., Elizabeth, Z., Eisenstein, W., & Matute, J. (2013). Infrastructure and automobile shifts: Positioning transit to reduce life-cycle environmental impacts for urban sustainability goals. Environmental Research Letters, 8(1), 015041. https://doi.org/10.1088/1748-9326/8/1/015041

Chester, M. V., & Horvath, A. (2009). Environmental assessment of passenger transportation should include infrastructure and supply chains. Environmental Research Letters, 4(2), 024008. https://doi.org/10.1088/1748-9326/4/2/024008

Chester, M. V., Horvath, A., & Madanat, S. (2010). Comparison of life-cycle energy and emissions footprints of passenger transportation in metropolitan regions. Atmospheric Environment, 44(8), 1071–1079. https://doi.org/10.1016/j.atmosenv.2009.12.012

Environment and Climate Change Canada. (2023). Canadian Environmental Sustainability Indicators: Greenhouse gas emissions. Environment and Climate Change Canada = Environnement et changement climatique Canada. www.canada.ca/en/environment-climate-change/services/environmental-indicators/greenhouse-gasemissions.html.

Environment Canada. (2022). Greenhouse gas sources and sinks in Canada: Executive summary 2022. https://www.canada.ca/en/environment-climate-change/services/climate-change/greenhouse-gas-emissions/sources-sinks-executive-summary-2022.html

Haseli, Y., Naterer, G., & Dincer, I. (2008). Comparative assessment of greenhouse gas mitigation of hydrogen passenger trains. International Journal of Hydrogen Energy, 33(7), 1788–1796. https://doi.org/10.1016/j.ijhydene.2008.02.005

HTEC. (2023). FAQs. HTEC. https://www.htec.ca/faqs/

Hydrogen Basics. (n.d.). Retrieved December 8, 2023, from https://www.fsec.ucf.edu/en/consumer/hydrogen/basics/index.htm

International Energy Agency. (2019). The Future of Rail: Opportunities for energy and the environment. OECD. https://doi.org/10.1787/9789264312821-en

ISO. (2006a). ISO 14044:2006 Environmental management—Life cycle assessment—Requirements and guidelines. https://www.iso.org/standard/38498.html

ISO. (2006b). ISO14040:2006 Environmental management—Life cycle assessment—Principles and framework.

Lu, Q., Zhang, B., Yang, S., & Peng, Z. (2022). Life cycle assessment on energy efficiency of hydrogen fuel cell vehicle in China. Energy, 257, 124731. https://doi.org/10.1016/j.energy.2022.124731

Miotti, M., Hofer, J., & Bauer, C. (2017). Integrated environmental and economic assessment of current and future fuel cell vehicles. The International Journal of Life Cycle Assessment, 22(1), 94–110. https://doi.org/10.1007/s11367-015-0986-4

Natural Resources Canada. (2020). Hydrogen strategy for Canada: Seizing the opportunities for hydrogen : a call to action. Natural Resources Canada.

Olateju, B., & Kumar, A. (2011). Hydrogen production from wind energy in Western Canada for upgrading bitumen from oil sands. Energy, 36(11), 6326–6339. https://doi.org/10.1016/j.energy.2011.09.045

Olateju, B., & Kumar, A. (2013). Techno-economic assessment of hydrogen production from underground coal gasification (UCG) in Western Canada with carbon capture and sequestration (CCS) for upgrading bitumen from oil sands. Applied Energy, 111, 428–440. https://doi.org/10.1016/j.apenergy.2013.05.014

Railway Association of Canada. (2023). Locomotive emissions monitoring report 2021. https://www.railcan.ca/resources/locomotive-emissions-monitoring/

Razi, F., & Dincer, I. (2022). Challenges, opportunities and future directions in hydrogen sector development in Canada. International Journal of Hydrogen Energy, 47(15), 9083–9102. https://doi.org/10.1016/j.ijhydene.2022.01.014

Ruf, Y., Zorn, T., De Neve, P. A., Andrae, P., Erofeeva, S., Garrison, F., & Schwilling, A. (2019). Study on the use of fuel cells and hydrogen in the railway environment. Report 2.

Siddiqui, O., & Dincer, I. (2021). A comparative life cycle assessment of clean aviation fuels. Energy, 234, 121126. https://doi.org/10.1016/j.energy.2021.121126

Stodolsky, F., Gaines, L., Cuenca, R., & Eberhardt, J. J. (1998). Lifecycle Analysis for Freight Transport.

Canadian & Cold Regions
Rail Research Conference
2024

Non-destructive approach for high strength rail steel characterization using ball indentation approach

Stephen Okocha[1], P.-Y. Ben Jar[1], Michael Hendry[2], & Feng Yu[3]
[1] *Department of Mechanical Engineering, University of Alberta, Edmonton, Alberta, Canada*
[2] *Department of Civil and Environmental Engineering, University of Alberta, Edmonton, Alberta, Canada*
[3] *School of Mechanical Engineering and Mechanics, Ningbo University, PR China*

ABSTRACT

It is eminent that the behaviour of rail steels is crucial towards the safe application and operation of main tracks especially in cold regions like Canada, where temperatures can become extreme to about -50°C. Steel properties like Young modulus, yield strength, hardness and fracture toughness become vital as they provide useful information for the rail-wear limits and resistance to fracture, which are critical concerns in several rail defects. In this paper, 3 different ball indenter sizes (3mm, 5mm and 6.35mm) are used to ascertain the properties of rail steels using contact mechanics principles in ambient condition. Investigation on the indentation size effect will be explored based on its consistency in rail deformation behaviour under contact. A critical limit load analysis is employed towards its ability to estimate the fracture toughness (K_{IC}) similar to what is obtainable in the conventional destructive fracture toughness test in accordance with the American Society for Testing Materials (ASTM). Result shows that the different indenter sizes provide similar pressure-normalized indentation depths curves with preferences towards the smaller indenter size for non-destructive testing. Comparison between hardness and fracture toughness estimated with the three indenters sizes are provided, opening the feasibility of in-service or rail stock inspection at various temperatures in the coming future.

1 INTRODUCTION

As the rail industry continuously experiences massive improvements in its value chain, the rail steels stand as one of the primal components towards an effective operation of the rail system. Thus, it is imperative to determine the structural integrity and behaviour of newly manufactured or in-service rail steels as this gives vital information about their ability to perform adequately in varying operating conditions. Apart from understanding the mechanical properties of rail steels, the fracture toughness, which is the critical energy required to initiate or propagate a crack or flaw is important owing to the records of broken rails in past years as seen in reports from Leishman et al. (2017), Behnia, Hendry & Abdulrazagh (2022) and Transport Canada (2020). The challenge arises when new rail stocks or newly welded rails joints need to be accessed quickly and efficiently of its mechanical properties, the conventional methods of doing these assessments comes with some drawbacks, which include cost of structural integrity assessment due to several tests and specimens needed as seen in Anderson & Osage (2000), technical difficulties involved in specimen preparation and as well applications with in-service structures according and unsuitable methods like the destructive tests recommended by ASTM E1820 and ASTM E8/E8M. Thus, a simpler, yet efficient and effective testing approach is required in ascertaining the mechanical properties of rail steels structures either newly manufactured or in-service.

One approach that has been regarded as a non-destructive technique, which has shown potential to quantify the mechanical properties is the instrumented indentation technique. Although in this study, specimens were cut out of parent material, the principles developed could be applied to structures for in-service or newly manufactured metallic alloys. For the young's modulus, Oliver & Pharr (1992) improved on the methodology of attaining the Elastic modulus of materials using the unloading curve of spherical indentation with the inclusion of pile-up and sink-in effects. This method originating from Doer and Nix (1986) approach opened the avenue to study material degradation with further indentation depth testing. Stinville et al. (2011) worked on using the Vickers micro-indentation to study the anisotropic changes in hardness and indentation modulus of 316L polycrystalline stainless steel induced by plasma nitriding noting that both hardness and indentation modulus exhibited an inverted anisotropy compared to the unprocessed 316L. Researchers like Haggag et al. (1989), Yu & Blanchard (1996), Lee et al. (2005) developed different techniques in estimating the yield strength for metallic materials. Haggag proposed

using the total indentation pressure and depth in the plastic deformation regime, whereby an extrapolation to zero in the log-log scale provides the stress where plastic deformation initiates. Yu & Blanchard (1996) developed an analytical relationship among hardness, yield stress, elastic modulus, Poisson's ratio, and indenter geometry for elastic perfectly plastic materials by combining the pressure distribution predicted by elastic theory and an approximate pressure distribution predicted by slip-line-field theory that predicts yield strength. Lee et al. (2005) predicted the yield strength using finite element analysis based on an incremental plasticity theory, where an iterative analysis procedure is employed that predicts the elastic modulus, yield strength, and the work hardening exponent of the test materials. To achieve this, finite element analysis was carried out based on the assumptions of an elastic tip, and an isotropic, rate independent solid that obeys von Mises yield criteria.

For hardness, the well-known expansion cavity model (ECM) using spherical indentation was studied by Gao (2006) for strain hardening materials, where demonstration about indentation hardness evolution was established by providing an elastic-plastic solution originating from a cylindrical cavity was attained. The solutions according to Gao (2006) of the stress, strain, and displacement components with strain hardening properties of the elastic and plastic deformation domains of an internally pressurized cylindrical cavity were provided. Other hardness approach is the standard Brinell hardness, which is in accordance with ASTM E10 approaches. Here test forces are used for hardness evaluation depending on the diameter of the indent created for spherical indentation. Apart from the Young's modulus, yield strength and other plastic properties, the fracture toughness (K_{IC}) has also been attempted to be estimated non-destructively. The works of Lee et al. (2006) and Yu et al. (2018) implemented a continuum damage model (CDM) approach by estimating a critical indentation depth required for estimating a critical indentation energy needed for fracture toughness estimation while the works of Haggag & Nanstad (1989) and Okocha et al. (2023b) focused on estimating fracture toughness using a modified critical fracture strain model originating from the demonstrations from the works of Ritchie et al. (1979), which observes the microstructural features of carbon steels. Kim et al. (2021) applied a flat-ended cylindrical indenter for fracture toughness estimation via a limit load approach, which defines a crack initiation point (CIP) required for structures with defects to fail. This approach by Kim et al. (2021) originated from the work of Miller (1988) relating the deformation from a flat-end cylindrical indentation with a virtually crack round bar (CRB) under tension. The CIP originates from Tresca's plane stress limit solutions and depends only on the plane of the ligament according to the work of Kim et al. (2021).

In this work, spherical indentation is used to characterize the mechanical properties of two high strength rail steels, where both materials used exhibit different manufacturing processes. The first (JP rail steel) is deep head hardened (DHH) at the rail head to achieve larger hardness and toughness while the second rail (CZ-rail) is not heat treated after manufacturing. Emphasises are focused on the methodologies for characterizing the high strength rail steels, where deviation on the 1st derivative of the pressure and normalized depths are conducted for identifying the yield strength and a modification of the ECM approach coupled a modified limit load approach is implemented to investigate differences in stress intensity factor for fracture toughness estimation is implemented. In the end, differences with the yield strength, hardness and fracture toughness were identified from the two different rail steels using data from one indentation cycle (loading-unloading). The critical stress intensity factor did not give close values with the conventional fracture toughness estimate but showed a trend and thus is subjected to further studies. Once fully comprehended, the methodologies presented in this report can be standardized for ascertaining the integrity of high strength rail steels and structures after being manufactured or even during in-service operations of which scheduled data acquisition can be collected based on operational changes, age effect or environmental factors especially in cold regions like Canada, where temperatures can become extreme at about -50°C.

2 MATERIALS AND METHODS

The rail steels used in this study are high strength rail steels. Table 1 shows two different rail steels provided by the Canadian National (CN) Railway Company. The table also shows the heat treatments included in the manufacturing process for the rail steels.

The mechanical properties of the rail steels were attained in previous studies using ASTM E8/E8M approach, which require a dog-bone smooth tensile rods while the facture toughness is attained using 3-point single-edge notch bend (SENB) specimens.

Table 1. Rail steel types.

Rail name	Microstructure	Locations	Company
JP	Deep head hardened	Rail head	CN
CZ	Nil[1]	Rail head	CN

[1] No surface heat treatment done after rail manufacture

To conduct the indentation tests, a 4140 HTSR steel was used as an intermediate between the MTS machine's grip and tungsten carbide ball indenters. The 4140 HTSR steel were first drilled to accommodate the indenter sizes and then the indenters were force fitted with an interference fit through thermal expansion on the drilled hole. Three different indenter sizes were considered, which were cylindrical tungsten carbide balls of 3mm, 5mm, and 6.35mm with Young's modulus (E_i) of 630GPa and Poisson's ratio (v_i) of 0.21.

The rail steel specimen (31.25Φ x 35mm) was indented following a stroke-controlled pre-determined depth. Figure 1 shows the experimental set-up and a sample of the loading-unloading force-depth curve used for each specimen and indenter size. From this

experimental data, crucial mechanical properties like the Young's modulus, yield strength, hardness and a proposed methodology for fracture toughness is estimated.

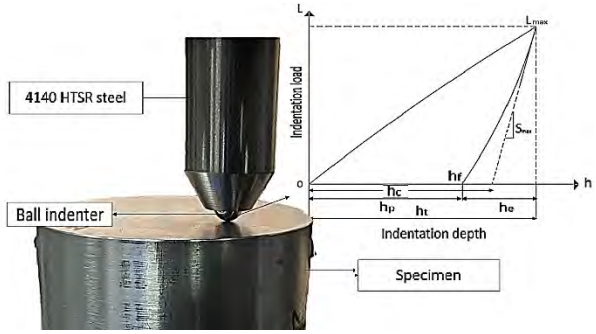

Figure 1. A typical ball indentation experiment

The Modulus is estimated by first estimating the maximum stiffness (S_{max}) using the Oliver & Pharr's (1992) method followed by Sneddon's (1965) elastic solution, which evaluates the reduced Modulus (E_r) as seen in Equation. 1

$$E_r = \frac{\sqrt{\pi}}{2\beta}\frac{S_{max}}{\sqrt{A(h_c)}} \quad [1]$$

where β is taken as 1 for spherical indentation, $A(h_c)$ is the contact area that is a function of the contact depth (h_c).

Once E_r is known, the Modulus of the specimen (E_s) can then be attained with the Modulus of the indenter (E_i) , Poisson's ratios of the indenter (v_i) and specimen (v_s) respectively. Equation 2 shows how E_s is attained.

$$E_s = \frac{1 - v_s^2}{\frac{1}{E_r} - \frac{1 - v_i^2}{E_i}} \quad [2]$$

For the spherical indentation, h_c as seen in Equation 3 is attained by considering the height of pile-up (h_{pile}) created at increased indentation depth, which was recorded using a dial ball tip indicator and a subtraction of the elastic recovery once the specimen is unloaded as seen from Oliver & Pharr's (1992) approach.

$$h_c = h_t + h_{pile} - \in \frac{P_{max}}{S(h_{max})} \quad [3]$$

Equation 3 indicates that the accurate determination of h_c is required for $A(h_c)$ (seen in Equation 4) and E_s estimation.

$$A(h_c) = \pi\left[Dh_c - h_c^2\right] \quad [4]$$

Where D is the diameter of the indenter

For the yield strength via indentation ($\sigma_{y,ind}$) as seen in Equation 5, the first derivative of the indentation pressure ($P = \frac{L}{\pi a_c^2}$) and normalized depth ($\frac{h}{a_c}$) is used to locate the yield strength based on the studies of Xu et al. (2022) and Gharaibeh & Aburub (2013).

$$\sigma_{y,ind} = \frac{P_y}{\delta} \quad [5]$$

Where δ is the stress constraint equals to 2.8 in accordance to works by Oliver & Pharr's (1992).

The hardness of the steels is evaluated using the Brinell hardness (H_B) evolution with indentation depth according to ASTM E10. Also, since the indentation diameter (d) can be a function of the indentation depth as expressed ($d = 2(hD - h^2)^{0.5}$), the H_B across the indentation depth during loading can be investigated. Equation 6 shows the expression for H_B estimation.

$$H_B = 0.1\frac{2L}{\pi D(D - \sqrt{D^2 - d^2})} \quad [6]$$

The work from Gao (2006) also demonstrates the indentation hardness evolution using spherical indentation by providing an elastic-plastic solution originating from the spherical expansion cavity model (ECM). The exact solution is expressed in Equation 7.

$$\frac{H_{ECM}}{\sigma_y} = \frac{2}{3}\left\{1 + \frac{1}{n}\left[\left(\frac{1}{4}\frac{E}{\sigma_y}\frac{a_c}{R}\right)^n - 1\right]\right\} \quad [7]$$

Where H_{ECM} is the indentation hardness due to an internally pressurized cylindrical cavity based on ECM and R the radius of the indenter (D=2R), n, the stain hardening exponent, which is 0.085 for JP rail steel and 0.082 for CZ rail steel as recorded in Okocha et al. (2023a) and Yu et al. (2018).

For the fracture toughness estimation via indentation, a critical limit load analysis is employed, which follows a series of procedures. The ideology stems from the concept introduced by Kim et al. (2021), which correlates the indentation of a flat-ended cylindrical indenter with that of a virtual cracked round bar specimen (CRB) in tension. Based on isotropy, the compression from indentation is likened to tension of which indentation energies during indentation can provide information on the critical energy for fracture in a virtual NRB tension test.

For the spherical indentation in this work, the depth of indentation is compared to the virtual displacements of the SENB specimen as seen in Figure 2, where the tip of the ball indenter is likened to the crack tip of a SENB specimen based on similar stress triaxiality experienced on both tips according to the works of Okocha et al (2023b), Lee et al. (2006) and Yu et al. (2018).

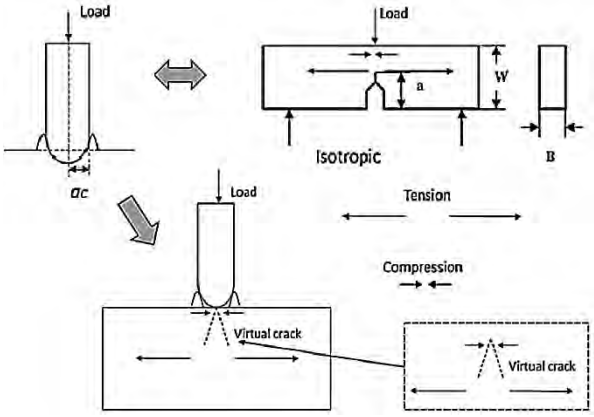

Figure 2. Geometrical similarity between spherical indentation and virtual SENB specimen

The correlation between the spherical indentation and the Virtual SENB is expressed in Equation 8

$$\frac{h^{'}}{a_c^{'}} = \frac{h}{a_c} \quad [8]$$

where $h^{'}$ and $a_c^{'}$, the pre-determined offset blunting line related to J-integral and crack tip opening distance (CTOD) respectively.

However, since there are no cracks formed during indentation to signify the critical depth or critical energy for fracture toughness estimation, recommendations from Kim et al. (2021) following the work of Miller (1988) suggests that the failure of metallic structures with flaws based on Tresca's failure criteria can be a function of the yield strength of the material. Here, Equation 9 suggests the critical limit load (L_P) is required for determining the crack initiation point (CIP). The crack initiation pressure ($P_{CIP}={}^{L_P}/_{\pi(a_c)^2}$) correlating to the critical limit load can be attained along with the corresponding h/a_c value. It is to note that due to the conservativeness of the Tresca's plastic yield surface, the von Mises plastic yield surface for the definition of the CIP is implemented in this study as seen in Equation 9.

$$L_P = 3.285 \cdot \sigma_y \cdot \pi(a_c)^2 \quad [9]$$

New virtual loads and depths ($L^{'}$-$h^{''}$) can then be constructed halting at the CIP point using different $h^{'}$ values. The $h^{'}$ is varied to tend to zero to establish different stress intensity factors (K_J) at different blunting line of J integral method. The fracture toughness is then attained by extrapolating the stress intensity factors following Irwin's (1964) solution for notches to cracks. The procedures are illustrated in Figure 3 from indentation test to fracture toughness.

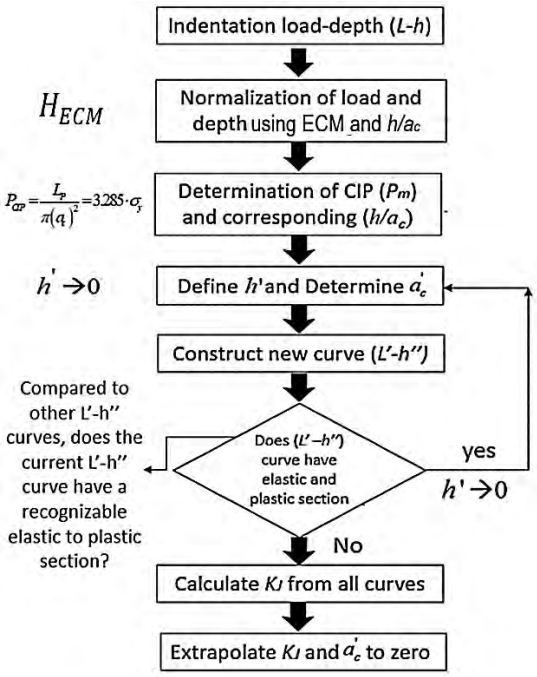

Figure 3. Procedure for determining indentation K_{IC}

The critical stress intensity factor (K_{JC}) is defined based on the virtually determined J-integral method.

$$K_{JC} = \lim_{a_c^{'} \to 0} f(K_J) \quad [10]$$

where $f(K_J) = \sqrt{\frac{J \cdot E_s}{(1-v_s^2)}}$, J the virtual J-integral consisting of the elastic (J_e) and plastic (J_p) parts of the load-depth curve. The J-integral is expressed in Equation 11.

$$J = \frac{(1-v_s^2)}{E_s} \cdot \left(\frac{L^{'}}{2a_c^{'}\sqrt{\pi a_c^{'}}}\right)^2 + \eta_{pl}\frac{A_{pl}}{\pi\left(a_c^{'}\right)^2} \quad [11]$$

where A_{pl} is the plastic area of the virtual load-depth curve, η_{pl} the plastic work factor which is a function of the specimen geometry taken as 0.969 for SENB specimen according to NASA's report as recorded by Sharobeam & Pomona (1994).

3 RESULTS AND DISUSSION

Following the indentation test conducted involved the spherical indenters for the 3 different sizes (6.35mm, 5mm, 3mm). The loading and unloading data were retrieved from the MTS data analyzer. After each pre-determined depth, the indenter was kept stable for 15 seconds to relax the multiaxial stresses before the unloading cycle. Figure 4 shows a typical loading-unloading cycle of different indentation depths.

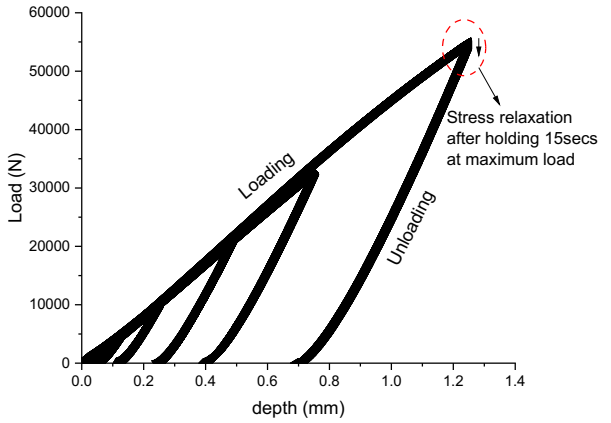

Figure 4. A typical loading-unload indentation cycle.

Following the procedures of Equations 1-4, different E_s are estimated for the different indentation cycles showing the degradation of the modulus. The E_s of the material is taken from the 1st and/or 2nd indentation cycles. Figure 5 shows the degradation of E_s, their average and standard deviation (std dev) from 3 tests along the indentation depth within the rail steel's sub-surface.

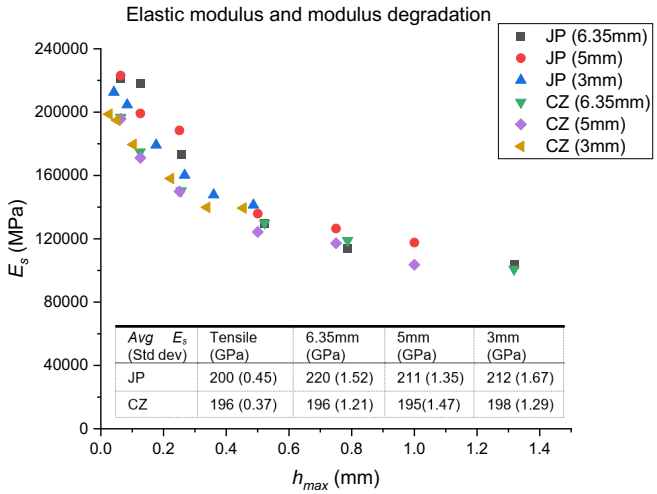

Avg E_s (Std dev)	Tensile (GPa)	6.35mm (GPa)	5mm (GPa)	3mm (GPa)
JP	200 (0.45)	220 (1.52)	211 (1.35)	212 (1.67)
CZ	196 (0.37)	196 (1.21)	195(1.47)	198 (1.29)

Figure 5. Elastic modulus and modulus degradation

As shown in Figure 5, further increase in depth deteriorates the E_s, which is in conjunction with the theories of continuum damage mechanics (CDM) as reported in works of Lee et al. (2006) and Yu et al. (2018). This is because anisotropic damage caused by the shear deformation in the indentation test contributed to the shear stress originated by friction effect.

The estimation of σ_y followed a series finding of 1st derivative of the indentation pressure and h/a_c and then locating the change in deformation stages through the changes in the slope of the 1st derivative of the average pressure. Figure 6 shows an illustration of the average stress and 1st derivative with h/a_c for JP-rail steel using the 3mm spherical indenter as an illustration.

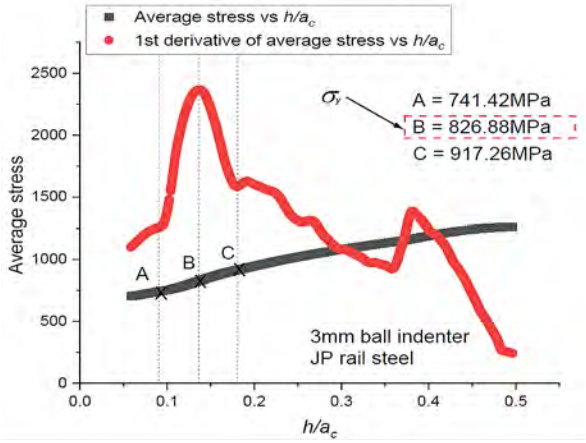

Figure 6. Average stress and its 1st derivative with h/a_c

The location σ_y fell on the maxima of the slopes which can refer to when pressure is saturated before strain hardening effect occurs as suggested by the works in Voce (1948) model. An estimate of σ_y is tabulated in Table 2 showing the average σ_y estimation from 3 different tests and their standard deviation (std dev). The table shows that JP-rail steel requires more stress to yield due to the DHH heat treatment introduced during the manufacturing process than CZ-rail steel.

Table 2. Yield strength indentation estimation.

Avg (Std dev)	Tensile	6.35mm	5mm	3mm
JP (MPa)	820	827 (9.3)	832 (10.7)	829 (10.2)
CZ (MPa)	632	648 (11.1)	649 (9.8)	639 (8.7)

The Brinell hardness was also estimated along the depth of the rail steels showing little differences across indenter sizes but differences in rail steel types.

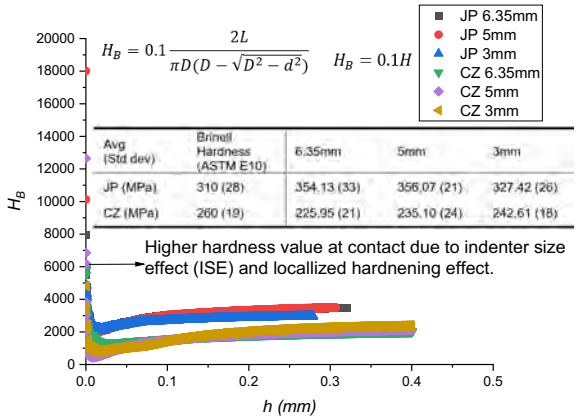

Figure 7. H_B estimation along indentation h_{max}

As shown in Figure 7, JP rail steel showed larger hardness as compared to CZ due to the DHH surface heat treatment introduced after manufacture. This invariably indicates the lower sensibility to wearing especially in curves and turns in the rail network. After the initial contact, indenter size effect (ISE) coupled with localized hardening effect occurred but gradually reduces to a relatively constant hardness value at further increase in depth as depicted in works in Okocha et al. (2023a)

Another important parameter is the variation of the indentation hardness (H_{ECM}) with the indentation depth according to the ECM. There is a gradual increase in indentation stress (representative pressure) as indentation depth increases. The three indenter sizes as seen in Figure 8 show no difference in H_{ECM} outcome due to similar pressure being initiated in the elastic-half space of the rail steel material during testing.

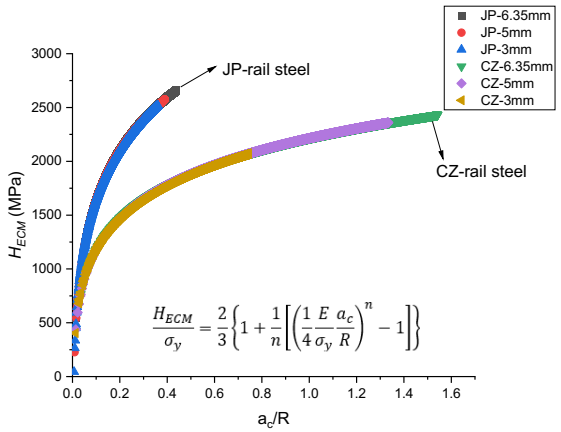

Figure 8. Variation of H_{ECM} with a_c/R of different rail steels

However, JP rail steel showed a higher H_{ECM} value than CZ due to heat treatment process. While H_{ECM} is used to indicate the variation in the indentation process with indentation depth, it also suggests the possibility of quantifying the rail steel's deformation behaviour as seen in tensile tests. With the information of H_{ECM}, K_J can be attained for the estimation of fracture toughness using the procedures outlined in Figure 3. Figure 9 shows an illustration of the variation of virtual SENB force and depth calculated by the varying h' values.

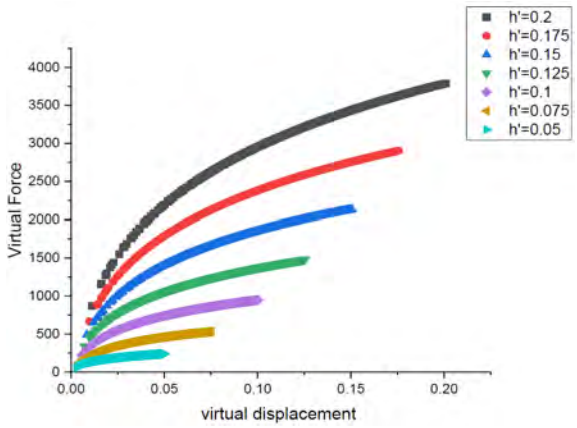

Figure 9. Virtual SENB force-displacement estimation

Important parameters like the J_e and J_p are estimated using Equations 10 - 11 for the determination of K_J. A summary of these parameters is shown in Table 3 for the 3mm spherical indentation for JP and CZ rail steels.

Table 3. Stress intensity factor estimation.

Rail steel	h' (mm)	ac' (mm)	P' (N)	Apl (mm)	K_J (MPa.m$^{0.5}$)
JP	0.2	0.4551	1622.55	231.30	277.85
	0.175	0.3982	1242.26	148.12	254.28
	0.15	0.3414	912.68	90.23	231.66
	0.125	0.2845	633.81	53.24	213.47
	0.1	0.2276	405.64	27.98	193.37
	0.075	0.1707	228.17	11.64	166.30
	0.05	0.1138	101.41	3.56	137.83
CZ	0.2	0.9882	5125.79	470.48	183.60
	0.175	0.8647	3924.44	315.18	171.74
	0.15	0.7412	2883.26	198.48	159.00
	0.125	0.6176	2002.26	114.86	145.15
	0.1	0.4941	1281.45	58.81	129.83
	0.075	0.3706	720.81	24.81	112.43
	0.05	0.2471	320.36	7.35	91.80

Hence, applying Equation 10 and extrapolating a_c' to zero, the critical stress intensity factor is estimated for both JP and CZ rail steels. Figure 10 and Table 4 shows an illustration of the critical indentation stress intensity factor estimation and a summary of the critical stress intensity factor estimated for all three indenter sizes compared with the ASTM 1820 approach for K_{IC} determination, respectively.

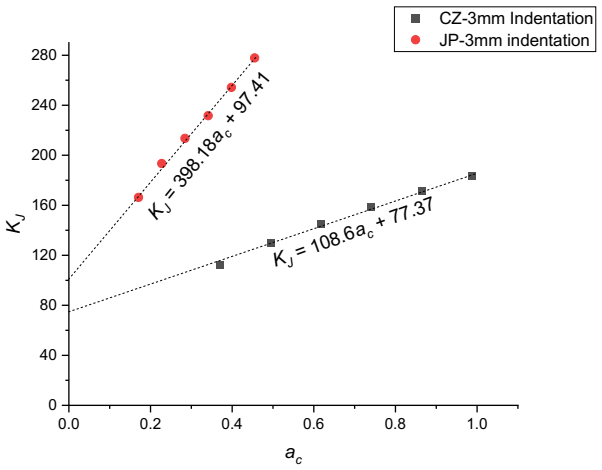

Figure 10. Critical stress intensity factor estimation for rail steels.

Although the K_{JC} estimated via the modified limit load analysis has a higher magnitude as compared with the ASTM approach for fracture toughness, the trend shows that JP rail steel has a higher fracture toughness than CZ rail steel, which needs further studies with other rail steels as well as in its methodology.

Table 4. A summary of critical stress intensity factor estimation.

Avg K_{IC} (MPa.m$^{0.5}$)	SENB	6.35mm	5mm	3mm
JP	39.5	97.78	98.23	97.41
CZ	34.00	77.02	76.31	77.37

4 CONCLUSIONS

The different approaches for Young's modulus, yield strength and hardness estimation showed that these mechanical properties can be effectively and closely estimated as compared with conventional testing approaches. The approach thus favors non-destructive testing for newly manufactured alloys or in-service materials if the indenter size is reduced significantly but at least at a size larger than the average grain sizes of the rail steels or other materials on interest in the aim of capturing an average value of its mechanical properties. The modified limit load analysis still has its challenges as it showed a promising trend to estimating fracture toughness but not the approximate value since it was possible to identify that JP has a higher fracture toughness than CZ. The modified limit load analysis still needs further study with other rail steels in capturing an estimate to the K_{IC} values as well as improving its methodology. Once fully understood, this means that fracture toughness values as well as mechanical properties can be estimated in different climate conditions, environments, inspection assessments (broken rails), new alloys and in-service monitoring exercise at a scheduled rate.

5 ACKNOWLEDGEMENT

This research was made possible through the Canadian Rail Research Laboratory (www. carrl. ca). The funding for this project was provided by the Natural Sciences and Engineering Research Council of Canada (NSERC-IRC 523369-18), the Canadian National (CN) Railway, the National Research Council of Canada, and Transport Canada.

REFERENCES

Anderson, T. L., & Osage, D. A. (2000). API 579: a comprehensive fitness-for-service guide. International Journal of Pressure Vessels and Piping, 77(14-15), 953-963.

A.S.T.M. Standard, E1820 Standard Test Method for Measurement of Fracture Toughness, ASTM International, West Conshohocken, PA, 2018. doi:10.1520/E1820-18.

ASTM (2010). ASTM E8/E8M standard test methods for tension testing of metallic materials 1. Annu B ASTM Standard, 4, 1-27.

Behnia, D., Hendry, M. T., Haji Abdulrazagh, P., & Wahba, A. (2022). Railway Dynamic Load Factors Developed from Instrumented Wheelset Measurements. Journal of Transportation Engineering, Part A: Systems, 148(7), 04022042.

Doerner, M. F., & Nix, W. D. (1986). A method for interpreting the data from depth-sensing indentation instruments. Journal of Materials research, 1(4), 601-609.

Leishman, E. M., Hendry, M. T., & Martin, C. D. (2017). Canadian main track derailment trends, 2001 to 2014. Canadian Journal of Civil Engineering, 44(11), 927-934.

Gao, X. L. (2006). An expanding cavity model incorporating strain-hardening and indentation size effects. International journal of solids and structures, 43(21), 6615-6629.

Gharaibeh, S. F., & Aburub, A. (2013). Use of first derivative of displacement vs. force profiles to determine deformation behavior of compressed powders. AAPS PharmSciTech, 14, 398-401.

Lee, H., Lee, J. H., & Pharr, G. M. (2005). A numerical approach to spherical indentation techniques for material property evaluation. Journal of the Mechanics and Physics of Solids, 53(9), 2037-2069.

Haggag, F. M., Nanstad, R. K., & Braski, D. N. (1989). Structural integrity evaluation based on an innovative field indentation microprobe (No. CONF-890721-25). Oak Ridge National Lab.(ORNL), Oak Ridge, TN (United States).

Haggag, F. M., & Nanstad, R. K. (1989). Estimating fracture toughness using tension or ball indentation tests and a modified critical strain model (No. CONF-890721-24). Oak Ridge National Lab. (ORNL), Oak Ridge, TN (United States).

Irwin, G. R. (1964). Structural aspects of brittle fracture. Applied materials research, 3(2), 65-81.

Kim, W., Choi, S., Kim, J., Jeon, S. W., Choi, M. J., & Kwon, D. (2021). Estimation of fracture toughness using flat-ended cylindrical indentation. Metals and Materials International, 27, 3186-3194. https://doi.org/10.1007/s12540-020-00753-2

Lee, J. S., Jang, J. I., Lee, B. W., Choi, Y., Lee, S. G., & Kwon, D. (2006). An instrumented indentation technique for estimating fracture toughness of ductile materials: A critical indentation energy model based on continuum damage mechanics. Acta materialia, 54(4), 1101-1109.

Miller, A. G. (1988). Review of limit loads of structures containing defects. International Journal of Pressure Vessels and Piping, 32(1-4), 197-327.

Okocha, S. I., Yu, F., Jar, P. Y. B., & Hendry, M. T. (2023a). Indentation Testing Method for Determining Mechanical Properties and Tensile Flow Curve of High-Strength Rail Steels. Experimental Mechanics, 63(5), 839-852.

Okocha, S. I., Yu, F., Jar, P. Y. B., & Hendry, M. T. (2023b). Use of a modified critical fracture strain model for fracture toughness estimation of high strength rail steels. Theoretical and Applied Fracture Mechanics, 127, 104069.

Oliver, W. C., & Pharr, G. M. (1992). An improved technique for determining hardness and elastic modulus using load and displacement sensing indentation experiments. *Journal of materials research*, *7*(6), 1564-1583. https://doi.org/10.1061/jtepbs.0000685.

Ritchie, R. O., Server, W. L., & Wullar, R. A. (1979). Critical fracture stress and fracture strain models for the prediction of lower and upper shelf toughness in nuclear pressure vessel steels. Metallurgical Transactions A, 10, 1557-1570.

Sharobeam, M. H., & Pomona, N. J. (1994, September). The load separation technique in the elastic-plastic fracture analysis of two-and three-dimensional geometries. In *NASA CONFERENCE PUBLICATION* (pp. 703-703). NASA.

Sneddon, I. N. (1965). The relation between load and penetration in the axisymmetric Boussinesq problem for a punch of arbitrary profile. International journal of engineering science, 3(1), 47-57. https:// Doi. org/ 10. 1016/ 0020- 7225(65) 90019-4

Stinville, J. C., Tromas, C., Villechaise, P., & Templier, C. (2011). Anisotropy changes in hardness and indentation modulus induced by plasma nitriding of 316L polycrystalline stainless steel. *Scripta Materialia*, *64*(1), 37-40.

TransportCanada, Rail transportation safety investigation report R20W0031. https://www.tsb.gc.ca/eng/rapports reports/rail/2020/r20w0031/r20w0031. html, 2020 (accessed 13 March 2022). https://www.tsb.gc.ca/eng/rapports-reports/rail/2020/r20w0031/r20w0031.html, 2020 (accessed 13 March 2022).

Voce, E. (1948). The relationship between stress and strain for homogeneous deformation. Journal of the Institute of Metals, 74, 537-562.

Xu, X., Kwok, T. W. J., Gong, P., & Dye, D. (2022). Tailoring the deformation behaviour of a medium Mn steel through isothermal anticritical annealing. Materialia, 22, 101422.

Yu, F., Jar, P. Y. B., & Hendry, M. T. (2018). Indentation for fracture toughness estimation of high-strength rail steels based on a stress triaxiality-dependent ductile damage model. Theoretical and Applied Fracture Mechanics, 94, 10-25.

Yu, W., & Blanchard, J. P. (1996). An elastic-plastic indentation model and its solutions. *Journal of materials research*, *11*(9), 2358-2367.

Canadian & Cold Regions
Rail Research Conference
2024

Injection of polyurethane foam for soil stabilization as part of a short line railway bridge wall repair

Rachel Mackenzie, & Wayne Bacon
Northern Lights Rail Ltd., Kinistino, Saskatchewan, Canada

Evan Manning PEng.
Pier Solutions / Fort Richmond Construction Inc., Saskatoon, Saskatchewan, Canada

ABSTRACT

As part of a bridge repair project on a short line railway, AP LIFT 430 polyurethane foam was injected behind the abutment walls of a timber bridge. The East abutment wall was not retaining soil following high Spring and storm runoffs and a longer-term solution for soil stability was sought by the railway. Of note, polyurethane foam was injected horizontally to fill the large and challenging soil void that would be impossible to fill from above. While it is too soon to assess improved soil stability, the installation process identified polyurethane foam as a material that is simple to source and install, appropriate for voids that are challenging to fill, and financially feasible for short lines and smaller operators.

1 INTRODUCTION

Northern Lights Rail Ltd. is a 37-mile short line railway operating between the communities of Birch Hills and Melfort in central Saskatchewan. West of Melfort at Milepost 108.8 of the Tisdale Subdivision, a 132' 8-span timber bridge crosses Goose Hunting Creek. Storm events in 2020 caused ice buildup, flooding, and high flow rates in Goose Hunting Creek, leading to bridge damage. Urgent repairs were undertaken in 2020 with further repairs to the stringers, piles, pilecaps, and backwalls recommended as part of a 5-year bridge maintenance plan. A 2022 inspection of Goose Hunting Creek bridge also noted that the East abutment backwall was not retaining soil.

It was important to Northern Lights Railway to make investments that both repaired existing damage and increased future climate resiliency. As water flow during storm and spring runoff events in this region is expected to increase (Pomeroy et al. 2009), it was important that the bridge infrastructure was prepared for future events and that the soil retention issue was addressed. A successful application to Transport Canada's Railway Climate Change Adaptation Program provided financial support towards necessary traditional bridge repairs in conjunction with the novel installation of injectable polyurethane foam in the East and West bridge walls. Important project considerations included the cost of the polyurethane foam versus traditional repair methods, access to foam and installation tools, and ease of installation.

The repairs to Goose Hunting Creek bridge included backwall plank replacement, pile stub rehabilitation, and polyurethane injection stabilization. Polyurethane foam was injected at regular intervals on the East and West walls of the bridge with a Ziplevel used to monitor track elevation. Foam installation was deemed complete when excess foam appeared at the injection points and monitoring showed that the backwall and rails were still in alignment.

Foam installation and bridge repairs were completed by PIER Solutions in late 2023. Inspection following Spring runoff and storm events in 2024 will provide indication of the foam and soil stability in the East abutment backwall of the Goose Hunting Bridge. Northern Lights Rail intends to share these findings with Transport Canada Innovation, the Western Canadian Short Line Railway Association, and any interested parties.

In the interim, this project demonstrates that polyurethane foam installation uses tools and processes easily available to bridge contractors, is either a feasible additional cost or potentially lower cost for smaller operators and can be used to fill challenging areas of soil erosion. If the foam remains stable through higher runoff events in 2024 and 2025, polyurethane foam could be recommended as an environmentally appropriate and cost-effective option for railway operators seeking soil stabilization for bridge projects.

2 MATERIALS AND METHODS

The repairs to Goose Hunting Creek bridge consisted of three activities: backwall plank replacement, pile stub rehabilitation, and polyurethane injection stabilization. This short paper focuses on the emerging technology of polyurethane injection stabilization.

2.1 Materials

AP Lift 430: AP LIFT 430 is a two component, high strength, high density, hydro insensitive structural polyurethane foam. Unconfined density is approximately 2.75 to 3.25 lbs/cubic foot (44 to 52 kg/cubic meter). Appropriate uses of AP Lift 430 include soil stabilization, filling voids, and lifting concrete slabs. AP Lift 430 bonds with soil, displaces water, and is appropriate for wet environments. The material is certified by ALS Global to NSF/ANSI/CAN 61 (approved for contact with drinking water). (Alchatek 2023).

Required tools for AP Lift 430 installation include proportioning pump with heated lines, drill bits, MixMaster Pro injection gun, ports, AS Pump Flush, soil probes. (Alchatek 2023)

A Ziplevel was used to monitor track elevation during polyurethane foam injection.

2.2 Methodology

1. Injection points are drilled at regular intervals to both provide a place to insert the probe and provide monitoring points to ensure even application of the product.
2. Working sequentially across the injection points, AP Lift 430 is injected with low pressure to allow the polyurethane resin to penetrate the soil, spread out, and fill all voids.
3. Soil lift must be monitored using specialized tools to ensure the rails do not get misaligned. Monitoring informs pressure regulation requirements for the operator.
4. The installation is finished when each of the injection points shows excess foam indicating that the voids are filled and monitoring shows that the backwall and rails have not been pushed out of their intended alignment.

3 RESULTS AND DISCUSSION

Extensive damage to the bridge walls and piles were visible prior to project commencement (Figures 1, 2, 3). Backwall and pile repairs were completed but soil voids remained behind the East abutment wall (Figures 4, 5). Polyurethane foam was injected into the soil voids in the East back and abutment walls (Figures 6, 7, 8). Due to the risk of track misalignment due to excessive pressure from below during and following the foam installation, track elevation was monitored throughout the installation process (Figure 9). Foam installation was completed with filled soil voids and consistent track elevation (Figure 10).

Figure 1. East abutment existing piles 1, 2, 3 prior to bridge repair and polyurethane foam injection. Note the granular falling through the undermined backing planks.

Figure 2. East abutment existing piles 2, 3, 4, 5 prior to bridge repair and polyurethane foam injection. Note the soil erosion near the bottom of the photo.

Figure 3. Damaged backing planks on the West abutment wall prior to bridge repair.

Figure 4. Following backwall and pile repairs, there were backwall soil voids that could not be filled or packed from above.

Figure 5. Backwall soil void on East abutment wall measured approximately 12 inches following backwall and pile repairs and prior to polyurethane foam injection.

Figure 6. Following armouring and rip rap installation on East abutment wall, voids in the soil were injected with polyurethane foam.

Figure 7. Polyurethane foam injection. Note excess foam at injection site.

Figure 8. Polyurethane foam is injected into the backwall voids of the East abutment wall.

Figure 9. The track elevation is monitored using a ZipLevel which provides pressure feedback to the injection operator during polyurethane foam injection.

Figure 10. East abutment wall following project completion.

4 CONCLUSIONS

This project utilized a combination of traditional materials (riprap, planks, piles) with the novel injection of AP LIFT 430 polyurethane foam to repair bridge damage and soil loss. Repairs to bridge piles and backwall were completed first and the contractor noted that backwall soil voids remained that could not be filled from above using traditional methods. In this instance, repair was still possible as the foam could be injected horizontally through the bridge wall timbers to fill the soil void. As the AP LIFT 430 product bonds with soil, displaces water, and is approved for use near water bodies, it was an appropriate choice to fill the void behind the back wall.

The installation of polyurethane foam on the East and West walls of Goose Hunting Creek bridge represented $30,000 of the project cost. Due to the challenging placement of the soil void and the inability to fill the void from above, a traditional repair of the backwall void without using AP LIFT 430 polyurethane foam would have involved shutting down the track, removing track and ties, digging up the abutment, installing geo backfill, and replacing the track materials at an additional cost of $70,000-100,000 plus mobilization. Compared to a traditional repair, the cost of using polyurethane foam is desirable and financially advantageous for small operators. Installation was straightforward for the contractors.

The stability of the foam and soil will be monitored following future Spring runoff and storm events. While it is too soon to know if the foam provides increased soil stability behind the bridge backwall in times of higher runoff, the existing soil loss demonstrated that traditional methods were no longer appropriate to protect Goose Hunting Creek bridge from higher water flows.

5 ACKNOWLEDGEMENT

The authors would like to express appreciation for the financial support of the Government of Canada through the Transport Canada Railway Climate Change Adaptation Program. Project Number: 164743.

REFERENCES

Alchatek. (2023). Technical Data Sheet: AP LIFT 430. Accessed January 15, 2024 from https://alchatek.com/wp-content/uploads/AP-Lift-430-TDS.pdf

Pomeroy, J.W., Fang, X., & Williams, B. (2009), Impacts of Climate Change on Saskatchewan's Water Resources. University of Saskatchewan Centre of Hydrology. Accessed January 15 2024 from https://citeseerx.ist.psu.edu/document?repid=rep1&type=pdf&doi=549181d4f82da4a8cc25af7d5e6c63adcdfd09f7